Thesis for the Degree of Doctor of Philosophy

INVESTIGATION OF FANO RESONANCES IN SYMMETRIC AND ASYMMETRIC THREE DIMENSIONAL PLASMONIC NANOSTRUCTURES

Adnan Daud Khan

Department of Electrical Engineering

University of Naples “Federico II”

Naples, Italy

March, 2013

INVESTIGATION OF FANO RESONANCES IN SYMMETRIC AND ASYMMETRIC THREE DIMENSIONAL PLASMONIC NANOSTRUCTURES

by

Adnan Daud Khan

Supervised by

Prof. Giovanni Miano, PhD

Submitted to the Department of Electrical Engineering

University of Naples, "Federico II" in partial fulfilment

of the requirements for the degree of

Doctor of Philosophy

Prof. Giovanni Miano (Ph.D Advisor) ……..

Prof. Guglielmo Rubinacci (Ph.D Co-advisor and Co-ordinator) ……..

Abstract

Line shaping of localized surface plasmon oscillations in plasmonic nanostructures is a fundamental and application driven research in biomedicine, sensing, energy and optical communication. Such metallic nanostructures with careful arrangement can also support Fano like resonances. These resonances usually crop up from the coupling and interference of a non-radiative mode (dark mode) and a continuum (bright mode) of radiative electromagnetic waves and are distinguished from their Lorentzian counterpart by a distinctive asymmetric line shape and they are typically more sensitive to the geometry of the nanoparticle and changes of the refractive index of the environment. The role of the symmetry breaking in the coupling between the plasmon modes of the individual parts of the layered and neighboring metallic nanoparticles is very important. The reduction of the symmetry of the system relaxes the dipole coupling selection rules resulting in a mixture of dipole and higher order modes. The understanding of this coherent mode coupling will enable the engineering of plasmon line shaping.

The focus of this work is to examine theoretically various symmetric and asymmetric plasmonic nanostructures to study the effect of Fano resonances. The proposed nanostructures include spherical, cubical, elliptical, cylindrical and conical geometries with multicomponents as well as nanoparticle pairs (dimer). These nanostructures are designed in such a way that the broad superradiant and narrow subradiant plasmon modes overlap in energy, resulting in a strong Fano resonance in the optical spectrum, which is characterized by a sharp dispersion than the conventional plasmon resonances. Different kinds of new symmetry breaking schemes have been introduced in the layered Fano resonators, which mixes plasmonic modes of distinct angular momenta and provides a set of unique and higher order tunable Fano resonances. The generation of multiple Fano resonances with large modulation depths in the asymmetric Fano resonators are greatly appropriate for multi-wavelength surface-enhanced Raman scattering and plasmon line shaping by modifying the plasmon lines at various spectral locations simultaneously. In addition, the tunable strong Fano like resonance obtained in the conical dimer resonator can be useful for plasmon induced transparency and the local near fields in the “hot spots” are essential for the near field applications. Among all the Fano resonators, the polarization dependent conical Fano resonators have shown striking properties such as high tunability of Fano resonances, as well as the control on resonant electromagnetic field enhancement and scattering direction. Eventually, the optical responses of all the symmetric and asymmetric Fano resonators are well replicated using a mass-spring mechanical analogy and analytical model of Fano line shape. The observations in this thesis may lead to new opportunities to tailor near and far-field optical properties of plasmonic nanoparticles for specific applications, such as high performance surface-enhanced spectroscopy, electromagnetic induced transparency, biosensing, plasmon line shaping, lasing, nonlinear and switching.

Acknowledgements

I would like to thank the University of Naples “Federico II” for the wonderful opportunity to let me contribute to the nanoscience research. Nanoscience research at Naples is very active, particularly; the faculty members represent the leading experts in the field of nanoplasmonics. I would like to express my heartiest appreciation and gratitude to my supervisors, Prof. Giovanni Miano and Prof. Guglielmo Rubinacci for their invaluable guidance and great support throughout my PhD course. I would like to thank them for giving me numerous opportunities to learn and grow as a PhD student. Particularly, I am truly grateful to Prof. Miano for his kind assistance towards the difficulties that I have faced in my personal life as well as his infinite passion in research work, which inspires me to work hard. Thank you for transmitting to me the taste for research during these three years spent at UNINA.

It is my pleasure to appreciate my lab members, Antonio Capretti and Simone Minucci as well as my friends in other departments, Naveed Ahmad, Tayyab Naqash, Muhammad Amin, Md. Arafatur Rahman, Muhammad Nauman and Yasir Iqbal. I am also grateful to Massimo Nicolazzo for helping me in COMSOL installation and teaching several commands in Linux. I deeply appreciate the time shared with all of you and wish you the best luck in your careers.

Finally, I would like to give my great thanks to my family members, Ghulam Daud Khan, Sultan, Sohail and Aimal for being supportive throughout.

Adnan Daud Khan

Naples, Italy.

March, 2013.

Table of Contents

List of Figures

Glossary

σ_{abs}	Absorption cross section
Q_{av}	Average dissipated power
H_0	Magnetic field
λ	Wavelength
ε_0	Electric field constant, 8.854×10^{-12} F/m
μ_0	Magnetic field constant, $4\pi \times 10^{-7}$ N/A^2
σ_{scat}	Scattering cross section
$\boldsymbol{E}_{far}$	Far field component of the scattered field
$\boldsymbol{E}_T$	Total electric field
η_p	Electromagnetic near field enhancement at a specific point
σ	Surface charge density
p	Dipole moment
x_1, x_2, x_3	Positions from rest
ω_1	Oscillator $\|1\rangle$ / bright mode's resonance frequency
ω_2, ω_3, ω_4	Oscillators $\|2\rangle$, $\|3\rangle$, and $\|4\rangle$ / dark mode's resonance frequency
Ω_{12}, Ω_{13}, Ω_{23}	Oscillators coupling
γ_1, γ_2, γ_3, γ_4	Harmonic oscillator damping constants
$F(t)$	Time harmonic force
$P(\omega)$	Absorbed power from the oscillator
σ_L	Lorentzian line shape
a	Resonance amplitude
ω_L	Bright mode's resonant frequency
W_L	Bright mode's spectral width
σ_F	Fano resonance line shape
ω_F	Fano resonance central spectral position

W_F	Fano resonance spectral width
q	Asymmetry parameter
b	Modulation damping parameter emerging with intrinsic losses
σ_T	Total line shape

Acronyms

LSPR	Localized surface plasmon resonance
EIT	Electromagnetic induced transparency
PIT	Plasmon induced transparency
SERS	Surface enhanced Raman spectroscopy
DDA	Discrete dipole approximation
FDTD	Finite difference time domain
FEM	Finite element method
IE	Integral equation
FEM	Finite element method
PML	Perfectly matched layer
MNS	Multilayered nanoshell
DNS	Double nanoshells
NC-MNS	Non-concentric multilayered nanoshell
DDF	Dipole-dipole Fano resonance
DQF	Dipole-quadrupole Fano resonance
DOF	Dipole-octupole Fano resonance
DHF	Dipole-hexadecapole Fano resonance
MNS-NG	Multilayered nanoshell nanoegg
NC-DNS	Non-concentric double nanoshells
NC-INS	DNS with non-concentric inner nanoshell
NC-SRINS	DNS with non-concentric symmetry reduced inner nanoshell
DNS-NG	DNS nanoegg
NC	Nanocone
CNS	Conical nanoshell
MNC	Multilayer nanocone
S_1, S_2, S_3	Outer, intermediate and inner surfaces of multilayer nanocone

NC-MNC	Non-coaxial Multilayer nanocone
MNEC	Multilayered nanoegg cone
MNFE	Maximum near field enhancement
PEC	Perfect electric conductor
PMC	Perfect magnetic conductor
MND	Multilayered nanodice
NC-MND	Non-concentric multilayered nanodice
MNE	Multilayered nanoellipsoid
MNCD	Multilayered nanocylinder
MNDK	Multilayered nanodisk
HNC	Hollow nanocone
NC-CNS	Non-concentric cone nanoshell
CNG	Conventional nanoegg
FoM	Figure of merit
CR	Contrast ratio
BW	Bandwidth
FWHM	Full width at half maximum
RIU	Refractive index unit
DDB	Dipole-dipole bonding mode
DQB	Dipole-quadrupole bonding mode

Chapter 1

Fano Resonances in Plasmonic Nanostructures

1.1. Introduction

The resonance phenomenon is typically considered to be an enhancement of the response of some system to an external excitation at a specific frequency. Many physical systems exhibit such phenomenon. It was first acknowledged by Galileo Galilei in 1602 while working on musical strings. Latter, it was established that mechanical, acoustic and electromagnetic resonances are a universal feature of many kinds of classical and quantum system [1]. These resonances were explained by the symmetrical Lorentzian formula, which was considered to be a fundamental line shape of a resonance for many years.

Ugo Fano, an Italian physicist experimentally observed a new kind of asymmetric line shape of a resonance in the absorption spectra of noble gases in 1935 [2]. The nature of the asymmetry is then theoretically explained by him in a quantum mechanical study of the auto-ionizing states of atoms in 1961 that now bears his name (Fano) [3]. Fano theory hence explained that the sharp asymmetric line profile arises due to the overlapping of a discrete state with a continuum state, where destructive and constructive interference phenomena take place at close energy positions. In 1931, Ettore Majorana draw similar conclusion while working on the selection rules for the non-radiative decay of two electronic excitations in atomic spectra, involving the configuration interaction between discrete and continuum channels [4]. His work presents a vital step for understanding the 1935 work of Ugo Fano on the asymmetric line shape of two electron excitations.

The first asymmetric line shape was traced by Wood in 1902 that now connects to plasmonics field [5]. While working on metallic grating, he was astonished to see that under special illumination conditions, the grating efficiency goes up and down. These hasty variations in the intensities were named Wood's anomalies. However, no satisfying description was found at that time. So the first understanding of the profile was provided by Fano by suggesting that anomalies could be associated with the excitation of a surface waves along the grating.

This phenomenon has been studied extensively for quantum systems and in the classical system of coupling oscillators [6]. Nowadays, Fano resonances have been observed in various systems including quantum dots [7], nanowires and tunnel junctions [8], bilayer graphene structures [9], plasmon scattering in Josephson-junction networks [10] and matter-wave scattering in ultra-cold atom systems [10] plus in numerous optical systems such as strong coupling between Mie and Bragg scattering in photonic crystals and metamaterials [1, 10]. In all these systems, the most emerging technology is the field of plasmonics that squeezes electromagnetic waves into nanoscale structures and this technology proved to be a keen platform in the generation of Fano resonances. The direct optical excitation of surface plasmons on metallic nanostructures offers several techniques to control and manipulate light at nanoscale dimensions such as varying the geometry or composition of nanoparticles etc. Localized surface plasmon resonances (LSPR) are charge density oscillations on the closed surfaces of the noble metal nanoparticles such as gold and silver. They have potential applications in chemical and bimolecular sensing because the LSPR can be tuned from visible to near infrared region by changing the shape, size and local dielectric environment of

the plasmonic nanoparticles [11, 12]. LSPR have the capability to effectively scatter, absorb and squash light, creating large enhancement of electromagnetic field amplitudes due to which it can be used for Raman scattering or infrared absorption spectroscopy applications.

Plasmonic systems are a perfect option to produce Fano resonances with sharp dispersion, which make them promising for sensing applications. In such systems, the Fano resonances are accomplished through the interference of a plasmon resonance, which acts as a continuum state, with a discrete state. For example, in the interference of two different excitation path ways, if in one path the continuum state is excited and in the other path a discrete state then Fano resonances will take place [13]. The Fano line shape is quite different from the symmetric Lorentzian line shape and is analogous to the electromagnetic induced transparency (EIT) in atomic system. In a three-level atomic system, EIT usually emerges due to a quantum destructive interference between two pathways provoked by another field that can build an absorptive medium transparent to the probe field. So in metallic nanostructures, Fano resonance is similar to EIT by rising a phenomenon known as Plasmon Induced Transparency (PIT) [14, 15]. Recently, several plasmonic nanostructures have been investigated widely both theoretically and experimentally to study the effect of higher order dark multipolar modes and Fano resonances. These nanostructures include nanodisks [16], nanorods [17-19], nanorice [20, 21], nanoshells [22-29], ring/disk nanocavities [30-35], nanocross [36-38], dolmen structures [39-42], dimers [18, 19, 26, 43-48], trimers [49, 50], quadrumers [51, 52], pentamers [53], heptamers [54] and nanoparticle chains [55]. These nanostructures are among the most important future optical materials for new devices, containing sensors, logic circuits, slow light components and metamaterials. The Fano resonances in these nanostructures can be achieved either by the interaction of (anti parallel) dipolar modes or by the interactions of the dipolar mode with higher order modes, like the quadrupole and the octupole modes. When the size of the nanostructure is very small compared to the wavelength of incident light (Rayleigh limit ($\lambda >> d$)) then only dipolar modes are excited by the incident light. The higher order dark modes can be excited either by increases the size of the nanoparticle or by symmetry breaking.

1.2. Literature review

As discussed before, surface plasmons are the combined oscillations of conduction and bound electrons in metallic nanoparticles driven by an external electromagnetic field at optical frequencies, which is accountable for the considerable enhancement of the electric field in the vicinity of metallic nanoparticles and for the rich and complex features of the scattered light. A number of applications, such as chemical and bimolecular sensing, photo thermal cancer therapy, metamaterials and surface-enhanced Raman spectroscopy (SERS), are based on surface plasmons. Several plasmonic nanostructures has been proposed to achieve Fano resonances in their optical spectra. They have received much attention due to hasty progress in the fabrication and characterization techniques [23, 43, 45, 56-59]. Single nanoparticle can support different plasmon modes with distinct line widths. Broad dipolar plasmon modes possess finite dipole moments and can couple well to incident light. They are usually named as bright modes. The resonance peak of the bright plasmon modes is spectrally broadened by reason of radiative damping. On the other hand, narrow plasmon modes acquire zero or almost zero dipole moments. They do not couple efficiently to the external electromagnetic field, therefore not radiatively broadened. They are usually named as dark modes [16]. The existence of both the bright and dark modes in a nanostructure results in Fano resonances. For complex nanostructures of arbitrary shape, the plasmonic response can be understand using a powerful tool know as plasmon hybridization model [60, 61]. The

splitting of the modal energies into bonding and antibonding modes is due to the coupling between individual plasmon modes. Several plasmonic nanostructures exhibiting Fano resonances in their optical responses are briefly explained below.

1.2.1. Fano resonance in single nanoparticle

Reported study showed that single nanoparticle usually exhibits a single bright dipole mode. However, Fang *et al*., have achieved Fano resonance in a single planar nanodisk nanoparticle by the symmetry breaking conception [16]. Symmetry is broken by removing a slice form the disk in wedge shape due to which the interactions between a hybridized dipolar plasmon mode of the disk and a narrower quadrupolar mode of the wedge-shaped slice occur, which results in a Fano resonance. Both the nanodisk size and wedge angle control the properties of the Fano resonance. They also demonstrated a semi-analytical method that provides a useful way to investigate coherent coupling and Fano line shapes in a single planar nanostructure. The reduced symmetry nanodisk was fabricated using electron-beam lithography in a positive resist on a silica substrate. The nanostructures were generated by electron beam evaporation followed by a lift-off process. Scanning electron microscopy was used to obtained the normal incidence images of the fabricated structures. They suggested that, this nanostructure can be used in metamaterials, slow light, electromagnetically induced transparency, and light bending and switching applications. Reed *et al*., have demonstrated theoretically the Fano line shapes resulting from silver nanorod, which is due to the coupling of an in plane quadrupole and a dipole mode in the nanostructure. They also observed a new Fano resonance, which occurs when the symmetry of the nanorod is broken and is a result of the asymmetric coupling between the two excited dipoles [62].

1.2.2. Nanoparticles near dielectric substrate

For a nanoparticle in vacuum, there is no coupling and interference between the bright dipolar and dark multipolar modes. Nevertheless, Zhang *et al*., reported that when the nanocube is deposited on a dielectric substrate, the image of a dipolar mode will have a substantial quadrupolar field component across the nanoparticle, which will introduce a coupling between the dipolar and quadrupolar plasmon modes resulting in a Fano resonance [63]. Their study presents an approach for optimizing the sensitivity of nanostructures, whether chemically synthesized or grown by deposition methods, as high performance localized surface plasmon resonance sensors. Chen *et al*., have reported a theoretical and experimental study of gold nanorod on dielectric substrate. They showed that, substrates with large dielectric constants can efficiently mediate the hybridization between different plasmon modes in a gold nanorod especially the coupling between quadrupole and octupole modes in a large nanorod, which can produce a Fano resonance in the spectrum [17]. The Fano resonance achieved in a nanorod deposited on dielectric substrate can be tuned or switch on and off by changing the space between the nanoparticle and substrate. Recently, Fernando *et al.*, have suggested two different arrangements of nanoparticles i.e., a colloidal suspension of nanospheroids (nanorice) and a single nanowire with rectangular cross section (nanobelt) on top of a dielectric substrate for which the Fano like interference of longitudinal plasmon resonances taking place at individual metallic nanoparticles that can be easily utilize in refractive index sensing [20]. They have studied numerically the performance of the two configurations in terms of their figures of merit, which were calculated under realistic conditions.

1.2.3. Multi-branched nanostructures

Multi-branched nanostructures include plasmonic nanocross and dolmen nanostructures that support higher order dark modes and Fano resonances. The nanocross geometry is usually made from intersecting nanobars while the dolmen nanostructure is made from three metallic beams, two parallel beams and the third beam is placed perpendicularly on top of the two beams. Verellen *et al*., proposed a wide experimental and theoretical study of a planar nanocross, supporting higher order plasmon modes [36, 37]. The symmetry breaking is introduced by adding extra arms, changing the arm angle and shifting the arm intersection point due to which pronounced dipole, quadrupole, octupole and Fano resonances are examined in individual nanocross structures. The Fano resonances can be tuned by changing the cross arm length and the angle between the arms [36, 37]. The nanocross geometry proves to be a valuable building block for coherently coupled plasmonic dimers and trimers, where the modes coupling produced hybridized subradiant and superradiant modes and multiple Fano interferences [37]. They also observed that high quality factor subradiant Fano resonances are produced in a nanocross and nanobar due to the coherent coupling and interference of the bright and dark plasmon modes. Furthermore, they obtained experimental sensitivities for these modes exceeding 1000 nm/RIU with a Figure of Merit approaching 5 in the near infrared region, which may provide a constructive platform for biochemical sensing applications as well as plasmonic lasing [36].

Plasmonic dolmen nanostructures have received much attention in metamaterials [40, 64-66]. The two parallel beams of a single dolmen support a quadrupolar dark mode with much narrow line width, while the third perpendicular beam supports a bright dipolar mode with broader line width. The interference between the two modes give rise to Fano like resonance, which can be tuned and enhanced by changing the gaps between the beams and beams locations [39, 41, 42, 67, 68]. Verellen *et al*., have presented theoretically and experimentally the appearance of Fano resonances in dolmen nanostructure, which arises due to the coupling of dark quadrupolar and higher order modes with bright dipolar modes. They observed that these Fano resonances strongly depend upon the polarization of incident light and nanoparticle geometry and such structure can be used for sensing applications [42]. Gallinet *et al*., have studied extensively the dolmen nanostructure supporting Fano resonances with an electromagnetic theory by deriving a closed-form analytical expressions of the resonance parameters. They suggested that, the insights into the physical understanding of Fano resonances achieve by the proposed model will be of huge attention for the design of plasmonic systems with specific spectral responses for applications such as sensing and optical metamaterials [39, 41, 68].

1.2.4. Plasmonic nanodimer

Plasmonic dimer nanostructure containing two closely adjacent metallic nanoparticles also support Fano like resonance [18, 19, 43-48, 69-71]. The plasmon modes of the first nanoparticle couple primarily with the plasmon modes of the second nanoparticle due to which a broad peak and a narrow peak emerges in the spectrum, which can be categorized as bright and dark plasmon modes. The coupling and interference between the two modes of the dimer results in a sharp Fano resonance which is characterized by a dip in the spectrum. The modulation depth of the Fano resonance can be tuned and enhanced either by varying the size of one of the nanoparticle or by varying the interparticle gap. Brown *et al*., have experimentally and theoretically analyzed heterodimers of different size and shapes that gives rise to properties such as Fano resonances, avoided crossing behavior, and optical nanodiode effect [44]. Yang *et al*., have theoretically investigated the plasmon coupling in metallic

nanorod dimers. They observed a pronounced dip in the optical spectrum due to plasmonic Fano resonance which is induced by destructive interference between bright dipole mode of the short nanorod and dark quadrupole mode of the long nanorod [19]. They also investigated the optical emission response of a single nanoemitter placed at either apex of the nanorod dimer, which couples with a dimer and induces Fano resonances. However, they observed no Fano resonance when the nanoemitter is placed in the gap of the dimer [18]. Rodríguez *et al*., have shown that gold and silver nanoparticle heterodimers can be optimized to create strong Fano resonance signals that can be measurable by standard spectroscopic techniques. They observed that maximum intensity of the Fano resonance is accomplished when the size ratio of the nanoparticles (gold:silver) is close to 3:1. The Fano resonance is also twice as sensitive as the corresponding surface plasmon resonance to changes in the refractive index of the surrounding medium for values below 1.5 and these results could be used for optical sensing applications [70]. Shao *et al*., have proposed the plasmon coupling between a gold nanorod and a small gold nanosphere both theoretically and experimentally. They observed that the plasmon resonance of the nanorod is highly modulated by that of a small nanosphere. The rotational symmetry of the nanorod and nanosphere heterodimer is broken as they moved the nanosphere around the nanorod, making the coupled plasmon modes and their Fano interference to vary and also the dipole of the nanosphere is rotated around the nanorod to achieve favourable attractive interaction for the bonding dipole-dipole mode. This heterodimers can be utilized as a potential plasmon ruler of two spatial coordinates for sensing and high resolution measurements of distance changes [43]. Wu *et al*., have reported Fano like resonances in the absorption spectrum of an asymmetric homodimer of gold elliptical nanowires, which arises from the coherent coupling between the superradiant bright mode and the subradiant dark mode. They observed that by increasing in the rotation angle of one nanowire, the Fano dip in the absorption of the asymmetric dimer enhances first and then decreases. The modulation depth and position of the Fano resonance is controlled by changing the separation between two nanowires, which may provide effective applications in sensing and PIT [47]. Wu *et al*., have also investigated the influence of symmetry breaking on the plasmon resonance couplings in the gold nanotube dimer and observed strong Fano like resonance in the scattering spectrum due to the interference of the bonding octupole mode of the dimer with the dipole modes in the weak coupling model. In the strong coupling model of the dimer, a strong electric field enhancement at the gap of the dimer is produced, which is much larger than that in the symmetric gold nanotube dimer [46]. Recently, Zhang *et al*., have presented a plasmonic nanodimer consisting of a nanodisk and a nanoring. They observed that the bright dipolar mode of the nanodisk excites the quadrupolar, hexapolar, and octupolar resonance modes of the nanoring and form strong Fano dips. They show that the dimer nanostructure offer both high contrast ratio and figure of merit due to which it can be used for chemical and biological sensors [71]. The plasmonic dimer nanostructure has also received a huge attention for surface-enhanced Raman spectroscopy applications due to the hot spot produced in the gap between nanoparticles when incident light is polarized along the dimer axis [19, 44, 45, 72-77].

1.2.5. Plasmonic nanoparticle aggregates

The plasmonic nanoparticle aggregates consisting of more than two nanoparticles such as trimer, quadrumer, pentamer, hexamer and heptamer etc. These nanoparticles have been studied extensively both theoretically and experimentally for the generation of Fano resonances [53, 54, 78-85]. For symmetric nanoparticle clusters, one can categorize the collective plasmon modes of each constituent nanoparticle using group theory [1, 79]. For trimer and larger clusters the optical spectra reveal two or more hybridized plasmon resonances (dipolar and higher multipolar) that red-shift with decreasing nanoparticle

separation. In nanoparticle aggregates, by varying the interparticle separation, relative particle size, or breaking the symmetry, there is a large tunability of the modulation depth as well as the spectral position of the Fano resonance. The strength of the Fano resonance in these types of clusters sturdily depends upon the polarization of the incident electric field and the enhancement normally crop up in the seam between neighboring nanoparticles. Sheikholeslami *et al*., have proposed plasmonic trimer, where Fano like resonances have been observed, which arises from the interference and interaction of electric and magnetic modes. The near and far field optical properties of the nanoparticle trimer can be significantly changed by extremely small variations in the geometry. They suggested that interactions between electric and magnetic modes in plasmonic systems can be used for controlled nanoscale optical emission, surface-enhanced spectroscopies, ultrasensitive sensors, and active metamaterials [49]. Fan *et al*., have demonstrated that clusters of four identical spherical particles (asymmetric quadrumer) exhibit strong Fano like interference. They observed that the strength of Fano resonance is highly sensitive to the polarization of the incident electric field due to orientation dependent coupling between particles in the cluster. They calculated the figure of merit and sensitivity of the quadrumer, which are 6.7 and 647 nm/RIU and suggested that quadrumer structure can be used for LSPR sensing application [51]. Rahmani *et al*., have designed and fabricated a symmetric quadrumer nanostructure, which consists a central nanodisk surrounded by three similar nanodisks belonging to the D_{3h} point group. They observed that the interference between the subradiant and superradiant modes in quadrumer leads to a strong Fano resonance at normal incident light and independent of the excitation polarization. They also established that the quadrumer's arrangement allows localization of the near field energy selectively by varying the excitation polarization due to which it can find applications in nano-lithography, optical switching and nonlinear spectroscopy [52]. Rahmani *et al*., further demonstrated the design and fabrication of arrays of plasmonic pentamers consisting of five metallic nanodisks to obtained a pronounced Fano resonance under normal incident light along all orientations of polarization. The pentamer was designed by adding a central disk into the center of quadrumer due to which an anti-parallel coupling of dipolar modes appears. The ratio between anti-parallel and parallel dipole modes were 2/3, which results in the generation of a pronounced Fano resonance [53]. Recently, Rahmani *et al*., have studied the effect of symmetry breaking in pentamers. They observed that by offsetting the central disk on an otherwise fixed geometry gives rise to additional Fano resonance in the same spectrum that can be used in LSPR sensing [80]. Bao *et al*., have proposed a hexamer and an octumer clusters consisting of a central particle and a surrounding ring of nanoparticles. The hexamer nanostructure consists of a central particle surrounded by five nanoparticles in ring shaped whereas; the octumer consists of a central nanoparticle surrounded by seven nanoparticles in ring shaped. For the hexamer of equally sized nanoparticles, the dipole moment of the ring is smaller than the dipole moment of the central particle, so no sharp Fano resonance is observed. By decreasing the size of the central particle, the antibonding mode becomes subradiant and a clear Fano resonance is produced. For the octumer consisting of equally sized nanoparticles, the dipole moment of the ring is larger than that of the central nanoparticle. Thus, by increasing the size of the central nanoparticle, the antibonding mode becomes subradiant and produces a sharp Fano resonance. They suggested that these clusters could be used for LSPR sensing [1, 79]. Mirin *et al*., have reported a symmetric septamer or heptamer, consisting of a central particle surrounded by six equivalent nanoparticles of the same sizes exhibiting a narrow Fano resonance in the spectrum. The interaction between the plasmon modes of the central particle with the plasmon modes of the surrounding ring nanoparticles results in hybridized bonding and antibonding plasmon modes, which interfere and produced a pronounced Fano resonance in the spectrum. This Fano resonance is observed to be well maintained by breaking the

symmetry of the heptamer [78]. Recently Liu *et al*., have reported a plasmonic heptamer composed of split nanorings with two gaps and achieved multiple Fano resonances that arises from the coupling of the quadrupole and dipole modes of each split nanoring with each other and there is a large tunability of the modulation depth for each Fano resonance by varying the geometry. They suggested that multiple Fano resonances are important for plasmon line shaping [54]. Chang *et al*., designed a plasmonic Fano switch by using an octamer cluster with a half disk as the central particle to achieve polarized Fano like and non Fano like spectra at orthogonal polarization directions [56]. Dregely *et al*., proposed large nanoparticle aggregates with multiple ring modes and elongated chains of nanoparticles surrounded by one ring of nanoparticles, which exhibit multiple Fano resonances due to the interference of one broad superradiant mode and multiple narrow subradiant modes. They showed that the number of nanoparticles and their respective arrangement in the cluster strongly influence the spectral position and modulation depth of the spectral signature of the supported modes. They suggested that large nanoparticle aggregates which supports higher order Fano resonances can be used for multi-wavelength SERS [86]. Recently, Jiao *et al*., have proposed a linear chain of nanoparticles. They observed that Fano resonances can be excited and tuned through nanoparticle number manipulation by adding or removing particles from the chain. The spectral overlapping of the fundamental bright dipole modes of the chain with different dark modes excited within the chain of different number of particles, resulting in the generation of Fano resonances [87].

1.2.6. Bimetallic nanostructures

The bimetallic nanostructures can be classified into ring/disk nanocavities, multilayer nanoshells and double nanoshells. These nanostructures offer highly tunable Fano resonances both in the visible and near infrared region that can be easily controlled by adjusting the dimensions of the nanoparticle. The ring/disk nanocavities consisting of a metallic nanodisk inside a thin metallic nanoring supports both the subradiant and superradiant dipolar plasmon modes with large associated field enhancements and high refractive index sensitivities [32, 88-90]. The ring provides higher order multipolar resonance modes (subradiant modes), which coupled with the disk dipolar mode (superradiant mode) resulting in Fano resonances. The symmetry breaking is introduced by moving the central nanodisk with respect to the surrounding ring due to which the interactions between bright dipolar mode of the disk and dark multipolar modes of the ring increases, which results in higher order Fano resonances [31, 33-35, 89]. Hao *et al*., have investigated both theoretically and experimentally the concentric and non concentric ring/disk nanocavities. They studied the effect of symmetry breaking in a plasmonic ring/disk cavity, where the quadrupolar ring resonance interacts with the dipolar disk resonance and an asymmetric Fano resonance emerges in the spectrum. They observed that the shape of the Fano resonance is altered and the resonance appears as a symmetric peak by changing the angle of incident light. They also presented large LSPR sensitivity and field enhancement of Fano resonance, which may be useful for LSPR sensing and surface-enhanced spectroscopies [33, 91]. Sonnefraud *et al*., demonstrated experimentally subradiant and superradiant plasmon modes in concentric ring/disk nanocavities and achieved multiple Fano resonances appear within the superradiant continuum when structural symmetry is broken, which could find applications in plasmon line shaping [35]. Cetin *et al*., have introduced a conducting metal layer underneath the asymmetric ring/disk nanocavity due to which stronger near field enhancements and Fano resonances with much sharper spectral features can be achieved. This kind of nanostructure with slight structural asymmetries, helps to reduce fabrication tolerance [89]. Niu *et al*., have reported dual disk ring nanostructure with broken symmetry, where the two disks are placed inside the ring to obtained Fano resonance in the visible range, which arises from coupling

between the subradiant octupolar mode of the ring and the superradiant dipole mode of the two disks. This kind of nanostructure can be used for refractive index sensing and surface-enhanced molecular sensing applications [34]. Fu *et al*., have further studied the dual-disk ring nanostructure and achieved a rich set of tunable Fano line shapes, which include quadrupolar, octupolar, hexadecapolar, and triakontadipolar Fano resonances by breaking the symmetry of the structure either by changing the sizes of the two disks or their asymmetric locations inside the ring. They suggested that, this nanostructure can be used as high performance biochemical sensor in the visible wavelength range [31].

Double nanoshells structure containing two alternating layers of dielectric and metal has been investigated in the plasmon hybridization picture. Due to its greater geometrical tunability from the visible to infrared regions of the spectrum, it has been mostly used for refractive index sensing based applications [22, 92-96]. Currently, Rodríguez *et al*., reported that by carefully selecting the geometrical parameters of such nanostructure, a dipole-dipole Fano resonance can be established in the optical spectrum, which can be tuned between 600 and 950 nm by varying the dimensions [22].

Recently, three dimensional multilayer nanoshells, containing a spherical metallic core, a dielectric spherical shell and an external metal spherical shell have attracted many researchers attention because of their controllably tunable plasmon resonances over the entire visible spectrum as well as near to mid infrared region by modifying the radius of the core, shell and the dielectric medium between them [22-24, 27, 96-104]. Xia *et al*., first reported the synthesis of multilayer nanoshells [105]. They coated gold colloid with a thin layer of silica using modified Stober method. Silica growth was preceded by a sodium silicate treatment in an aqueous solution with a controlled pH. The outer gold coating was created by the same method as that of a single nanoshell. So in this way, multilayer nanoshells can be synthesized. This method has been further refined by Bardhan *et al*., [23] and Mukherjee *et al*., [27] to fabricate multilayer nanoshells. Compared to conventional single layered nanoshell, a multilayered nanoshell has an advantage of realizing the localized surface plasmon resonance at wavelength of 1300 nm or longer, which is believed to be more beneficial to ultrahigh resolution optical coherent imaging and drug delivery applications [97, 106]. The extra degree of tunability is provided by the inner metallic core as explained by plasmon hybridization model. The plasmon oscillations of multilayer nanoparticles can be explained in terms of the interaction between the plasmon modes of the inner metallic core and the outer nanoshell, which will split the plasmon into lower energy bonding mode and higher energy antibonding mode. This nanostructure also supports large electromagnetic near field enhancement inside the dielectric layer, which is an influential attribute of SERS. Reported results show that the multilayered nanoshell can be designed and synthesized in such a manner that the broad superradiant and narrow subradiant plasmon modes overlap in energy and result in a strong Fano resonance in the optical spectrum. Shaunak *et al*., have studied gold-silica-gold multilayered nanoshell and achieved dipole-dipole Fano resonance in the concentric case by carefully arranged the dimensions of the nanoparticle. Higher order Fano resonances were obtained by breaking the symmetry of the structure [27]. Jin *et al*., have worked on weakly dissipating metal i.e., silver and achieved dipole-quadrupole Fano resonance in silver-silica-silver multilayered nanoshell in the concentric case. They observed that symmetry breaking via the introduction of core offset further enhances these Fano effects and leads to the emergence of higher order resonances [24]. Dajian *et al*., worked on gold-silica-silver multilayered nanoshell and obtained dipole-dipole and dipole-quadrupole Fano resonances in the concentric case, which can be tuned and enhanced by varying the radius of the inner core, middle silica layer and outer silver shell [29]. Rodríguez *et al*., studied gold-

silica-gold multilayered nanoshell and suggested that by carefully selecting the geometrical parameters, the position of the dipole-dipole Fano resonance can be tuned between 600 and 950 nm and its intensity can be amplified up to four fold with respect to the non-optimized structures [22]. Wu *et al*., reported the effects of anisotropic permittivity and permeability in inner core on the Fano resonance in silver nanoshell. They observed that the Fano resonance shows a red-shift and the magnitude of Fano profile increases by enhancing the tangential permittivity or permeability of inner core. They further demonstrated that enhancing both the tangential permittivity and permeability of inner core can produced a strong enhancement of Fano resonance [107]. Wu *et al*., have further reported the affect of the spherical anisotropy of a middle layer on the plasmon resonance couplings in the sandwiched gold nanoshell. They observed that, the couplings in such nanostructure are more sensitive to the permittivity along the radial direction of spherical anisotropy layer than the permittivity along the tangential direction. They also established that, the middle spherical anisotropy layer with smaller anisotropic value is useful to attain larger electric fields inside the nanoshells, which may be useful in nonlinear optics and SERS [100]. Chen *et al*., have demonstrated a symmetric system of gold nanosphere coated with dielectric shells that can induce distinct Fano resonance, which arises from the interference of the narrow plasmon resonance of the gold nanosphere core and the broad scattering background of the dielectric shell. They further examined that, the refractive index of the dielectric shell can also affect the Fano resonance behaviour, including its spectral position and shape. They proposed that, this nanostructure can be used in optoelectronic and sensing applications that exploit Fano resonances [108]. In all the study of the multilayered nanoshell reported before, the symmetry breaking is introduced by offsetting the inner metallic core, which will enhanced the interaction between the plasmon modes. The increased interactions causes higher order dark multipolar modes emerges in the spectrum, which couples to the superradiant dipole mode and induces higher order Fano resonances [24, 27].

In the light of the above findings in the existing literature by different researchers, In this thesis, we focus on the theoretical study of Fano resonances in different hybrid plasmonic double and multilayered nanostructures as well as a dimer nanostructure. All the nanostructures support subradiant and superradiant plasmon modes together with Fano resonances. Different kinds of new symmetry breaking conception has been introduced in all the layered nanostructures to achieve unique multiple Fano resonances with large modulation depths, which play an important role in varying the plasmon lines at several spectral locations simultaneously compared to a single Fano resonance and also these multi-Fano resonances are constructive in multi-wavelength SERS and biosensing. In addition, the tunable strong Fano like resonance in the conical dimer nanostructure can be useful for plasmon induced transparency and the local near fields in the "hot spots" are essential for the near field applications. To sum up the symmetry breaking conception, mode coupling effects and Fano resonance generation in plasmonic nanostructures, besides the plasmon hybridization theory, we used mass-spring coupled oscillator analogy and analytical expressions of Lorentzian and Fano line shapes.

1.3. Methodology

For theoretical studies of plasmonic nanostructures, several tools have been developed. The nanostructures with spherical and ellipsoidal symmetries, the analytical theories like Mie and Gans respectively have been used but these theories are limited only to spherical, ellipsoidal and concentric geometries [109]. For irregular complex nanostructures or symmetry broken nanoparticles various numerical techniques are used, which provide results

that are more accurate and become the preferred method. These includes Discrete Dipole Approximation (DDA) [28], Finite Difference Time Domain (FDTD) [34], Finite Element Method (FEM) [110] and Integral Equation (IE) [111]. Recently, numerous research groups have employed the commercially available software "COMSOL" in studying the electromagnetic field interactions on plasmonic nanostructures [25, 28, 45, 63, 69, 98, 110]. COMSOL Multiphysics is numerical simulation software based on Finite Element Method (FEM), which accurately solves electromagnetic problems at the nanoscale level.

Both the near and far field optical properties were calculated in the frequency domain using the scattered field formulation. The 3D simulation space is composed of a nanoparticle, an embedding medium and a perfectly matched layer (PML), which eliminate the reflections at the domain boundaries. The embedding medium was considered air for all the considered cases. In the calculations, Johnson and Christy data have been utilized for the dielectric constant of both the gold and silver instead of Drude model, which neglects the damping caused by interband transitions [112]. The permeability of both the metals are $\mu = 1$. A spherical far field integration boundary is brought in between the inner PML boundary and the nanostructure. We chose the dimensions of the embedding volume and the PML in such a way that varying the size of the nanoparticle would not influence the simulation results. A free built-in meshing algorithm in COMSOL was used to discretized the simulation space, which will divide the simulation space into a set of tetrahedral finite elements [25]. A plane wave, used for excitation, was inserted on the inside of PMLs surrounding the embedding medium. The absorption cross section is calculated by integrating the average dissipated power Q_{av} over all space occupied by metal.

$$\sigma_{abs} = \frac{\iiint_{Metal} Q_{av} dV}{\frac{1}{2} Z_0 \left| H_0 \right|^2} \tag{1.1}$$

where H_0 is the incident magnetic field amplitude and Z_0 is the characteristic impedance of vacuum.

The scattering cross section is calculated as the ratio between the scattered electromagnetic power and incident power density.

$$\sigma_{scat} = \frac{\frac{1}{Z_0 R_f^2} \oiint_f \left| R_f E_{far} \right|^2 dS}{\frac{1}{2} Z_0 \left| H_0 \right|^2} \tag{1.2}$$

E_{far} is the far field component of the scattered field calculated using the Stratton-Chu transformation which is implemented in COMSOL and R_f is the radius of the spherical surface on which the far field is evaluated. The extinction cross section is given by the sum of the scattering and absorption cross sections. The electromagnetic near field enhancement at a specific point is obtained by dividing the amplitude of the total electric field (E_T) at that point with the amplitude of the incident electric field E_0.

$$\eta = \frac{E_T}{E_0} \tag{1.3}$$

1.4. Thesis organization

This thesis is directed towards the design, simulation and theoretical characterization of various types of plasmonic layered and dimer nanostructures. The scope of this thesis is to generate and optimize single and multiple Fano resonances and localized near-field energy by changing the size, composition, geometry and interparticle gap as well as symmetry breaking in the nanostructures.

Chapter 2 presents a detailed study on the far field and near field optical properties of multilayered spherical nanostructures. Two kinds of Fano resonators have been proposed; a multilayered Fano resonator, which consists of an inner metal core, a middle dielectric layer and an outer metal shell and a double nanoshell Fano resonator, which consists of two alternating layers of single nanoshells. Different kinds of new symmetry breaking schemes have been introduced in both the Fano resonators due to which a unique and multiple Fano resonance bands have been obtained in the optical spectrum. The double nanoshell Fano resonator is proved to provide better tunability of resonant modes due to which it is highly suitable for biomedical applications. However, the multilayered Fano resonator provides large field enhancement and multiple Fano resonances due to which it can be used for high performance SERS and plasmon line shaping.

In chapter 3, we investigated the plasmon coupling in multilayer nanostructures based on silica and truncated gold nanocones. The unique feature of multilayered conical nanostructures is that a symmetry breaking in the coupling mechanism with the incident electromagnetic field can be simply obtained by rotating them. This cannot be accomplished in nanostructures with spherical symmetries. Fano resonances are achieved at different frequencies by rotating the nanostructure axis with respect to the incident polarization. The extinction spectra of all the nanostructures are proved to be strongly dependent on the angle and polarization of the incident light. Eventually, the optical response of the multilayered nanocones is compared to the concentric and non-concentric multilayered nanospheres and the former nanostructures are discovered to provide higher order dark modes and sharp tunable Fano resonances than the latter nanostructures. The large field enhancement and higher order tunable Fano resonances in multilayered conical nanostructure suggest that this resonator is highly appropriate for multi-wavelength SERS, biosensing, switching and plasmon line shaping.

In chapter 4, we extended the conception of multilayered structures to cubic, elliptical and cylindrical structures with multi-components and observed the same effect of higher order dark hybridized modes and Fano resonances. These nanostructures have been designed in such a manner that the broad superradiant and narrow subradiant plasmon modes overlap in energy and result in a strong Fano resonance in the optical spectrum. By observing the bright and dark modes in these nanostructures with different geometries, we end up with a conclusion that this trend is very general in bimetallic nanostructures. Any type of geometry with multicoated structure like multilayered spherical nanoshell can be designed with its bright and dark modes exhibiting Fano resonances.

In chapter 5, we analyzed the optical properties of new geometries of gold nanocones. The effect of Fano like resonances are obtained in a single resonator structure which contains only a single metal piece. The symmetric conical resonator also offers dimensional angularly selectivity of the plasmonic properties like the nanocups and gold nanoshell with holes but it has an advantage to exhibit Fano resonance in the spectrum, which can be used for additional

applications like PIT and switching. The asymmetric conical Fano resonator is found to be highly capable in the generation of higher order Fano resonances, which may be suitable for plasmon line shaping and SERS. The spectral sensitivity of asymmetric conical Fano resonator to the surrounding medium is also studied and high values of figure of merit and contrast ratio are observed, which shows the performance of Fano resonator as a biological sensor.

In chapter 6, we studied the plasmonic properties of nanoparticle pairs based on gold nanocones. The Fano dimer resonator is designed to realize plasmonic EIT capable of strongly dispersive and low loss transmission behavior in the spectrum. Several configurations of the dimer resonator have been demonstrated, which suggest that the plasmon coupling in the dimer is not only dependent on the interparticle distance and size of the nanoparticles but also on the spatial arrangement of the two components. The localized near-field energy known as hot-spots of the dimer nanostructure are essential for the surface-enhanced Raman spectroscopy applications by detecting biomolecules.

In chapter 7, we characterize the interaction between the plasmon modes of different Fano resonators through the mass-spring coupled oscillator analogy and the analytical model of Fano and Lorentzian line shapes developed by Gallinet and Martin. These analysis make the existence and understanding of Fano resonances easier in complex plasmonic nanostructures.

Finally, in chapter 8, we present the main conclusions of this thesis.

Chapter 2

Optical Properties of Multilayered Spherical Nanostructures

2.1. Introduction

In this chapter, we studied extensively the optical properties of spherical nanostructures using plasmon hybridization model. These nanostructures have attracted many researchers attention due to the generation of higher order tunable Fano resonance over the entire visible spectrum as well as near to mid infrared region [22, 24, 27, 107, 108]. Such nanostructures include multilayered nanoshell (MNS), which contains a spherical metallic core, a dielectric spherical shell, and an external metal spherical shell and double nanoshells (DNS), which contains two alternative layers of metal and dielectric. The plasmon oscillations of multilayer nanoparticles can be explained in terms of the interaction between the plasmon modes of the single parts of the nanostructure, as they act one by one. For example, the plasmon modes of a metallic nanoshell, composed of a dielectric core and a metallic layer, can be considered as arising from the interaction between the dipolar mode of the metallic sphere $|S\rangle$ and the dipolar mode of the dielectric cavity $|C\rangle$ [61, 113]. The hybridization of the sphere and cavity plasmons created two new plasmon modes, that is, the higher energy *antibonding mode* $|+\rangle$ and the lower energy *bonding mode* $|-\rangle$, corresponding to the antisymmetric and symmetric interactions between the $|S\rangle$ and $|C\rangle$ modes, respectively. A more fine classification consists in distinguishing the plasmon modes of these nanostructures is *superradiant* and *subradiant* modes. A superradiant plasmon mode radiates strongly because the dipole modes of the single parts of the multilayer nanostructure are aligned and oscillate in phase, instead a subradiant plasmon mode radiates weakly because the dipolar modes of single parts are aligned oppositely.

Here we analyzed theoretically, the near and far field optical properties of MNS and DNS nanostructures. Tunable Fano resonances have been obtained both in the symmetric and asymmetric nanostructures. Different kinds of new symmetry breaking have been introduced both in MNS and DNS nanostructures due to which unique higher order tunable Fano resonances are perceived in the optical spectrum. For all the considered nanostructures, we set the polarization of incident light along *x* and the wave propagation in the *z*-direction as shown in figure 2.1. The embedding medium considered is air for all the cases. The dielectric constant of silica is chosen to be 2.04.

2.2. Multilayered nanoshell (MNS)

Multilayered nanoshell (MNS) contains a spherical metallic core, a dielectric spherical shell and an external metal spherical shell. This type of nanostructure start to become the focus of strong attention in chemical and bimolecular sensing, lasing and SERS [23, 28, 96-98, 114]. The MNS nanostructure has also the ability to generate higher order tunable Fano resonances, which could find applications in plasmon line shaping and multi-wavelength SERS. The geometries of a concentric and non-concentric gold-silica-silver MNS are illustrated in figure 2.1(a) and (b), where the inner metal core is selected to be gold and the

outer metal shell is selected to be silver. The dimensions of MNS are R_1=50/ R_2=65/ R_3=75 nm, respectively.

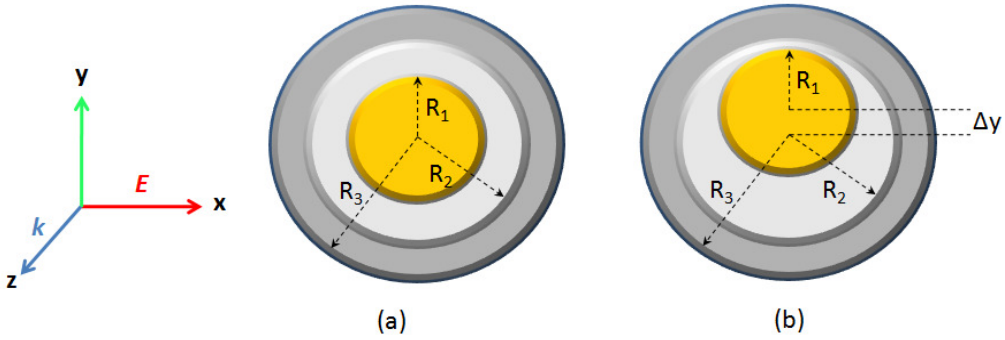

Figure 2. 1. Geometry of (a) concentric MNS and (b) Non-concentric MNS with offset core in y-direction (Δy). $R_1/R_2/R_3$ represents the radius of the inner core, middle silica layer and outer silver shell.

2.2.1. Plasmon hybridization

The hybridization model has been developed to understand the plasmonic response of metallic nanostructures [61]. For MNS, the plasmon hybridization will occur between a spherical metallic core and the outer nanoshell. Only the low-energy bonding mode $|\omega_-\rangle$ of the nanoshell is considered to interact with the dipole mode of the core because it has a large dipole moment. The high-energy antibonding mode $|\omega_+\rangle$ of the nanoshell has a small dipole moment and its interaction with the core mode is very week and cannot be observed in the spectrum. Thus, the interaction between the dipole mode of the core and the dipole bonding mode of the shell hybridized and produce a high-energy symmetric dipole antibonding mode $|\omega_-^+\rangle_{(1)}$ and a low-energy asymmetric dipole bonding mode $|\omega_-^-\rangle_{(1)}$. The $|\omega_-^+\rangle_{(1)}$ mode is a superradiant mode that arises by the symmetric coupling between the core dipole mode $|\omega_s\rangle$ and the dipole bonding mode $|\omega_-\rangle$ of the outer nanoshell, while $|\omega_-^-\rangle_{(1)}$ is a subradiant mode that arises by the antisymmetric coupling between $|\omega_s\rangle$ and $|\omega_-\rangle$ modes [29, 98]. For the concentric MNS, only those modes which have the same angular momenta will interact as shown in figure 2.2(a), where the dipole mode of the core $|\omega_s\rangle_{(1)}$ interacts with the dipole mode of the shell $|\omega_-\rangle_{(1)}$. Likewise the quadrupole mode of the core $|\omega_s\rangle_{(2)}$ interacts with the quadrupole mode of the shell $|\omega_-\rangle_{(2)}$ and so on. For the non-concentric MNS, where we offset the inner core on an otherwise fixed geometry, modes of different order will mix i.e., those modes which have distinctive angular momenta starts to interact as shown in figure 2.2(b). For instance, $|\omega_s\rangle_{(1)}$ mode of the core will not only interact with $|\omega_-\rangle_{(1)}$ mode of the shell but also with the higher order modes of the shell like the quadrupole $|\omega_-\rangle_{(2)}$ and octupole $|\omega_-\rangle_{(3)}$ modes etc. Also the lower order modes would be red-shifted because by offsetting the inner core, the gap between the core and the shell decreases due to which the plasmon interactions between the modes increases, as a result we obtained a strong red-shift in the optical spectrum [99].

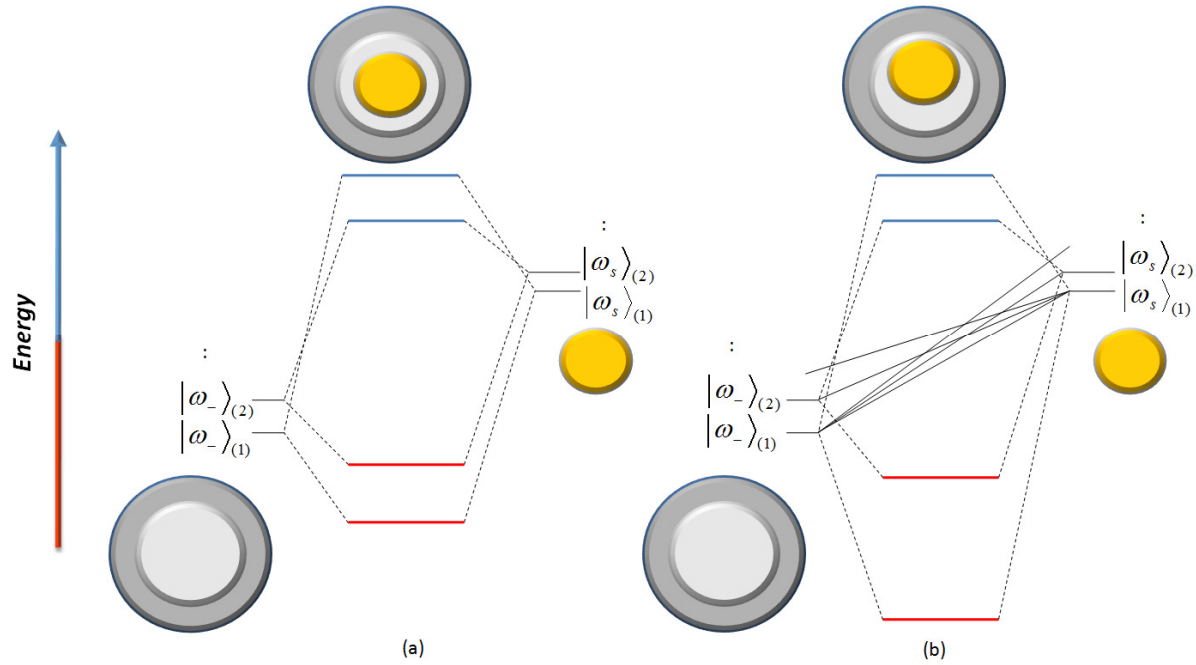

Figure 2. 2. Plasmon hybridization diagram. (a) Concentric MNS, where the interaction between modes having the same angular momentum takes place. (b) Non-concentric MNS, where the black solid lines show additional interactions between the modes. Photon energy increases from bottom to top.

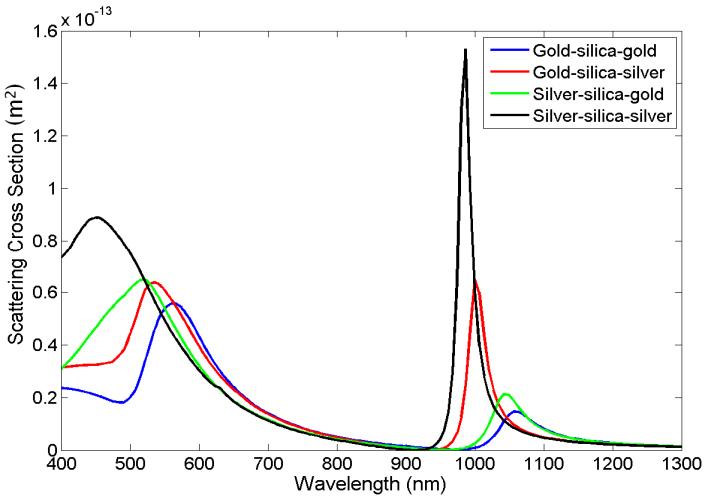

Figure 2. 3. Scattering cross sections of concentric MNS. Blue line corresponds to gold-silica-gold MNS, red line corresponds to gold-silica-silver MNS, green line corresponds to silver-silica-gold MNS and black line corresponds to silver-silica-silver MNS.

2.2.2. Far field optical properties

Figure 2.3 demonstrates the scattering spectra of concentric MNS using different materials. The blue line corresponds to gold-silica-gold MNS, red line corresponds to gold-silica-silver MNS, green line corresponds to silver-silica-gold MNS and black line corresponds to silver-silica-silver MNS. For all types of MNS, we obtained two distinct resonant peaks in the spectrum. The high-energy broad superradiant antibonding plasmon mode $|\omega_-^+\rangle_{(1)}$ and the low-energy narrow subradiant bonding plasmon mode $|\omega_-^-\rangle_{(1)}$. Both the resonant peaks arises from the dipole-dipole interaction between a metallic core and the shell.

The subradiant and superradiant dipole modes are well separated from each other. Spectrally, the subradiant mode does not overlap the superradiant mode and therefore, both the peaks couple directly to the incident light and we observed no Fano resonance in the spectrum [24].

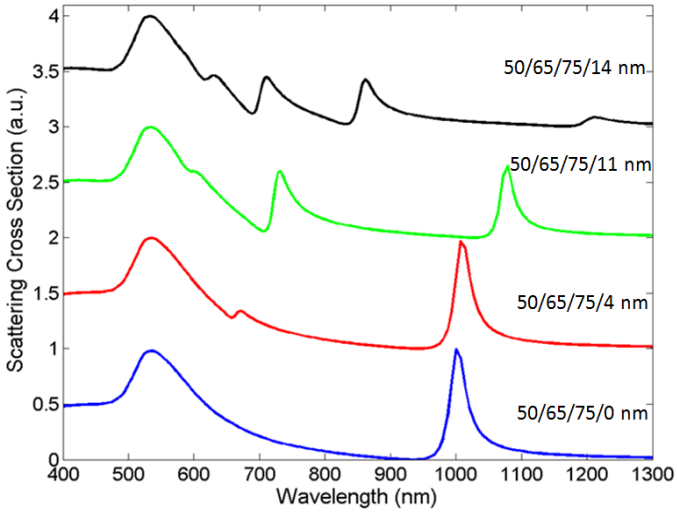

Figure 2. 4. Scattering spectra of NC-MNS as a function of core offset Δy. Δy = 0 (blue line), Δy = 4 nm (red line), Δy = 11 nm (green line) and Δy = 14 nm (black line).

2.2.2.1. Symmetry breaking in MNS

We consider gold-silica-silver MNS and broke its symmetry by offsetting the inner gold core with respect to the shell as a result modes of different orders will mix [24, 27, 98]. Figure 2.4 shows the scattering spectrum of a non-concentric MNS (NC-MNS) with different core offsets. The blue line corresponds to the concentric MNS as we discussed before where we obtained two distinct resonant modes, i.e., the high-energy superradiant antibonding mode near 536 nm and the low-energy subradiant bonding mode near 1000 nm. The red line corresponds to the NC-MNS with a core offset of 4 nm. In this case, a new peak emerges near 670 nm in the vicinity of superradiant mode. This mode represents a subradiant quadrupole mode $\left|\omega_{-}^{-}\right\rangle_{(2)}$. This mode was dark in the concentric case due to orthogonality. The $\left|\omega_{-}^{-}\right\rangle_{(1)}$ mode is also red-shifted as the interactions between the core and shell increases by offsetting the core. The $\left|\omega_{-}^{+}\right\rangle_{(1)}$ mode overlap $\left|\omega_{-}^{-}\right\rangle_{(2)}$ mode due to near field interaction and induces a dipole-quadrupole Fano resonance (DQF) in the spectrum. As the core offset increases further, more dark modes starts to appear and the resonance peaks also red-shifted more. For instance, at 11 nm core offset, the $\left|\omega_{-}^{-}\right\rangle_{(1)}$ mode shifts to around 1080 nm, while the $\left|\omega_{-}^{-}\right\rangle_{(2)}$ mode shifts to 732 nm and its peak amplitude increases because of the addition of the dipolar component into quadrupole mode [98]. A slight peak appears in the spectrum near 604 nm (green line), which represents a subradiant octupole mode $\left|\omega_{-}^{-}\right\rangle_{(3)}$. The near field coupling between $\left|\omega_{-}^{+}\right\rangle_{(1)}$ and $\left|\omega_{-}^{-}\right\rangle_{(3)}$ modes gives rise to dipole-octupole Fano resonance (DOF) in the spectrum. By further offsetting the core (14 nm), a subradiant hexadecapole mode $\left|\omega_{-}^{-}\right\rangle_{(4)}$ emerges in the spectrum near 630 nm (black line), which couples to $\left|\omega_{-}^{+}\right\rangle_{(1)}$ mode and engenders dipole-hexadecapole Fano resonance (DHF). The $\left|\omega_{-}^{-}\right\rangle_{(1)}$ mode remains uncouple

to $\left|\omega_{-}^{+}\right\rangle_{(1)}$ mode. It is also to be noted here that $\left|\omega_{-}^{+}\right\rangle_{(1)}$ mode is faintly blue-shifted, because it is a high-energy mode and has an extremely feeble interaction with the gold core dipolar mode [98, 99].

We introduced another two types of symmetry breaking in MNS nanostructure i.e., the middle silica layer and the outer metal shell has also been displaced from their respective positions to break the symmetry of the structure as shown in figure 2.5(a) and (b). By offsetting the silica layer on an otherwise fixed geometry will change the shape of the silica and outer silver shell but the total volume of both the silica layer and silver shell remains the same. In this case, the symmetry of the single nanoshell is broken and the higher order modes emerges on the nanoshell will interact with the modes of the core. This is explained by the plasmon hybridization diagram shown in figure 2.6. Figure 2.6(a) shows the plasmon hybridization of a non-concentric single nanoshell, where we offset the silica core from its center. The plasmon hybridization process will occur between the primitive cavity modes ω_c and the sphere plasmon modes ω_s [61]. Breaking the symmetry of the structure will introduce the hybridization between all multipolar indices and form low-energy bonding hybridized modes and high-energy antibonding hybridized modes [73, 115]. Only the bonding modes are considered because they are usually visualized by the surface plasmon resonant peak of the nanoshell whereas, the antibonding mode has a small dipole moment and cannot be visualized in the spectrum. Figure 2.6(b) shows the hybridization of the combined structure i.e., NC-MNS. Here the hybridized plasmon modes of the non-concentric shell and gold core mixed and produce low-energy bonding and high-energy antibonding plasmon modes. Figure 2.7 shows the scattering spectra of NC-MNS by offsetting the silica layer 11% from its centre (middle panel). We observed a slight red-shift of the subradiant bonding modes comparing to the core offset (bottom panel) because of the stronger interactions between the core and non-concentric nanoshell. Figure 2.5(b) shows the geometry of a non-concentric MNS by displacing the outer silver shell from its center. Here the shape of the shell is changed but the total volume would remain the same. The plasmon hybridization will occur between the hybridized plasmon modes of the non-concentric nanoshell and core modes, which will schism the plasmon into low-energy bonding mode and high-energy antibonding mode as discussed before. Figure 2.7 shows the scattering spectra of NC-MNS by offsetting the outer silver shell (top panel). Here, we observed a very week subradiant quadrupole mode near 735 nm, which shows that this setup is not good enough to produce hybridized multipolar modes. So in all the three scenarios of symmetry breaking, we encourage the first case where we offset the inner core on an otherwise fixed geometry because it provides a more clear picture of the modes coupling and also it is suitable for the generation of higher order hybridized modes.

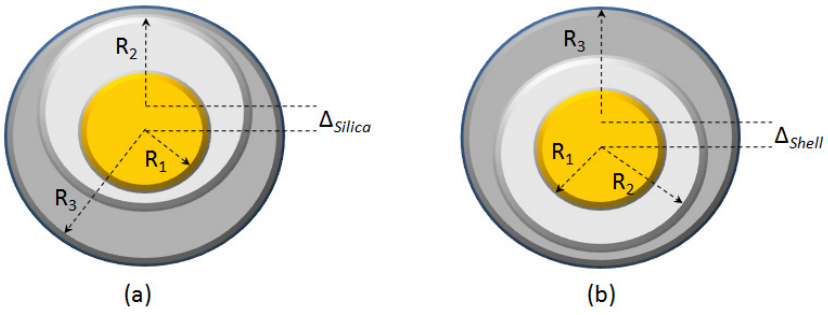

Figure 2. 5. Geometries of (a) NC-MNS with silica layer offset Δ_{Silica} (b) NC-MNS with outer metal shell offset Δ_{Shell}.

Breaking the symmetry of MNS cause three things; (1) red-shifting of the dark hybridized modes and Fano resonances (2) suppression of the dipole mode and (3) generation of higher order Fano resonances [24, 27].

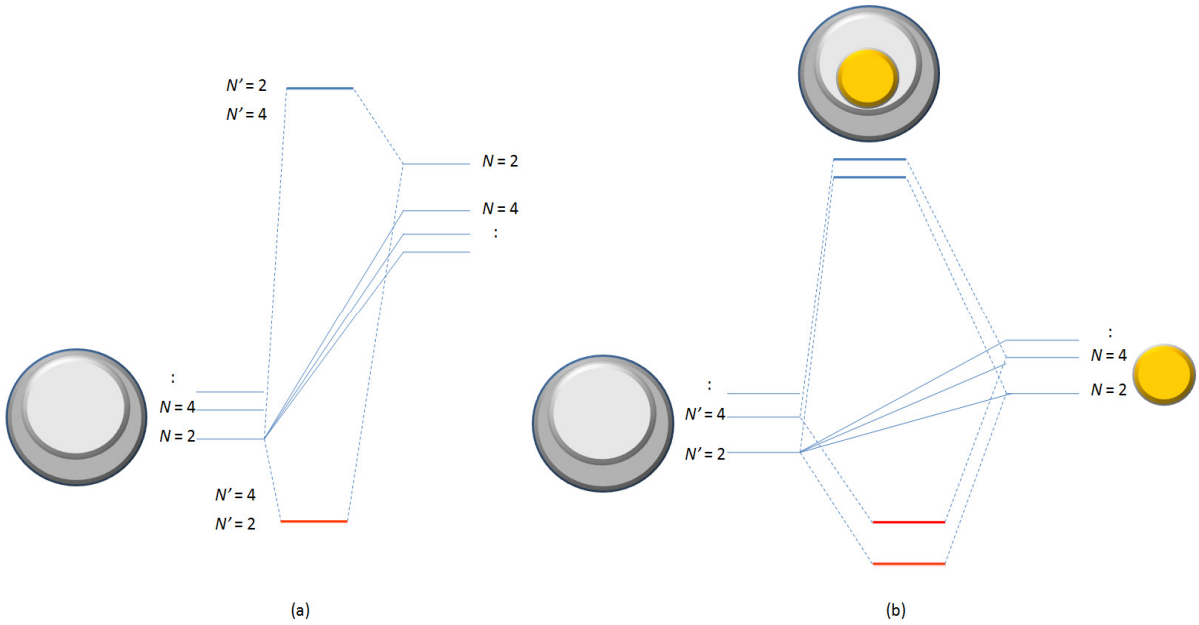

Figure 2. 6. The energy level diagram for plasmon hybridization of (a) Single non-concentric core-shell nanoparticle; (b) NC-MNS. N (N') = 2, 4 … represents dipole, quadrupole and higher order multipolar modes.

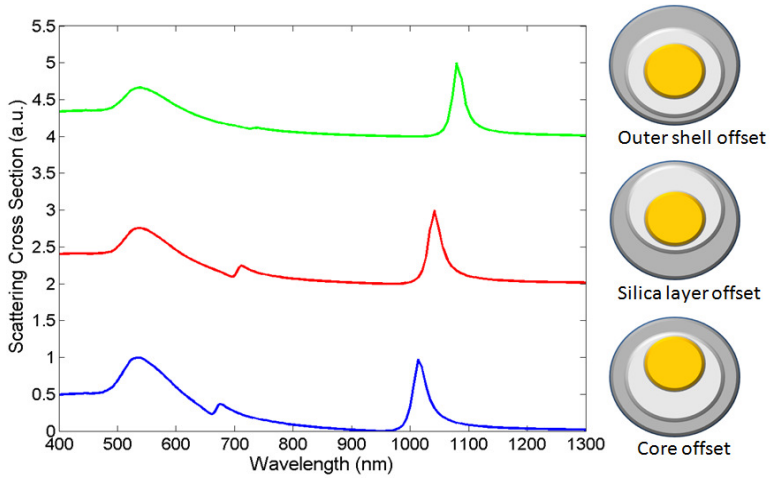

Figure 2. 7. Scattering spectra of NC-MNS. Blue line shows NC-MNS with core offset, red line shows NC-MNS with silica layer offset and green line shows NC-MNS with outer shell offset.

2.2.2.2. Effect of polarization

We compare the scattering spectra of MNS with 11 nm core offset for two different polarizations as shown in figure 2.8. The blue line corresponds to transverse polarization, where the incident field is polarized perpendicular with respect to the core offset and the red line corresponds to axial polarization, where the incident field is polarized parallel with respect to the core offset as shown in the inset of figure 2.8. The $\left|\omega_{-}^{-}\right\rangle_{(1)}$, $\left|\omega_{-}^{-}\right\rangle_{(2)}$ and $\left|\omega_{-}^{-}\right\rangle_{(3)}$ modes are discovered for both the polarizations, which shows the near isotropic response of MNS. The scattering spectrum for the axially polarized light shows a red-shift of few

nanometers and also $\left|\omega_{-}^{-}\right\rangle_{(1)}$ mode suppresses and $\left|\omega_{-}^{-}\right\rangle_{(2)}$ mode enhances, which illustrates a stronger interaction between modes of different order.

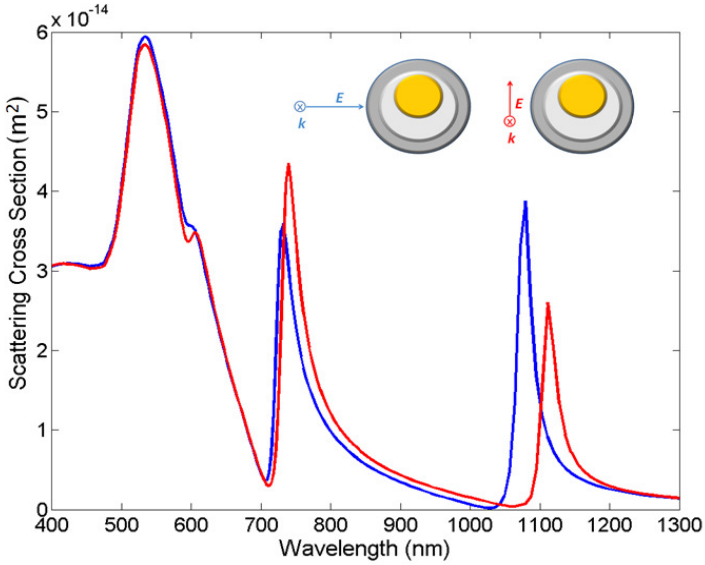

Figure 2. 8. Scattering spectra of the NC-MNS with 11 nm core offset. Blue line, incident light is transversely polarized with respect to the offset; red line, incident light is axially polarized along the offset.

2.2.3. Near field optical properties

We also investigated the electromagnetic near field optical properties of the gold-silica-silver MNS. We observed that offsetting the core, causes major changes in the intensity of the near field enhancement of the MNS. When light hits the MNS structure, then part of energy diffuses into the outer metal shell and move towards the inner metal core from which reflects back and gets trapped inside the silica layer. For all resonances, the maximum field enhancement happens inside the silica layer instead of the outside the metal shell like in the conventional single layer nanoshell, where the maximum field enhancement occurs outside the nanoshell [25, 27]. Figure 2.9 shows the near field distributions and the corresponding enhancement values at each scattering peak for both the concentric and non-concentric cases. For the non-concentric MNS, the maximum value of the enhancement is found at the thinnest part of the nanoparticle. The blue line corresponds to the concentric MNS, where the maximum value of the field enhancement for $\left|\omega_{-}^{-}\right\rangle_{(1)}$ mode is observed to be 55. For a 4 nm core offset, the maximum value of the field enhancement for $\left|\omega_{-}^{-}\right\rangle_{(1)}$ mode increases to 59 and for $\left|\omega_{-}^{-}\right\rangle_{(2)}$ mode the value is observed to be 14 (red line). By further offsetting the core (11 nm), the enhancement value for the $\left|\omega_{-}^{-}\right\rangle_{(1)}$ mode further increases (84) and for $\left|\omega_{-}^{-}\right\rangle_{(2)}$ mode, the enhancement value boosts up (61). So the higher order hybridized modes will increase the value of the near field enhancement because of the stronger interactions between the modes at the thinner layer. Thus, the MNS nanostructure provides the maximum values of the near field enhancement at various regions in the spectrum, which is an essential attribute of SERS [38, 116].

The similar results can be obtained by selecting gold-silica-gold, silver-silica-gold and silver-silica-silver MNS.

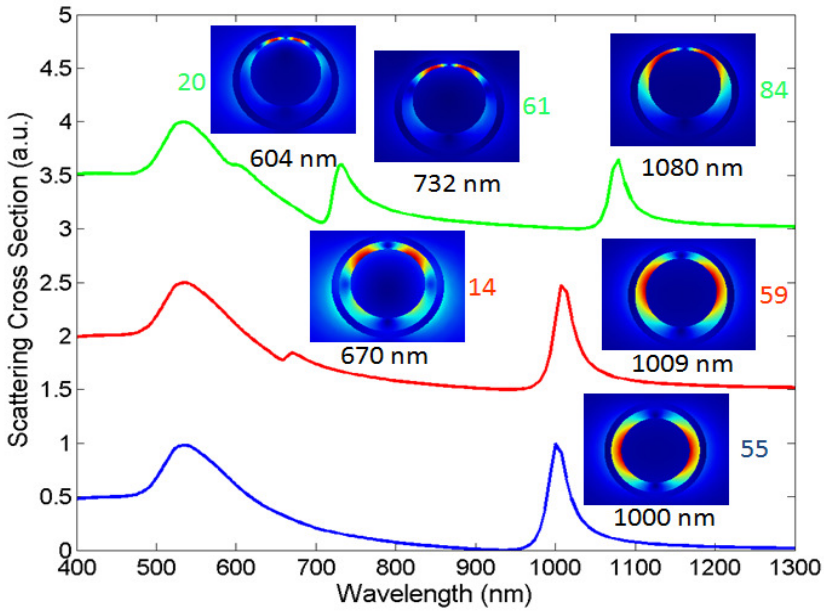

Figure 2. 9. Electromagnetic near field distributions at each scattering peak with various core offsets. Blue line $\Delta y = 0$, red line $\Delta y = 4$ nm and green line $\Delta y = 11$ nm. The wavelength of the scattering peaks and the enhancement values are also shown.

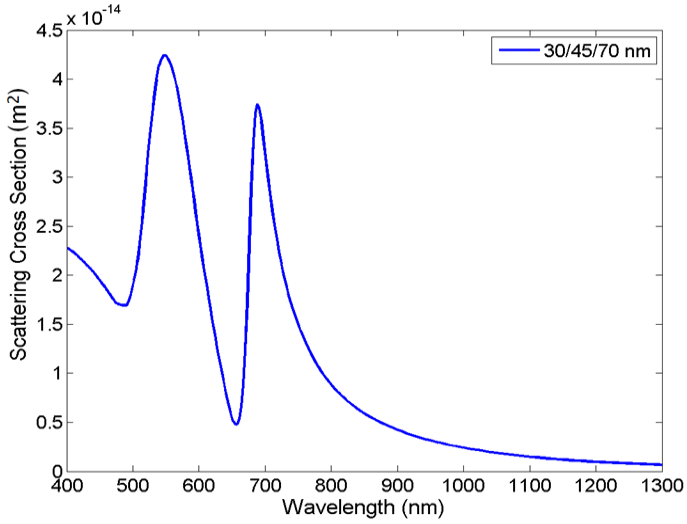

Figure 2. 10. Scattering cross section of a gold-silica-gold MNS.

2.2.4. Fano resonance in symmetric MNS

By careful arrangement of different layers in MNS, we can have a Fano resonance in the concentric case as well. Figure 2.10 demonstrates the scattering spectra of a 30/45/70 nm gold-silica-gold MNS, where we obtained a strong Fano resonance in the concentric case. The broad peak near 550 nm corresponds to $\left|\omega_{-}^{+}\right\rangle_{(1)}$ mode and the narrow peak which arises in the vicinity of broad resonance (690 nm) corresponds to $\left|\omega_{-}^{-}\right\rangle_{(1)}$ mode. The near field coupling between the two modes induces a dipole-dipole Fano resonance (DDF) in the spectrum near 655 nm. The higher order modes will be absent in the concentric case and they will not interact with the dipole mode because they are orthogonal [24].

2.2.4.1. Geometrical tunability of symmetric MNS

The DDF can be tuned in the spectrum by changing the parameters of MNS nanostructure. Figure 2.11 shows the scattering spectra of MNS by varying the radius of the inner gold core (R_1) and fixing $R_2 = 45$ nm and $R_3 = 70$ nm. When R_1 is small, the thickness of the middle silica layer increases, due to which the plasmon interactions between the gold core and shell decreases as a result of which we obtained a blue-shift of $\left|\omega_{-}^{-}\right\rangle_{(1)}$ mode in the spectrum. By increasing R_1, the thickness of silica layer decreases, which will increase the plasmon interactions between the gold core and shell. The increase in the plasmon interactions will red-shift $\left|\omega_{-}^{-}\right\rangle_{(1)}$ mode. For $R_1 \geq 35$ nm, both the $\left|\omega_{-}^{+}\right\rangle_{(1)}$ and $\left|\omega_{-}^{-}\right\rangle_{(1)}$ modes are far away from each other, they couple directly to the incident light and we observed no Fano resonance. For all the values of R_1, the $\left|\omega_{-}^{+}\right\rangle_{(1)}$ mode maintains its spectral position, while its peak amplitude increases with increasing R_1.

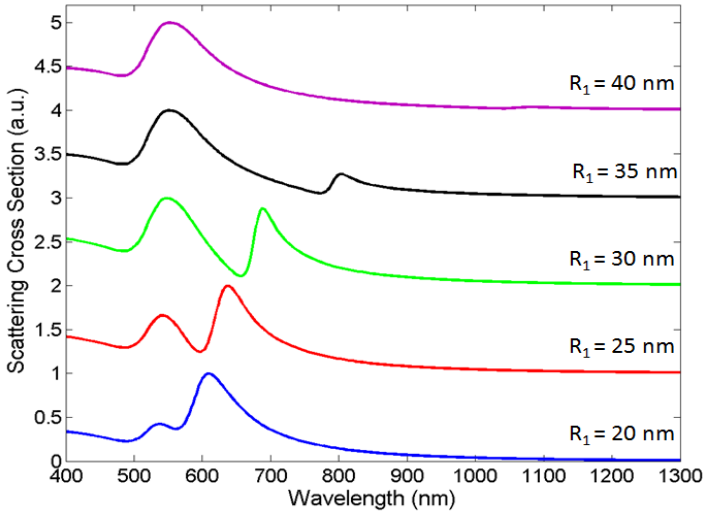

Figure 2. 11. Scattering spectra of MNS for different values of R_1 at fixed $R_2 =$ 45 nm and $R_3 = 70$ nm.

Next we fix the value of $R_1 = 30$ nm and $R_3 = 70$ nm and vary R_2. Figure 2.12 shows the scattering spectra of MNS with different values of R_2. Small values of R_2 will lead to the increase in the outer shell thickness and increase in the plasmon interactions between the gold core and shell due to which we observed a red-shift of $\left|\omega_{-}^{-}\right\rangle_{(1)}$ mode in the spectrum. The increasing of R_2 leads to the decrease in the outer gold shell thickness and decrease in the plasmon interactions between the gold core and shell. This decrease in the plasmon interaction will blue-shift the $\left|\omega_{-}^{-}\right\rangle_{(1)}$ mode, which will enhance the coupling between symmetric and antisymmetric modes and a sharp DDF arises in the spectrum for $R_2 = 45$ nm. By further increasing the value of R_2, the $\left|\omega_{-}^{-}\right\rangle_{(1)}$ mode shows a red-shift due to which the coupling between the modes becomes weak and Fano resonance disappear again.

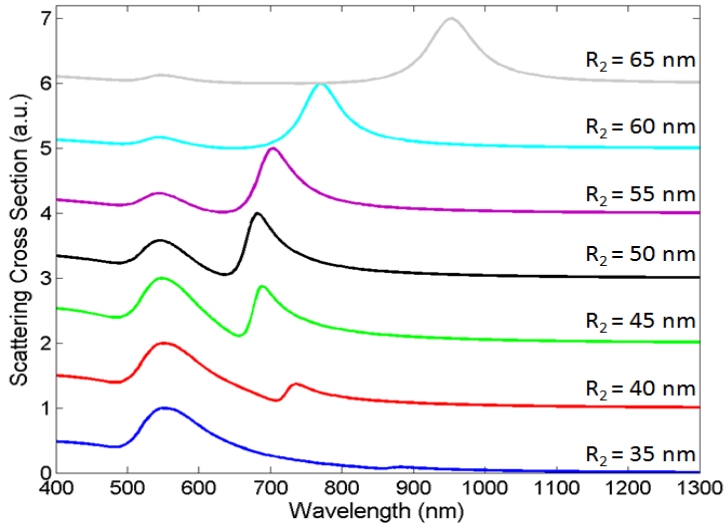

Figure 2. 12. Scattering spectra of MNS for different values of R_2 at fixed R_1 = 30 nm and R_3 = 70 nm.

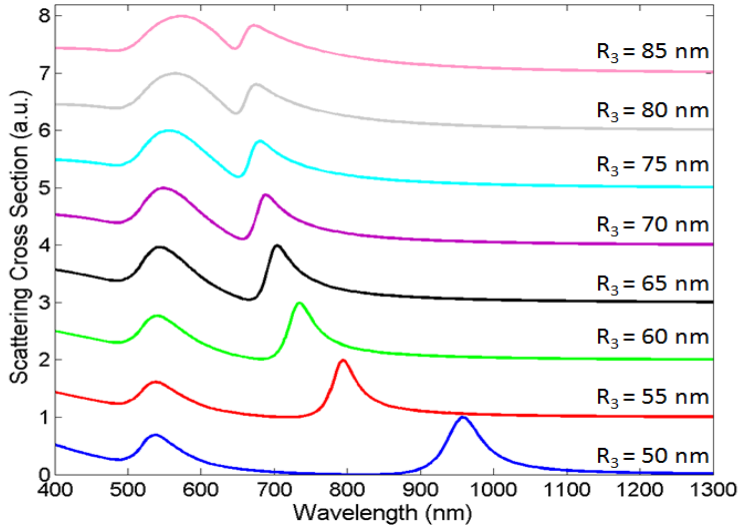

Figure 2. 13. Scattering spectra of MNS for different values of R_3 at fixed R_1 = 30 nm and R_2 = 45 nm.

In the last, we fix the value of R_1 = 30 nm and R_2 = 45 nm and vary R_3. Figure 2.13 shows the scattering spectra of MNS with different values of R_3. When R_3 is small enough then we observed a strong red-shift in the spectrum because of the stronger interactions between the inner core and the outer shell. Both the $|\omega_-^+\rangle_{(1)}$ and $|\omega_-^-\rangle_{(1)}$ modes are far away from each other and couple directly to the incident field and Fano resonance is absent. By keep increasing the value of R_3, we observed a large blue-shift of $|\omega_-^-\rangle_{(1)}$ mode. When R_3 reaches to 60 nm, the coupling between $|\omega_-^+\rangle_{(1)}$ and $|\omega_-^-\rangle_{(1)}$ modes are established due to which the DDF starts to appear in the spectrum. With further increase of the R_3 value, the modulation depth of the DDF decreases and also blue-shifted.

Figure 2.14 shows the spectral shift of the symmetric and asymmetric resonances with respect to the radii of different layers in MNS nanostructure. For all the values of the radii, the symmetric resonance almost sustains its spectral position while the asymmetric resonance

shows a strong shifting. It has also been observed that the asymmetric resonance shows a large shift by varying R_1, compared to R_2 and R_3.

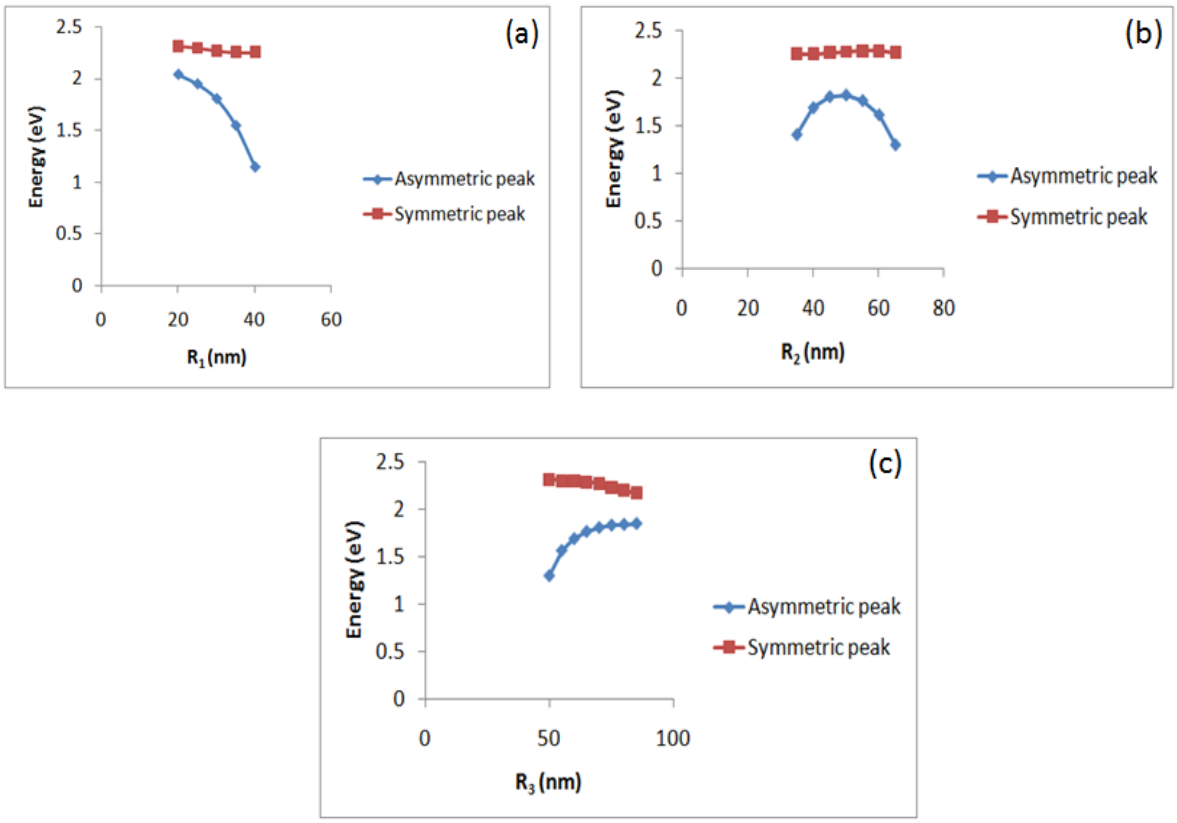

Figure 2. 14. The spectral shifting of the subradiant and superradiant modes with different (a) R_1 (b) R_2 and (c) R_3 values.

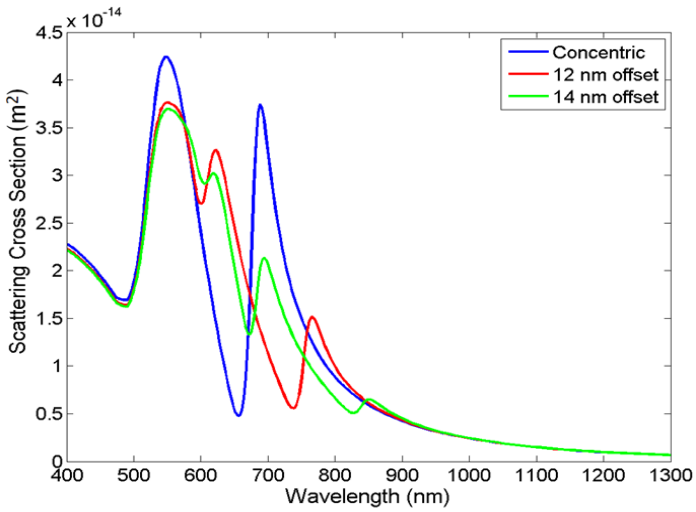

Figure 2. 15. Scattering spectra of gold-silica-gold NC-MNS as a function of core offset Δy. Δy = 0 (blue line), Δy = 12 nm (red line) and Δy = 14 nm (green line).

2.2.4.2. Symmetry breaking in gold-silica-gold MNS

We introduced a symmetry breaking conception in MNS by displacing the inner gold core with respect to the shell. Figure 2.15 shows the scattering spectra of gold-silica-gold

MNS with various core offsets. The blue line corresponds to the concentric MNS where we obtained a strong DDF. For a 12 nm core offset (red line), $\left|\omega_{-}^{-}\right\rangle_{(2)}$ mode appears, which couple to $\left|\omega_{-}^{+}\right\rangle_{(1)}$ mode and crop up DQF near 600 nm. The DDF red-shits from 655 nm to around 740 nm and the amplitude of $\left|\omega_{-}^{-}\right\rangle_{(1)}$ mode decreases. By further displacing the inner core (14 nm), $\left|\omega_{-}^{-}\right\rangle_{(3)}$ mode appears, which couples to $\left|\omega_{-}^{+}\right\rangle_{(1)}$ mode and induces DOF near 605 nm. The DDF and DQF are also red-shifted. Thus, the Fano resonances can be tuned as a function of the core offset.

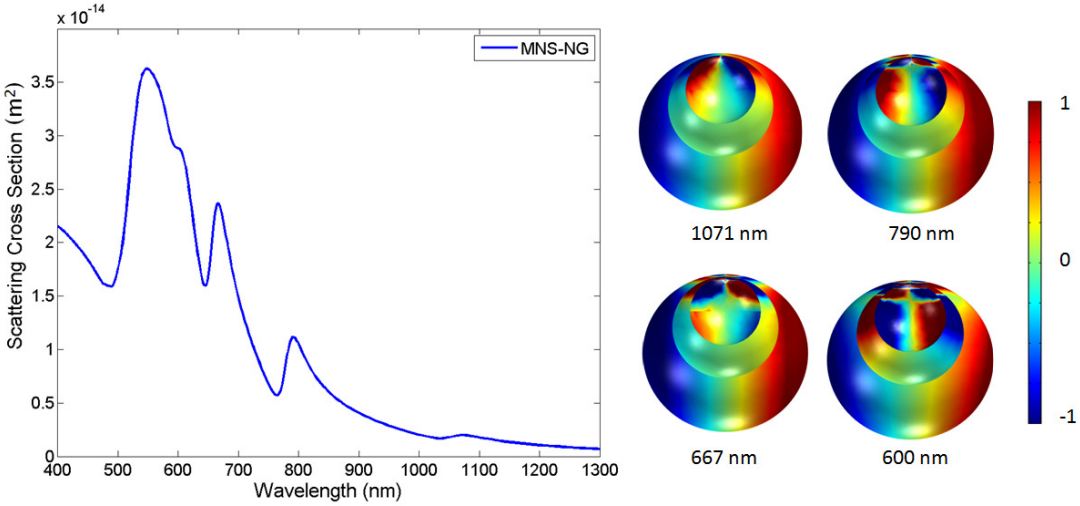

Figure 2. 16. Scattering spectra of MNS-NG. Inset shows surface charge distributions corresponding to each peak.

Next we moved away both the inner metallic core and silica layer simultaneously to make a nanoegg. In this nanostructure, the symmetry of the nanoshell is also broken. We named this nanostructure as *MNS nanoegg* (MNS-NG). Figure 2.16 illustrates the scattering spectra of MNS-NG, where we obtained five scattering peaks in the spectrum. In order to better understand the higher order modes in MNS-NG nanostructure, we calculated the surface charge distributions on the metal-dielectric boundaries using Gauss law. So, the surface charge density will be equal to the difference between the normal components of the electric field on the different sides of the metal-dielectric boundary [57].

$$\sigma = \varepsilon_0 \vec{n}_0 \cdot (\vec{E}_d - \vec{E}_m) \qquad (2.1)$$

We applied the above expression and calculate the surface charge distributions for each scattering peak observed in MNS-NG nanostructure as shown in the inset of figure 2.16. The surface charges near 1071 nm shows a subradiant dipole mode because both the inner core and outer shell exhibit a dipolar pattern. The surface charges near 790 nm presents a quadrupole-quadrupole mode because both the inner core and outer shell reveal a quadrupolar pattern. The surface charges near 667 nm shows a mixture of octupole modes while the surface charge distribution near 600 nm shows a quadrupole pattern on the outer layer and hexadecapolar distribution on the inner core, so this slight peak is a combination of quadrupole-hexadecapole mode. Thus, multicomponents offset in MNS provide distinct higher order modes and Fano resonances.

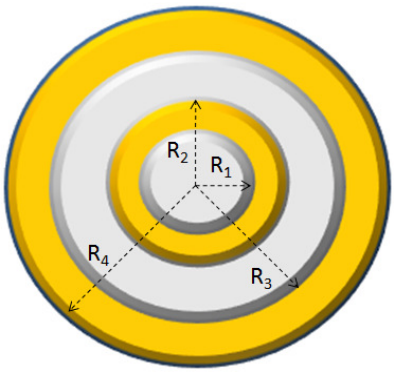

Figure 2. 17. Geometric sketch of silica-gold-silica-gold nanoshells, where $R_1/R_2/R_3/R_4$ represents the represents its dimensions.

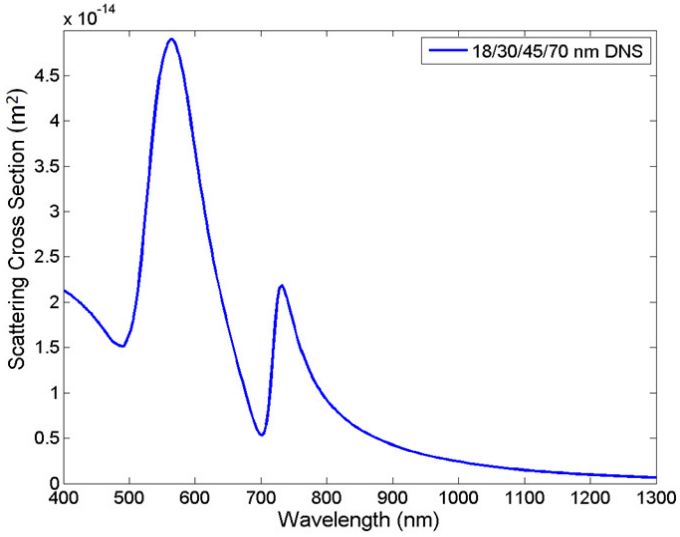

Figure 2. 18. Scattering cross section of a concentric DNS nanostructure.

2.3. Double nanoshells

We next construct double nanoshells (DNS) by inserting a dielectric sphere of 18 nm radius inside the inner metallic sphere of gold-silica-gold MNS. So in this way, we obtained bi-dielectric, bi-metallic nanostructure having dimensions R_1=18/ R_2=30/ R_3=45/ R_4=70 nm as shown in figure 2.17. As discussed before that in a single nanoshell, the plasmon hybridization will occur between the sphere and cavity plasmon modes, which will split the plasmon into lower energy bonding mode $|\omega_-\rangle$ (symmetric) and high energy antibonding mode $|\omega_+\rangle$ (antisymmetric). The $|\omega_+\rangle$ mode has a very weak dipole moment because the cavity plasmons are oppositely aligned to the sphere plasmons due to which the corresponding resonant peak is too weak to be observed in the optical spectrum. For this reason, the plasmon hybridization in DNS will only occur between $|\omega_-\rangle$ modes of the inner and outer nanoshells forming high energy symmetric antibonding mode $|\omega_-^+\rangle$ and low energy antisymmetric bonding mode $|\omega_-^-\rangle$ [22, 92].

Figure 2.18 demonstrates the scattering spectra of concentric DNS obtained by the interaction of the dipole bonding modes of the two nanoshells. The high energy peak near

564 nm is $|\omega_-^+\rangle$ mode and the lower energy peak near 732 nm is $|\omega_-^-\rangle$ mode. The dip appear near 700 nm representing DDF that originates from the near field coupling between $|\omega_-^+\rangle$ and $|\omega_-^-\rangle$ modes. This hybridization seems much similar to the MNS nanostructure.

Figure 2.19 shows the tunability of DNS nanostructure by changing R_3 and fixing R_1 = 18 nm, R_2 = 30 nm and R_4 = 70 nm. Results show that $|\omega_-^+\rangle$ mode does not change its spectral location while its peak amplitude reduces by increasing R_3. On the other hand, $|\omega_-^-\rangle$ mode can be tuned from visible to near infrared region by varying R_3. The DNS nanostructure is found be provide slightly better tunability of the resonant modes compared to MNS nanostructure due to which, it can be a better choice for biomedical applications [22].

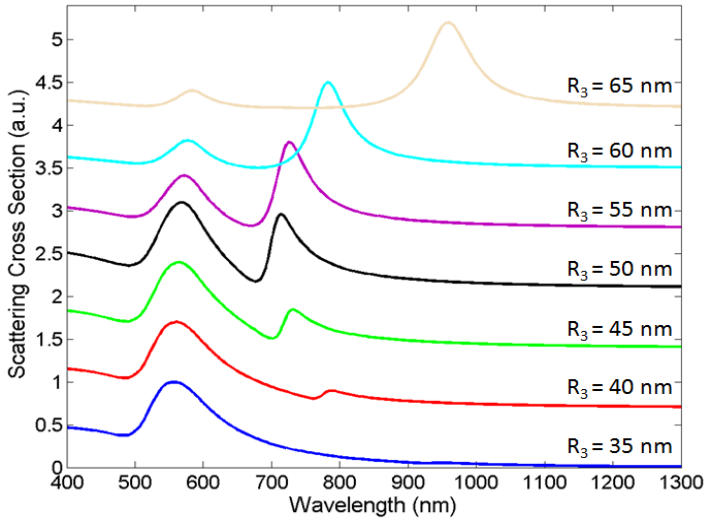

Figure 2. 19. Scattering spectra of DNS with different values of R_3 at fixed R_1 = 18 nm, R_2 = 30 nm and R_4 = 70 nm.

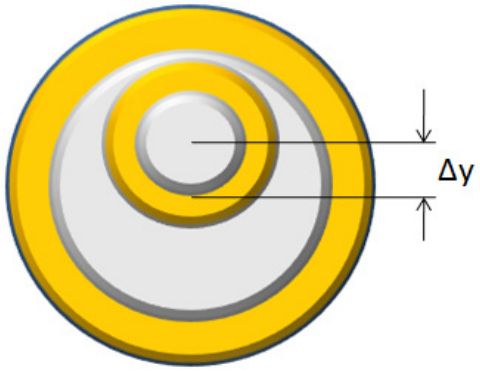

Figure 2. 20. Geometry of NC-DNS with inner nanoshell offset Δy.

2.3.1. Symmetry breaking in DNS

Next we break the symmetry of the DNS nanostructure by moving the inner nanoshell in the *y*-direction due to which the higher order hybridized modes come into view. The geometry of the non-concentric DNS (NC-DNS) is presented in figure 2.20.

Figure 2.21 shows the scattering spectra of concentric DNS and NC-DNS with various inner shell offsets. For the concentric DNS, we obtained $\left|\omega_{-}^{+}\right\rangle_{(1)}$ and $\left|\omega_{-}^{-}\right\rangle_{(1)}$ modes (blue line). For NC-DNS, higher order hybridized modes emerges in the spectrum. By observing the surface charges shown in the inset for 14 nm inner nanoshell offset, it becomes clear that the resonant peak near 872 nm is subradiant dipole mode. The surface charge distributions near 692 nm shows a dipole distribution on the outer nanoshell and quadrupole distribution on the inner nanoshell, so this clearly demonstrates a mixed dipole-quadrupole mode. Similarly, the surface charges near 612 nm (small peak) showing the mixing of dipole and octupole modes corresponding to dipole-octupole mode. So the NC-DNS exhibit the similar higher order hybridized modes and Fano resonances like the NC-MNS nanostructure.

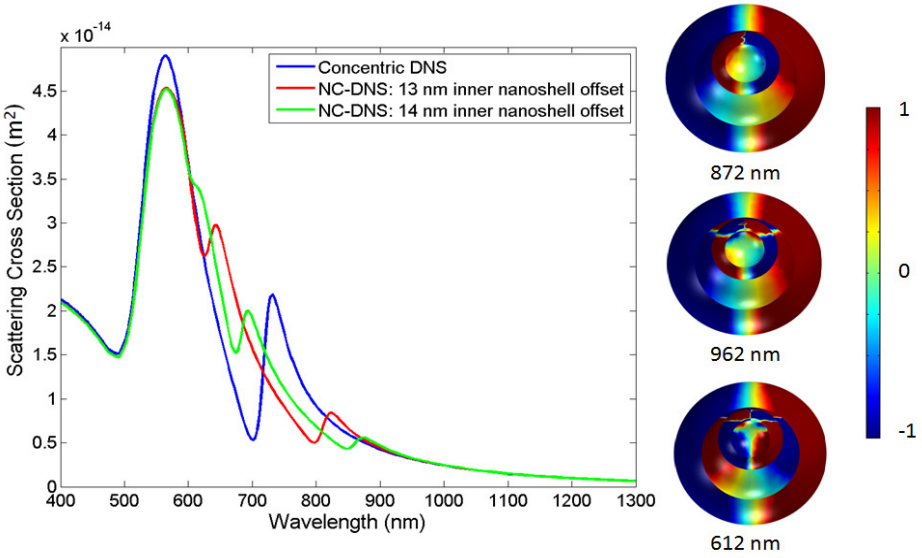

Figure 2. 21. Scattering spectra of NC-DNS with various inner nanoshell offsets. Blue line Δy = 0, red line Δy = 13 nm and green line Δy = 14 nm. Insets shows surface charge distributions for Δy = 14 nm.

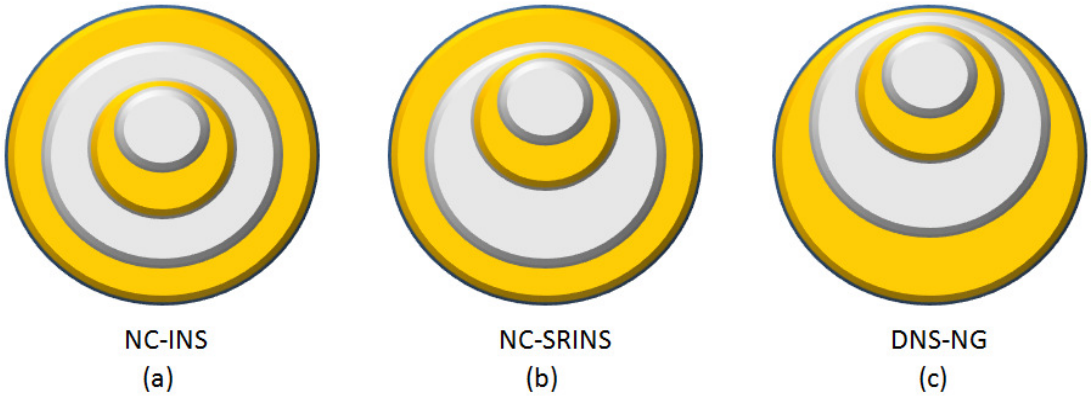

Figure 2. 22. Geometric sketches of (a) NC-INS, (b) NC-SRINS and (c) DNS-NG nanostructures.

We next introduced three other types of symmetry breaking in DNS nanostructure. The first one is to displace the inner silica core of the inner nanoshell 11 nm on an otherwise fixed geometry, the second one is to offset the symmetry broken inner nanoshell 14 nm on an otherwise fixed geometry and the third one is to offset both the symmetry reduced inner nanoshell (37 nm) and the silica layer of the outer nanoshell (23 nm) simultaneously, which adopts the shape of a nanoegg. All geometries of all the nanostructures are shown in figure 2.22. We named the first nanostructure as *DNS with non-concentric inner nanoshell* (NC-

INS), the second one as *DNS with non-concentric symmetry reduced inner nanoshell* (NC-SRINS) and the third one as *DNS nanoegg* (DNS-NG).

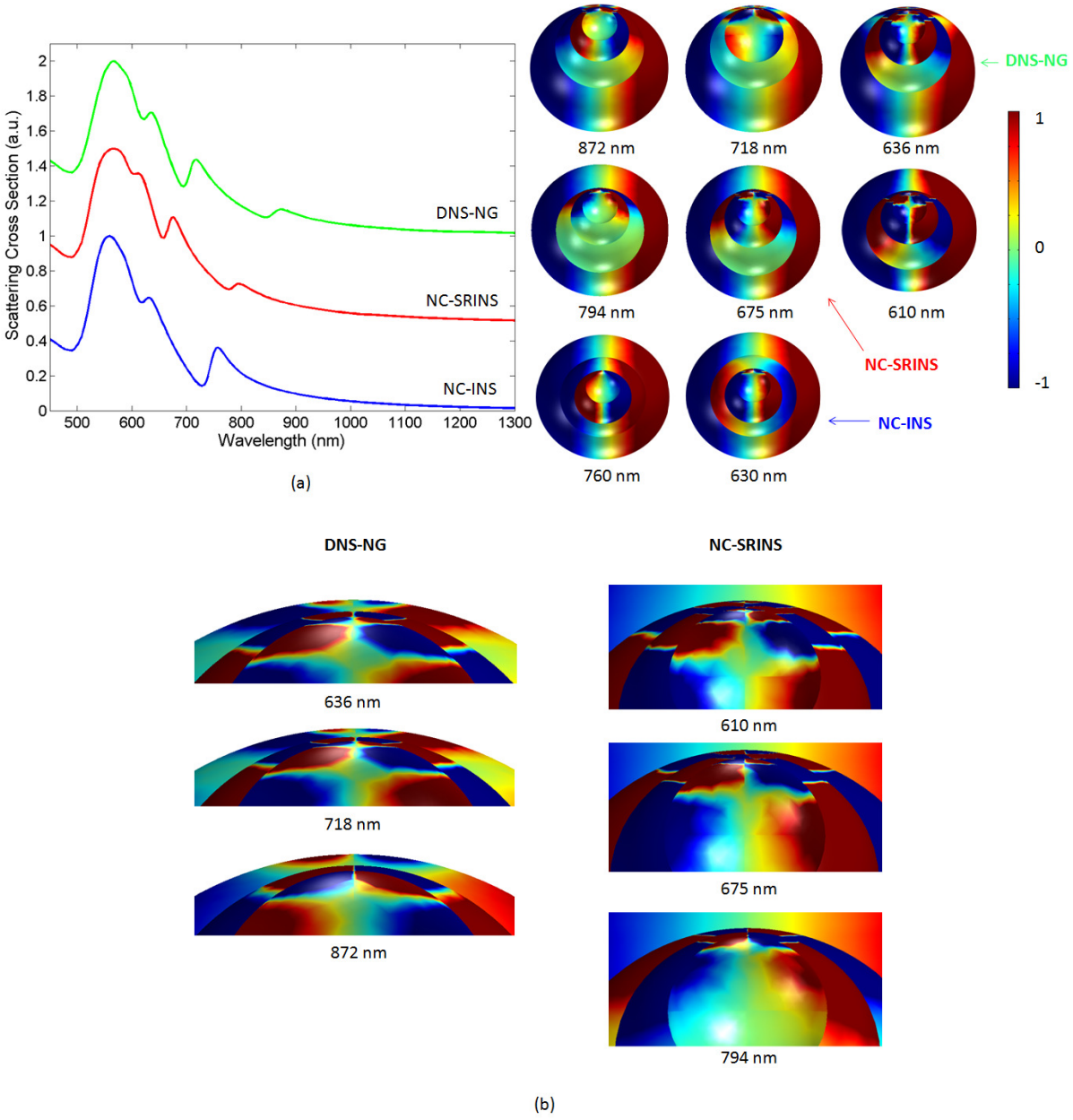

Figure 2. 23. (a) Scattering cross sections. Blue line corresponds to NC-INS, red line corresponds to NC-SRINS and green line corresponds to DNS-NG nanostructure. Insets show surface charge distributions for NC-INS (bottom panel), NC-SRINS (middle panel) and DNS-NG (top panel) nanostructures. (b) Closer view of surface charges corresponding to DNS-NG and NC-SRINS nanostructures.

The scattering spectra of NC-INS, NC-SRINS and DNS-NG nanostructures are presented in figure 2.23. For NC-INS nanostructure, we obtained only subradiant dipole and quadrupole modes, which are demonstrated by the surface charge distributions in the lower panel. By observing the surface charge distributions of NC-SRINS nanostructure given in the middle panel, the resonant peak near 794 nm shows the mixed dipole-quadrupole character of the dipole-quadrupole mode. The peak near 675 nm is the mixture of dipole and octupole modes, while the peak near 610 nm shows a dipole distributions on the outer nanoshell and hexadecapolar distributions on the inner nanoshell depicting dipole-hexadecapolar mode. The

lower order subradiant dipole mode remains absent in the NC-SRINS nanostructure. For the DNS-NG nanostructure, the higher order modes will also be appeared on the outer nanoshell because the symmetry of the outer nanoshell is also broken (similar like MNS-NG). Therefore, by examining the surface charge distributions near 872 nm, a quadrupole pattern emerges on both the outer and inner nanoshells, which represent a quadrupole-quadrupole mode. The surface charges near 718 nm shows a combination of octupole modes. The surface charges near 636 nm exhibit quadrupole distribution on the outer nanoshell and an octupole distribution on the inner nanoshell, which clear shows the mixed quadrupole-octupole character of the quadrupole-octupole mode. Figure 2.23(b) shows the closer view of the surface charges corresponding to DNS-NG and NC-SRINS nanostructures. For all the considered cases, the superradiant bright mode has sustained its spectral position. Symmetry breaking conception has never been reported in DNS nanostructure before. Breaking the symmetry of DNS nanostructure provide a set of unique Fano resonances, which could find applications in plasmon line shaping, multi-wavelength SERS and biosensing [31, 54].

2.4. Comparison of MNS and DNS nanostructures

We compared the near and far field properties of both the MNS and DNS by taking both the nanostructures with equal volumes. Figure 2.24(a) shows the scattering spectra of both the nanostructures for a concentric case. A comparatively much stronger Fano resonance with large modulation depth has been observed in MNS nanostructure. Figure 2.24(b) shows the scattering spectra of both the nanostructures for non-concentric cases, i.e., the inner metal core in MNS has been offset 47% from its center and with a similar offset value, the inner nanoshell in DNS has been moved. The figure depicts that both the nanostructures exhibit higher order Fano resonances, however the modulation depth of the Fano resonances in case of NC-MNS is observed to be stronger. For instance, the octupole Fano resonance in case of NC-DNS is found to be much weaker compared to NC-MNS nanostructure. Figure 2.24(c) shows the scattering spectra of MNS and DNS nanostructures with nanoegg like shapes, where the symmetry of both the nanostructures are broken with the same degree of offset. The MNS-NG exhibit five scattering peaks in the spectrum compared to DNS-NG nanostructure. Thus, the MNS, NC-MNS and MNS-NG nanostructures have the potential in the generation of higher order Fano resonances with large modulation depths.

Figure 2.25 shows the near field enhancement distributions of NC-DNS, NC-MNS, DNS-NG and MNS-NG nanostructures, which are calculated at each scattering peak. In figure 2.25(a), the NC-DNS field enhancement has been calculated for each subradiant mode. It has been observed that the maximum enhancement occur in the thinnest region i.e., in the dielectric layer of the outer nanoshell. The maximum field enhancement value is examined for the subradiant quadrupole mode which is around 170. Figure 2.25(b) shows field enhancement distributions of NC-MNS nanostructure. Here the maximum value of the field enhancement was obtained for subradiant quadrupole mode which is around 257. Figure 2.25(c) shows the field enhancement distributions for DNS-NG nanostructure. Here the maximum value of the enhancement was found to be 249 for a subradiant octupole-octupole mode. Figure 2.25(d) shows the field enhancement distributions for MNC-NG nanostructure, where the maximum value of the enhancement was discovered to be 252 for a subradiant octupole-octupole mode. In all the figures of the near field enhancement, the higher energy hybridized modes increase the larger near field enhancement. From field enhancement calculations, it has been established that NC-MNS and MNS-NG nanostructures show strong near field enhancements in several regions compared to NC-DNS and DNS-NG

nanostructures, which may provide effective applications in surface enhanced spectroscopy and localized surface plasmon resonance biosensor.

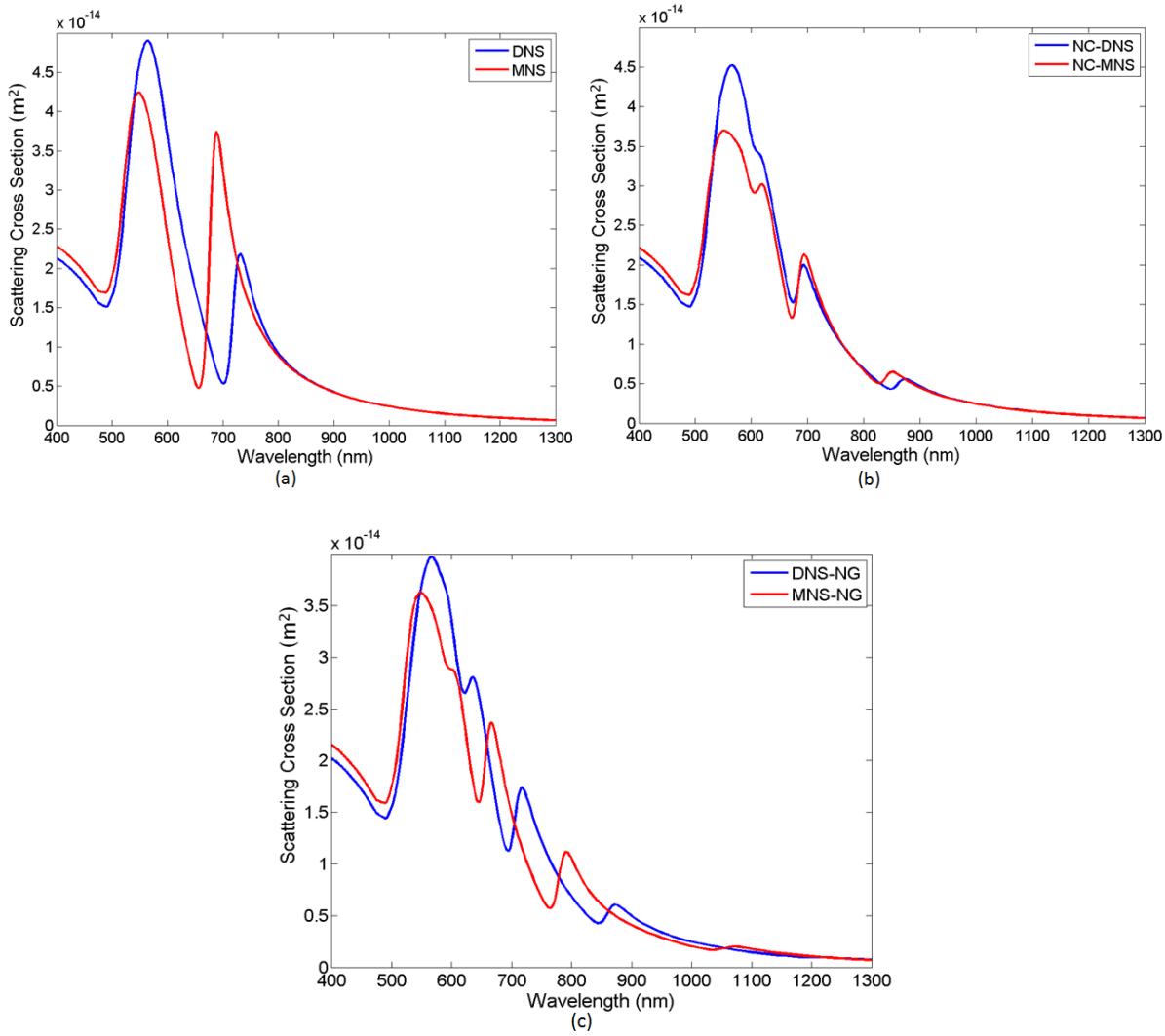

Figure 2. 24. Scattering spectra (a) DNS and MNS nanostructures. (b) NC-DNS and NC-MNS nanostructures. (c) DNS-NG and MNS-NG nanostructures.

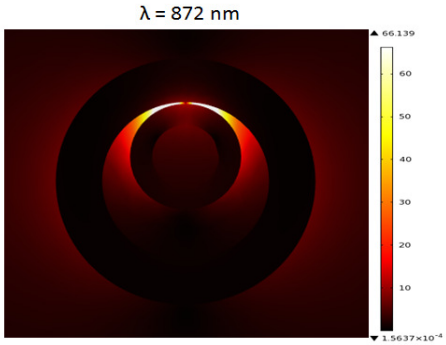
λ = 872 nm
66.139
60
50
40
30
20
10
1.5637×10⁻⁴

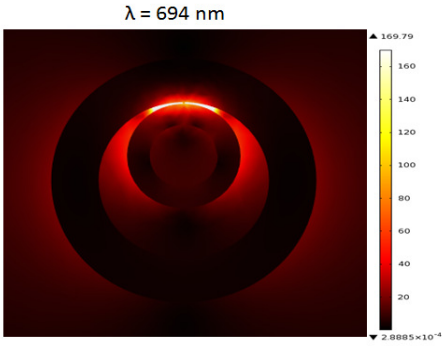
λ = 694 nm
169.79
160
140
120
100
80
60
40
20
2.8885×10⁻⁴

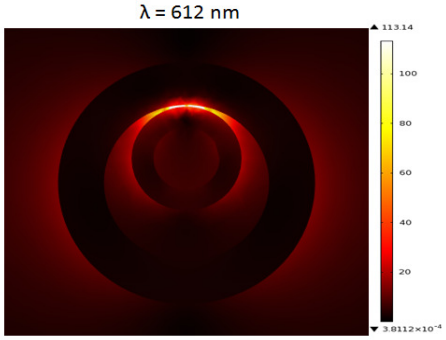
λ = 612 nm
113.14
100
80
60
40
20
3.8112×10⁻⁴

(a)

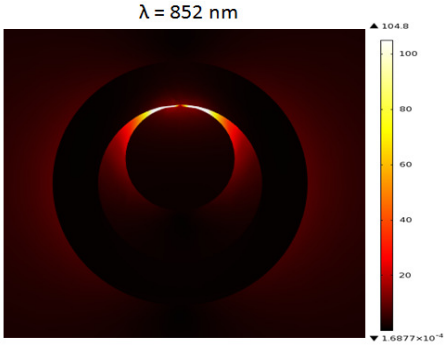
λ = 852 nm
104.8
100
80
60
40
20
1.6877×10⁻⁴

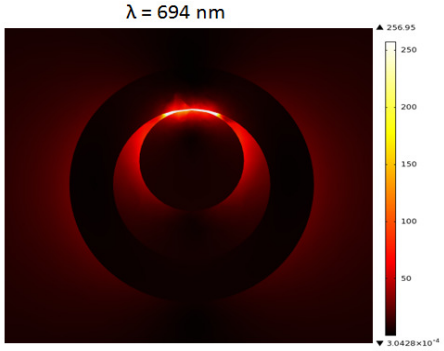
λ = 694 nm
256.95
250
200
150
100
50
3.0428×10⁻⁴

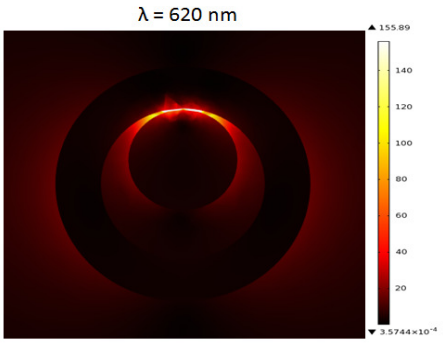
λ = 620 nm
155.89
140
120
100
80
60
40
20
3.5744×10⁻⁴

(b)

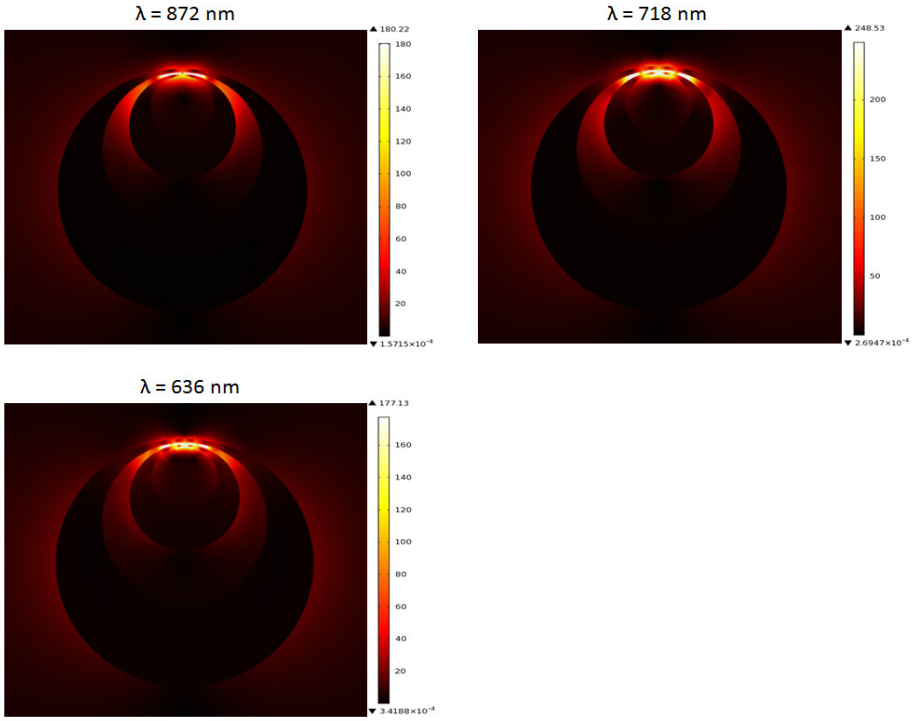

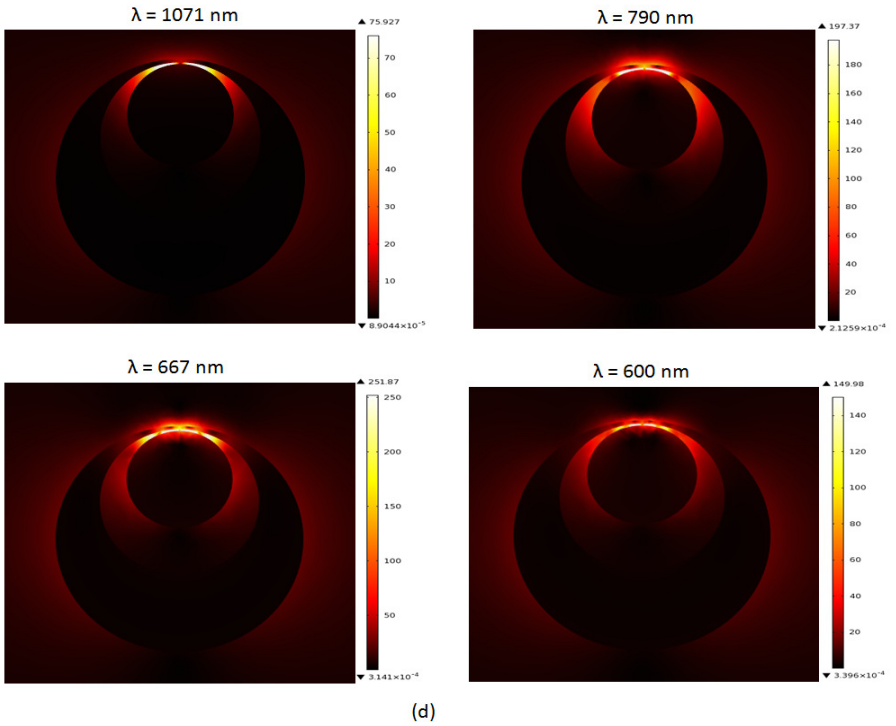

Figure 2. 25. Electromagnetic near field distributions. (a) NC-DNS. (b) NC-MNS. (c) DNS-NG. (d) MNS-NG.

2.5. Concluding remarks

To conclude, we started our study from a concentric MNS and presented new symmetry breaking conceptions in the nanoparticle by offsetting different layers on an otherwise fixed geometry to achieve multiple Fano resonances. By adjusting the dimensions of MNS, we obtained a DDF in the concentric nanoparticle geometry, which can be tuned by changing the

core/shell aspect ratio. DNS nanostructure has been constructed by adding a dielectric nanosphere inside the metallic core of MNS nanostructure. It has been observed that the DNS nanostructure provide a slightly better tunability of DDF compared to MNS nanostructure, which could be useful for biomedical applications. Different kinds of symmetry breaking in DNS nanostructure have been introduced for the first time due to which a set of unique higher order Fano resonances have been obtained. A comparison of both the MNS and DNS nanostructures has been analyzed. The MNS nanostructure is proved to be a better choice for the generation of higher order tunable Fano resonances.

Chapter 3

Higher Order Tunable Fano Resonances in Multilayer Nanocones

3.1. Introduction

In this chapter, we present a computational study of the plasmonic response of a gold-silica-gold multi-layered nanostructure based on truncated nanocones. Symmetry breaking is introduced by rotating the nanostructure and by offsetting the layers. Nanocones with coaxial multilayers show dipole-dipole Fano resonances with resonance frequencies depending on the polarization of the incident light, which can be changed by rotating the nanostructure. By breaking the axial symmetry, plasmonic modes of distinct angular momenta are strongly mixed, which provide a set of unique and higher order tunable Fano resonances. The plasmonic response of the multilayered nanocones is compared to that of multishell nanostructures with the same volume and the former are discovered to render visible high order dark modes and to provide sharp tunable Fano resonances. In particular, higher order tunable Fano resonances arising in non-coaxial multilayer nanocones can vary the plasmon lines at various spectral regions simultaneously, which makes these nanostructures greatly suitable for plasmon line shaping both in the extinction and near field spectra.

We know from our previous knowledge that multilayer nanostructures display Fano-like resonances in their optical spectra, which appear from the coupling and interference of bright and dark plasmon modes. The interactions between hybridized bright modes and dark modes can be increased through the symmetry breaking, due to which bright dipolar modes both constructively and destructively interfere with the higher order dark multipolar modes, which results in additional Fano resonances [27, 33, 117, 118].

Here, we investigated the plasmon coupling in multilayer nanostructures based on silica and truncated gold nanocones. The unique feature of multi-layered conical nanostructures is that a symmetry breaking in the coupling mechanism with the incident electromagnetic field can be simply obtained by rotating them. This cannot be accomplished in nanostructures with spherical symmetries. We started our discussion from a single gold nanocone and moved towards coaxial multilayered nanostructures. Fano resonances are achieved at different frequencies by rotating the nanostructure axis with respect to the incident polarization. Furthermore, the axial symmetry has been broken in two manners. First by offsetting the inner gold cone with respect to the outer shell to make a non-coaxial multilayer nanostructure and then by offsetting both the inner gold cone and middle silica cone to make a multilayered nanoegg cone, which provide unique higher order tunable Fano resonances. The extinction spectra of all the nanostructures are proved to be strongly dependent on the angle and polarization of the incident light. Eventually, the optical response of the multilayered nanocones is compared to the concentric and non-concentric multilayered nanospheres and the former nanostructures are discovered to provide higher order dark modes and sharp tunable Fano resonances than the latter nanostructures. Furthermore, we studied the optical characterization of the nanostructure by extracting the scattering parameters.

The incident light was a time harmonic linearly polarized plane wave. We used a Cartesian reference system (x,y,z) with the x-axis parallel to the electric field of the incident

wave and the *z*-axis parallel to its propagation direction. We analyzed the optical properties of the nanoparticles by rotating its axis around the *y*-axis of an angle θ, from θ = 0° to 90°, Figure 3.1. For θ = 0°, the incident light propagates along the nanostructure axis and its electric field is directed transversally, instead for θ = 90°, the incident light propagates transversally to the nanostructure and its electric field is directed longitudinally. We also observed that the optical properties of the proposed nanostructures were not very sensitive to the precise value of the semi-angle α of the conical shape, we chose α = 27°.

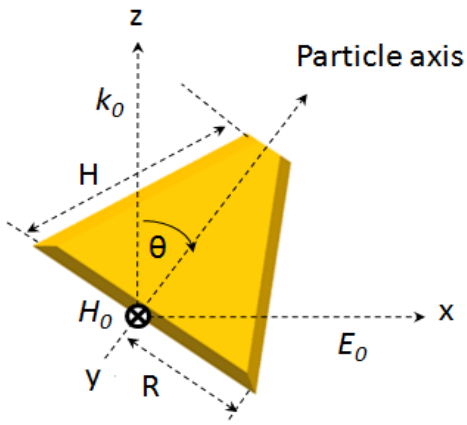

Figure 3. 1. Sketch of the nanostructure. The incident field is linearly polarized along the *x*-direction and propagates along the *z*-direction. The nanoparticle axis is rotated around the *y*-axis of an angle θ from 0° to 90°.

3.2. Optical properties of a multi-layered nanocone

In order to better understand the optical properties of a multi-layer gold-silica-gold nanocone, it is appropriate to first study a gold nanocone and then a silica-gold conical nanoshell. The optical response of the multi-layer nanocone is analyzed by using the plasmon hybridization theory [61].

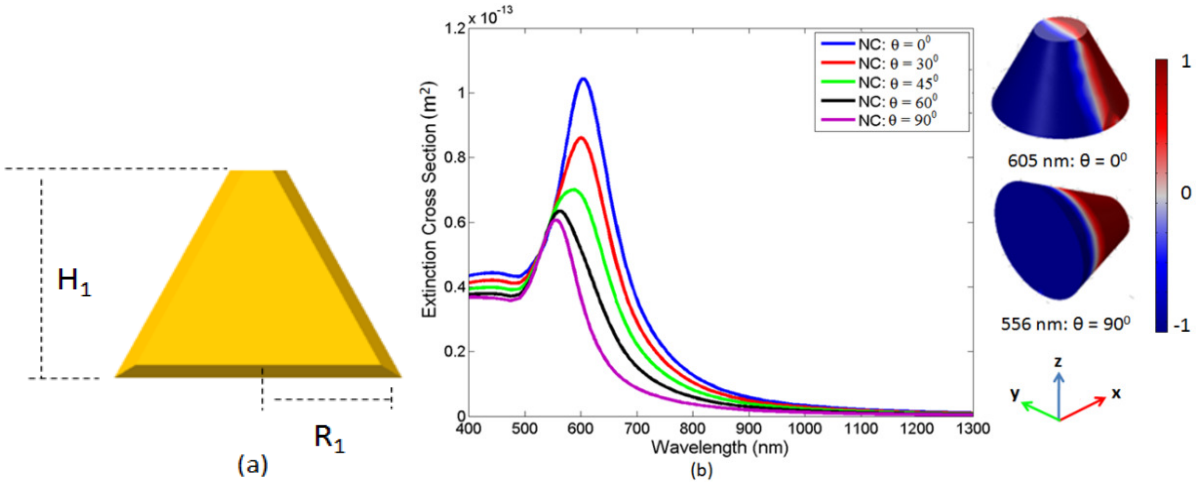

Figure 3. 2. (a) Gold nanocone with R_1=85 nm, H_1=95 nm. (b) Extinction spectra at different angles θ. Inset shows the surface charge distributions relevant to the transverse (at 605 nm) and axial (at 556 nm) dipolar modes.

3.2.1. Gold nanocone (NC)

We consider the truncated gold nanocone (NC) shown in Figure 3.2(a). Its radius R_1 and its height H_1 are 85 nm and 95 nm, respectively. The extinction spectrum is slightly affected by rotating its axis around the *y*-axis, as shown in figure 3.2(b). The resonance peak at $\theta = 0^{\circ}$ (blue line) is relevant to the transverse dipolar mode as it is corroborated by the charge distribution on the gold surface at 605 nm shown in the inset of Figure 3.2(b). By increasing θ, the peak amplitude of the transverse dipolar mode weakens, shifts towards the blue and an axial dipolar mode appears. At $\theta = 90^{\circ}$ (purple line), the dipolar mode is purely axial, as it is confirmed by the surface charge distribution at 556 nm shown in the insets of Figure 3.2(b). These extinction spectra are typical of gold nanoparticles with cylindrical symmetries.

3.2.2. Silica-gold conical nanoshell (CNS)

We consider now a conical nanoshell (CNS) composed of a conical silica core, with a relative dielectric constant of 2.04, and a coaxial gold conical shell surrounding the silica cone, Figure 3.3(a). The dimensions are R_1=85 nm, H_1=95 nm /R_2=60 nm, H_2=70 nm. This nanostructure is obtained by replacing the inner part of the truncated gold nanocone with a truncated silica cone.

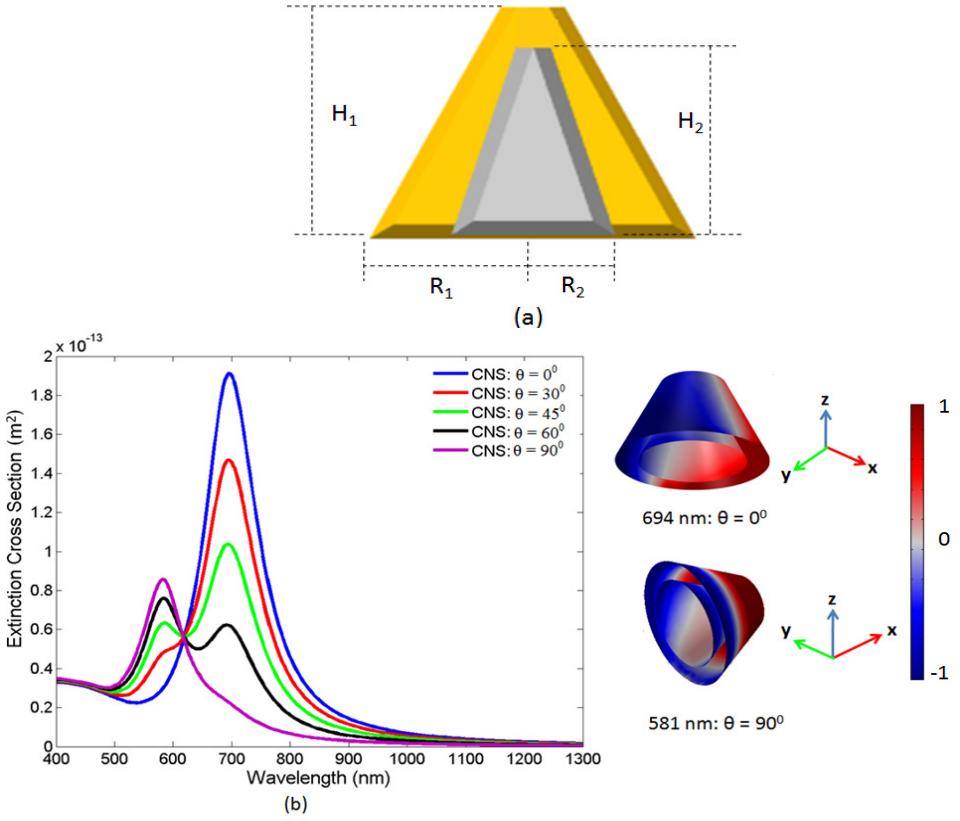

Figure 3. 3. (a) Silica-gold conical nanoshell with R_1=85 nm, H_1=95 nm /R_2=60 nm, H_2=70nm. (b) Extinction spectra at different values of the angle θ. Inset shows the surface charge distributions relevant to the transverse (at 694 nm) and axial (at 581 nm) dipolar modes.

We first discuss the optical properties of the CNS for $\theta = 0^{\circ}$. They can be understood by using the plasmon hybridization theory [61]. From the discussion of a single nanoshell structure in chapter 2, we know that, the plasmon oscillations of the CNS arise from the interaction of the plasmon oscillations supported by the solid gold nanocone and the silica cavity in a gold environment. The interaction occurs between the transverse dipolar mode of

the gold nanocone and that of the silica cavity, which splits the transverse dipolar mode into the higher-energy antibonding mode $|\omega_+\rangle$ and the lower-energy bonding mode $|\omega_-\rangle$. The antibonding mode arises from the antisymmetric coupling between the cone and cavity dipolar modes, which is characterized by a small electric dipole moment. For this reason, the antibonding mode does not appear in the extinction spectrum. Instead, the bonding mode, which arises from the symmetric coupling between the cone and cavity dipolar modes, contributes significantly to the scattered field.

The extinction spectrum of the CNS is highly influenced by the rotation of its axis around the *y*-axis, as shown in Figure 3.3(b). For inclined incident wave ($\theta \neq 0^\circ$), both the transverse and the longitudinal bonding modes are excited. At $\theta = 0^\circ$ (blue line), the hybridization phenomenon of the primitive dipolar modes is stronger than at $\theta = 90^\circ$ (purple line). The charge distributions on the outer surface of the gold shell and at the gold-silica interface, relevant to the transverse (at 694 nm, $\theta = 0^\circ$) and axial (at 581 nm, $\theta = 90^\circ$) bonding modes are shown in the inset of figure 3.3(b). They are the typical distributions of the dipolar charge configurations.

3.2.3. Multi-layered nanocone (MNC)

We here consider a truncated multilayer nanocone (MNC) composed of an inner gold cone, a middle silica layer and an outer gold shell, as shown in figure 3.4(a) (side view) and 3.4(b) (top view). This nanostructure is obtained by replacing the inner part of a silica-gold conical nanoshell with a coaxial gold nanocone. The addition of the inner gold nanocone will provide an extra degree of tunability as in spherical multilayer nanoshells [27, 28, 98, 99]. The dimensions of the nanostructure are R_1=85 nm, H_1=95 nm /R_2=60 nm, H_2=70 nm /R_3=40 nm, H_3=50 nm.

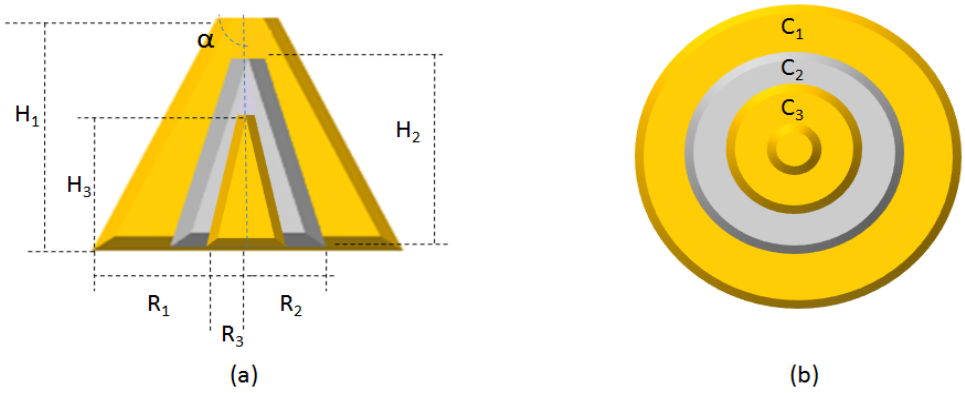

Figure 3. 4. Side (a) and top (b) views of the gold-silica-gold multilayer nanocone.

To interpret the optical response of the MNC, we again employ the plasmon hybridization theory, but at this time we apply it to the inner gold nanocone and the outer silica-gold conical nanoshells [24, 29, 98]. Figure 3.5 shows the extinction spectra of the MNC for $\theta = 0^\circ$ (transverse polarization of the incident field), including the extinction spectra of the inner gold nanocone and the outer silica-gold conical nanoshell. The extinction spectrum of the inner gold cone is very similar to that shown in Figure 3.2(b) for $\theta = 0^\circ$, apart a blue shift of some tens of nanometers. The hybridization will emerge between the dipole mode $|\omega_b\rangle$ of the inner gold cone, which has a resonance at roughly 560 nm, and the dipole-bonding mode $|\omega_-\rangle$ of the outer conical nanoshell, which has a resonance at roughly 694 nm. The mode $|\omega_b\rangle$ interacts with the mode $|\omega_-\rangle$ and give arises two different resonant peaks in

the extinction spectrum as in spherical multilayer nanoshells [27, 29, 114]. The high-energy peak near 600 nm is relevant to a broad antibonding plasmon mode $|\omega_-^+\rangle_{(1)}$ that arises from the symmetric coupling between the modes $|\omega_b\rangle$ and $|\omega_-\rangle$. Instead, the lower-energy peak near 811 nm is relevant to a narrow bonding plasmon mode $|\omega_-^-\rangle_{(1)}$ that originates from the antisymmetric coupling between the modes $|\omega_b\rangle$ and $|\omega_-\rangle$. The surface charge distributions in correspondence of the two peaks and the dip in the extinction spectrum are shown in the insets of Figure 3.5. They are of dipolar type. The charges are induced on three surfaces: the air-gold shell interface S_1 (outer surface), the gold shell-silica shell interface S_2 (intermediate interface) and the silica shell-gold cone interface S_3 (inner interface). At 600 nm, the dipole moment $\mathbf{p}_3$ of the charge distribution on S_3 and the overall dipole moment $\mathbf{p}_{1-2}$ of the charge distributions on S_1 and S_2 oscillate in phase (superradiant dipolar mode), whereas at 811 nm they oscillate out of phase (subradiant dipolar mode). At 719 nm, where a deep dip appears in the extinction spectrum, the surface charge distribution is very similar to that corresponding to the peak at 600 nm, but the intensity of $\mathbf{p}_{1-2}$ is much weaker.

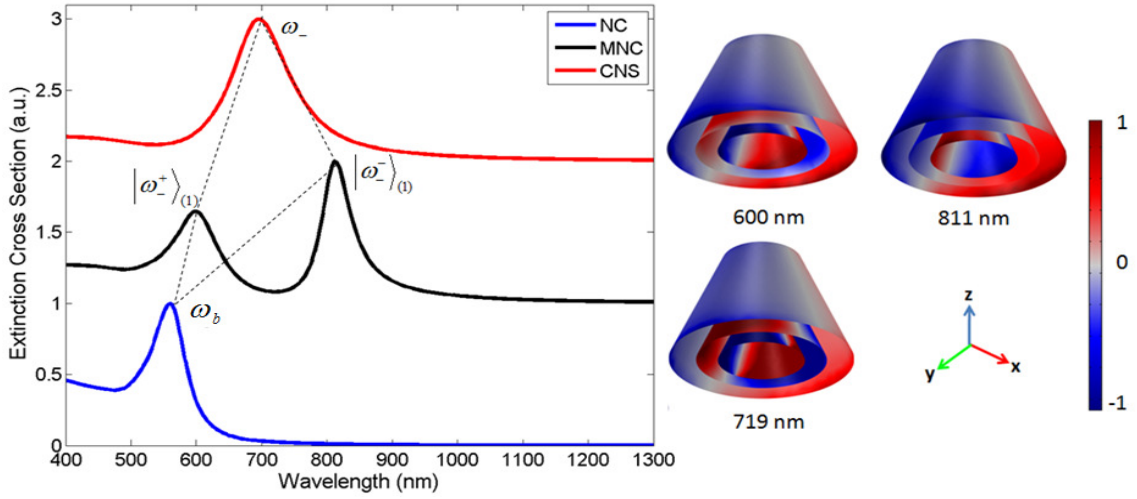

Figure 3. 5. Plasmon mode hybridization in the multilayer nanocone with R_1=85 nm, H_1=95 nm / R_2=60 nm, H_2=70 nm /R_3=40 nm, H_3=50 nm. Bottom and top panel show, respectively, the extinction cross-sections of the gold nanocone and the silica-gold conical nanoshells, while middle panel shows the extinction cross-section of the combined structure. Inset shows the charge distributions corresponding to the peaks at 600 nm and 811 nm, as well as to the dip at 719 nm.

The coexistence of the broad dipolar mode $|\omega_-^+\rangle_{(1)}$ and the narrow dipolar mode $|\omega_-^-\rangle_{(1)}$, which are resonant over the same range of wavelengths, can result in a coupling between them and, therefore, they can produce a dipole-dipole Fano resonance. Figure 3.6 shows the extinction spectra of the MNC with different values of the core-shell aspect ratio. Here (H_1,R_1) and (H_3,R_3) are fixed at (85 nm,95 nm) and (40 nm,50 nm), respectively, instead, the values of H_2 and R_2 are increased in such a way to leave unchanged the semi-angle α. The increasing of R_2 leads to the increase of the separation between the inner gold core and outer gold shell and the decrease of the outer gold shell thickness. The intensity of the $|\omega_-^+\rangle_{(1)}$ dipole peak decreases significantly as the radius of the silica R_2 increases, while its position is practically unaffected. When the R_2 value is small, with the increase of R_2, the $|\omega_-^-\rangle_{(1)}$ dipole peak shows a blue shift, which will enhance the coupling between the $|\omega_-^+\rangle_{(1)}$ and $|\omega_-^-\rangle_{(1)}$

modes. They interact through the near field and a sharp dipole-dipole Fano resonance turns up in the extinction spectrum, with a Fano dip around 719 nm for R_2 = 60 nm [24, 29, 55]. When the R_2 value is large enough, by increasing further the R_2 value, the $\left|\omega_{-}^{-}\right\rangle_{(1)}$ dipole peak shows a red shift and the coupling becomes weak. When the distance is sufficiently high the $\left|\omega_{-}^{-}\right\rangle_{(1)}$ dipole mode does not couple with the $\left|\omega_{-}^{+}\right\rangle_{(1)}$ dipole mode and, hence, the dipole-dipole Fano resonance vanishes. Thus, by controlling the dimensions of the MNC, we can have a pronounced Fano resonance for the coaxial case as well. Higher order dark modes do not appear for $\theta = 0^{\circ}$.

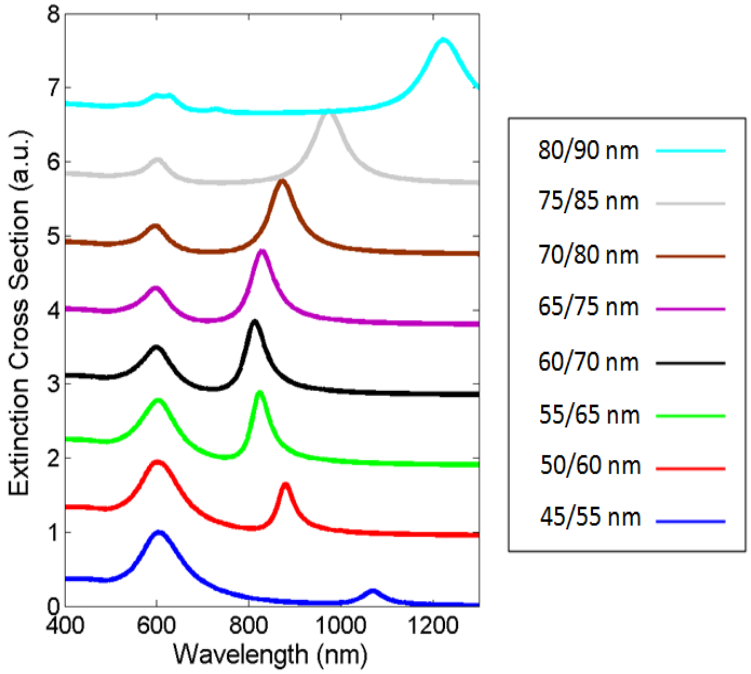

Figure 3. 6. Extinction spectra of the multilayer nanocone for different values of (H_2, R_2) with R_1=85 nm, H_1=95 nm /R_3=40 nm, H_3=50 nm.

Figure 3.7 shows the extinction spectra obtained by rotating the MNC axis around the *y*-axis for different values of θ and the surface charge distributions for $\theta = 90^{\circ}$ in correspondence of the peaks and dips in the extinction spectrum. The peak at 807 nm weakens but does not disappear at $\theta = 90^{\circ}$ like in the simple CNS. The phase variation of the incident wave produces a strong hybridization between the axial and transverse dipolar modes. The surface charge distribution corresponding to the weakly dip at 758 nm shows a similar hybridization even if in a more weak form. A new peak at 661 nm emerges in the spectrum, which clearly shows the appearance of a further axial dipolar mode, beside that relevant to the peak at 566 nm. The dipolar mode at 566 nm is a superradiant longitudinal mode, while that at 661 nm is a subradiant one. The interaction between them give arises to a dipole-dipole Fano dip at 638 nm. The charge distribution relevant to this dip is very similar to that of the superradiant mode as for $\theta = 0^{\circ}$. The considered MNC shows two dipole-dipole Fano resonances, one at 638 nm and the other at 758 nm, which can be switched on and off by rotating the nanostructure or by changing the polarization of the incident field. To our knowledge, this hybridization has never been seen in a symmetric multilayered plasmonic nanostructures reported before.

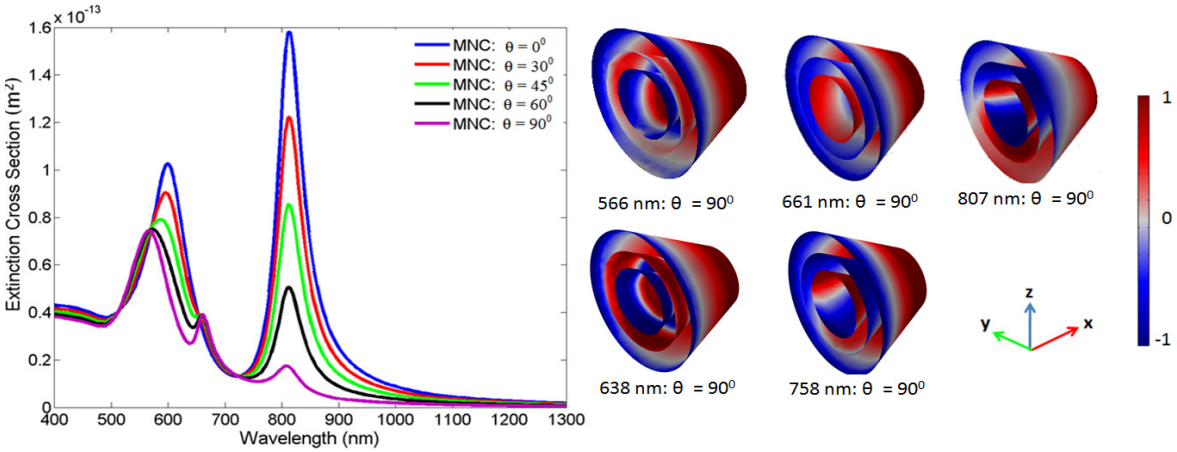

Figure 3. 7. Extinction spectra of the multilayer nanocone with R_1=85 nm, H_1=95 nm / R_2=60 nm, H_2=70 nm /R_3=40 nm, H_3=50 nm for different values of the rotation angle θ. Inset shows the surface charge distributions at five values of the wavelength for θ = 90°.

Figure 3.8 shows the tunability of MNC at θ = 90° for different values of R_2/H_2 with fixed R_1=85 nm, H_1=95 nm /R_3=40 nm, H_3=50 nm. At small values of R_2, the first subradiant dipole mode (D_1) was absent and no Fano resonance was observed in the extinction spectrum (blue line). By increasing the value of R_2, D_1 started to appear and a significant blue-shift of second subradiant dipole mode (D_2) is examined. By keep increasing the value of R_2, D_1 strengthen and slightly blue-shifted. At larger value of R_2 (brown line), the amplitude of D_2 intensifies, broadened and red-shift, while D_1 decreases again. So, by changing the parameters of MNC, we can tuned both the dipole-dipole Fano resonances.

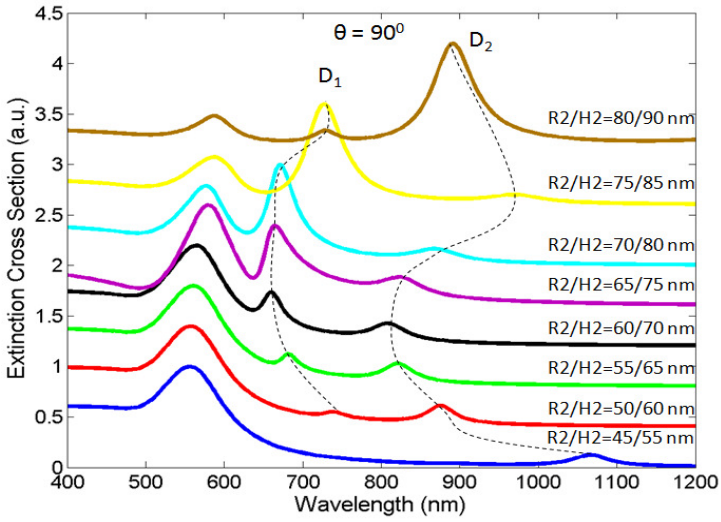

Figure 3. 8. Extinction spectra of the multilayer nanocone at θ = 90° for different values of (H_2, R_2) with R_1=85 nm, H_1=95 nm /R_3=40 nm, H_3=50 nm.

3.2.4. Non-coaxial MNC (NC-MNC)

We consider now a MNC in which the inner gold cone is offset with respect to the shell nanostructure. We named this nanostructure a *non-coaxial MNC* (NC-MNC). In it, modes with different orders and having distinctive angular momenta will mix due to the symmetry breaking introduced by the offset [24, 27, 91, 98]. We analyze the consequences of this symmetry breaking by distinguishing between the case in which the inner gold cone is offset

along the direction of the incident E-field or it is offset along the orthogonal direction, Figure 3.9.

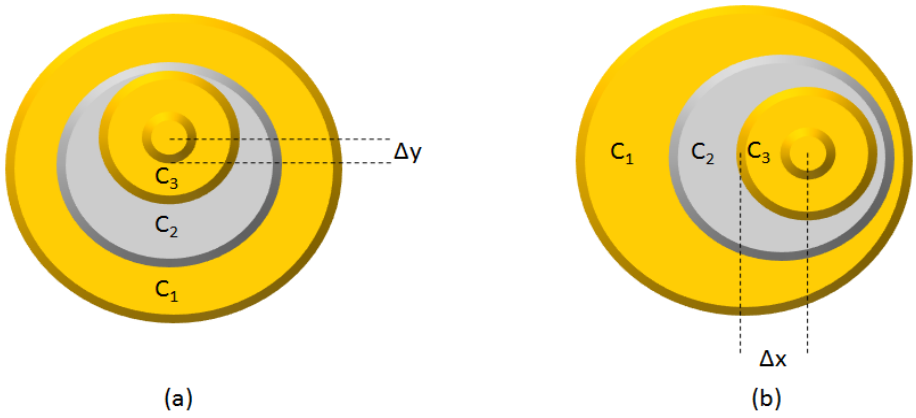

Figure 3. 9. Geometry of a NC-MNC with core offset Δy, orthogonally to the incident E-field (a). Geometry of a MNEC with two components offset Δx, parallel to the incident E-field (b).

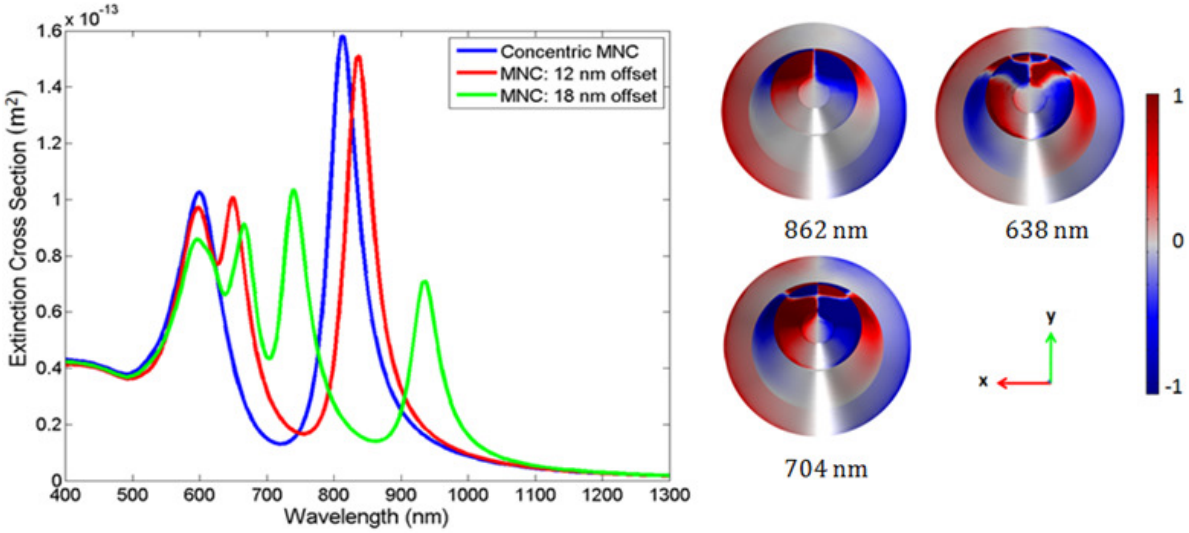

Figure 3. 10. Extinction spectra of a MNC (R_1=85 nm, H_1=95 nm / R_2=60 nm, H_2=70 nm /R_3=40 nm, H_3=50 nm) with core offset orthogonally to the incident E-field. Blue line corresponds to the coaxial MNC, while the red and green lines correspond to NC-MNC with 12 and 18 nm core offsets, respectively. The inset shows the surface charge distributions associated with the dipole-dipole, dipole-quadrupole and dipole-octupole Fano resonances for the 18 nm core offset.

In Figure 3.10, we show the extinction spectra of a NC-MNC in which the inner gold cone is offset orthogonally to the incident E-field, for two values of the offset and $\theta = 0^{\circ}$. They are compared with the extinction spectrum of the corresponding coaxial MNC (blue curve). For a 12 nm core offset (red curve), a dark quadrupolar peak $\left|\omega_{-}^{-}\right\rangle_{(2)}$ with added dipolar components emerges in the spectrum, which couples to the $\left|\omega_{-}^{+}\right\rangle_{(1)}$ mode and engenders a dipole-quadrupole Fano resonance with a minimum near 625 nm. By offsetting the gold cone slightly more (18 nm), besides the red-shift of the Fano resonances, a dark octupolar peak $\left|\omega_{-}^{-}\right\rangle_{(3)}$ emerges, which couples to the $\left|\omega_{-}^{+}\right\rangle_{(1)}$ mode and churn out a dipole-octupole Fano resonance with a dip near 646 nm (green curve). We also note that the modes

$\left|\omega_{-}^{-}\right\rangle_{(1)}$ and $\left|\omega_{-}^{-}\right\rangle_{(2)}$ are red-shifted and their peak amplitudes reduce with the core offset, whereas the $\left|\omega_{-}^{+}\right\rangle_{(1)}$ mode is faintly blue-shifted, because it is a high energy mode and has an extremely feeble interaction with the gold cone dipolar mode [99]. The surface charge distributions corresponding to the dipole, quadrupole and octupole Fano resonances with added dipolar components are shown in the inset of figure 3.10 for the 18 nm core offset. For the dipole-quadrupole Fano resonance, the charges on the shell exhibit a dipolar arrangement, while that on the surface of the inner core exhibit a quadrupolar arrangement, which evidently reveals the mixing of dipole and quadrupole modes. Likewise, for the dipole-octupole Fano resonance, the surface charge distribution exhibits the mixing of dipole and octupole modes.

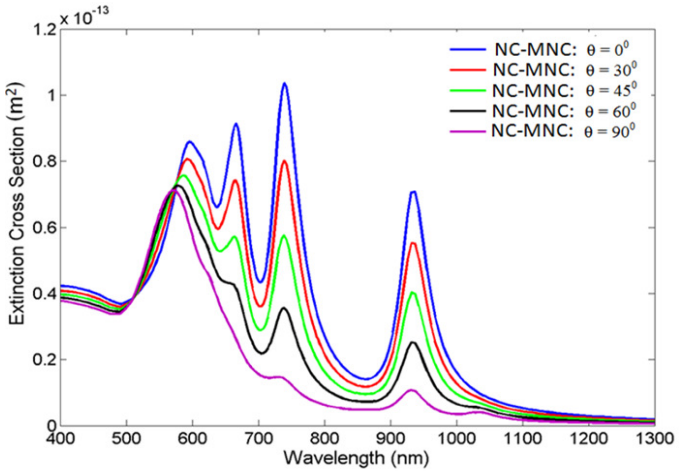

Figure 3. 11. Extinction spectra of the NC-MNC (R_1=85 nm, H_1=95 nm / R_2=60 nm, H_2=70 nm /R_3=40 nm, H_3=50 nm) with core offset of 18 nm orthogonally to the incident E-field, for different values of the rotation angle of the nanostructure axis around the *y*-axis.

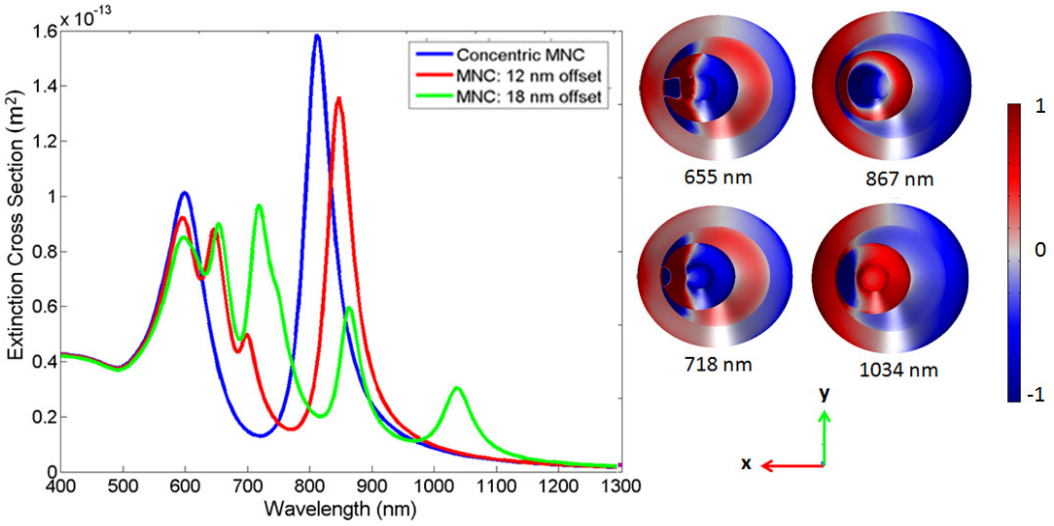

Figure 3. 12. Extinction spectra of a MNC (R_1=85 nm, H_1=95 nm / R_2=60 nm, H_2=70 nm /R_3=40 nm, H_3=50 nm) with core offset parallel to the incident E-field. Blue line corresponds to the coaxial MNC, while the red and green lines correspond to NC-MNC with 12 and 18 nm core offsets. Inset shows surface charge distributions of the plasmon modes relevant to peaks in the extinction spectrum for the 18 nm core offset.

Figure 3.11 shows the extinction spectra of the NC-MNC with 18 nm core offset obtained by rotating the nanoparticle axis around the *y*-axis. At θ = 90°, the higher order modes weaken and start to disappear in the spectrum but still the $|\omega_-^-\rangle_{(1)}$ and $|\omega_-^-\rangle_{(2)}$ modes are present somewhat. The peak positions relevant to the $|\omega_-^-\rangle_{(1)}$ and $|\omega_-^-\rangle_{(2)}$ modes are almost independent of the angle θ. A slightly new peak appears at the low energy level near 1034 nm, which also represents a bonding $|\omega_-^-\rangle_{(1)}$ mode. At θ = 90°, we obtained almost no Fano resonance in the spectrum.

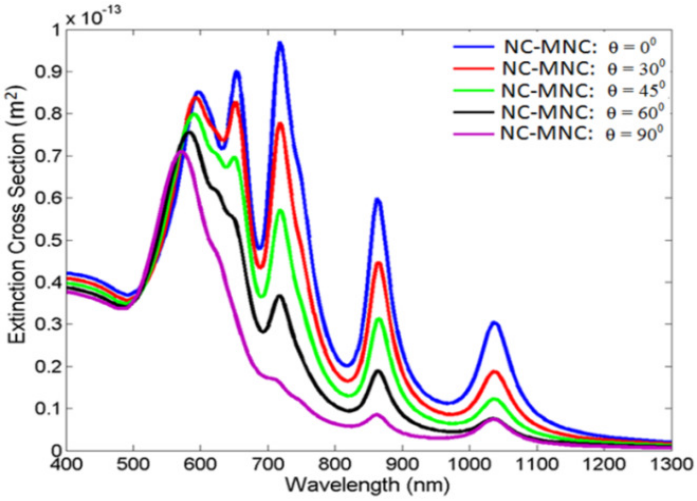

Figure 3. 13. Extinction spectra of the NC-MNC (R_1=85 nm, H_1=95 nm / R_2=60 nm, H_2=70 nm /R_3=40 nm, H_3=50 nm) with core offset of 18 nm parallel to the incident E-field, for different values of the rotation angle of the nanostructure axis around the *y*-axis.

Figure 3.12 shows the extinction spectra of a NC-MNC in which the inner gold cone is offset parallel to the direction of the incident E-field, for the two values of the offset (12 and 18 nanometers), together with the charge distributions for the 18 nm core offset. Here we obtain one more peak in the extinction spectra for both the offset values. For 12 nm core offset (red line), we obtained four extinction peaks in the spectrum. The peak near 698 nm also represents a subradiant dipole mode while the peak near 647 nm represents a quadrupole mode. For 18 nm core offset, both the dipole and quadrupole peaks red-shifts and a new quadrupole peak is observed near 655 nm as shown by the surface charge distributions. The peak near 1034 nm is relevant to the $|\omega_-^-\rangle_{(1)}$ plasmon mode. The peak around 867 nm exhibit a ring shaped dipolar pattern on the inner cone and a half ring shaped on the outer cone, it is also relevant to a $|\omega_-^-\rangle_{(1)}$ plasmon mode. The peaks near 718 nm and 655 nm are relevant to the $|\omega_-^-\rangle_{(2)}$ plasmon mode. Thus by offsetting the gold cone parallel to the incident E-field, we can have twin dipole and quadrupole Fano resonances at different frequencies both in the visible and near infrared region. Figure 3.13 shows the extinction spectra of the NC-MNC with 18 nm core offset parallel to the incident E-field, obtained by rotating the nanoparticle axis around the y-axis. Again at θ = 90°, the higher order modes weaken and start to disappear in the spectrum but still the $|\omega_-^-\rangle_{(1)}$ modes are present somewhat. The peak position of $|\omega_-^-\rangle_{(1)}$ modes are almost independent of the angle θ. Again at θ = 90°, we obtained almost no Fano resonance in the spectrum.

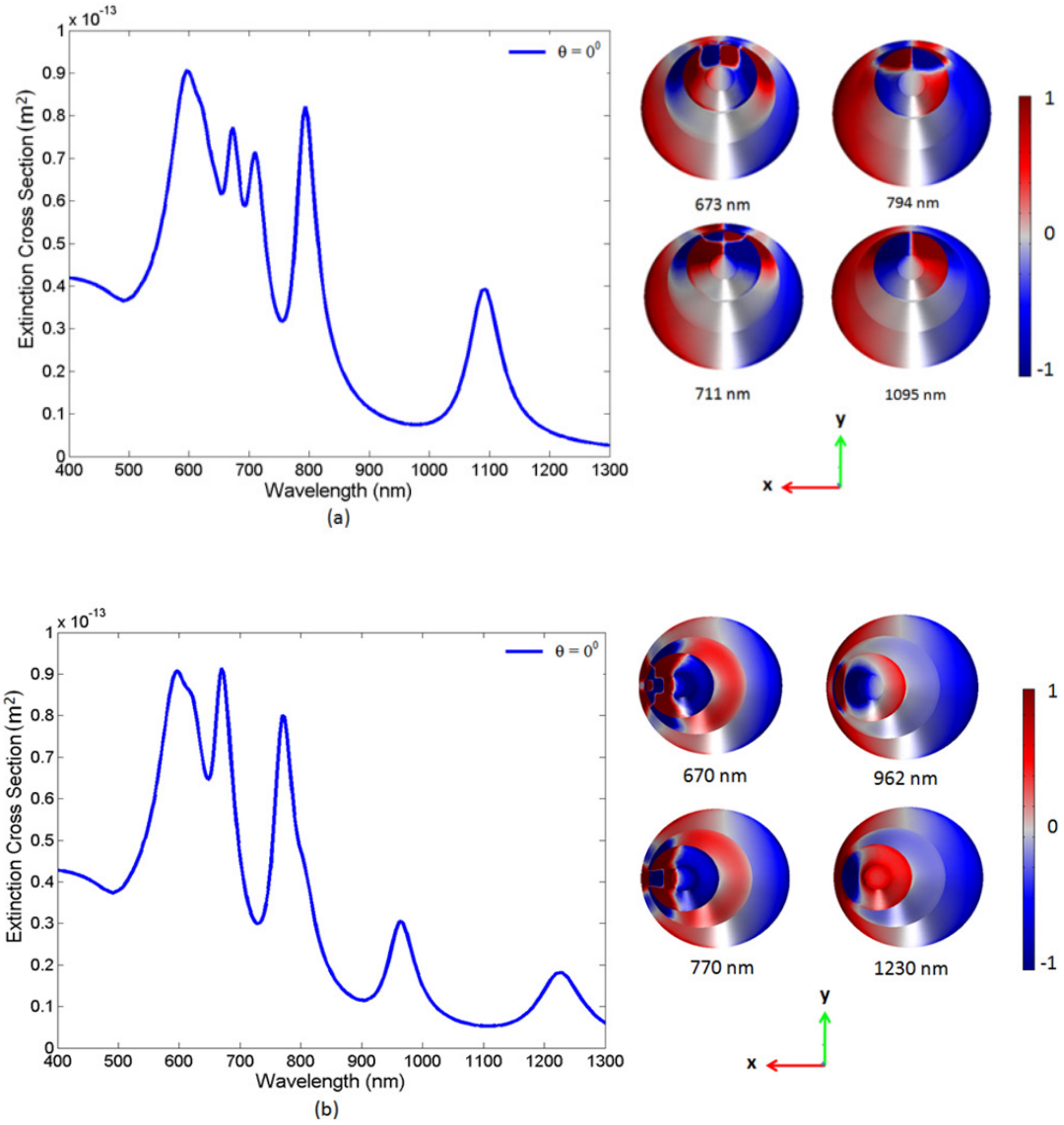

Figure 3. 14. Extinction spectra of a MNEC (R_1=85 nm, H_1=95 nm / R_2=60 nm, H_2=70 nm /R_3=40 nm, H_3=50 nm) with multi-component offsets orthogonal (a) and parallel (b) to the incident E-field, for $\theta = 0^{\circ}$. Inset shows the surface charge distributions (top view) relevant to the last four peaks.

3.2.4.1. Multi-component offset in MNC (MNEC)

We finally break the symmetry of the MNC with two offsets, i.e., both the inner gold cone and silica cone are moved with respect to the outer gold cone. In this way, we obtain a shape that seen from the top it looks like a multilayered nanoegg. We named this nanostructure a *multilayered nanoegg cone* (MNEC). Figure 3.14(a) shows the extinction spectrum of the MNEC in which the silica shell has been moved 18 nm and the inner gold cone has been moved 36 nm in the *y*-direction (orthogonal to the incident E-field) for $\theta = 0^{\circ}$. Figure 3.14(b) shows the same configuration but with the offset in the *x*-direction (parallel to the incident E-field). Five peaks emerge in the extinction spectrum. Observing the surface charge distribution corresponding to each peak of the extinction spectrum of figure 3.14(a), we perceive that the resonant peak near1095 nm is a subradiant dipole mode. The resonant peak near 794 nm is a quadrupole-quadrupole mode, as the surface charges on both the shell and inner cone exhibits a quadrupole pattern, which apparently reveals the mixing. Since, the symmetry of the CNS is also broken in this structure, so higher order modes of the outer cone

will also become visible. The peak around 711 nm patently exhibits the mixed octupole-quadrupole character of the octupole-quadrupole mode and the peak around 673 nm is the combination of octupole modes. Figure 3.14(b) shows the extinction spectrum of the MNEC when the multi-component offset is parallel to the E-field. The peaks near 962 nm and 1230 nm represents dipole-dipole modes, while the peak near 770 nm displays an octupole-quadrupole pattern and the peak around 670 nm is a mixture of octupole modes. Therefore, geometries with multi-component offset have five distinct peaks and pronounced Fano resonances in the extinction spectrum.

3.3. Comparison with multilayered spherical nanostructure

We conclusively compare the near and far field optical properties of the gold-silica-gold MNC and NC-MNC with a concentric multilayered nanosphere (MNS) and a non-concentric MNS (NC-MNS), by taking all the nanostructures with the same volume.

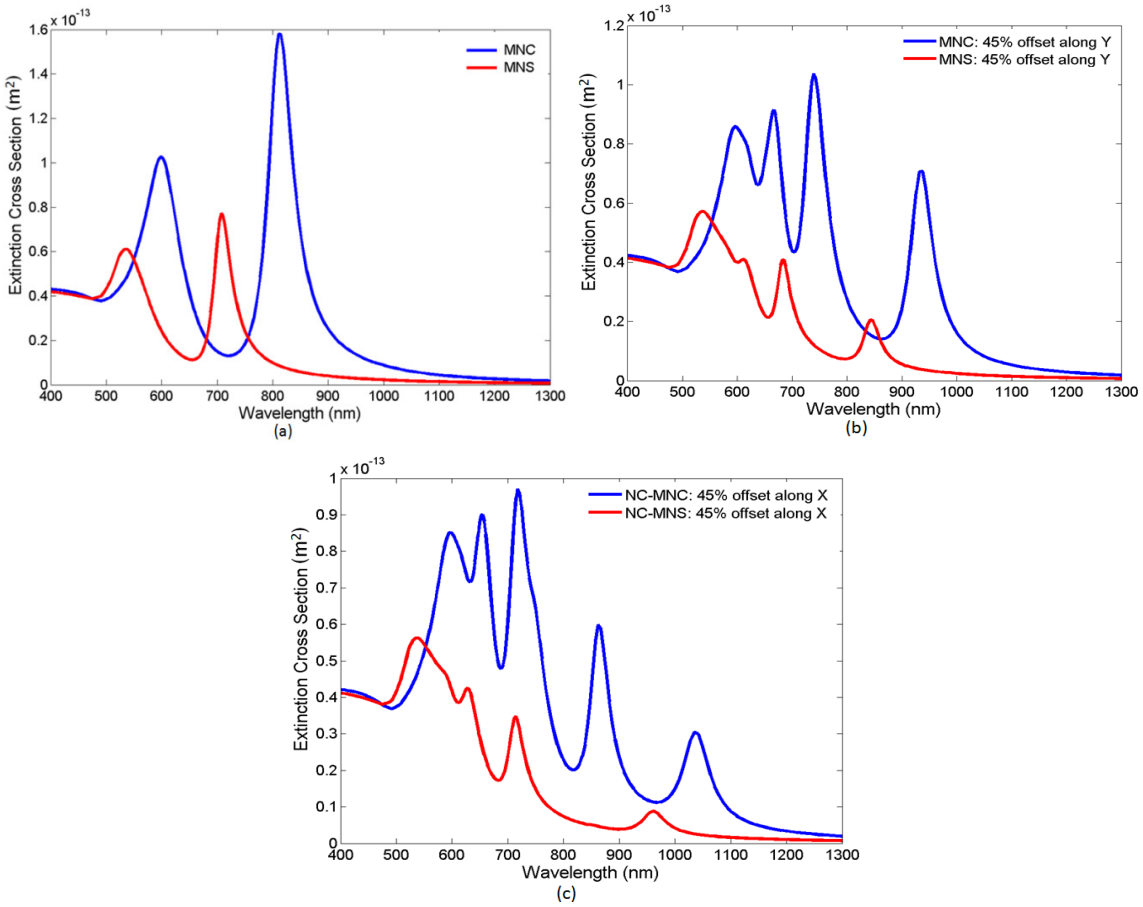

Figure 3. 15. Extinction cross-section. (a) MNC and MNS nanostructures. (b) NC-MNC and NC-MNS with 45% core offset orthogonally to the incident E-field. (c) NC-MNC and NC-MNS with 45% core offset parallel to the incident E-field.

By considering the far field properties first, we observed a sharp dipole-dipole Fano resonance in the extinction spectrum of the MNC compared to those observed in the MNS, as shown in Figure 3.15(a). Figure 3.15(b) shows the extinction spectra of the NC-MNC and the NC-MNS with a 45% core offset orthogonally to the direction of the incident E-field. As a consequence of the symmetry breaking, additional Fano resonances arise in the spectrum. The modulation depths of the dipole, quadrupole and octupole Fano resonances in the case of

the NC-MNC are found to be larger and sharper compared to those observed in the NC-MNS nanostructure. Figure 3.15(c) shows the extinction spectra of both the structures with a 45% core offset parallel to the direction of the incident E-field. We obtained five peaks in case of NC-MNC, which proves its strength in the generation of higher order Fano resonances compared to NC-MNS. The dominant scattering and absorption cross sections of both the MNC and NC-MNC may be considered as excellent candidates for the bio-imaging and photo-thermal treatment applications [97].

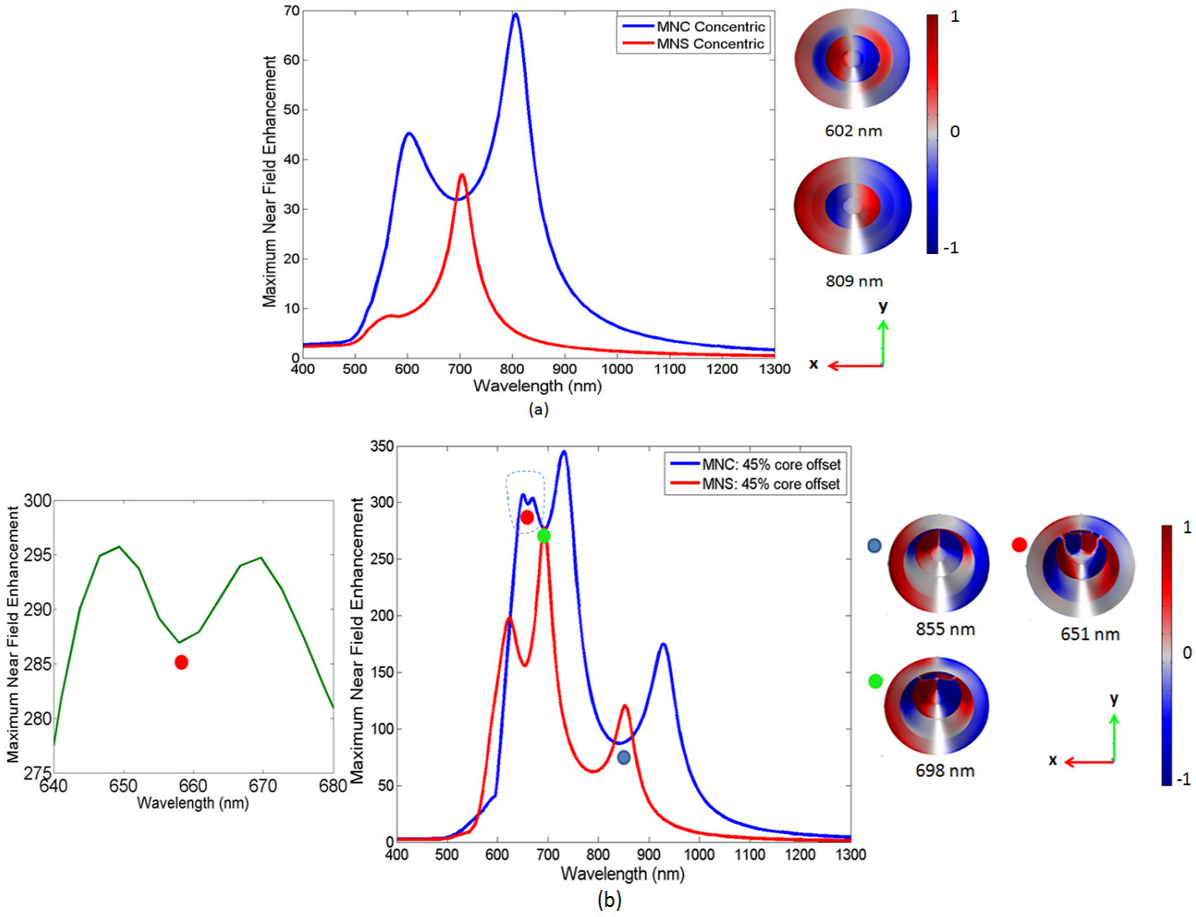

Figure 3. 16. (a) Maximum near field enhancement of MNC and MNS nanostructures. Insets shows surface charge distributions (top view) corresponding to each peak in the MNC. (b) NC-MNC and NC-MNS with 45% core offset orthogonally to the incident E-field. The displayed small window corresponds to the dashed box, which shows the octupole Fano resonance. Insets shows surface charge distributions (top view) corresponding to each Fano dip (dot) in NC-MNC.

We eventually compare the Fano resonances in the near field optical properties of the MNC and the NC-MNC with those observed in the MNS and the NC-MNS nanostructures. Figure 3.16(a) shows the maximum near field enhancement (MNFE) as a function of wavelength of both the MNC and MNS nanostructures. It is seen that the peaks of near field enhancement for both the MNC and MNS nanostructures emerge almost at the same wavelengths as in the extinction spectra. The MNFE value of the MNC $\left|\omega_{-}^{-}\right\rangle_{(1)}$ mode is around 70, which is quite high than the MNS $\left|\omega_{-}^{-}\right\rangle_{(1)}$ mode. Figure 3.16(b) shows the MNFE of both the NC-MNC and NC-MNS for a 45% core offset orthogonally to the direction of E-field. It appears that the NC-MNC can provide the excellent enhancement values at various regions in the spectrum compared to NC-MNS nanostructure, which is an important attribute

of SERS. The surface charge distributions corresponding to each Fano dip are shown in the inset. On the other hand, for the NC-MNS, the octupole mode is missing in the MNFE spectra. From the MNFE spectra it becomes clear that the energy stored in the dark hybridized modes is larger than those stored in the bright modes due to the weak radiation losses [39]. Thus, based on the above findings, we concluded that MNC and NC-MNC nanostructures exhibit sharp tunable Fano resonances with large modulation depths both in the near and far field optical properties compared to MNS and NC-MNS nanostructures, which would be useful for multi-wavelength SERS and bio-sensing [95, 119, 120].

3.4. Optical characterization of MNC

Finally, for optical characterization of MNC, we investigated the scattering parameters by making use of image theory to make periodic images of the nanostructure adjacent to unit cell. Perfect electric conductor (PEC) boundaries are used perpendicular to E-field polarization and perfect magnetic conductor (PMC) boundaries are used perpendicular to H-field polarization. We studied the effect of coupling of adjacent nanoparticles in a periodic lattice constant. The periodic arrangement of concentric MNC are shown in figure 3.17(a), where '*a*' denotes the lattice constant. Due to lower physical cross section relative to lattice constant area, we have higher transmission for large lattice constants and vice versa. For the symmetric periodic nanostructures, the transmission spectra reveals the dipolar modes, Figure 3.17(b). An overall red-shift in the spectrum due to smaller lattice constant have been observed. For instance the dipole mode (green) red-shifts from 802 nm to around 820 nm. For asymmetric periodic nanostructures, the transmission spectra demonstrates the dipole, quadrupole and octupole modes, Figure 3.17(c). An overall red-shift of the modes have also been monitored here by reducing the lattice constant.

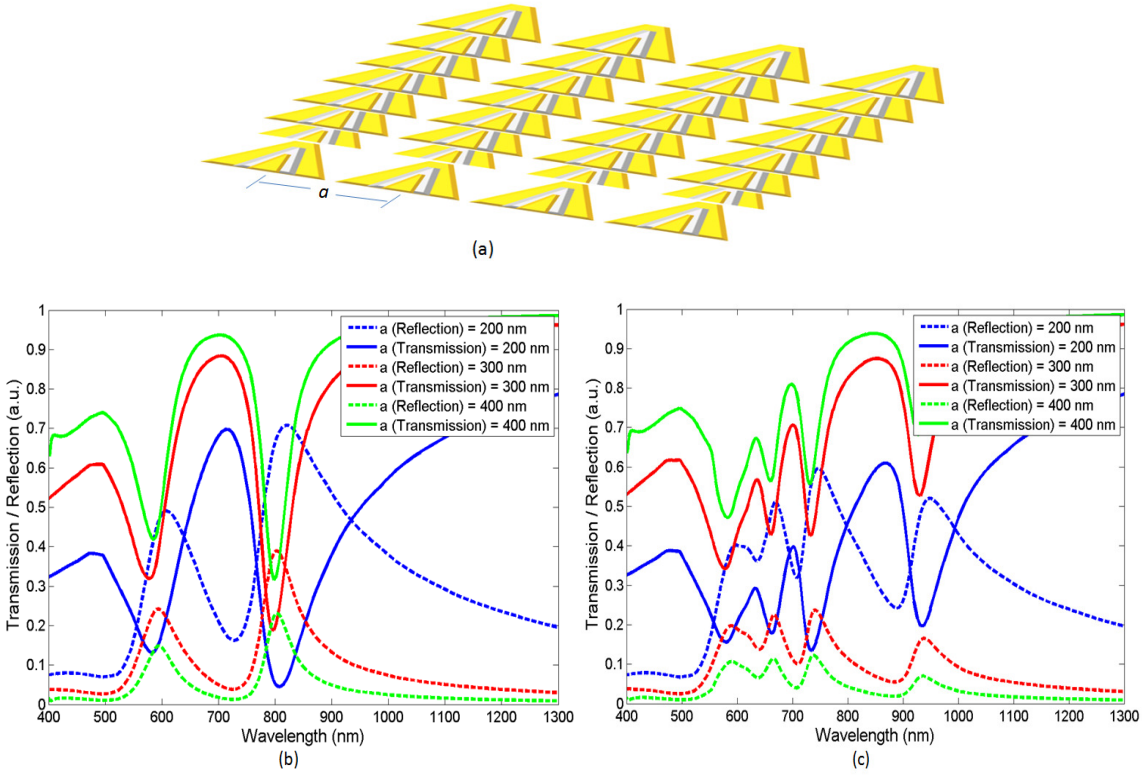

Figure 3. 17. (a) Periodic array of MNC. Transmission and reflection spectrum of: (a) concentric MNC. (b) NC-MNC.

3.5. Concluding remarks

In conclusion, we have investigated the generation of higher order Fano resonances in a multilayered gold-silica-gold nanostructure with conical shape illuminated by a linearly polarized light. For a coaxial multi-layered nanostructure a sharp dipole-dipole Fano resonance is obtained by varying the relative dimensions of the layers, whose resonance frequencies can be changed by rotating the nanostructure. Two types of breaking of the axial symmetry have been introduced in the multilayered nanostructure, first by offsetting the inner core with respect to the outer shell to make a non-coaxial multilayered nanostructure and then by offsetting simultaneously the inner gold cone and the middle silica cone. In the first case, the coupling between the superradiant dipolar and subradiant higher multipolar modes results in additional Fano resonances in the optical spectrum compared to the coaxial multilayered nanostructure. If the offset is parallel to the incident E-field, we have twin dipole and quadrupole Fano resonances at different frequencies both in the visible and near infrared region. Multi-component offsetting in MNEC nanostructures renders visible high order dark modes and provides sharp tunable Fano resonances. Finally, we relate the near and far field optical properties of MNC and NC-MNC with MNS and NC-MNS nanostructures and observed strong tunable higher order Fano resonances in case of MNC and NC-MNC. The maximum near field enhancement is also found to be greater in various regions in both the MNC and NC-MNC nanostructures, which is an essential feature of SERS. To conclude, MNC, NC-MNC and MNEC nanostructures are ideal for producing pronounced tunable Fano resonances and higher order dark hybridized modes in the visible and near infrared region, which may be useful for plasmon sensing, electromagnetic induced transparency, lasing, slowing light, switching and SERS applications.

Chapter 4

Fano Nanostructures

4.1. Introduction

After the extensive study of spherical and conical structures with multi-components, in this chapter, we extended the similar conception to cubic, elliptical and cylindrical structures with multi-components and observed the same effect of higher order dark hybridized modes and Fano resonances. These nanostructures have been designed in such a manner that the broad superradiant and narrow subradiant plasmon modes overlap in energy and result in a strong Fano resonance in the optical spectrum. The similar symmetry breaking scheme have been introduced for the generation of multiple Fano resonances. These metallodielectric nanostructures with reduced symmetry also reveals considerably high local-field enhancement. For all the considered nanostructures, the polarization of the incident field is set along *x*-axis and the wave propagation along *z*-axis.

4.2. Multilayered nanodice

This complex nanostructure contains an inner metal core, a middle dielectric layer and the outer metal dice as shown in figure 4.1. The dimensions of a gold-silica-gold multilayered nanodice (MND) are 40/60/95 nm, where 40 nm is the size of the inner gold dice, 60 nm is the size of the middle dielectric dice and 95 nm is the size of the outer gold dice, respectively. The edges and corners of the nanostructure have been smoothened to avoid unexpected peaks in the spectrum.

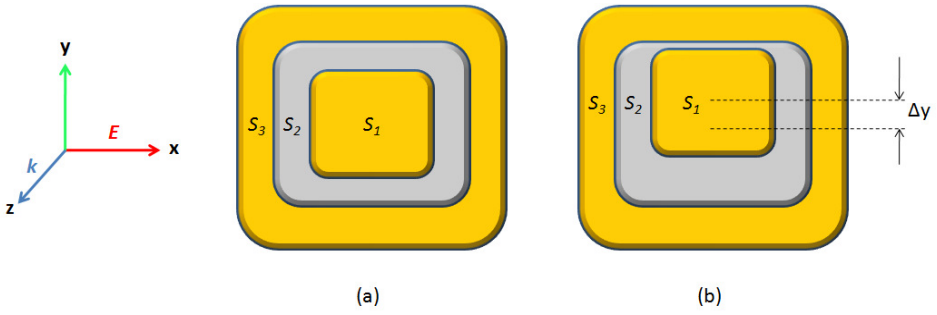

Figure 4. 1. Geometry of (a) concentric MND and (b) non-concentric MND with offset core Δy.

4.2.1. Far field optical properties of MND

Figure 4.2 demonstrates the scattering spectra of concentric gold-silica-gold MND. In consonance with the hybridization theory, for the concentric situation only those modes that have the same "angular momentum" will interact [61, 98]. Thus we dig up two different resonant peaks in the spectrum. The high energy peak around 566 nm is the broad superradiant antibonding plasmon mode $\left|\omega_{-}^{+}\right\rangle_{(1)}$ of the dipole-dipole interaction between the inner gold core and the shell and the lower energy peak around 708 nm is the narrow subradiant bonding plasmon mode $\left|\omega_{-}^{-}\right\rangle_{(1)}$. Due to the near field coupling between $\left|\omega_{-}^{+}\right\rangle_{(1)}$ and $\left|\omega_{-}^{-}\right\rangle_{(1)}$ modes of MND, a Fano resonance with a minimum around 676 nm appears in the

spectrum, which is named as dipole-dipole Fano resonance (DDF) [22, 27]. This hybridization and modes coupling is convincingly similar to multilayered nanoshell (MNS). Gauss's law was applied to the E-field near the boundary to account for both bound and free surface charge densities. At 566 nm, the charge distributions on the inner dice and outer layer are the same, so this corresponds to $\left|\omega_{-}^{+}\right\rangle_{(1)}$ mode. At 708 nm, the charge distributions on the inner dice and outer layer are opposite, which corresponds to $\left|\omega_{-}^{-}\right\rangle_{(1)}$ mode. The spectral minimum at 676 nm corresponds to DDF.

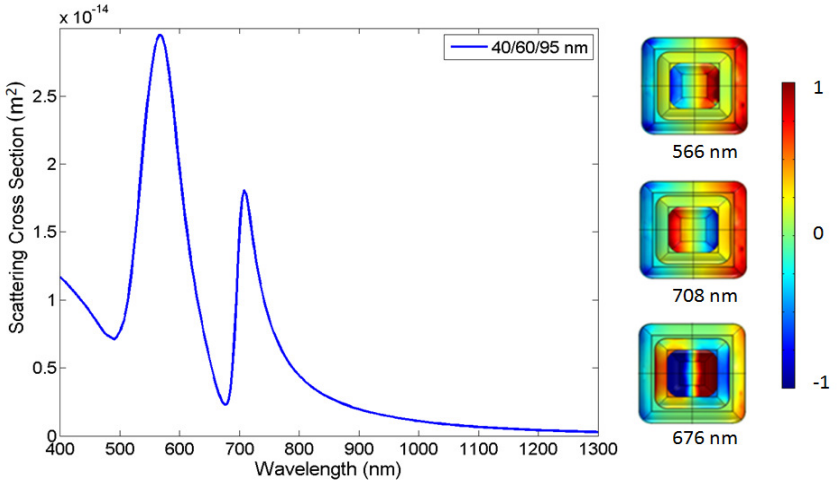

Figure 4. 2. Scattering cross section of concentric MND. Inset shows surface charge distributions corresponding to superradiant mode, subradiant mode and Fano dip.

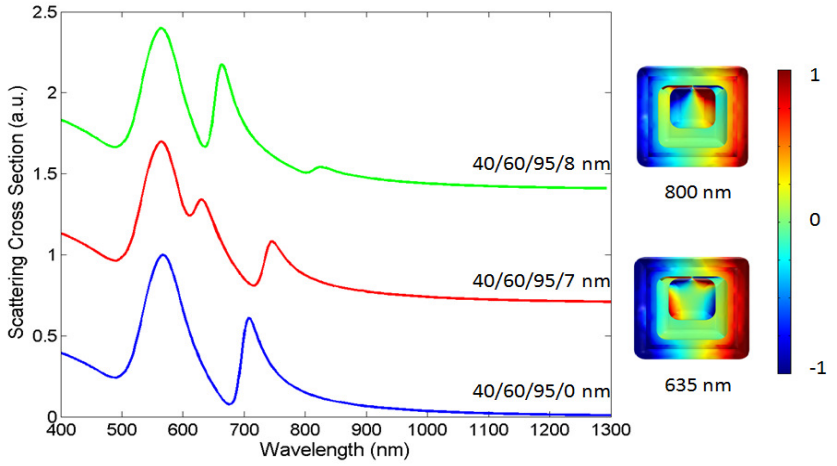

Figure 4. 3. Scattering spectra of NC-MND nanostructure. Δy = 0 (blue line), Δy = 7 (red line) and Δy = 8 (green line). Insets shows surface charge distributions corresponding to DDF and DQF for 8 nm offset.

4.2.1.1. Symmetry breaking in MND

Figure 4.3 shows the effect of symmetry breaking in MND having dimensions 40/60/95 nm by offsetting the inner gold dice in the *y*-direction from its center, due to which modes of different orders will mix [91, 98]. The blue line corresponds to the concentric MND. For a 7 nm core offset, a dipole active quadrupolar mode $\left|\omega_{-}^{-}\right\rangle_{(2)}$ emerges in the spectrum, which

couples to $\left|\omega_{-}^{+}\right\rangle_{(1)}$ mode and engenders a dipole-quadrupole Fano resonance (DQF) with a minimum around 610 nm (red line). The DDF also is red-shifts with the core offset. If we move the core slightly more to around 8 nm, the DDF and the DQF are red-shifted to around 800 nm and 635 nm. It is also to be noted here that the $\left|\omega_{-}^{-}\right\rangle_{(1)}$ mode is also red-shifted and its peak amplitude decreases with the core offset, whereas $\left|\omega_{-}^{+}\right\rangle_{(1)}$ mode is faintly blue-shifted. This shows the similarity of non-concentric MND (NC-MND) with non-concentric MNS (NC-MNS). The surface charges corresponding to DDF and DQF for 8 nm core offset are also shown in the inset of figure 4.3. For the DQF, the surface charges on the shell exhibits a dipolar pattern, while the core exhibits a quadrupolar pattern, showing the mixed dipolar-quadrupolar character of DQF.

4.2.1.2. Effect of polarization

Figure 4.4 shows the scattering spectra of NC-MND with different particle orientations i.e., we displaced the inner gold core 8 nm from its center both perpendicular and parallel to the incident field polarization. The blue line shows that the incident field is polarized perpendicular to the axis of symmetry, while the red line shows that the incident field is polarized parallel to the axis of symmetry. Different orientation of the nanoparticle produces the same $\left|\omega_{-}^{-}\right\rangle_{(1)}$ and $\left|\omega_{-}^{-}\right\rangle_{(2)}$ modes but does not show much similarity because of the peaks amplitudes and spectral positions. Thus, the optical response of MND is somewhat polarization dependent in contrast to the MNS nanostructure.

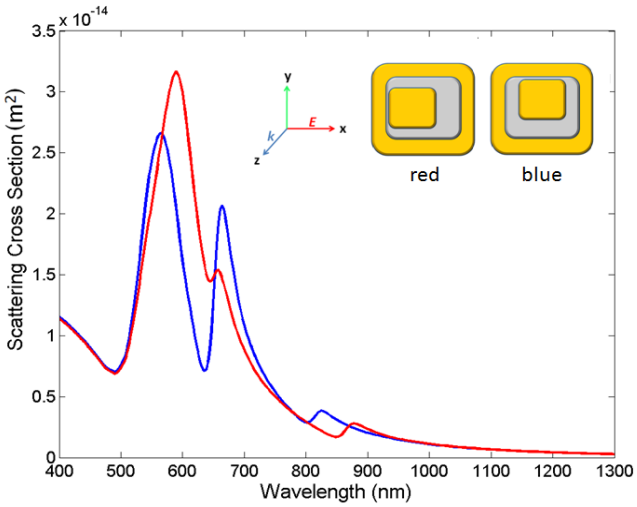

Figure 4. 4. Scattering spectra for NC-MND with different particle orientations. Blue line: incident electric field is polarized perpendicular to axis of symmetry. Red line: incident electric field is polarized parallel to axis of symmetry.

4.2.2. Near field properties of MND

The electromagnetic near field distributions of MND for various core offsets is also investigated. For all resonances, the maximum near field enhancement was observed within the silica layer like in MNS nanostructure. Figure 4.5 shows the maximum near field enhancement of $\left|\omega_{-}^{-}\right\rangle_{(1)}$ and $\left|\omega_{-}^{-}\right\rangle_{(2)}$ modes, which turn out to be more localized and strenuous with enhancing core offset [25, 27]. For instance, the electromagnetic near field enhancement

for $\left|\bar{\omega}_{-}\right\rangle_{(1)}$ mode (concentric case) is 29, which become 96 with 8 nm core offset. Similarly, the maximum value of the enhancement for $\left|\bar{\omega}_{-}\right\rangle_{(2)}$ mode is also booted up with the core offset, which is an imperious attribute of SERS [45, 75]. So higher order hybridized modes increases the value of the near field enhancement in MND, which proves a similitude with MNS.

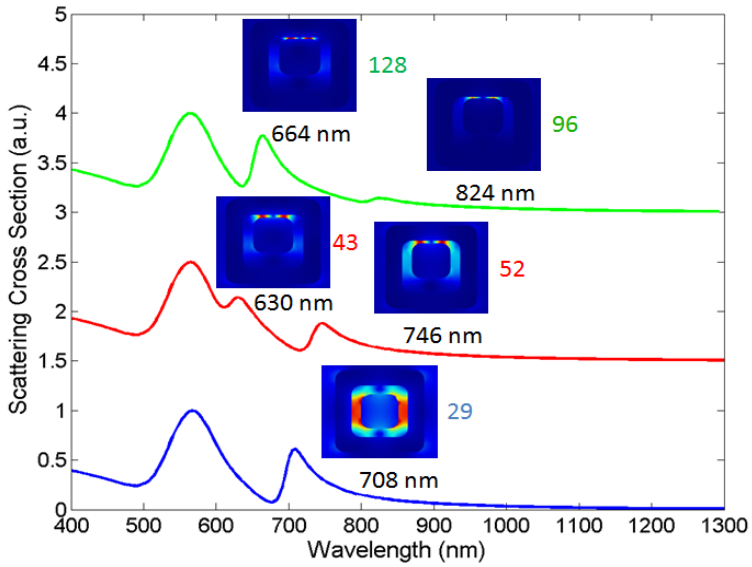

Figure 4. 5. Electromagnetic near field distributions at each scattering peak with various core offsets. Blue line Δy = 0, red line Δy = 7 nm and green line Δy = 8 nm. The wavelength of the scattering peaks and the enhancement values are also shown.

4.3. Multilayered nanoellipsoid

This complex nanostructure contains an inner metal core, a middle dielectric layer and an outer metal shell like MNS. Figure 4.6(a) shows the geometry of a single three dimensional ellipsoid. Figure 4.6(b) shows a gold-silica-gold multilayered nanoellipsoid (MNE) with an offset core. Here E_1 denotes the inner ellipse having dimensions a_1-semiaxis = 40 nm, b_1-semiaxis = 30 nm, c_1-semiaxis = 30 nm, E_2 denotes the middle ellipse having dimensions a_2-semiaxis = 60 nm, b_2-semiaxis = 40 nm, c_2-semiaxis = 40 nm and E_3 denotes the outer ellipse having dimensions a_3-semiaxis = 75 nm, b_3-semiaxis = 55 nm, c_3-semiaxis = 55 nm, respectively. The electric field is directed along x and the wave propagates in the z-direction.

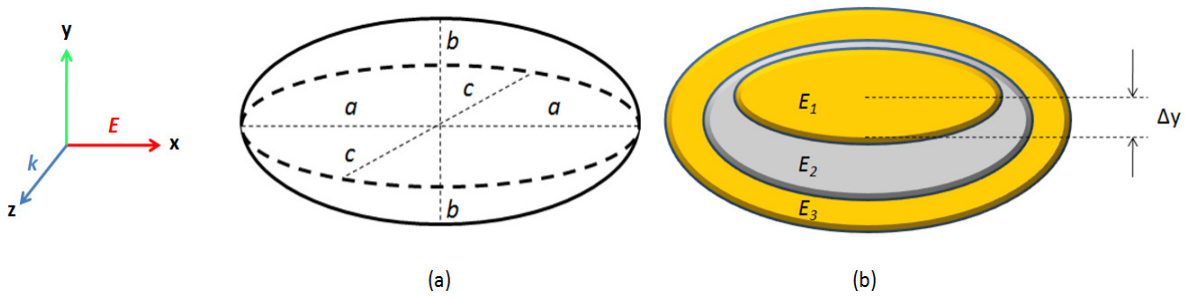

Figure 4. 6. (a) Sketch of a single three dimensional nanoellipsoid. *'a'*, *'b'* and *'c'* representing the major and minor axis of the ellipsoid. (b) Sketch of a non-concentric MNE with inner core offset Δy. E_1, E_2 and E_3 denotes the inner, middle and outer ellipsoids.

4.3.1. Far field optical properties of MNE

Figure 4.7 shows the scattering cross section of a concentric MNE. The coupling and interference of the superradiant antibonding dipole mode $\left|\omega_{-}^{+}\right\rangle_{(1)}$ near 580 nm and subradiant bonding dipole mode $\left|\omega_{-}^{-}\right\rangle_{(1)}$ near 824 nm gives rise a Fano dip near 777 nm. The higher order modes remain dark in the concentric case. This confirms the resemblance of MNE with MNS nanostructure. The surface charge distributions associated with $\left|\omega_{-}^{+}\right\rangle_{(1)}$, $\left|\omega_{-}^{-}\right\rangle_{(1)}$ and Fano dip are shown in the inset.

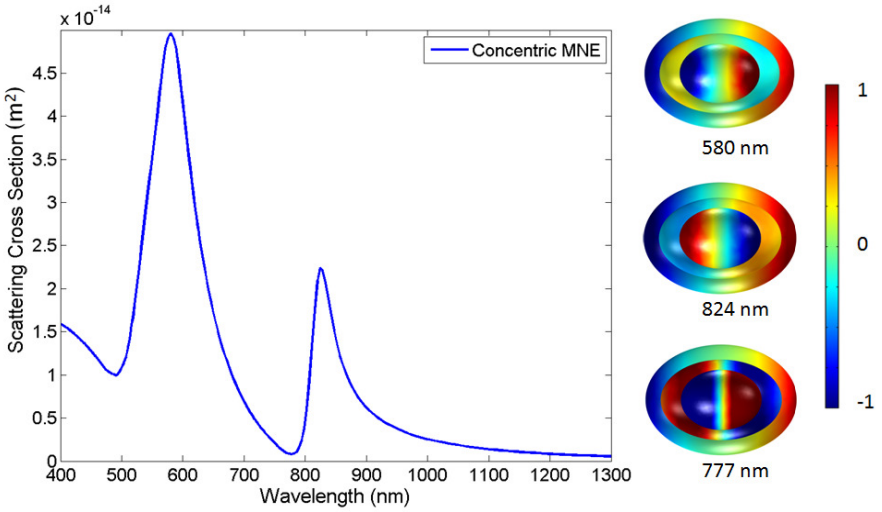

Figure 4. 7. Scattering cross section of a concentric MNE. Inset shows surface charge distributions corresponding to superradiant mode, subradiant mode and Fano minimum.

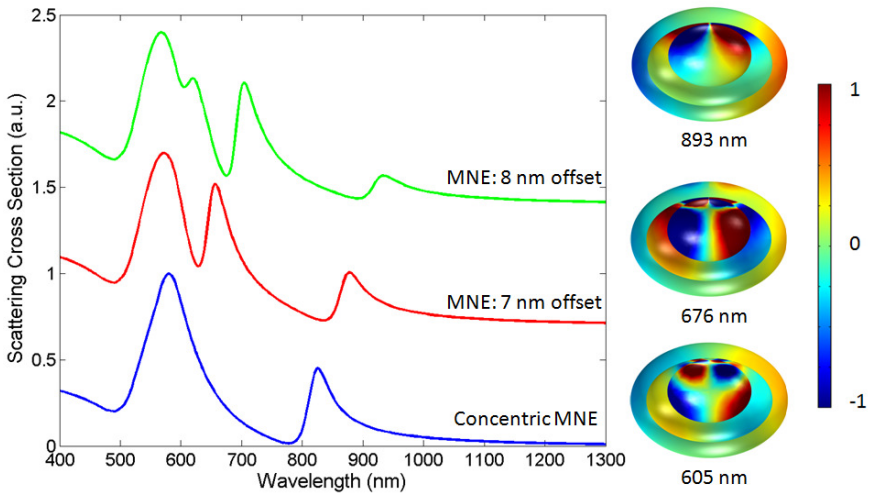

Figure 4. 8. Scattering spectra of MNE nanostructure with various core offsets. Δy = 0 (blue line), Δy = 7 (red line) and Δy = 8 (green line). Insets shows surface charge distributions corresponding to DDF, DQF and DOF for 8 nm offset.

4.3.1.1. Symmetry breaking in MNE

To excite the higher order modes in the spectrum, we break the symmetry of the structure in a similar fashion i.e., offsetting the inner gold core in the *y*-direction, Figure 4.6(b). Figure

4.8 shows the scattering spectra of MNE for various core offsets. For a 7 nm core offset (red line), $\left|\omega_{-}^{-}\right\rangle_{(2)}$ mode near 656 nm arises in the vicinity of $\left|\omega_{-}^{+}\right\rangle_{(1)}$ mode, due to which the coupling between the two modes results in a DQF near 628 nm. By further offsetting the core (green line), a dipole active octupolar mode $\left|\omega_{-}^{-}\right\rangle_{(3)}$ emerges in the spectrum, which couples to $\left|\omega_{-}^{+}\right\rangle_{(1)}$ mode and induces dipole-octupole Fano resonance (DOF) near 605 nm. The DDF and DQF are also red-shifted with the core offset, which shows a strong similarity with the NC-MNS nanostructure. The surface charge distributions corresponding to each Fano dip for 8 nm core offset are shown in the inset, which clear illustrates the mixing of dipole and higher dark multipolar modes.

Figure 4.9 shows the effect of symmetry breaking in MNE by rotating the inner gold ellipse towards *y*-axis. For $\theta = 0^{\circ}$, we have two dipole peaks i.e., superradiant and subradiant (D_1). For $\theta = 10^{\circ}$, a new peak appears at the lower energy side near 769 nm, which also represents a subradiant dipole mode (D_2). The D_1 mode is slightly red-shifted and eventually disappeared by increasing the value of θ, while the D_2 mode enhances and slightly blue-shifted. The surface charge distributions corresponding to each peak at $\theta = 20^{\circ}$ are shown in the inset. At 777 nm, the surface charges on the inner core and outer shell oscillate out of phase, which shows a D_2 mode. So in this way, the dipole moment rotates as we increase θ and D_1 mode splits and converted to D_2 mode.

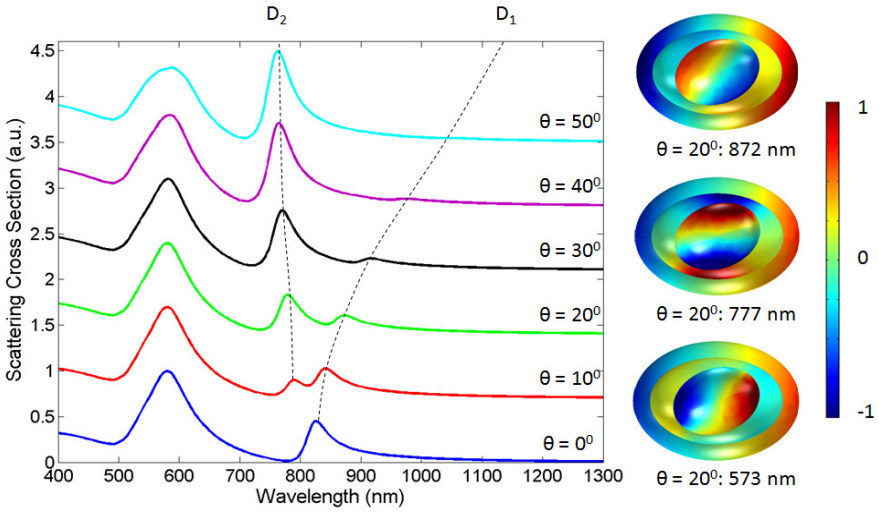

Figure 4. 9. Scattering spectra of MNE with different values of the rotation angle θ. Insets shows surface charge distributions corresponding to superradiant and two subradiant modes for $\theta = 20^{\circ}$.

4.3.1.2. Effect of polarization

Figure 4.10 shows the effect of symmetry breaking by displacing the inner gold core 18 nm from its center in the *x*-direction. We obtained the higher order dark hybridized modes and Fano resonances, which are also confirmed from the surface charge distributions shown in the inset for axial polarization (blue line). By rotating the nanoparticle towards *y*-axis (red line), we observed the similar effect of multipolar modes and Fano resonances but the strength and modulation depth of the Fano resonances are quite weak for this polarization (transversely polarized light) compared to axially polarized light. This shows the effect of polarization on MNE.

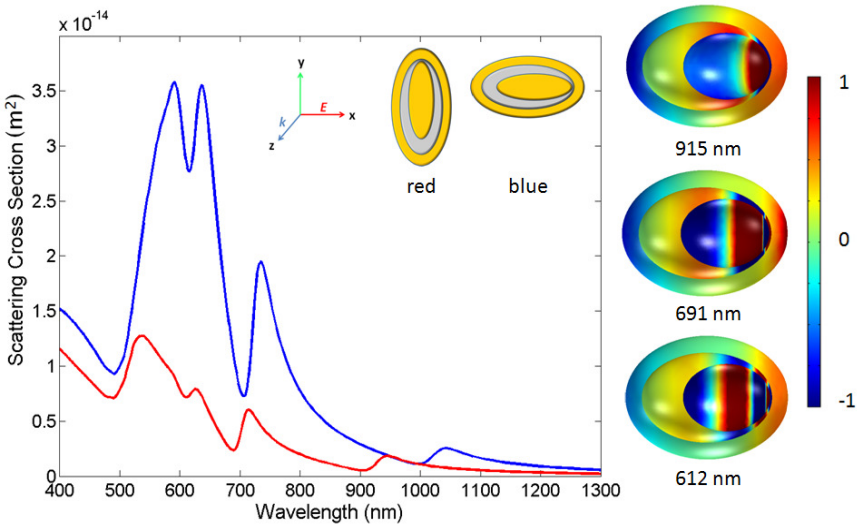

Figure 4. 10. Scattering spectra for non-concentric MNE with different particle orientations. Blue line: incident electric field is polarized parallel to axis of symmetry. Red line: incident electric field is polarized perpendicular to axis of symmetry. Inset shows surface charge distributions corresponding to DDF, DQF and DOF for axially polarized light.

4.4. Multilayered nanocylinder

Next we consider a cylindrical structure with multi-components. The schematic diagram of gold-silica-gold multilayered nanocylinder (MNCD) is shown in figure 4.11. The dimensions of the nanostructure are R_1=45 nm, H_1=95 nm /R_2=30 nm, H_2=75 nm /R_3=20 nm, H_3=60 nm. The electromagnetic field is linearly polarized. The electric field is directed along *x* and the wave propagates in *z*-direction.

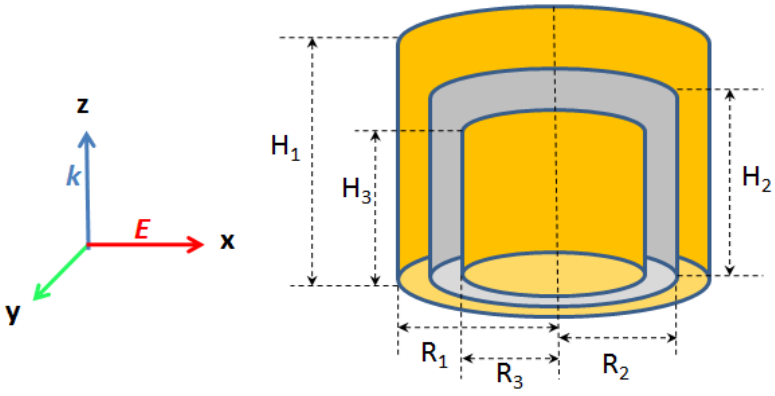

Figure 4. 11. Sketch of gold-silica-gold MNCD (side view).

4.4.1. Far field optical properties of MNCD

Figure 4.12 shows the scattering cross section of a concentric MNCD. We observed the similar two resonant peaks in the spectrum, which are obtained by the interaction of the modes having same angular momenta. The coupling and interference of $\left|\omega_{-}^{+}\right\rangle_{(1)}$ mode near 546 nm and $\left|\omega_{-}^{-}\right\rangle_{(1)}$ mode near 790 nm give rise DDF near 735 nm. This presents the likeness

of MNCD with the MNS nanostructure. The surface charge distributions (top view) corresponding to $\left|\omega_{-}^{+}\right\rangle_{(1)}$, $\left|\omega_{-}^{-}\right\rangle_{(1)}$ and Fano dip are revealed in the inset.

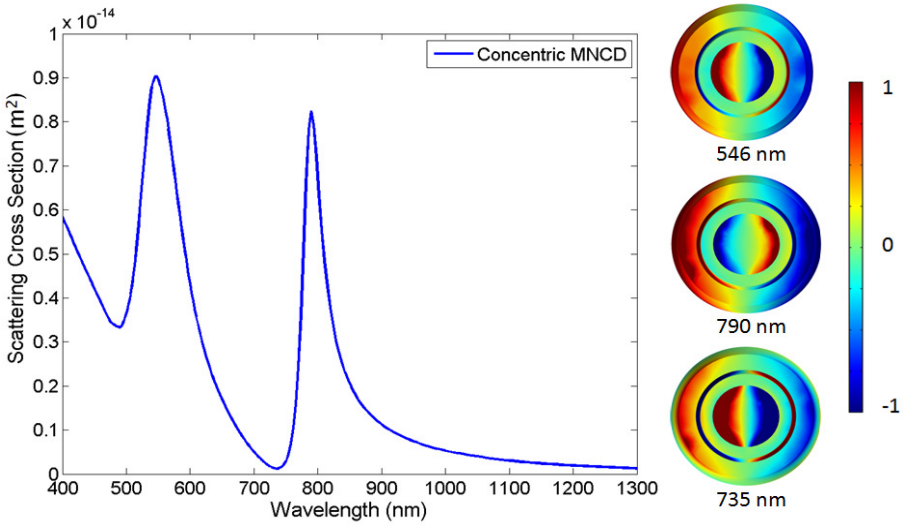

Figure 4. 12. Scattering cross section of concentric MNCD. Inset shows surface charge distributions (top view) corresponding to superradiant mode, subradiant mode and Fano minimum.

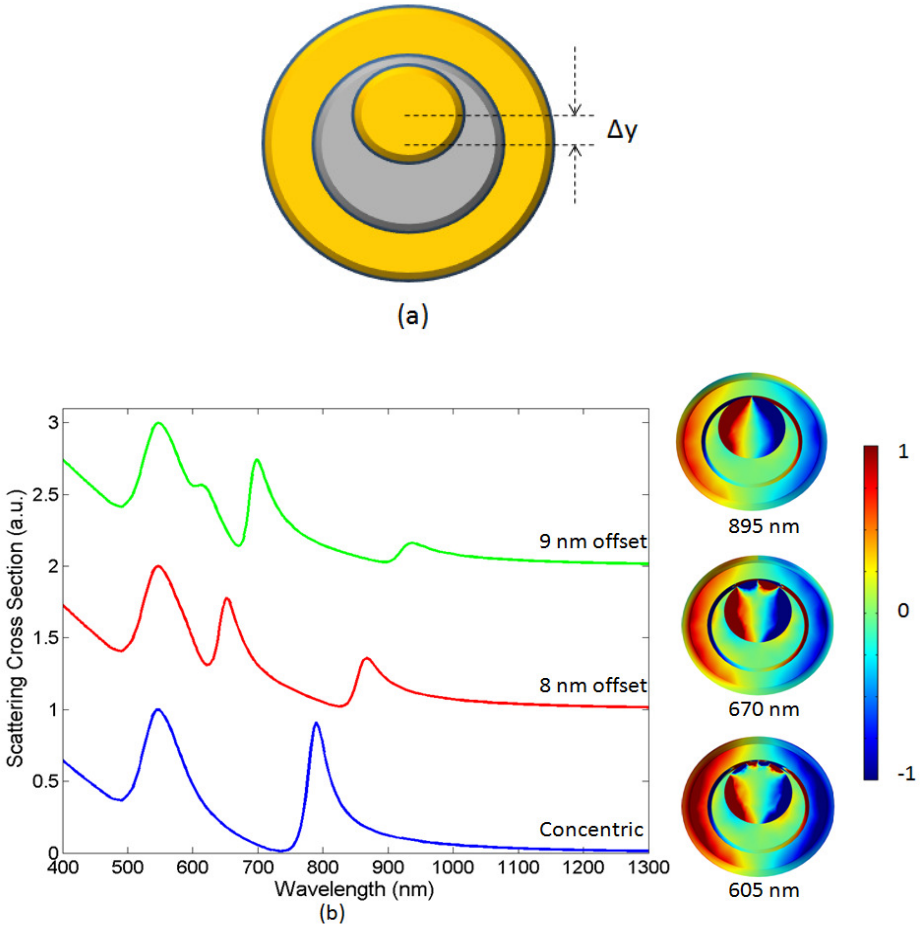

Figure 4. 13. (a) Top view of non-concentric MNCD nanostructure with core offset in *y*-direction. (b) Δy = 0 (blue line), Δy = 8 (red line) and Δy = 9 (green line). Insets show surface charge distributions corresponding to DDF, DQF and DOF for 9 nm offset.

4.4.1.1. Symmetry breaking in MNCD

We break the symmetry of the nanostructure in a similar manner like before (figure 4.13(a)), due to which the interactions between the modes enhances and results in the emergence of the higher order dark hybridized modes in the spectrum, Figure 4.13(b). The coupling and interference of these modes give rise additional Fano resonances in the spectrum, which are confirm from the surface charge distributions shown in the inset of figure 4.13(b). The DDF, DQF and DOF explain similarity with NC-MNS nanostructure.

We next rotate the concentric MNCD along *y*-axis for different values of the rotation angle θ and calculate the scattering cross section, Figure 4.14. For θ = 90°, the polarization of the incident light is directed along the axis of MNCD, so in this case, the peak amplitude of $\left|\omega_{-}^{+}\right\rangle_{(1)}$ mode is highly intensified but $\left|\omega_{-}^{-}\right\rangle_{(1)}$ mode peak's amplitude reduces and the corresponding DDF suffers from weak modulation depth.

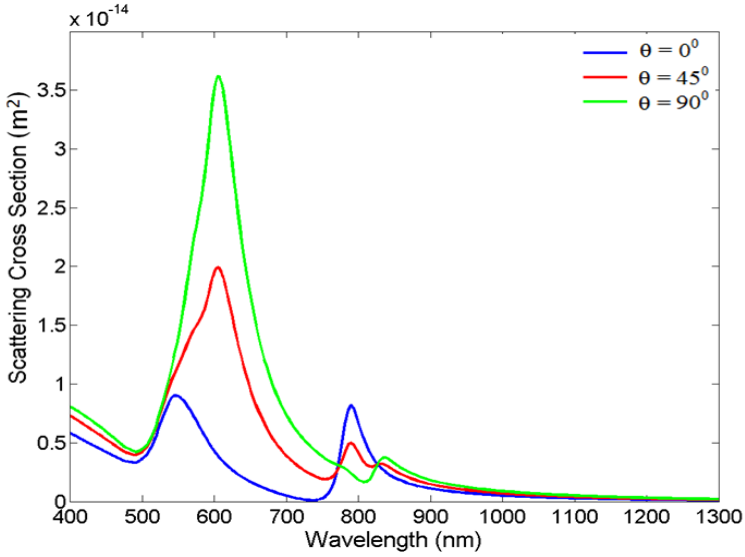

Figure 4. 14. Scattering spectra of concentric MNCD for different values of the rotation angle θ along *y*-axis.

Figure 4.15 shows the scattering spectra of MNCD with 9 nm core offset for different values of θ. For θ = 45°, we obtained five peaks in the spectrum due to the splitting of $\left|\omega_{-}^{-}\right\rangle_{(1)}$ mode i.e., the weak peak near 955 nm and the peak near 746 nm represent $\left|\omega_{-}^{-}\right\rangle_{(1)}$ modes, while the other two peaks represent $\left|\omega_{-}^{-}\right\rangle_{(2)}$ and $\left|\omega_{-}^{-}\right\rangle_{(3)}$ modes. For θ = 90°, the $\left|\omega_{-}^{-}\right\rangle_{(3)}$ mode disappeared leaving only $\left|\omega_{-}^{-}\right\rangle_{(1)}$ and $\left|\omega_{-}^{-}\right\rangle_{(2)}$ modes, respectively. This shows that the MNCD is highly sensitive to the polarization of the incident light i.e., for transversely polarized incident light, we obtained four peaks in the spectrum but for the axially polarized incident light, only three peaks are observed in the scattering spectrum. We also examined the case, where the core is displaced along the *x*-axis for different values of θ. The scattering spectra obtained in this case demonstrate a close resemblance to that of the offset along *y*-axis (result not shown here).

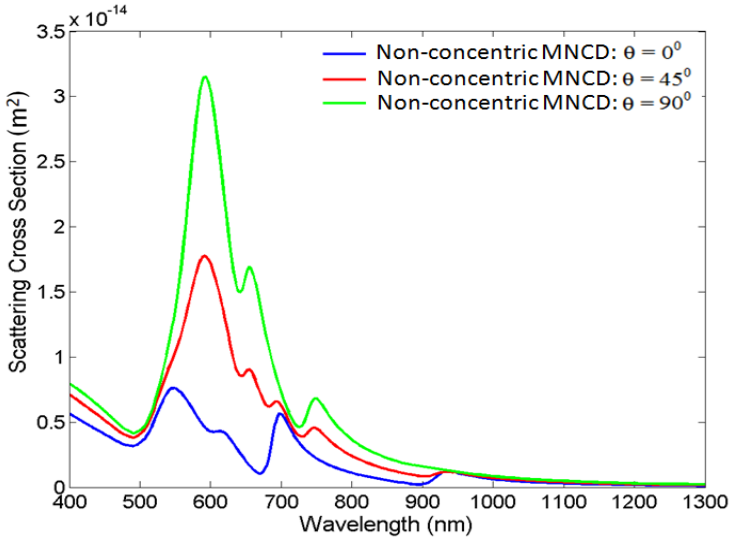

Figure 4. 15. Scattering spectra of non-concentric MNCD for different values of the rotation angle θ along *y*-axis.

4.4.1.2. Geometrical tunability of concentric MNCD

We modified the parameters of MNCD and analyzed its plasmon resonances. Figure 4.16(a) shows the scattering cross section of MNCD for different values of H_1, H_2 and H_3 at fixed R_1=45 nm, R_2=30 nm, R_3=20 nm and θ = 90°. It appears that decreasing the values of H_1, H_2 and H_3, both $\left|\omega_{-}^{+}\right\rangle_{(1)}$ and $\left|\omega_{-}^{-}\right\rangle_{(1)}$ modes are strongly blue-shifted and a new mode emerges at the lower energy side near 760 nm (red line). By further decreasing the values of H_1, H_2 and H_3, all the peaks are slightly blue-shifted. The surface charge distributions for the case of H_1=95 nm, H_2=75 nm and H_3=60 nm (blue line) are calculated, which are displayed in the inset (lower panel). The broad peak near 605 nm shows an axial $\left|\omega_{-}^{+}\right\rangle_{(1)}$ mode and the narrow peak near 838 nm shows an axial $\left|\omega_{-}^{-}\right\rangle_{(1)}$ mode. The surface charges for the case of H_1=45 nm, H_2=30 nm and H_3=20 nm (green line) are shown in the top panel. The peak near 534 nm shows a ring shaped dipolar pattern on both the outer and inner metals and the charges oscillate in phase, so this shows an axial $\left|\omega_{-}^{+}\right\rangle_{(1)}$ mode. The peak near 605 nm shows a ring shaped dipolar mode on both the outer and inner metals and the charges oscillate out of phase, so this shows an axial $\left|\omega_{-}^{-}\right\rangle_{(1)}$ mode, while the peak near 750 nm shows a half ring shaped dipolar pattern on the inner and somewhat on the outer metal and the charges oscillate out of phase, which shows a transverse $\left|\omega_{-}^{-}\right\rangle_{(1)}$ mode. Thus, by varying the heights of MNCD, we can have twin dipole-dipole Fano resonances in the concentric case for θ = 90°. Figure 4.16(b) shows the scattering cross section of MNCD for θ = 0°. For all the values of H_1, H_2 and H_3, we obtained only two peaks i.e., the $\left|\omega_{-}^{+}\right\rangle_{(1)}$ and $\left|\omega_{-}^{-}\right\rangle_{(1)}$ modes. The $\left|\omega_{-}^{+}\right\rangle_{(1)}$ mode maintains its spectral position, while $\left|\omega_{-}^{-}\right\rangle_{(1)}$ mode is slightly blue-shifted as we decrease the values of the heights. Therefore, when the incident light is axially polarized with respect to the MNCD axis, we can have dual dipole Fano resonances when the heights of MNCD are reduced and fall into a certain range. The new Fano resonance can be switched on and off by

changing the polarization of incident light due to which it may be used as switching and PIT applications [44, 56].

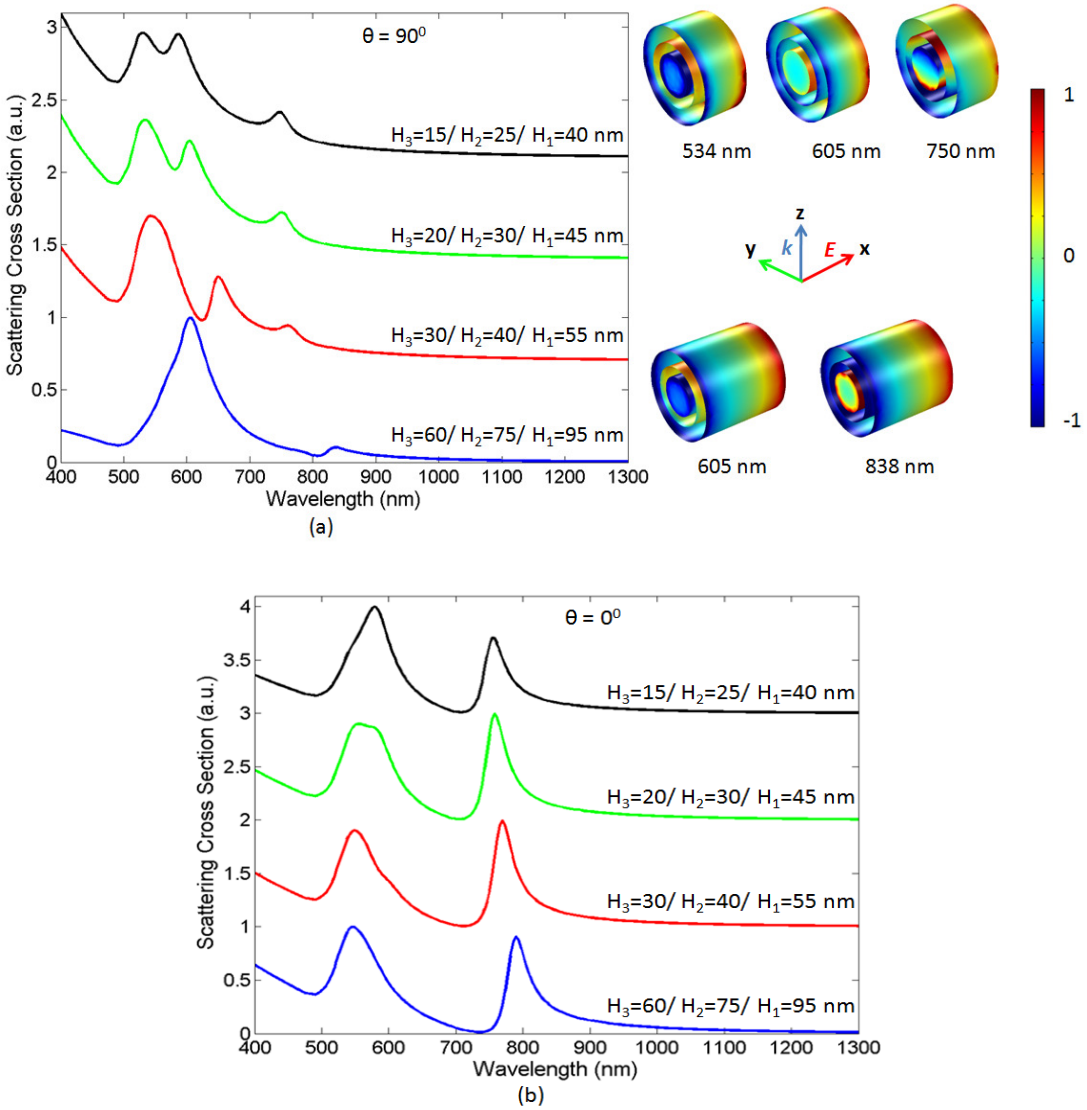

Figure 4. 16. (a) Scattering cross section of a concentric MNCD for different values of H_1, H_2 and H_3 at fixed R_1=45 nm, R_2=30 nm, R_3=20 nm and θ = 90°. Insets shows surface charge distributions for the case of H_1=95 nm, H_2=75 nm and H_3=60 nm (bottom panel) and the case H_1=45 nm, H_2=30 nm and H_3=20 nm (top panel). (b) Scattering cross section of a concentric MNCD for different values of H_1, H_2 and H_3 at fixed R_1=45 nm, R_2=30 nm, R_3=20 nm and θ = 0°.

Figure 4.17(a) shows the scattering cross section of MNCD for different values of R_1, R_2 and R_3 at fixed H_1=45 nm, H_2=30 nm, H_3=20 nm and θ = 90°. For all the values of R_1, R_2 and R_3, we observed three resonant peaks in the spectrum. When the values of the radii of MNCD are large enough then we have a single dipole Fano resonance near 637 nm (blue line). The second subradiant transverse dipole peak is far enough from $\left|\omega_{-}^{+}\right\rangle_{(1)}$ mode due to which the near field coupling between the two modes do not occur and the Fano resonance is absent in the scattering spectrum. By decreasing the values of the radii, the two $\left|\omega_{-}^{-}\right\rangle_{(1)}$ modes blue-shifted, while the $\left|\omega_{-}^{+}\right\rangle_{(1)}$ mode sustains its spectral position. At certain range (green line), the

second $\left|\omega_{-}^{-}\right\rangle_{(1)}$ mode is close enough to $\left|\omega_{-}^{+}\right\rangle_{(1)}$ mode due which the near field coupling between the two modes results in an additional dipole Fano resonance. By further decreasing the radii of MNCD, the peaks amplitude of the two $\left|\omega_{-}^{-}\right\rangle_{(1)}$ modes decreases and we obtained Fano resonances with weak modulation depths. Figure 4.17(b) shows the scattering spectra of MNCD for $\theta = 0^{\circ}$. For all values of the radii, we obtained two peaks in the spectrum i.e., $\left|\omega_{-}^{+}\right\rangle_{(1)}$ and $\left|\omega_{-}^{-}\right\rangle_{(1)}$ modes. By decreasing the values of the radii, both the modes are blue-shifted and the peak amplitude of the $\left|\omega_{-}^{+}\right\rangle_{(1)}$ mode decreases while that of the $\left|\omega_{-}^{-}\right\rangle_{(1)}$ mode increases and become close enough to induce a Fano resonance.

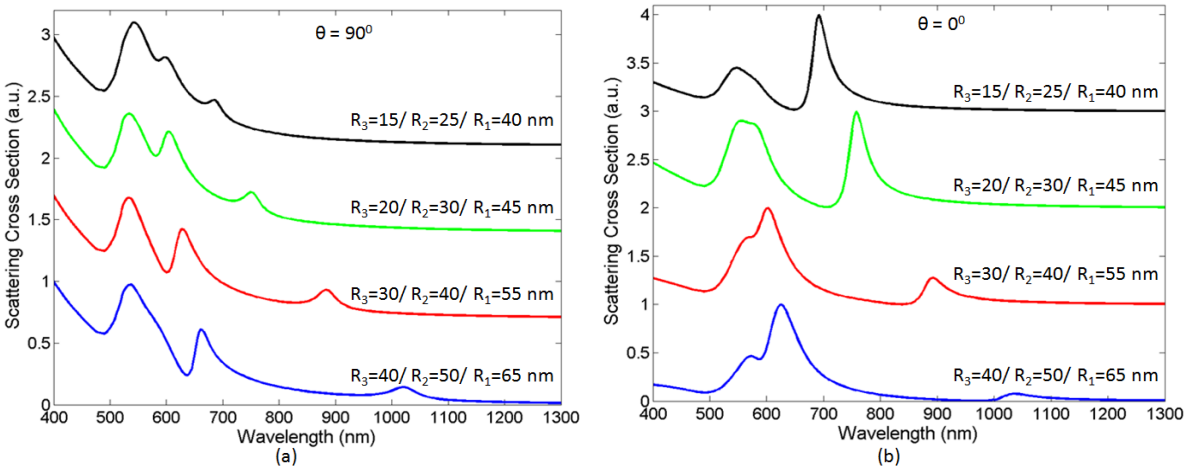

Figure 4. 17. Scattering cross section of MNCD for different values of R_1, R_2 and R_3 at fixed H_1=45 nm, H_2=30 nm, H_3=20 nm (a) $\theta = 90^{\circ}$ (b) $\theta = 0^{\circ}$.

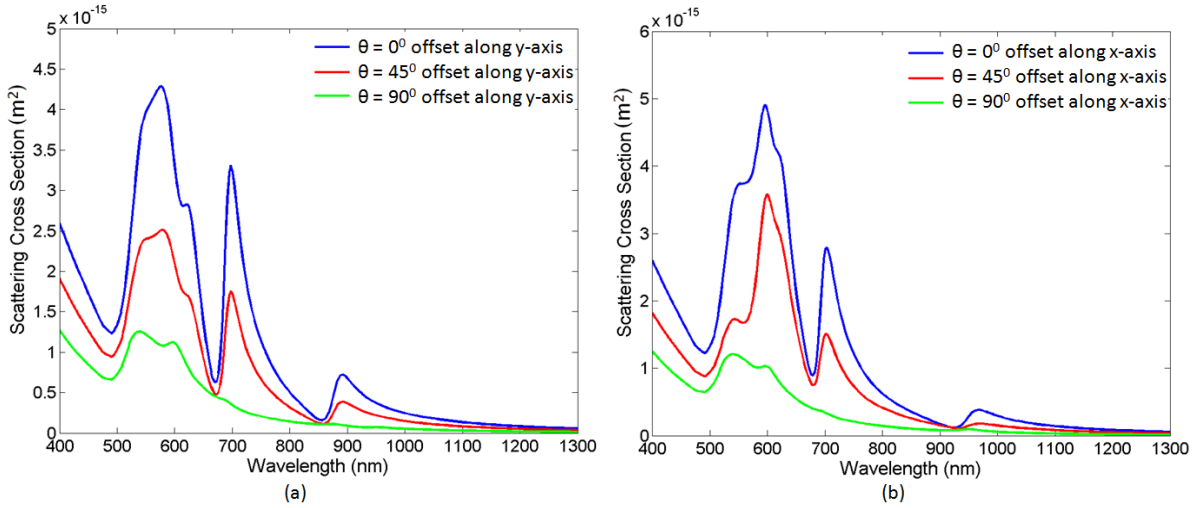

Figure 4. 18. Scattering spectra of a non-concentric MNDK for different values of θ with 9 nm core offset along (a) *y*-axis (b) *x*-axis.

In figure 4.18, we chose MNCD with dimensions R_1=45 nm, H_1=45 nm /R_2=30 nm, H_2=30 nm /R_3=20 nm, H_3=20 nm and calculate its scattering spectra for a 9 nm core offset at different values of θ. The MNCD with such dimensions looks like a disk, therefore, we named this nanostructure a *multilayered nanodisk* (MNDK). The scattering spectra of a concentric MNDK for $\theta = 0^{\circ}$ and 90° are calculated in figure 4.17(a) and (b) (green line).

Figure 4.18(a) shows scattering spectra of non-concentric MNDK with 9 nm core offset along *y*-axis at different values of θ. For θ = 0°, we obtained dipole, quadrupole and a weak octupole Fano resonances in the spectrum. By increasing the value of θ, it appears that the peak amplitudes of all the modes reduces and almost disappeared at θ = 90° except a weak $\left|\omega_{-}^{+}\right\rangle_{(1)}$ and $\left|\omega_{-}^{-}\right\rangle_{(2)}$ modes. Figure 4.18(b) shows the scattering spectra of non-concentric MNDK with 9 nm core offset along *x*-axis at different values of θ. For θ = 0°, we obtained dipole and quadrupole Fano resonances but again the peak amplitudes of all the modes decreases by increasing the value of θ. Thus, the MNDK scattering spectra strongly depends on the incident field polarization like the MNCD nanostructure. Form all the above findings, we obtained distinct Fano resonances in a cylindrical structure with multi-components, which may be useful for plasmon line shaping and multi-wavelength SERS [54, 119, 121].

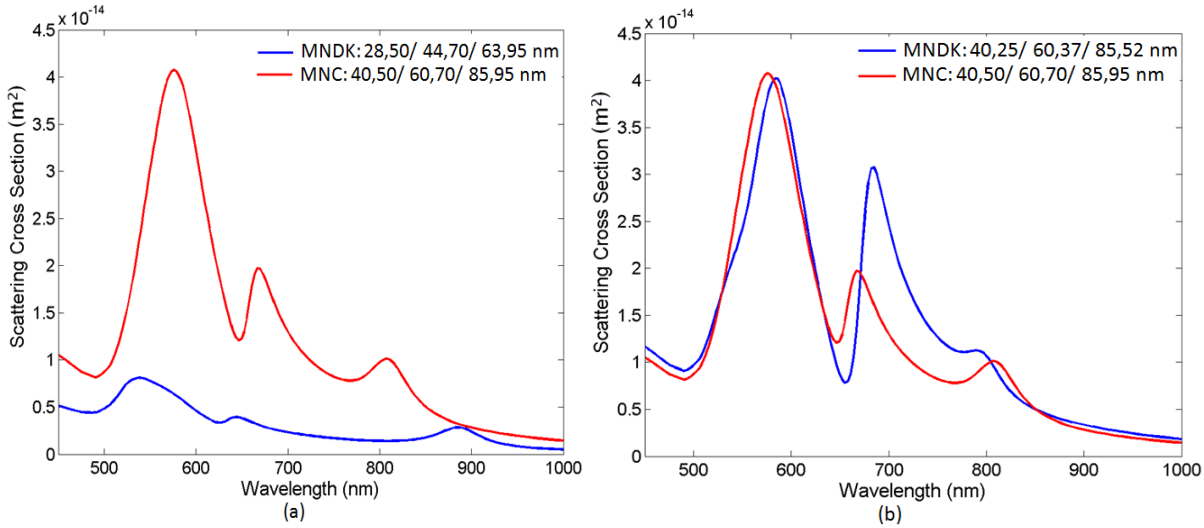

Figure 4. 19. Scattering spectra of (θ = 90°) (a) MNDK: 28,50/ 44,70/ 63,95 nm and MNC: 40,50/ 60,70/ 85,95 nm (b) MNDK: 40,25/ 60,37/ 85,52 and MNC: 40,50/ 60,70/ 85,95 nm.

4.4.2. Comparison with multilayered nanocone

The scattering spectra of concentric MNDK at θ = 90° is very similar to that of multilayered nanocone (MNC) because both the nanostructures exhibit dual dipole Fano resonances in the optical spectra. For this reason, we compared the optical responses of both the nanostructures with equal volumes. At first, we fixed the height of MNC having dimensions 40,50/ 60,70/ 85,95 nm and extract the volume of MNDK with dimensions 28,50/ 44,70/ 63,95 nm and then we fixed the radius of MNC and obtained the volume of MNDK with dimensions 28,50/ 44,70/ 63,95. So in this way, we equate both the nanostructures. The scattering spectra of MNC with dimensions 40,50/ 60,70/ 85,95 nm and MNDK with dimensions 28,50/ 44,70/ 63,95 nm at 90° are demonstrated in figure 4.19(a). The MNDK with such dimensions appeared more like a nanocylinder instead of a nanodisk. From the scattering spectra, we observed that the strength of the resonant peaks and Fano dips in case of MNC are significant compared to MNDK nanostructure. The optical response of MNDK is almost negligible by comparing to MNC nanostructure. Figure 4.19(b) shows the scattering spectra of MNDK with dimensions 40,25/ 60,37/ 85,52 nm and MNC having same dimensions. In this case, the first $\left|\omega_{-}^{-}\right\rangle_{(1)}$ mode and the corresponding Fano dip near 660 nm of MNDK shows a greater strength, while the second $\left|\omega_{-}^{-}\right\rangle_{(1)}$ mode and Fano dip near 780 nm turns out to be very weak compared to MNC nanostructure. Thus monitoring these figures, it

becomes understandable that the twin dipole Fano resonances appeared to be more obvious in case of MNC nanostructure.

4.5. Concluding remarks

By observing the bright and dark modes in the nanostructures with different geometries, we end up with a conclusion that this trend is very general in bimetallic nanostructures. Any type of geometry with multicoated structure like MNS can be designed with its bright and dark modes exhibiting Fano resonances. All the Fano resonators are found to depend upon the polarization of incident light. Particularly, the MNCD and MNDK resonators are discovered to strongly depend upon the polarization of incident light. The twin dipole Fano resonances observed in MNDK nanostructure are compared to MNC nanostructure, which proves that the strength and modulation depth of the dual Fano resonances in MNDK nanostructure are weak compared to MNC nanostructure. Unlike the previously reported Fano resonators, the MNDK and MNC Fano resonators provides dual dipole Fano resonances in the symmetric case, which is particularly significant because as they are easier to fabricate compared to asymmetric nanostructures and can be used in a wider range of technological applications. But the role of higher order multiple Fano resonances in asymmetric plasmonic nanostructures cannot be rebuff as they play an important part in multi-wavelength SERS and plasmon line shaping.

Chapter 5

Plasmonic Fano Like Resonances in Single Metallic Conical Nanoshells

5.1. Introduction

In this chapter, new geometries of gold nanocones with proper perforation in the gold nanocone and inserting a dielectric cone inside a gold nanocone to construct a cone nanoshell are proposed. Plasmonic Fano resonances arise even in a symmetric case, which can be switched on and off by rotating the structure around different symmetrical axis with respect to the incident field polarization. The effect of symmetry breaking has been initiated in conical nanoshell at different values of the rotation angle θ due to which higher order dark hybridized modes emerges in the spectrum, which couple to the superradiant bright mode and induces higher order Fano resonances. From a comparison with spherical nanostructures it comes out that conical nanoshells are found to be highly capable in the generation of higher order Fano resonances with larger modulation depths in the optical spectra. Such nanostructures are also found to offer high values of figure of merit and contrast ratio due to which they are highly suitable for biological sensors.

The plasmonic Fano resonances induced in gold conical nanostructures are not only sensitive to the size and shape but also to the angle and polarization of the incident light. The optical properties of the proposed nanostructures are almost similar to the conventional nanoshells [25], nanoeggs [122], perforated nanoshells [28, 57, 123] and nanocups [124], which can be fabricated by the methods given in [57, 122, 124, 125]. However, we have found that conical nanostructures have the advantage to exhibit more pronounced plasmonic Fano resonances and hence can be useful for EIT and SERS applications. Symmetry breaking induces multiple Fano resonances, which may be very useful for plasmon line shaping.

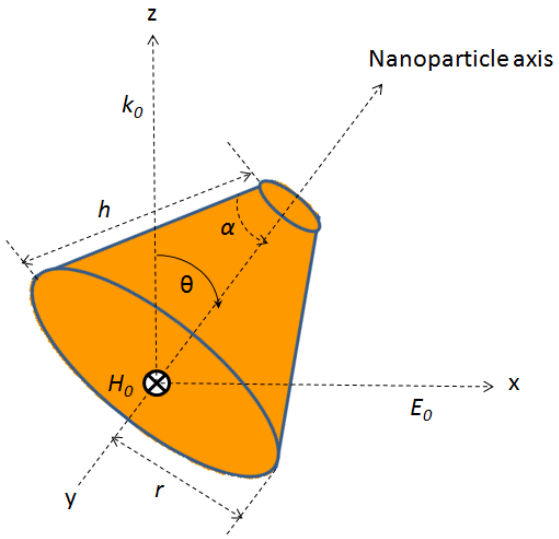

Figure 5. 1. Sketch of the nanoparticle. The incident field is linearly polarized along the *x*-direction and propagates along the *z*-direction. The nanoparticle axis is rotated around the *y*-axis of an angle θ from 0° to 90°.

The illuminating electromagnetic wave is linearly polarized, the electric field is directed along x and the wave propagates in z-direction. The optical properties of the nanoparticles are examined by rotating its axis around y-axis of an angle θ, from θ = 0° to 90° as shown in figure 5.1. This is equivalent to change the polarization direction of the incident light.

5.2. Optical properties of hollow gold nanocones

We start our study from an open structure i.e., hollow gold nanocone (HNC), derived from the gold cone with a proper perforation. The thickness of HNC is t = 13 nm, height h = 95 nm, radius r = 72 nm and semi angle α = 26° as shown in figure 5.2(a). The scattering spectra of HNC strongly depend upon the polarization of the incident light. Figure 5.2(b) shows the scattering cross section of HNC for different values of the rotation angle θ. For θ = 0°, the incident light propagates along the HNC axis and the electric field is directed transversally, so the peak near 1.5 eV is a transverse dipole mode (blue line). A plasmon hybridization occurs between the cavity plasmon mode and the metallic cone plasmon mode as discussed before [25, 61]. The two modes interact and form a lower-energy bonding mode and a higher-energy antibonding mode. The higher-energy antibonding mode does not appear in the spectrum because the cavity and cone plasmons oscillate out of phase, so only the lower-energy transverse bonding mode $|\omega_-\rangle_1^T$ will emerge in the scattering cross section due to its larger dipole moment. By breaking the rotational symmetry other modes appear. At θ = 30°, a new peak appears around 1.94 eV (red line), which represents a subradiant quadrupole mode $|\omega_-\rangle_2$. This mode was almost absent at θ = 0°. The peak amplitude of $|\omega_-\rangle_1^T$ mode decreases by increasing θ but remains at the same spectral position and almost disappears at 90°, where the E-field is aligned with HNC axis (purple line). At 90°, the peak near 1.96 eV is relevant to the high-energy axial dipole bonging mode $|\omega_-\rangle_1^A$. The high-energy $|\omega_-\rangle_2$ mode also turn out to be disappeared at θ = 90°. Thus, the optical properties of HNC are angularly and spectrally selective [123].

The coupling and interference of the two scattering peaks at θ = 45°, results in a dip in the spectrum, which reveals a Fano like resonance. The surface charge distributions corresponding to $|\omega_-\rangle_1^T$, $|\omega_-\rangle_2$ and Fano dip at θ = 45° are shown in the inset of figure 5.2(b). The charge distribution near 1.5 eV represents a half ring shaped dipolar pattern (transverse dipole mode), the charge distribution near 1.96 eV shows a quadrupolar pattern, while the surface charges at the Fano minimum is a mixture of dipole and quadrupole modes.

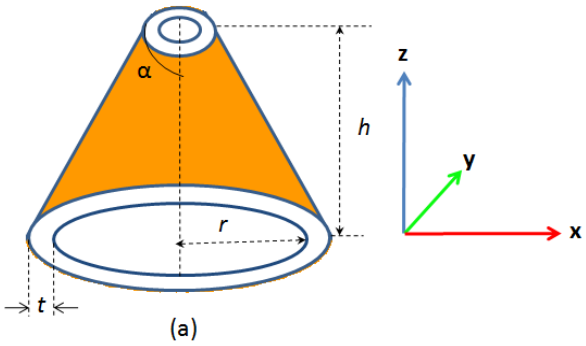

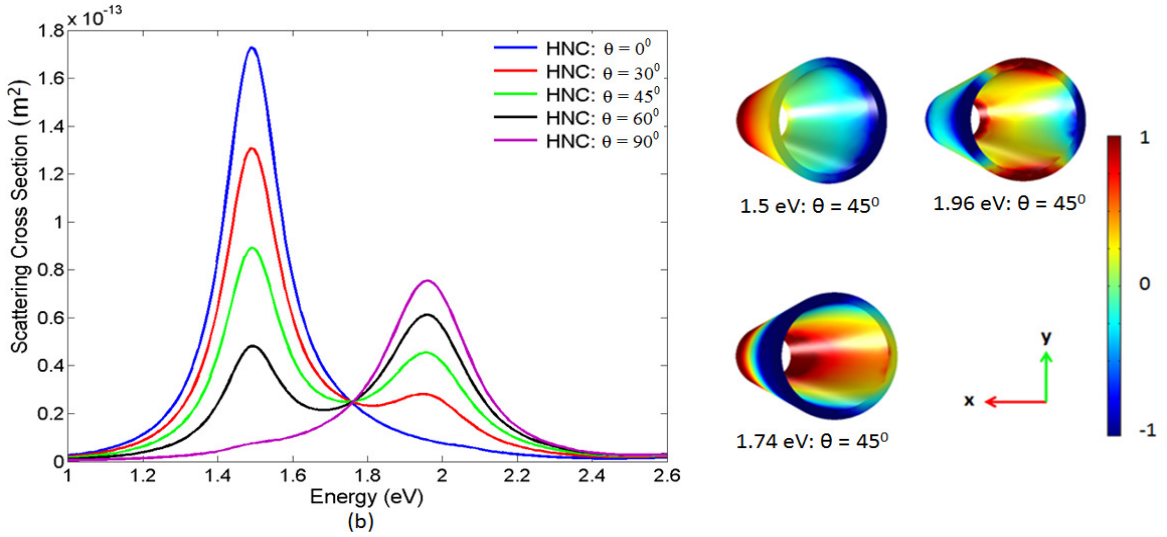

Figure 5. 2. (a) Geometry of HNC having dimensions r = 72 nm, height h = 95 nm, t = 13 nm and semi angle α = 26°. (b) Scattering spectra of HNC at different values of rotation angles θ. Inset shows surface charge distributions calculated using Gauss's law.

5.2.1. Geometrical tunability of HNC

In this section, the geometrical tunability of plasmon resonances of HNC is analyzed. Figure 5.3 demonstrates the scattering spectra of HNC with different values of t at fixed θ = 45°, r = 72 nm and h = 95 nm. It appears that decreasing t, results in a simultaneous red-shift of both the high and low-energy peaks and vice versa. At smaller values of t, the modulation depth of the Fano resonance and the scattering peaks amplitudes are enhanced. By filling the HNC with silica (relative dielectric constant 2.04) also results in a red-shift of both the scattering peaks and Fano dip as shown by the black line. Thus the modulation depth of the Fano resonance can be controlled and enhanced by varying t.

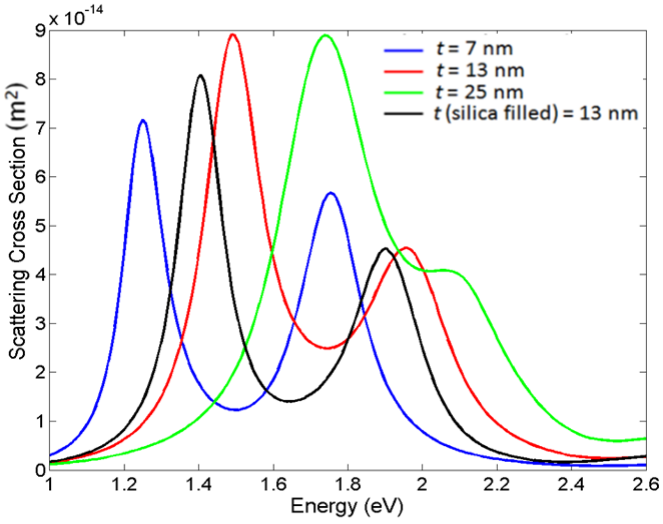

Figure 5. 3. Scattering spectra of HNC for different values of t and fixed r = 72 nm, h = 95 nm, α = 26° and θ = 45°.

Figure 5.4 shows the scattering spectra of HNC for different values of r at fixed h = 95 nm, t = 13 nm and θ = 45°. It has been observed that $|\omega_-\rangle_2$ mode completely vanishes by

reducing r and a single dipole plasmon mode is obtained at the high-energy level (green line). So decreasing r will destroy the Fano resonance in HNC nanostructure.

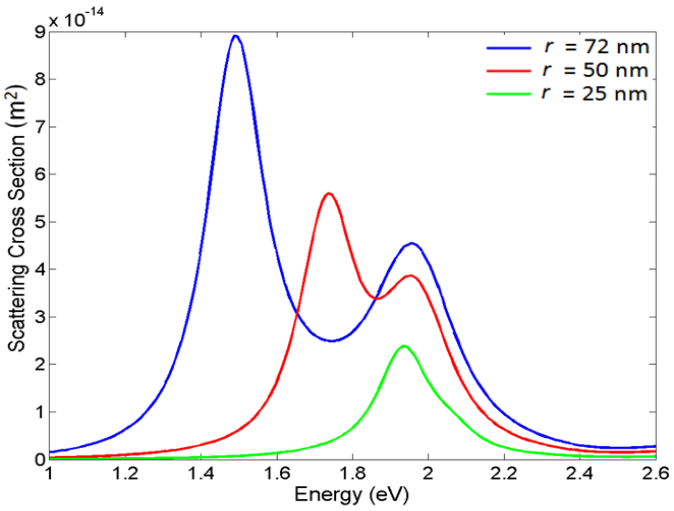

Figure 5. 4. Scattering spectra of HNC for different values of r at fixed h = 95 nm, t = 13 nm, α = 26° and θ = 45°.

Figure 5.5 shows the scattering spectra of HNC for different values of h at fixed θ = 45°, r = 72 nm and t = 13 nm. By decreasing the value of h, the peak amplitudes of $|\omega_-\rangle_1$ and $|\omega_-\rangle_2$ modes decreases and the separation between them increases due to which the coupling between them reduces and we perceived almost no Fano resonance in the spectrum. For instance, at h = 25 nm, the $|\omega_-\rangle_1$ peak does not overlap $|\omega_-\rangle_2$ peak spectrally, due to which no Fano resonance can be established in the spectrum. In this case, both the peaks couple directly to the incident light.

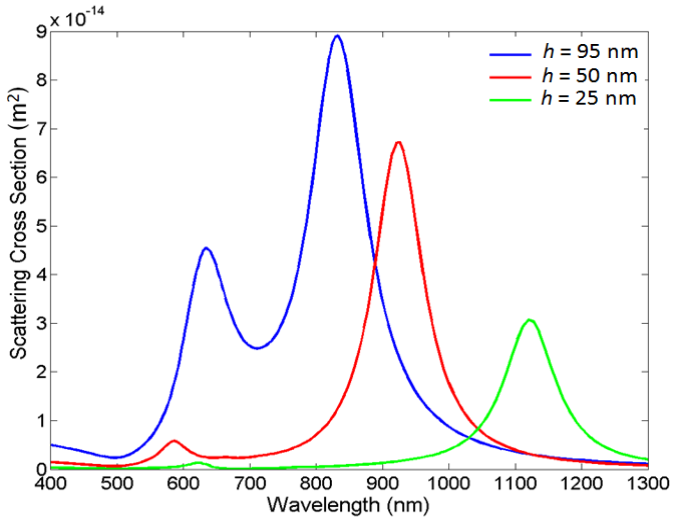

Figure 5. 5. Scattering spectra of HNC for different values of h at fixed r = 72 nm, t = 13 nm, α = 26° and θ = 45°.

Figure 5.6 illustrates the scattering spectra of HNC with different values of α at fixed θ = 45°, t = 13 nm, r = 72 nm and h = 95 nm. At α = 5° (blue line), the HNC adopts the shape of a cylinder as shown in the inset. By increasing the value of α, the low-energy peak blue-shifts

while the high-energy peak red-shifts and their peak amplitudes decreases. The surface charge distributions for α = 5° and 36° are demonstrated in the inset, which clearly shows the dipolar and quadrupolar characters.

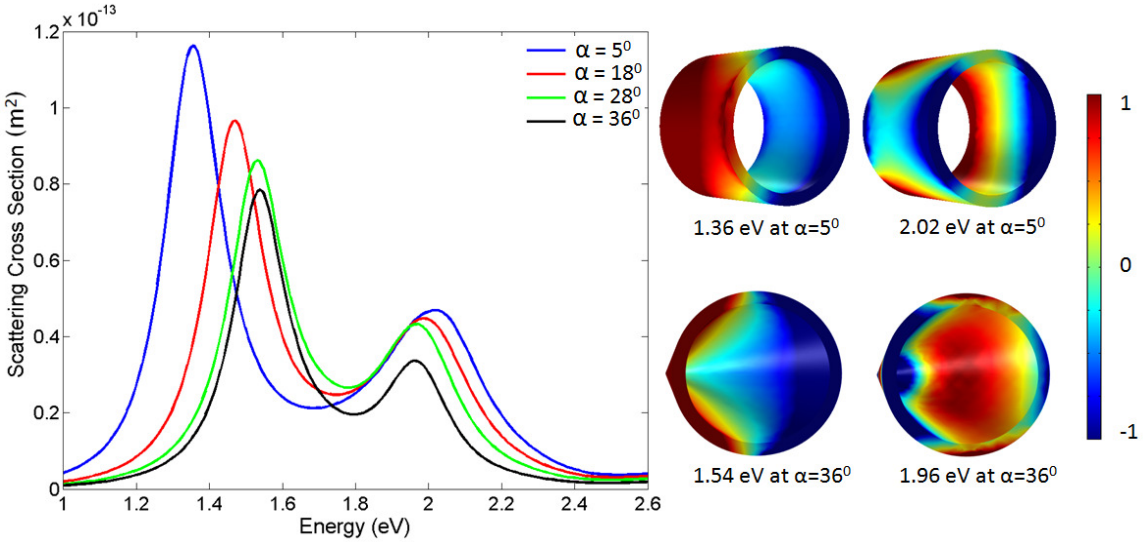

Figure 5. 6. Scattering spectra of HNC for different values of α at fixed r = 72 nm, h = 95 nm, t = 13 nm and θ = 45°. Inset shows surface charge distributions for α = 5° and 36°.

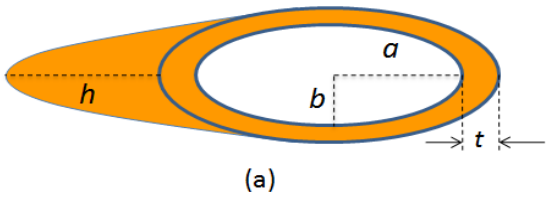

(a)

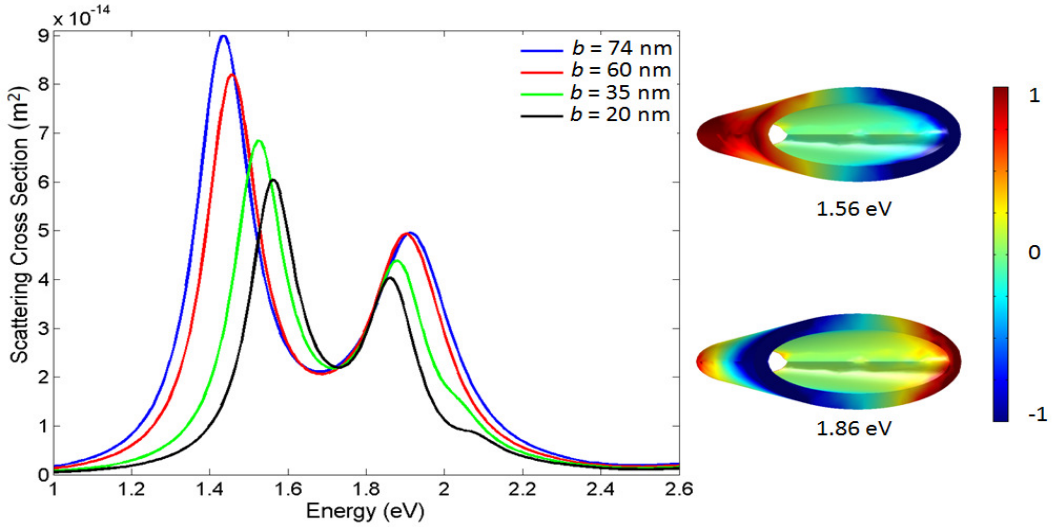

Figure 5. 7. (a) Geometry of ENC having dimensions t = 11 nm, r (a) = 74 nm, height h = 95 nm and semi angle α = 26°. (b) Scattering spectra of ENC for different values of b at fixed a = 74 nm, h = 95 nm and θ = 45°. Inset shows surface charge distributions for b = 20 nm.

We next vary the *b*-semiaxis and take fix the *a*-semiaxis (74 nm) of the HNC due to which its geometrical shape looks like an elliptical nanocone (ENC) as shown in figure 5.7(a). The thickness of the ENC is t = 11 nm, radius r (a) = 74 nm, height h = 95 nm and its semi angle is $\alpha = 26^{\circ}$. Figure 5.7(b) shows the scattering spectra of ENC at different values of *b*-semiaxis, which is rather similar to the scattering spectra of HNC. It has been observed that by decreasing the value of *b* results in a blue-shift of the lower-energy dipole peak and a red-shift of the higher-energy quadrupole peak and their peak amplitudes decreases. The surface charge distribution for b = 20 nm are shown in the inset, which clearly shows dipole and quadrupole modes.

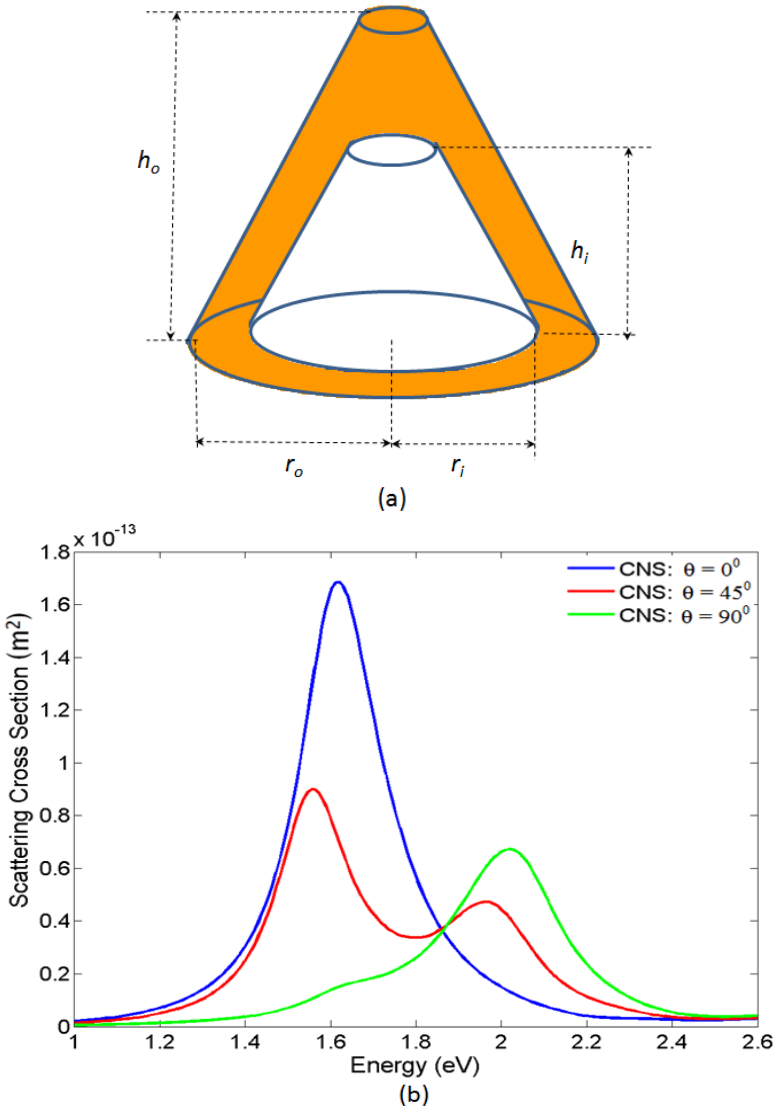

Figure 5. 8. (a) Geometry of CNS having dimensions r_i=72, h_i=82/ r_o=85, h_o=95 nm and semi angle $\alpha = 26^{\circ}$. (b) Scattering spectra of CNS for different values of θ.

5.3. Conical nanoshell (CNS)

In this section, we inserted a cone filled with air inside a metallic gold cone to make a conical nanoshell (CNS) as shown in figure 5.8(a). In this case, the CNS will no more be an open structure like before. The dimensions of CNS are r_i=72, h_i=82/ r_o=85, h_o=95 nm, where r_i, h_i are the radius and height of the inner dielectric cone and r_o, h_o are the radius and height

of the outer gold cone, respectively. The semi angle is fixed at $\alpha = 26^{\circ}$. Figure 5.8(b) shows the calculated scattering spectra of CNS at different values of θ, which is approximately analogous to the scattering spectra of HNC by obtaining the same transverse and axial dipole modes and Fano resonance.

Next we examined the scattering spectra of CNS by changing the height of inner dielectric cone i.e., h_i at fixed h_o = 95 nm, r_i = 72 nm, r_o = 85 nm and $\theta = 45^{\circ}$. It has been observed from the scattering spectra of CNS that decreasing h_i results in a blue-shift of the scattering peaks and decrease in the modulation depth of the Fano resonance as shown in figure 5.9.

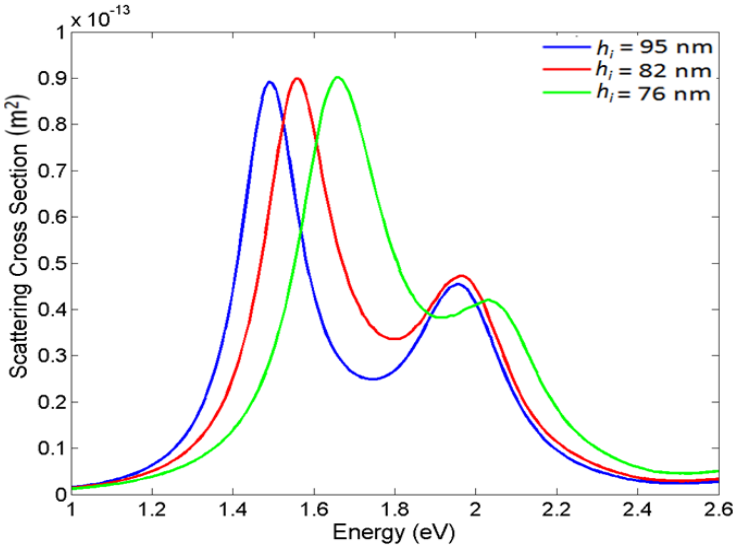

Figure 5. 9. Scattering spectra of CNS for different values of h_i at fixed h_o = 95 nm, r_i=72 nm, r_o=85 nm and $\theta = 45^{\circ}$.

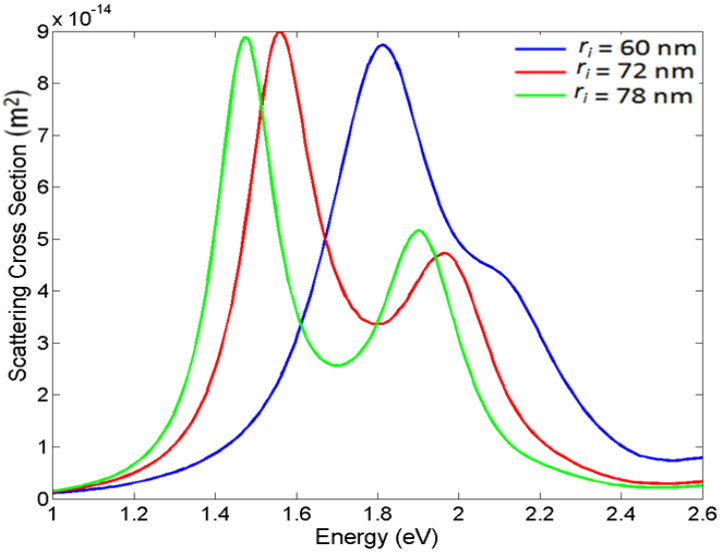

Figure 5. 10. Scattering spectra of CNS for different values of r_i at fixed r_o = 85 nm h_i = 72 nm, h_o = 95 nm, and $\theta = 45^{\circ}$.

Varying the radius of the inner dielectric cone also affect the scattering spectra of CNS as shown in figure 5.10. By increasing the radius of the inner cone, the scattering peaks and Fano dip red-shifts simultaneously as well as the modulation depth of Fano resonance

intensifies. The similar situation was also observed in HNC nanostructure by varying the thickness *t*.

The optical properties of HNC and CNS nanostructures are rather similar to the symmetry reduced perforated gold nanoshells and nanocups because their scattering spectra are also highly sensitive to the geometric asymmetry and the angle between the polarization of incident light and the nanoparticle axis, which may be used for applications like angularly selective filters and biological sensors [28, 123] but the conical nanostructures have the advantage to exhibit a Fano like resonance in the spectrum due to which it can be used for additional applications like EIT and switching [14, 56].

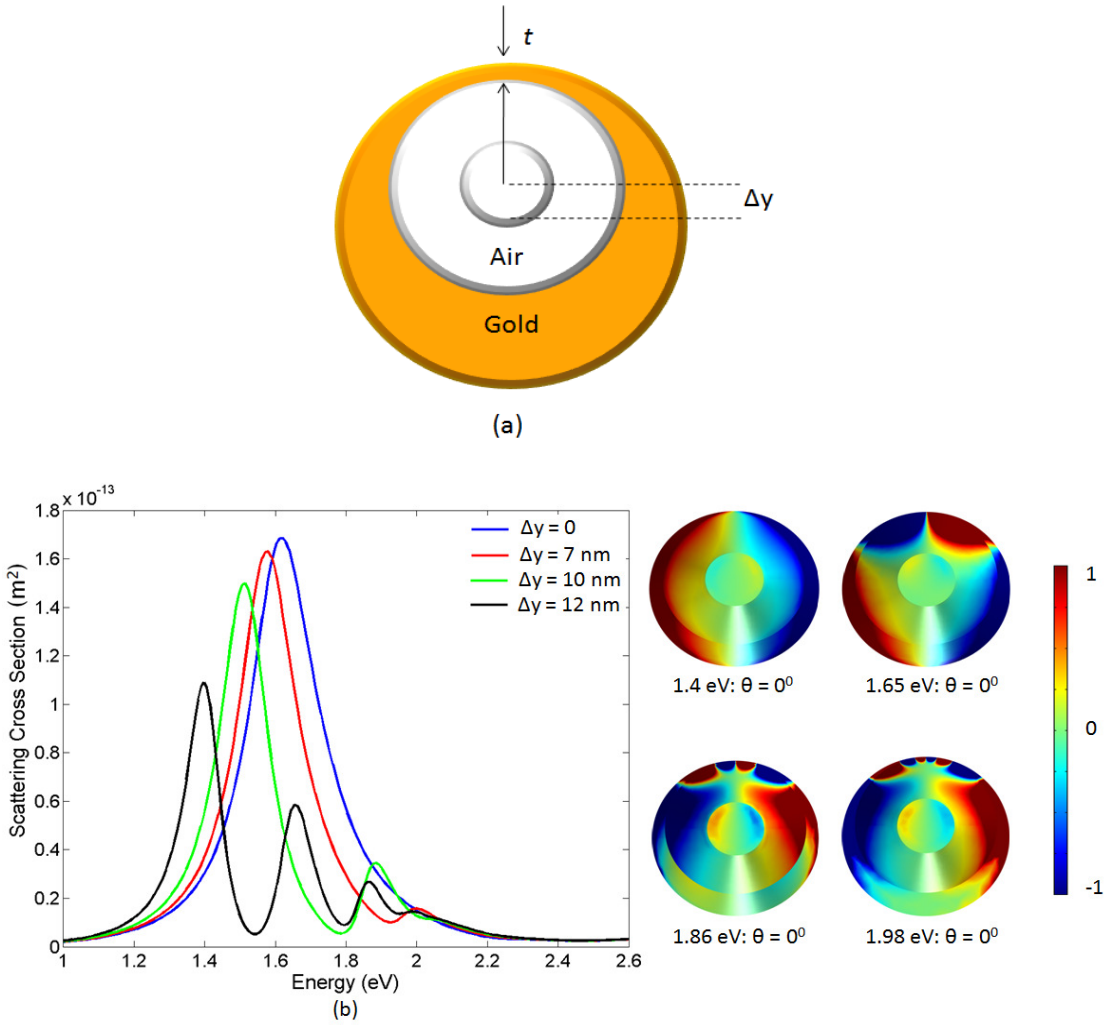

Figure 5. 11. (a) Geometry of NC-CNS with core offset Δy (top view) having dimensions r_i=72, h_i=82/ r_o=85, h_o=95 nm, t = 2 nm and semi-angle α = 26°. (b) Scattering spectra of NC-CNS for different values of Δy. Inset shows surface charge distributions corresponding to $\left|\omega_{-}\right\rangle_1^T$, $\left|\omega_{-}\right\rangle_2$, $\left|\omega_{-}\right\rangle_3$ and $\left|\omega_{-}\right\rangle_4$ modes.

5.3.1. Symmetry breaking in CNS

The effect of symmetry breaking is introduced in CNS by displacing the inner air cone on an otherwise fixed geometry due to which modes of distinctive angular momenta starts to interact [61, 98, 115]. The dimensions of non-concentric conical nanoshell (NC-CNS) with 17% core offset in the *y*-direction (Δy = 12 nm) are r_i=72, h_i=82/ r_o=85, h_o=95 nm with the same semi-angle α = 26^0 as shown in figure 5.11(a) (top view). The thickness of the thin layer

is '*t*', which is fixed at 1 nm. In this layer, the resonant modes amplitude will be greater because the plasmon interactions between the air cone and gold shell is robust in this locality. Figure 5.11(b) shows the scattering spectra of NC-CNS for different values of Δy at θ = 0°. By increasing the value of Δy, the peak amplitude of the fundamental mode $|\omega_-\rangle_1^T$ decreases and higher order dark modes emerges in the spectrum. The higher order hybridized modes interact with the mode $|\omega_-\rangle_1^T$ and induce Fano-like resonances. For instance, at Δy = 12 nm, the bonding quadrupole $|\omega_-\rangle_2$, the octupole mode $|\omega_-\rangle_3$ and the hexadecapolar mode $|\omega_-\rangle_4$ appears in the spectrum at high-energy levels, couple to the mode $|\omega_-\rangle_1^T$ and engenders Fano like resonances. The first Fano dip near 1.54 eV is formed by the interaction of the mode $|\omega_-\rangle_1^T$ with the mode $|\omega_-\rangle_2$, the second Fano dip near 1.8 eV arises from the interaction of the mode $|\omega_-\rangle_1^T$ with the mode $|\omega_-\rangle_3$, while the third Fano dip near 1.95 eV arises from the interaction of the mode $|\omega_-\rangle_1^T$ with the mode $|\omega_-\rangle_4$. The surface charge distributions corresponding to each peak are shown in the inset of figure 5.11(b), which clearly reveal the nature of the modes $|\omega_-\rangle_1^T$, $|\omega_-\rangle_2$, $|\omega_-\rangle_3$ and $|\omega_-\rangle_4$.

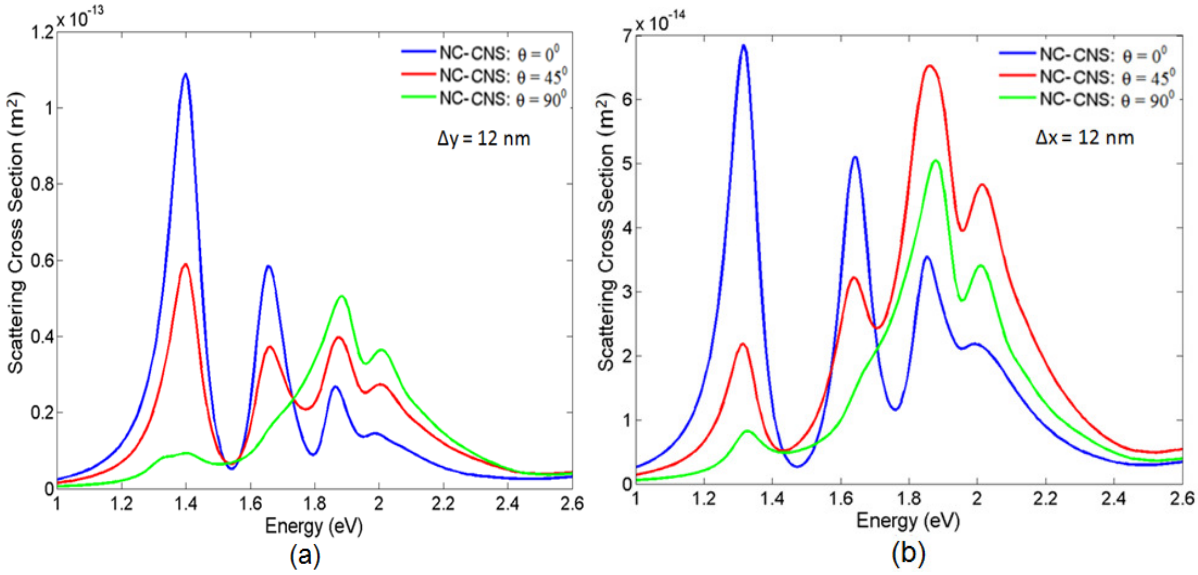

Figure 5. 12. Scattering spectra of NC-CNS for different values of θ at fixed (a) Δy = 12 nm and (b) Δx = 12 nm.

Figure 5.12(a) shows the scattering spectra of NC-CNS nanostructure for Δy = 12 nm and different values of θ. By increasing the value of θ, the peak amplitude of all the hybridized modes starts to decrease. At θ = 90°, the mode $|\omega_-\rangle_1^T$ weakens significantly and the mode $|\omega_-\rangle_2$ entirely vanishes. Figure 5.12(b) shows the scattering spectra of the NC-CNS by offsetting the core in the *x*-direction (Δx = 12 nm) for different values of θ. For θ = 0°, we obtain higher order hybridized modes and Fano-like resonances that are similar to those obtained by offsetting the core along the *y*-direction. Since the core offset is along the polarization direction, the coupling between the modes is stronger compared to the previous case and this gives arise to broad peaks in the spectrum. The first Fano resonance near 1.47

eV appears to be broader compared to the previous sharp Fano dip, the second Fano resonance near 1.76 eV is sharper due to its large modulation depth, while the third Fano resonance near 1.95 eV is also relatively strong. The scattering spectrum for the axially polarized light shows a red-shift of a few electron volts and a stronger interaction between modes of different order. By increasing the value of θ, the peak amplitude of the mode $|\omega_-\rangle_1^T$ declines, while the mode $|\omega_-\rangle_2$ disappeared completely at θ = 90°, like in the previous case. Also in this case, the modes $|\omega_-\rangle_3$ and $|\omega_-\rangle_4$ slightly amplify and a weak Fano resonance is observed near 1.95 eV, which emerges from the coupling of the mode $|\omega_-\rangle_1^T$ with the mode $|\omega_-\rangle_4$. However, this Fano resonance is suffered from weak modulation depth. Thus by offsetting the inner shell in different directions with respect to the incident field polarization, we obtained distinct Fano resonances, which can be used for plasmon line shaping and SERS [54].

Figure 5.13(a) shows the near field enhancement spectra of NC-CNS with different values of Δy. The maximum value of the field enhancement was found for the $|\omega_-\rangle_3$ mode, which is equal to roughly 130. Figure 5.13(b) shows the near field enhancement spectra of the NC-CNS with the core offset along the *x* direction (blue line) and the *y*-direction (red line) with *t* = 1 nm. Both the configurations provide maximum field enhancement at various regions in the spectrum, which was observed at the thinner side of the nanostructure. For the core offset in *x*-direction, we examined a slight red-shift of the resonant peaks and large field enhancement.

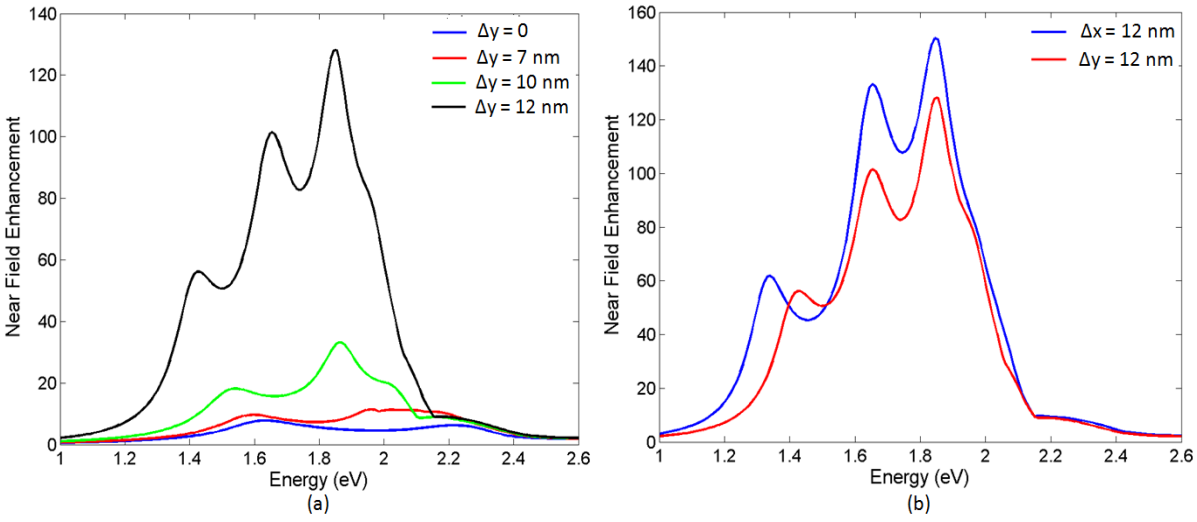

Figure 5. 13. Near field enhancement spectra for: (a) different values of Δy. (b) Δ*x* and Δ*y* at fixed *t* = 1 nm.

We next fixed the value of *t* = 1 nm (core offset along *y*-axis) and vary the dimensions of the inner shell on an otherwise fixed geometry and studied the scattering cross section for different cases. Figure 5.14(a) shows the scattering spectra of NC-CNS by modifying r_i and h_i. For all the cases, we obtained higher order hybridized modes in the spectrum. It has been observed that by increasing the value of r_i, a simultaneous red-shift of the resonant modes occur because of the stronger interaction between the inner and outer cone modes. Also the peak amplitudes of $|\omega_-\rangle_2$ and $|\omega_-\rangle_3$ modes reduces by increasing the value of r_i. Figure

5.14(b) shows the spectral shift of the hybridized modes as a function of r_i, which clearly demonstrates the red-shifting of the modes.

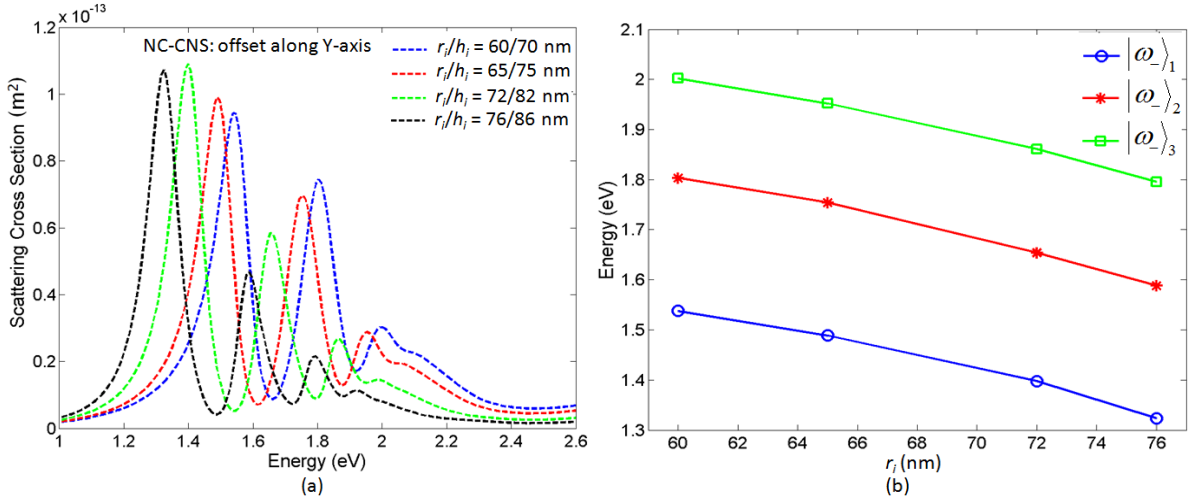

Figure 5. 14. (a) Scattering spectra of NC-CNS with different values of r_i and h_i at fixed t = 1 nm (core offset along y-axis). (b) Energy shifts as a function of r_i.

5.3.2. Comparison with spherical nanostructures

The NC-CNS nanostructure is analogous to conventional nanoegg (CNG), which contains a spherical offset dielectric core, embedded in a thin metallic shell [25, 57]. For this reason, we equate the volumes of both the nanostructures and examined their optical spectra. The dimensions of NC-CNS are chosen to be r_i=72, h_i=82/ r_o=85, h_o=95 nm and the equivalent CNG are r_i=55/ r_o=67 nm. Figure 5.15(a) shows the scattering spectra of both the nanostructures with 17% core offset along y-axis at $\theta = 0^\circ$ and figure 5.15(b) shows the near field enhancement spectra. The CNG spectrum (red line) contains a weak mode $|\omega_-\rangle_2$ and a Fano like resonance. It is clear that the NC-CNS nanostructures exhibit large field enhancement and sharp tunable Fano resonances with large modulation depths in the optical spectra compared to the CNG nanostructures. This would be useful for plasmon line shaping, EIT and SERS applications.

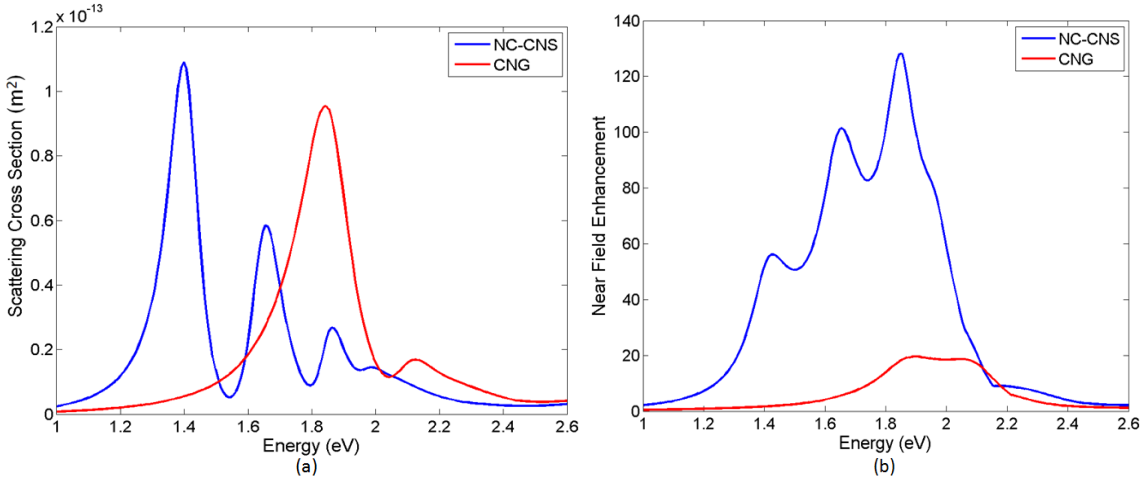

Figure 5. 15. (a) Scattering spectra of NC-CNS and CNG nanostructures at $\theta = 0^\circ$. (b) Near field enhancement spectra of NC-CNS and CNG nanostructures at $\theta = 0^\circ$.

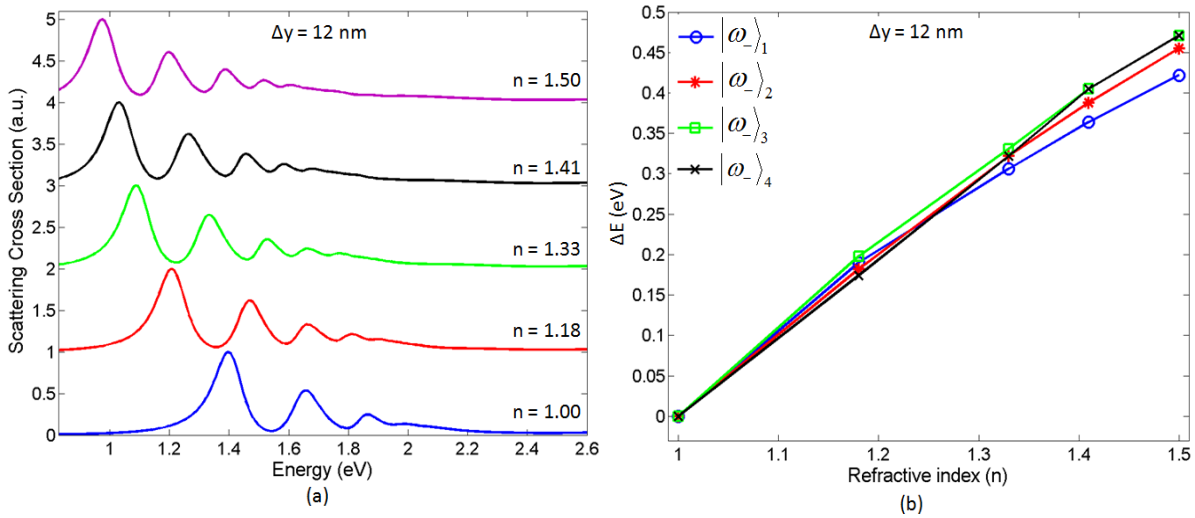

Figure 5. 16. (a) Local refractive index sensitivity of NC-CNS at θ = 0°. The refractive index of the surrounding media is n = 1.00, 1.18, 1.33, 1.41 and 1.50. (b) Energy shifts of $|\omega_-\rangle_1$, $|\omega_-\rangle_2$, $|\omega_-\rangle_3$ and $|\omega_-\rangle_4$ modes as a function of the refractive index.

5.3.3. Spectral sensitivity of NC-CNS to the surrounding medium

To analyse the performance of the nanoparticle (NC-CNS) as chemical or biological sensors, we use figure of merit (FoM) and contrast ratio (CR) by changing the refractive index (n) of the local environment [31, 63, 126]. The FoM is given by equation (5.2), which is the ratio of the sensitivity to the bandwidth (BW) of the resonance. For a symmetric resonance, the bandwidth is the full width at half maximum (FWHM) of the resonance but for the asymmetric resonance, the bandwidth is the line width from the peak to the dip of the resonance as proposed by Hao *et al*., [91]. The contrast ratio is given by equation (5.3), which is the ratio of the difference between the peak value and the dip value to the sum of these two values [31]. Figure 5.16(a) shows the scattering spectra of NC-CNS for different values of the refractive index of the embedding medium. It has been observed that, increasing the refractive index of the medium results in a red-shift of the plasmonic peaks. Figure 5.16(b) shows the energy shifts of the resonant peaks as a function of the refractive index. The sensitivity of the mode $|\omega_-\rangle_1^T$ is 0.844 eV RIU^{-1}, FoM and CR are 7.3 and 91%, respectively. The sensitivity of the mode $|\omega_-\rangle_2$ is 0.910 eV RIU^{-1}, FoM and CR are 7.9 and 83%, respectively. The sensitivity of the mode $|\omega_-\rangle_3$ is 0.942 eV RIU^{-1}, the FoM and CR values are 14.3 and 50% respectively. The sensitivity of the mode $|\omega_-\rangle_4$ is 0.942 eV RIU^{-1}, the FoM and CR values are 28.5 and 3%, respectively. Thus the NC-CNS nanostructure presents both the high CR and FoM values, so it shows good performances as a biological sensor.

$$Sensitivity = \frac{E_{\max}(1) - E_{\max}(n)}{n-1}\left[eVRIU^{-1}\right] \qquad (5.1)$$

$$FoM = \frac{Sensitivity}{BW_{\lambda(1)}} \qquad (5.2)$$

$$CR = \left| \frac{peak\ value - dip\ value}{peak\ value + dip\ value} \right|_{\lambda(1)} \tag{5.3}$$

5.4. Concluding remarks

We analyzed the optical properties of new geometries of gold nanocones. The effect of Fano like resonances are obtained in a single resonator structure (contains only a single metal piece), which can be switched on and off by rotating the structure around different symmetrical axis with respect to the incident field polarization. The symmetric conical resonator also offers dimensional angularly selectivity of the plasmonic properties like the nanocups and gold nanoshell with holes but it has an advantage to exhibit Fano resonance in the spectrum, which can be used for additional applications like PIT and switching. The asymmetric conical Fano resonator is found to be highly capable in the generation of higher order Fano resonances, which may be appropriate for plasmon line shaping and SERS. A comparison of conical and spherical Fano resonators have been examined. The conical Fano resonator is found to exhibit high field enhancement and sharp tunable Fano resonances with large modulation depths in the optical spectra compared to spherical Fano resonator. The spectral sensitivity of asymmetric conical Fano resonator to the surrounding medium is also studied and high values of FoM and CR are observed, which shows the performance of Fano resonator as a biological sensor.

Chapter 6

Fano resonant plasmonic conical nanodimer

6.1. Introduction

In this chapter we studied the plasmonic properties of two closely adjacent metallic conical nanoparticles. The plasmon modes of the first nanocone couple primarily with the plasmon modes of the second nanocone due to which a broad peak and a narrow peak emerges in the extinction spectrum, which can be categorized as bright and dark plasmon modes. The destructive interference of the two modes results in a sharp Fano dip in the spectrum. Several configuration of the conical nanodimer have been demonstrated, which suggest that the plasmon coupling in the dimer is not only dependent on the interparticle distance and size of the nanoparticles but also on the spatial arrangement of the two components. The localized near-field energy known as hot-spots of the dimer nanostructure are essential for the surface-enhanced Raman spectroscopy applications by detecting biomolecules.

Surface plasmons of metal nanoparticles are able to produce very strong and confined optical fields at deep sub-wavelength volumes, far beyond the diffraction limit. When the two metal nanoparticles are placed closed to each other to make a dimer, their optical properties are highly changed because the plasmon resonances of both the metals couple together and forming new hybridized plasmon modes. Reported study showed that by decreasing the gap between the two nanoparticles, the plasmon coupling of the nanoparticles can be increased, which results in the amplification of the field intensity by orders of magnitude. Because of this property, the dimer nanostructure has received a huge attention for surface-enhanced Raman spectroscopy (SERS) applications due to the hot spot produced in the gap between nanoparticles when incident light is polarized along the dimer axis [45, 46, 72, 127].

Recently, it has been established that the plasmonic dimer nanostructure also support Fano like resonances [18, 19, 43, 44, 46-48]. Various geometries based on dimer structure have been proposed to achieve Fano resonances. Brown *et al*., have experimentally and theoretically analyzed mismatched nanoparticle pairs of different size and shapes that gives rise to properties such as Fano resonances, avoided crossing behavior, and optical nanodiode effect [44]. Yang *et al*., have theoretically investigated the plasmon coupling in metallic nanorod dimers. They observed a pronounced dip in the optical spectrum due to plasmonic Fano resonance which is induced by destructive interference between bright dipole mode of the short nanorod and dark quadrupole mode of the long nanorod [19]. Wu *et al*., have reported Fano like resonances in the absorption spectrum of an asymmetric homodimer of gold elliptical nanowires, which arises from the coherent coupling between the superradiant bright mode and the subradiant dark mode [47]. Wu *et al*., have also demonstrated the influence of symmetry breaking on the plasmon resonance couplings in the gold nanotube dimer and observed strong Fano like resonance in the scattering spectrum due to the interference of the bonding octupole mode of the dimer with the dipole modes in the weak coupling model [46]. Recently, Zheng *et al*., have observed Fano resonance in a T-shaped dimer, which arises from the interference of the bright mode of the short nanoparticle and the dark mode of the long nanoparticle [128].

We present here for the first time, the observation of Fano resonance in a dimer based on gold nanocones, which are highly polarization dependent nanostructures [129]. The Fano resonance can be tuned and enhanced by modifying the size of one of the nanoparticle or the interparticle gap between the two nanocones. Several configurations of the dimer structure have been proposed to attained Fano resonances.

6.2. Optical properties of a dimer

Figure 6.1 shows the schematic diagram of a mismatched gold nanodimer. The dimensions of the nanodimer are R_1, H_1/ R_2, H_2, where 'R_1' and 'H_1' the radius and height of the large nanocone and are 'R_2' and 'H_2' the radius and height of the small nanocone, respectively. The gap size between the two nanocones is '*G*'. The illuminating electromagnetic wave is linearly polarized, the electric field is directed along *x* and the wave propagates in the *y*-direction.

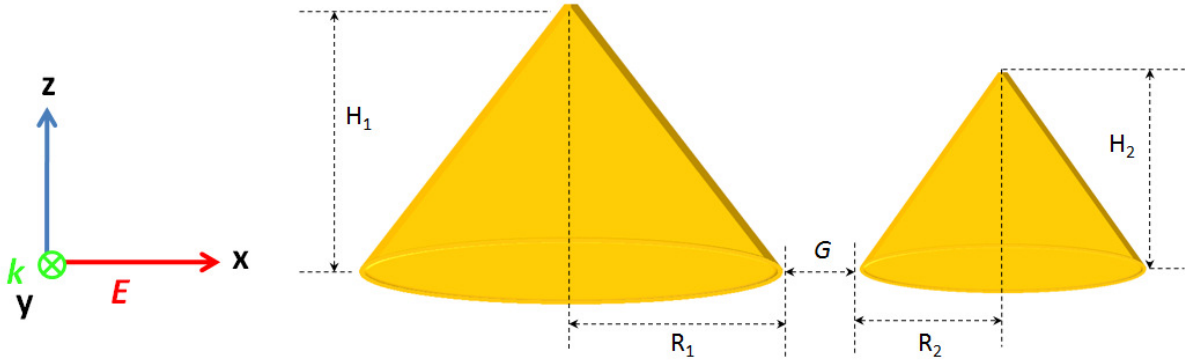

Figure 6. 1. Sketch of the dimer nanostructure. The incident field is linearly polarized along the *x*-direction and propagates along the *y*-direction.

Figure 6.2(a) shows the calculated extinction spectra of the large and small nanocones having dimensions R_1, H_1 = 90, 110 and R_2, H_2 = 50, 70 nm, respectively. The large nanocone exhibit a sharp extinction peak near 638 nm and the small nanocone at 552 nm. Both the peaks represent the fundamental dipole mode. Now when the two nanocones are brought close enough to from a dimer, then according to the plasmon hybridization model, the plasmon modes of the first nanocone couple primarily with the plasmon modes of the second nanocone due to which a low-energy bonding and a high-energy antibonding modes are formed [130]. The antibonding mode cannot be visualized in the spectrum due to its extremely small dipole moment, so only the bonding mode emerges in the spectrum due to its large dipole moment [77, 130]. In a mismatched nanodimer (heterodimer), the dipole mode of the small nanocone interacts with the dipole and higher order modes of the large nanocone forming hybridized dipole-dipole (DDB), dipole-quadrupole (DQB) and dipole-multipolar bonding modes [43, 44]. Figure 6.2(b) shows the extinction spectra of a heterodimer with a gap of *G* = 1 nm, which possesses a mixture of the hybridized bright DDB mode near 770 nm and dark DQB mode near 630 nm. The higher-energy peak is much weaker than the lower-energy peak. The two modes overlap in energy and induces a sharp Fano resonance in the visible range near 682 nm, which is characterized by a dip in the spectrum. It has also been observed that swapping both the nanoparticles does not affect the extinction spectra of a nanodimer. The surface charge distributions (top view) corresponding to each peak and Fano dip are shown in the inset of figure 6.2(b). The surface charges near 770 nm shows a dipole

distribution on both the nanoparticles, which clearly represents a DDB mode. The surface charges near 630 shows a quadrupolar like distribution on both the nanoparticles depicting DQB mode, while the surface charges at the dip shows a mixture of dipole and quadrupole modes. We named this configuration of a nanodimer as *type I*.

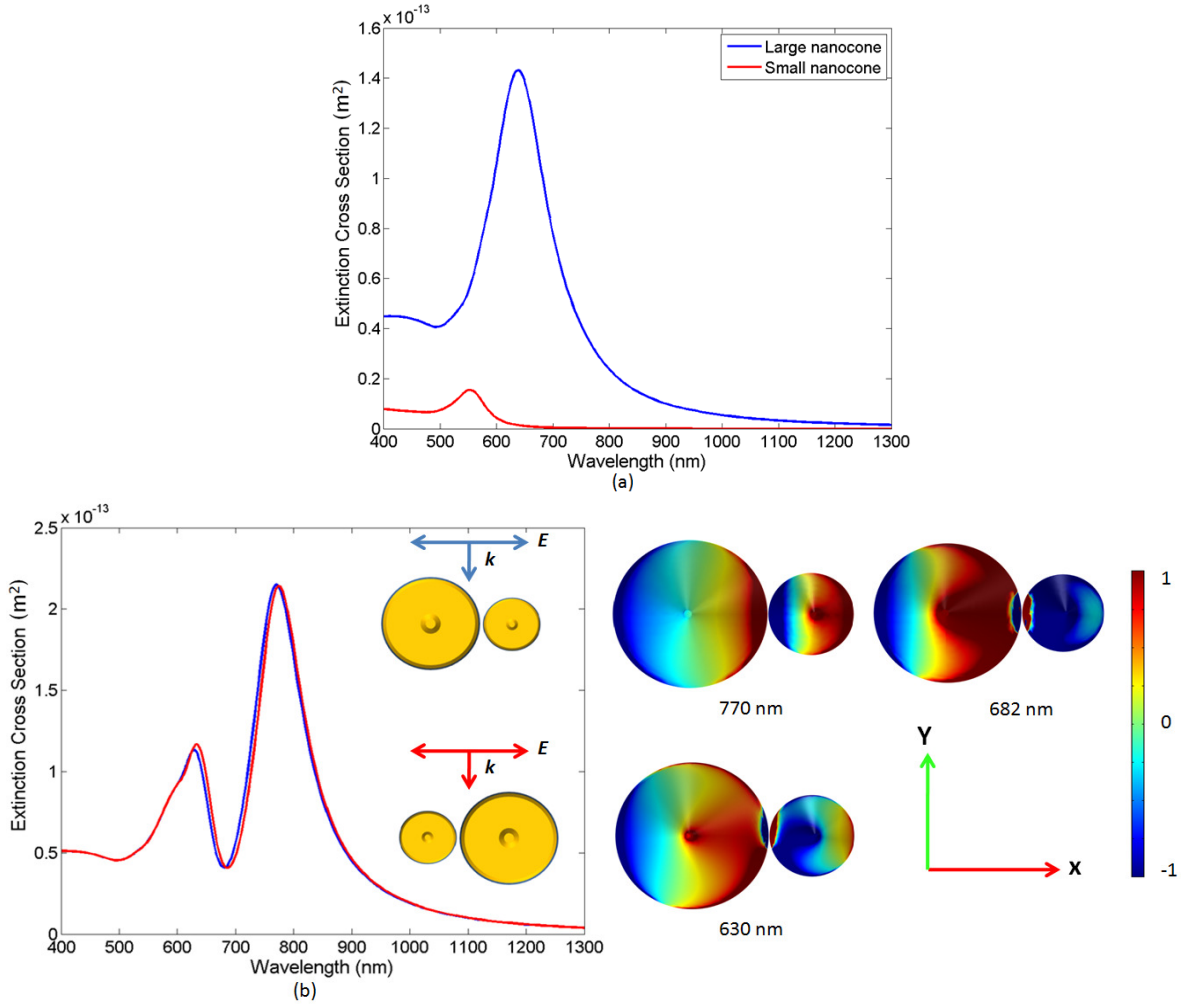

Figure 6. 2. Extinction spectra of a (a) large and small nanocones (b) nanodimer. Inset shows surface charge distributions calculated using Gauss's law.

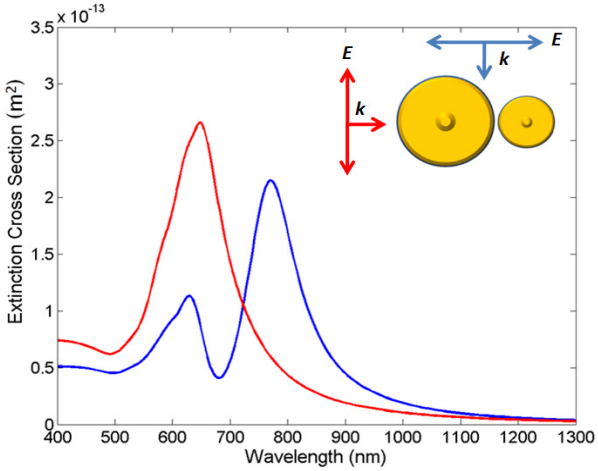

Figure 6. 3. Extinction spectra of a dimer with longitudinal (blue) and transverse (red) polarizations.

The polarization state of the incident light also has a great effect on the extinction spectra of the dimer. Figure 6.3 shows the extinction spectra of a nanodimer with both the longitudinal (blue line) and transverse (red line) excitations at fixed G = 1 nm. For a transverse polarized incident light, the electrostatic coupling between the nanoparticles is predicted to be of less significance. Here, the field enhancement and plasmon coupling are very weak compared to the longitudinal excitation because the hybridization effects are limited [44, 77]. So, for the transverse polarization, the Fano dip disappears and we observed only a single dipole peak near 650 nm. The higher order hybridized modes remain absent in this case and the dimer acts as a monomer. Thus, by changing the polarization of incident field, the Fano resonance can be switched on and off.

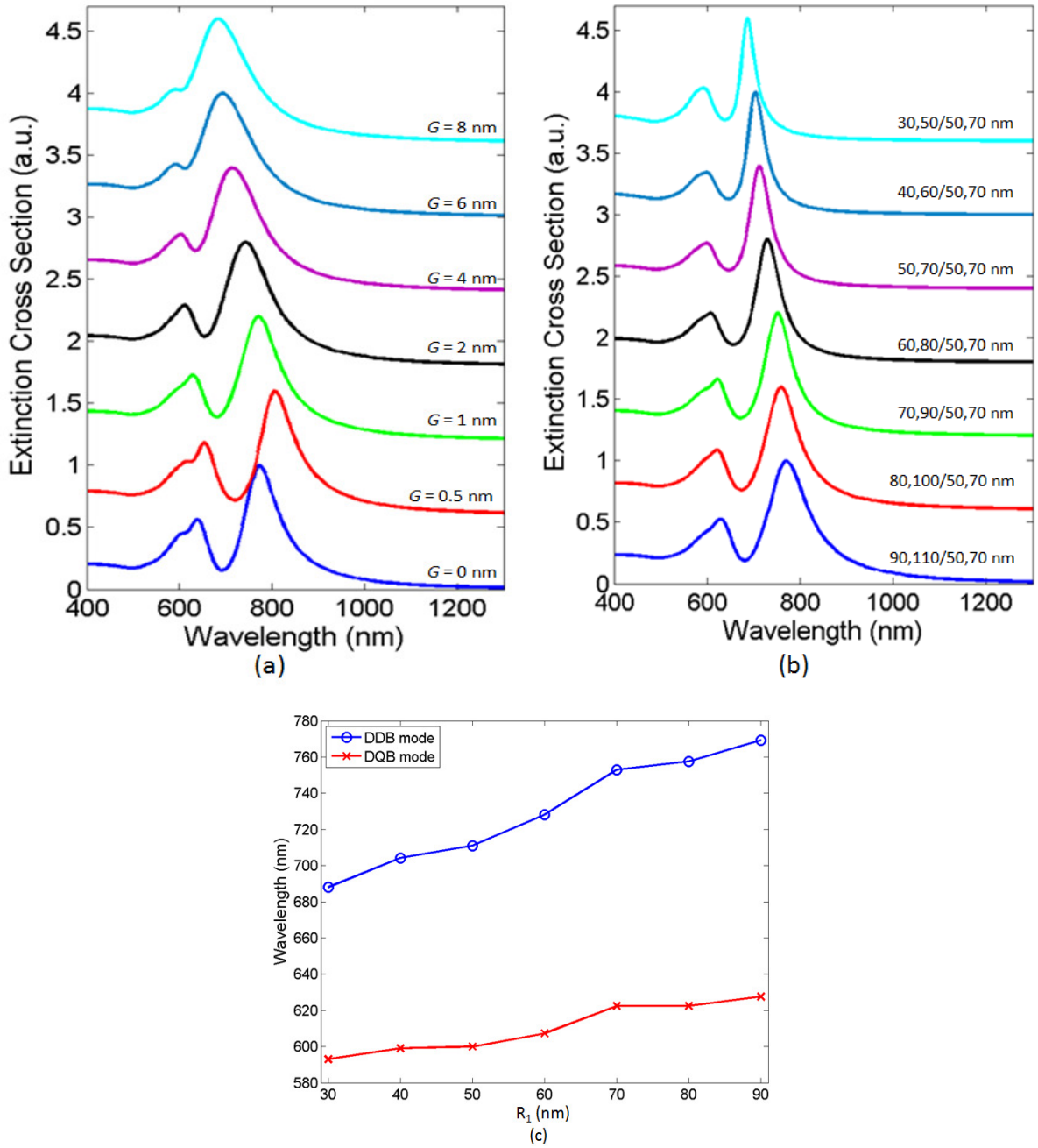

Figure 6. 4. Extinction spectra for (a) different value of G; (b) R_1 and H_1. (c) Wavelength shift as a function of R_1.

The appearance of higher order modes in the nanodimer depends upon the gap between the two nanoparticles. When the gap is small, than the plasmon interactions between the two nanocones increases, which results in the emergence of higher order multipolar modes as shown in figure 6.4(a). For instance, at $G = 0$ and 0.5 nm, a slight octupolar peak arises at the high-energy level. It is further to be noted that, by decreasing the value of G, a simultaneous red-shift of the resonant peaks occur and the modulation depth of the Fano resonance increases. However, when $G = 0$ nm, the resonant peaks blue-shifted. By increasing the value of G, the DQB mode gets weaker while the DDB mode becomes stronger, which results in the weakening of Fano resonance. For a very large value of G, the plasmon hybridization between the two nanocones are reduced due to which the dimer acts as an isolated monomer because only a single resonance dominates the extinction spectrum and no Fano resonance can be perceived. Figure 6.4(b) shows the extinction spectra of a dimer by modifying the dimensions of the first nanocone at fix $G = 1$ nm due to which the intensity and the spectral position of both resonances vary. It appears that for smaller values of R_1 and H_1, the DDB mode losses its strength and become narrow because of the decrease in the polarizability of the first nanocone as R_1 gets smaller. Also the Fano resonance is comparatively weak for smaller values of R_1 and H_1. Figure 6.4(c) shows the gradual red-shifting of the DDB and DQB modes as a function of R_1. The blue line corresponds to DDB mode, which shows a red-shift of around 80 nm by increasing the value of R_1 while the DQB mode (red line) shows a red-shift of around 35 nm, almost half of the DDB mode. This suggest that the DQB mode has somewhat maintains its spectral position. Thus, the spectral location and modulation depth of the Fano resonance can be controlled by modifying G or size of the nanoparticle.

We named the dimer with dimensions 30,50/50,70 nm as *type IA* and the dimer with dimensions 90,110/50,70 nm as *type IB* nanodimer. Figure 6.5 shows the near field enhancement and vector distributions of type IB nanodimer at different wavelengths, where the maximum value is observed in the gap region between the two nanoparticles. The directions of field vectors are determined by the real parts of the electric fields indicating the DDB and DQB modes as well as a Fano resonance [90, 131]. For the type IB nanodimer, the maximum value of the field enhancement for the DDB mode is found to be 245 and that for the DQB mode is 330. For the type IA nanodimer the maximum value of the enhancement for the DDB mode is 400 and that for the DQB mode is 260, which are reasonably high than the type IB nanodimer. So, in this configuration of a nanodimer, the type IB exhibit strong Fano resonance, which may be useful for plasmon-induced transparency (PIT) [14], whereas the type IA provides large field enhancement, which is an important feature of SERS [38, 75].

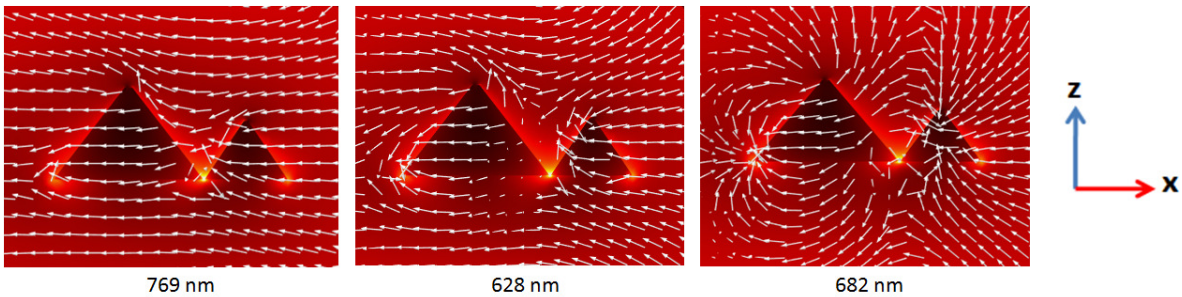

Figure 6. 5. The distributions of field intensities and vectors in the *xz*-plane of type IB nanodimer for the DDB and DQB modes and Fano resonance.

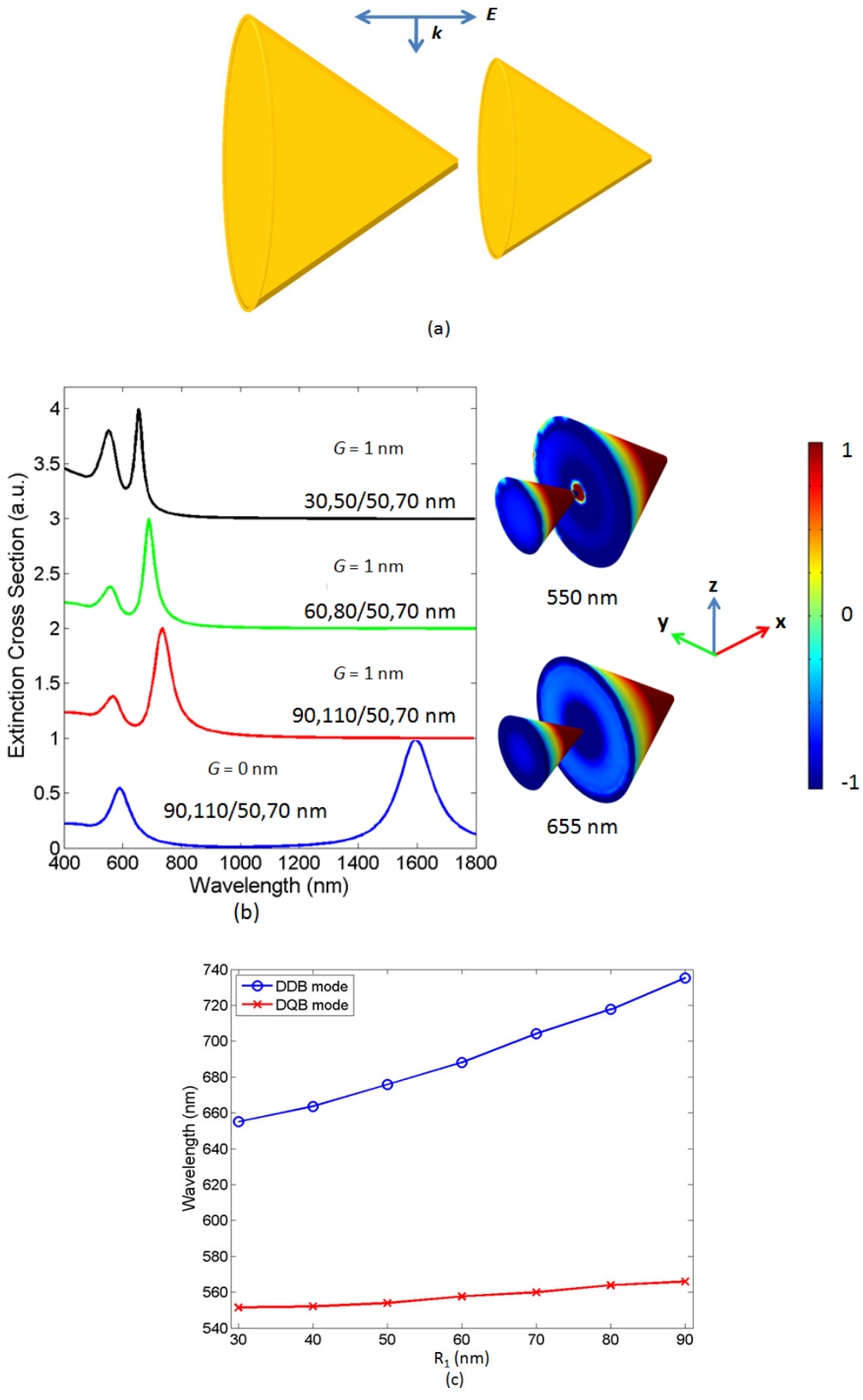

Figure 6. 6. (a) Sketch of type II nanodimer. (b) Extinction cross section of type II nanodimer. Insets shows surface charge distributions. (c) Wavelength shift as a function of R_1.

Next we make a nanodimer in such a way that its axis is aligned with the incident field polarization as shown in figure 6.6(a). Here the tips of both the nanocones are in the same

direction. We name this arrangement of a nanodimer as *type II*. Figure 6.6(b) shows the extinction spectra of type II nanodimer for different values of R_1 and H_1. The results obtained for this type is quite different from the type I configuration. When the dimensions of the dimer are 90,110/50,70 nm and G = 0 nm, the DDB mode is strongly damped and red-shifted in the spectrum and no coupling between the bright and dark modes are observed due to which no Fano resonance can be perceived. For the red, green and black lines in figure 6.6(b), we fixed G = 1 nm due which the modes coupling occur and Fano resonance started to appear in the spectrum. When the first nanocone size reaches to R_1 = 30 nm and H_1 = 50 nm, the DDB mode loses its strength and becomes narrow, while on the other hand the DQB mode gained enough strength and became broad due to which a Fano resonance with sharp modulation depth is observed in the spectrum. This Fano resonance was weak in the type IA nanodimer. We named the nanodimer with such dimensions as *type IIA* and the dimer with dimensions 90,110/50,70 nm as *type IIB*. The surface charge distribution corresponding to the two extinction peaks for type IIA nanodimer are shown in the inset. The peak near 655 nm corresponds to DDB mode, while the peak near 550 nm shows a quadrupolar like pattern. Here at the narrow gap between the two nanocones, the transfer of the charges occur. For instance, the negative charges of the large nanocone migrates to small nanocone and the positive charges of the small nanocone migrates to large nanocone due to which the nature of this mode appears as quadrupolar. Figure 6.6(c) shows the wavelength shift of both the DDB and DQB modes as a function of R_1 at fixed G = 1 nm. The DDB mode (blue line) shows a red-shift of around 80 nm, while the DQB mode shows a shift of just 15 nm. This shows that by reducing the size of the first nanocone, the DDB mode strongly blue-shift, while the DQB mode has essentially retains its spectral location.

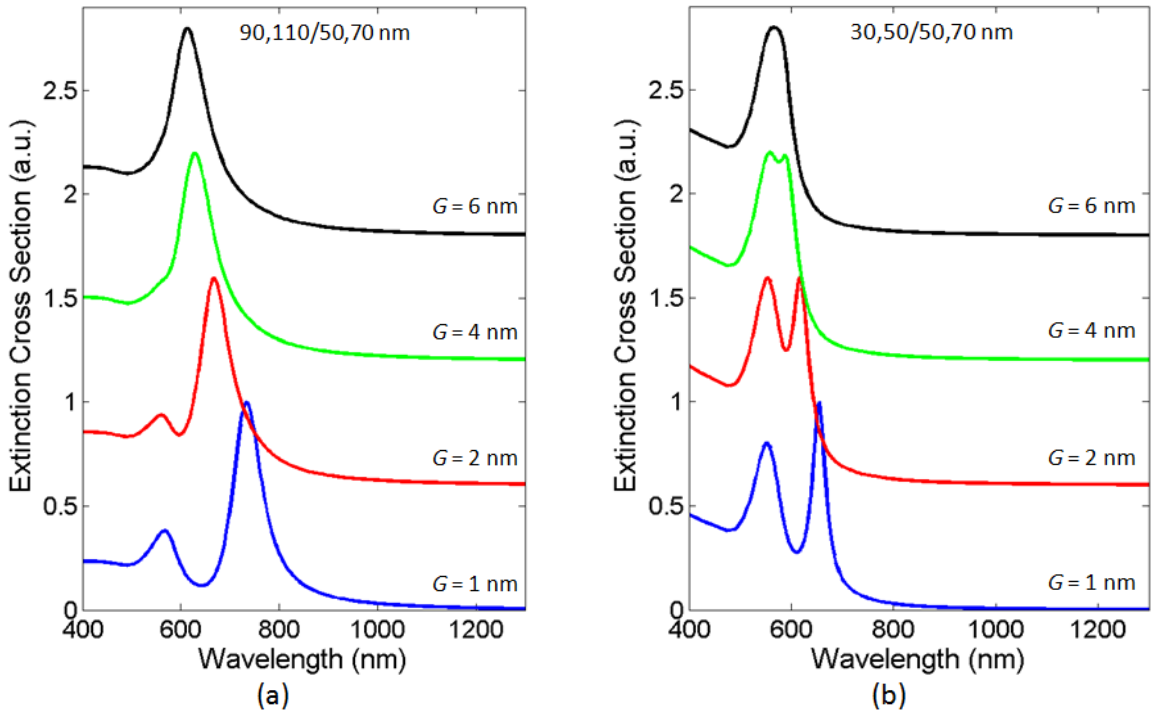

Figure 6. 7. Extinction spectra of (a) type IIB; (b) type IIA nanodimers for different values of *G*.

Figure 6.7(a, b) shows the extinction spectra of type IIB and IIA nanodimers for different values of *G*. It appears that by increasing the value of G, the DDB mode blue-shifted and the strength of the Fano resonance decreases. For high value of *G*, the double peak spectral feature vanishes and no Fano resonance is observed in both the types. This situation is

different from the type I nanodimer, where for high values of G, the Fano resonance still exist. So the type I nanodimer has the potential to exhibit strong Fano resonances in the extinction spectrum even for high value of G. However, the type IIA nanodimer has shown striking feature due to the appearance of intense Fano resonance for G = 1 nm.

Figure 6.8 shows the near field and vector distributions of type IIB nanodimer at fixed G = 1 nm, which reveals high values of the enhancement at the narrow gap between the two nanocones. For the type IIA nanodimer, the maximum value of the enhancement for the DDB mode is 255 while that of the DQB mode is 100. For the type IIB nanodimer, the maximum value for the DDB mode is observed to be 86 while that for the DQB mode is 46. So in this configuration, the type IIA nanodimer can be a better choice for both the PIT and SERS applications [14, 38]. From the near field distributions, it also becomes clear that, whatever the arrangement of the nanoparticles, the maximum near field enhancement always takes place at the junction between the two nanoparticles by forming a so-called “hot spot”.

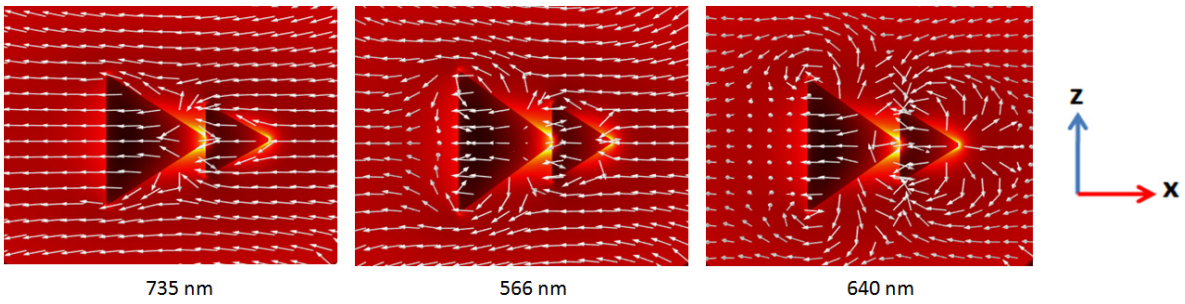

Figure 6. 8. The distributions of field intensities and vectors in the *xz*-plane of type IIB nanodimer for the DDB and DQB modes and Fano resonance.

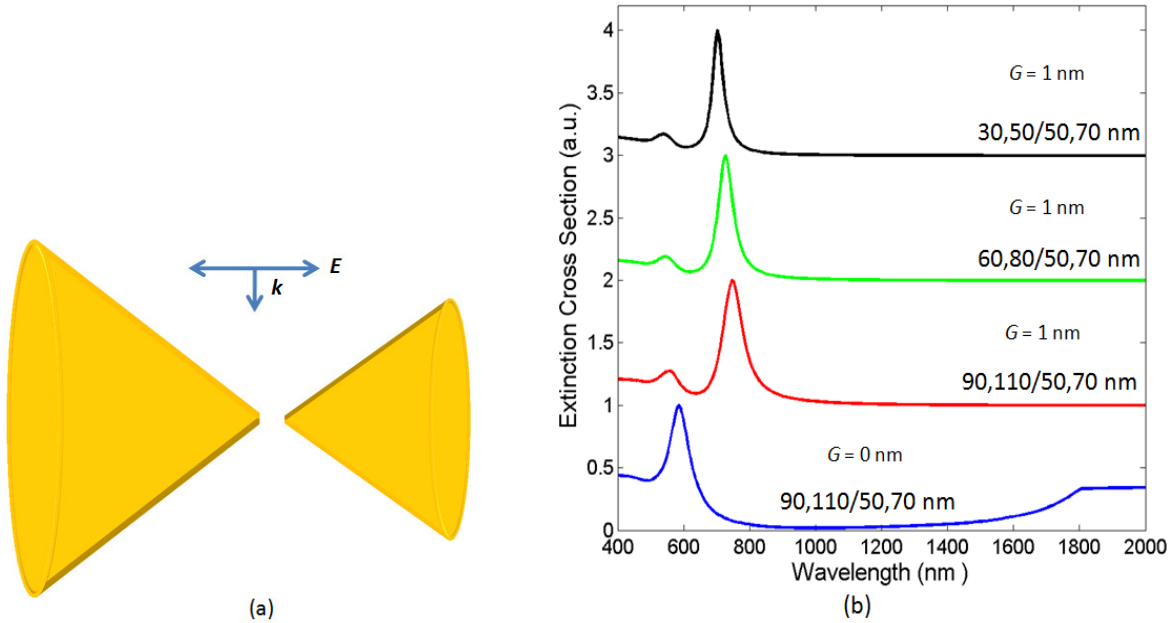

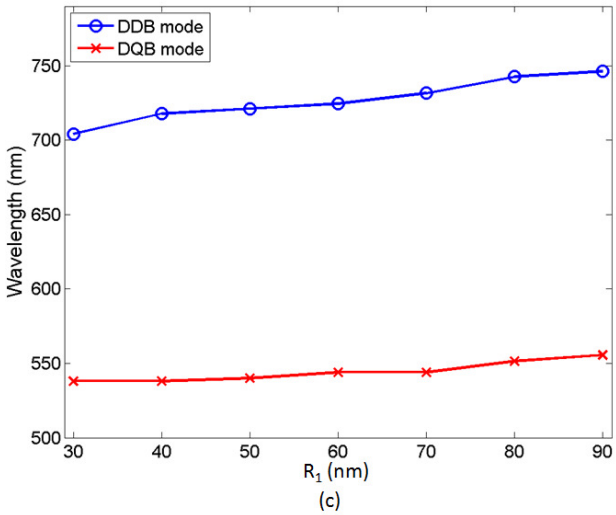

Figure 6. 9. (a) Sketch of type III nanodimer. (b) Extinction cross section of type III nanodimer. (c) Wavelength shift as a function of R_1.

Another type of the nanodimer arrangement are shown in figure 6.9(a), where we place the tips of both the nanocones in front of each other. We named this configuration of the nanodimer as *type III*. Figure 6.9(b) shows the extinction spectra of the type III nanodimer. For the blue line where $G = 0$ nm, a tremendous red-shift of the DDB mode is observed and no Fano resonance is found. This situation is similar to type II configuration for $G = 0$ nm. For $G = 1$ nm, a strong blue-shift of the DDB mode take place (red line) but by decreasing the size of the first nanocone, an extremely small movement of the DDB mode occur and also the Fano resonance obtained in this case is very weak compared to the previous two cases. So the type III configuration is producing only weak Fano resonances. Figure 6.9(c) shows the wavelength shift as a function of R_1. It appears that the DDB mode shows a red-shift of only 21 nm while the DQB mode shifts around 11 nm. This suggest that, in the type III configuration, the Fano resonance and the hybridized modes are not very sensitive to the size of the nanoparticle unlike the previous two types.

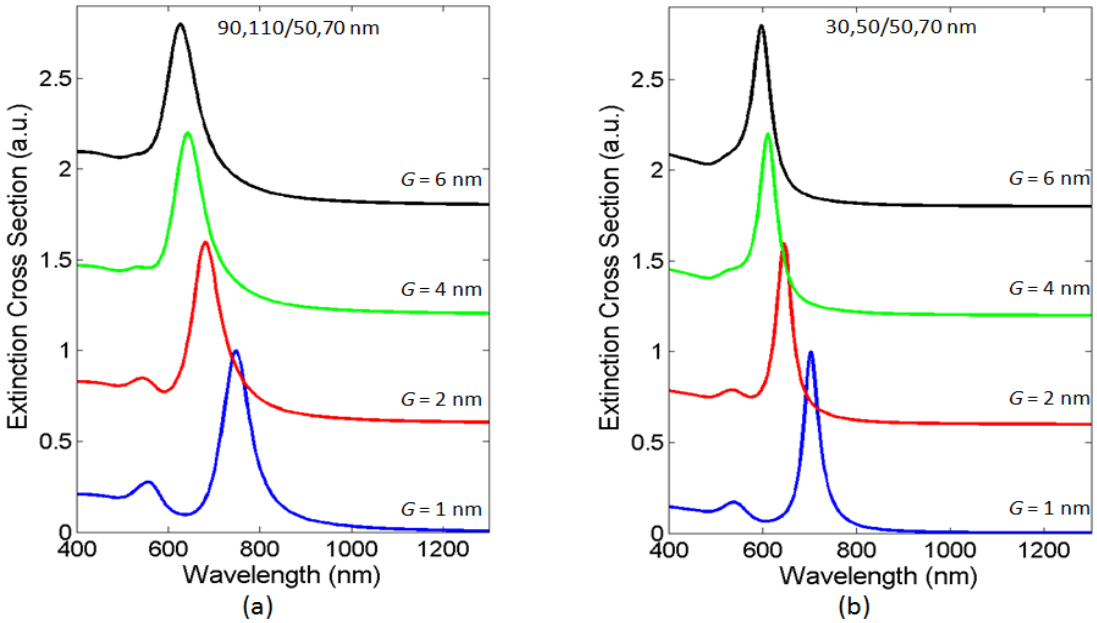

Figure 6. 10. Extinction spectra of (a) type IIIB; (b) type IIIA nanodimers for different values of *G*.

Figure 6.10 shows the extinction spectrum of the type III nanodimer with different dimensions for various values of *G*. The dimer with dimensions 30,50/50,70 nm and 90,110/50,70 nm are named as *type IIIA* and *type IIIB*. In both the type IIIA and IIIB nanodimers, the blue-shifting of the DDB mode is similar to the previous discussed cases but no pronounced Fano resonance is observed. So, for the type III nanodimer, changing the gap *G* or the parameters of the nanoparticle do not yield strong Fano resonance.

Figure 6.11 shows the near field and vector distributions of type IIIB nanodimer for the DDB and DQB modes and Fano resonance. The highest value of the enhancement for type IIIA nanodimer is observed to be 180 for the DDB mode while that for the DQB mode is 60. On the other hand, for the type IIIB nanodimer, the maximum value of the enhancement for the DDB mode is 150 while that for the DQB mode is 87. These values of the enhancement are less than the previous two types. Therefore, we can say that the type III nanodimer is not so proficient for high performance SERS. The near field enhancement distributions of type I, II and III nanodimers show that the lower-energy DDB mode will always exhibit large value of the enhancement like the previous reported studies [43, 46, 73]. However, the type IB nanodimer shows maximum value of the enhancement for the DQB mode, which is different from the other cases.

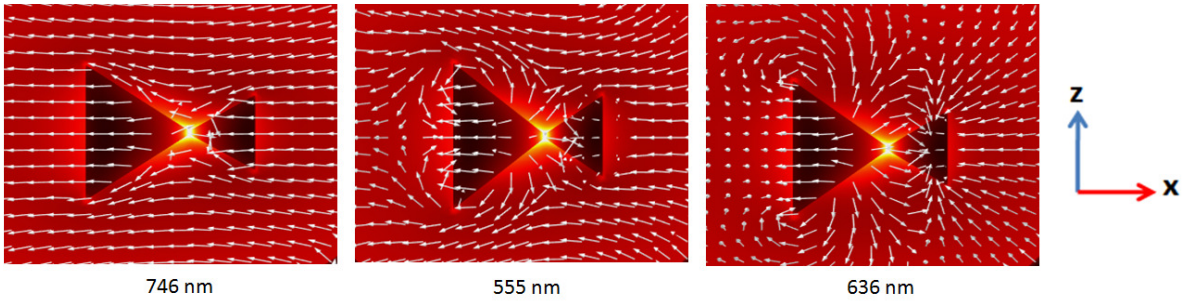

Figure 6. 11. The distributions of field intensities and vectors in the *xz*-plane of type IIIB nanodimer for the DDB and DQB modes and Fano resonance..

Finally, we make a nanodimer by placing the tips of both the nanocones in the opposite direction as shown in figure 6.12(a). We named this nanostructure as *type IV*. Figure 6.12(b) shows the extinction spectra of the type IV nanodimer. For the blue line, where the interparticle distance vanishes i.e., $G = 0$ nm, only a DDB mode at the higher-energy level is observed, which involves electrons flowing between the two particles [26]. In this situation, the nanodimer act as a monomer and such case is quite different from the previously addressed cases for $G = 0$ nm. When the value of *G* increases from 0 to 1 nm, a slight peak at the lower energy level near 1430 nm appears. This peak is far ahead from the DDB mode due to which no coupling between the two modes will takes place. By reducing the size of the first nanocone, no distinct Fano profile is observed in the extinction spectrum because the two peaks are not close spectrally. So, the type IV nanodimer is incorrigible of producing Fano resonances. However, by changing the interparticle gap, it is surprising to see that the two peaks come closer, overlap in energy and induces a Fano resonance with a weak modulation depth. This situation is quite obvious for type IVB (90,110/50,70 nm) nanodimer at $G = 6$ nm showing in figure 6.12(c). This implies that, the type IV nanodimer exhibit a remarkable sensitivity to the gap region.

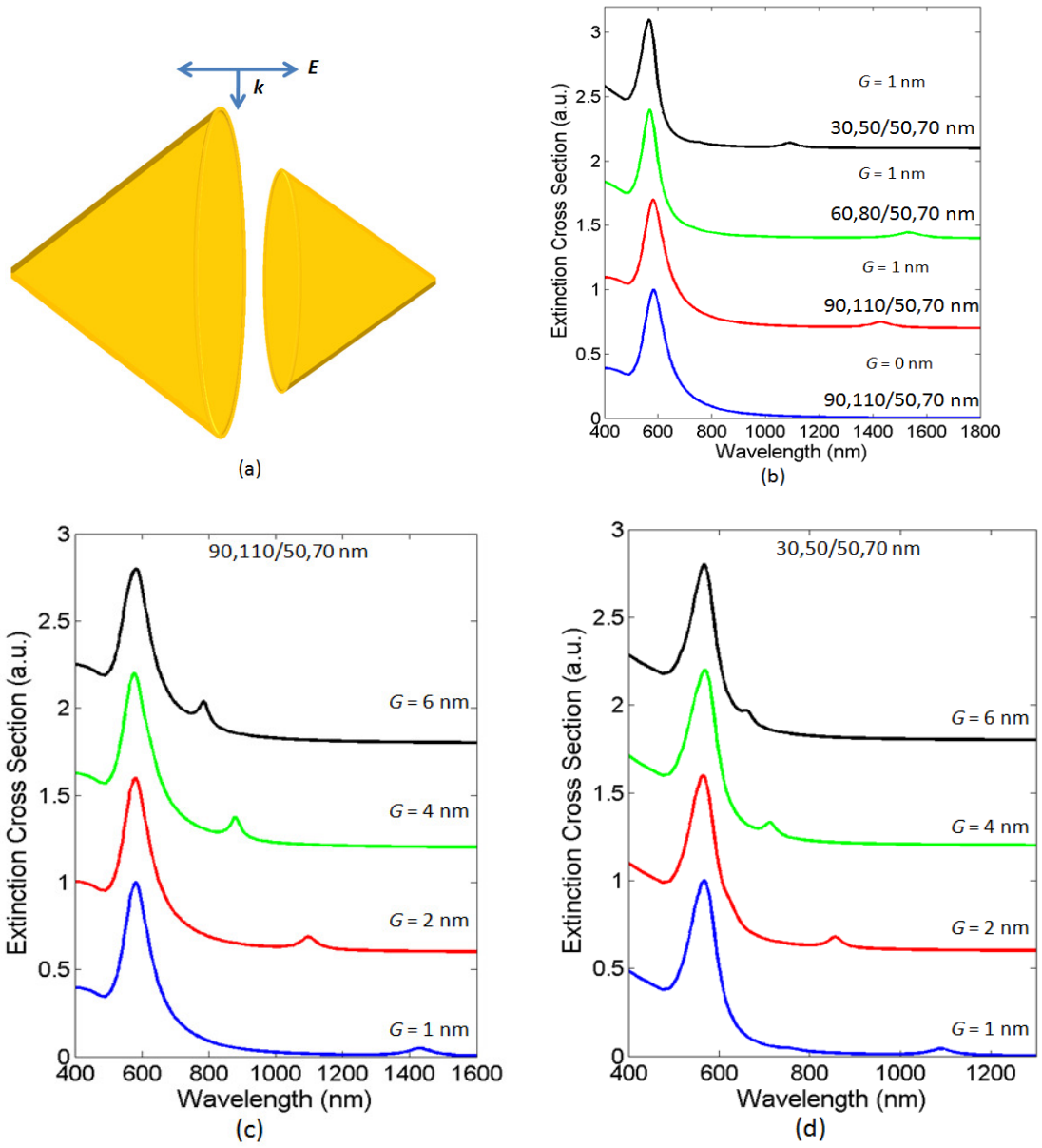

Figure 6. 12. (a) Sketch of type IV nanodimer. (b) Extinction spectra of type IV nanodimer. Extinction spectra of (c) type IVB; (d) type IVA nanodimers for different values of *G*.

6.3. Concluding remarks

We studied theoretically, the plasmonic Fano resonance in a dimer based on gold nanocones. By adjusting the geometry parameters, a Fano line shape is observed in the extinction spectrum, which is induced by the interference of bright and dark plasmon modes. Several geometrical configurations have been used to attain Fano resonances. The maximum enhancement for all the types of nanodimer is observed to be typically occur in the gap region between the two nanoparticles. Among all the types, type I arrangement is discovered to provide maximum field enhancement and sharp Fano resonance with greater tunability. However, type IIB nanodimer exhibit a Fano resonance with large modulation depth, typically more capable for PIT application. The plasmonic responses of type IV nanodimer are found to be highly sensitive to the interparticle distance and less affected by the size of the nanoparticle. The results obtained in this work open up the advantageous possibility of using the Fano resonance band for plasmon sensing, PIT, switching and SERS applications.

Chapter 7

Theory of Fano resonances in Plasmonic nanostructures

7.1. Introduction

In this chapter, a mass-spring coupled oscillator analogy and analytical expressions of Lorentzian and Fano line shapes based on Maxwell's equations have been used to explain the Fano resonances instead of hybridization model. Plasmonic nanostructures exhibiting bright and dark modes and Fano resonances have been successfully reproduce using the mechanical analogy and analytical formulae of Lorentzian and Fano line shapes. These analysis make the existence and understanding of Fano resonances easier in complex plasmonic nanostructures.

7.2. Mass-spring coupled oscillator analogy

Fano resonances have been analyzed in various plasmonic nanostructures but the in-depth theory illustrating Fano resonances is complex and difficult to understand. For this reason, the analogy of Fano resonances in plasmonic systems to the classical resonances in the harmonic oscillator system has been reported recently [27, 65, 132]. The coupled oscillator model offers an admirable explanation of the plasmon coupling and the corresponding optical response of the nanostructure.

The nanostructure, we take into our consideration is a three dimensional gold-silica-gold multilayered nanocone (MNC) having dimensions 40,50/60,70/85,95 nm. The illuminating electromagnetic field is linearly polarized, the electric field is directed along x and the wave propagates in z-direction. The scattering spectra of MNC nanostructure consists of a broad bright mode and narrow dark mode and the coupling and interference of the two modes results in a Fano resonance as shown in figure 7.1(b) (blue circles). The optical response of this nanostructure can be described by using a mechanical analogy of coupled oscillators shown in figure 7.1(a). All the mass values are considered to be 1. Oscillator $|1\rangle$ is driven by the time harmonic force *F(t),* which is analogous to the optical excitation of the superradiant bright mode. The subradiant dark modes are represented by oscillators $|2\rangle$ and $|3\rangle$, which will be excited only by coupling with oscillator $|1\rangle$ [27, 54]. The equations of motion of the oscillators $|1\rangle$, $|2\rangle$ and $|3\rangle$ are,

$$\begin{aligned}
&\ddot{x}_1(t) + \gamma_1 \dot{x}_1(t) + \omega_1^2 x_1(t) - \Omega_{12}^2 x_2(t) - \Omega_{13}^2 x_3(t) = F e^{-i\omega t} \\
&\ddot{x}_2(t) + \gamma_2 \dot{x}_2(t) + \omega_2^2 x_2(t) - \Omega_{12}^2 x_1(t) - \Omega_{23}^2 x_3(t) = 0 \\
&\ddot{x}_3(t) + \gamma_3 \dot{x}_3(t) + \omega_3^2 x_3(t) - \Omega_{13}^2 x_1(t) - \Omega_{23}^2 x_2(t) = 0
\end{aligned} \qquad (7.1)$$

where x_1, x_2 and x_3 are the displacements of each oscillator from their respective equilibrium position, ω_1, ω_2 and ω_3 are the superradiant dipole, subradiant quadrupole and octupole frequencies, Ω_{12}, Ω_{13} and Ω_{23} take into account the coupling between the modes and γ_1, γ_2 and γ_3 are the "friction coefficients" taking into account both radiation and metal losses. By solving equations (7.1), we find the absorbed power from the oscillator $|1\rangle$,

$$P(\omega) = \frac{F(\Omega_{23}^4 - (k_2 k_3))}{\Omega_{12}^4 k_3 - 2\Omega_{12}^2\Omega_{13}^2\Omega_{23}^2 + k_2(\Omega_{13}^4 - k_1 k_3) + \Omega_{23}^4 k_1} \tag{7.2}$$

where $k_1 = j\gamma_1\omega - \omega^2 + \omega_1^2$, $k_2 = j\gamma_2\omega - \omega^2 + \omega_2^2$ and $k_3 = j\gamma_3\omega - \omega^2 + \omega_3^2$. The free parameters are identified in such a way that $P(\omega)$ fits the extinction cross section of the nanostructure. We obtain the following values for the coupling frequencies: $\Omega_{13}{}^2 = \Omega_{23}{}^2 = 0$ and $\Omega_{12}{}^2 = 0.792$. The other parameters are $\omega_1 = 1.857$ eV, $\omega_2 = 1.703$ eV, $\gamma_1 = 0.252$ and $\gamma_2 = 0.011$.

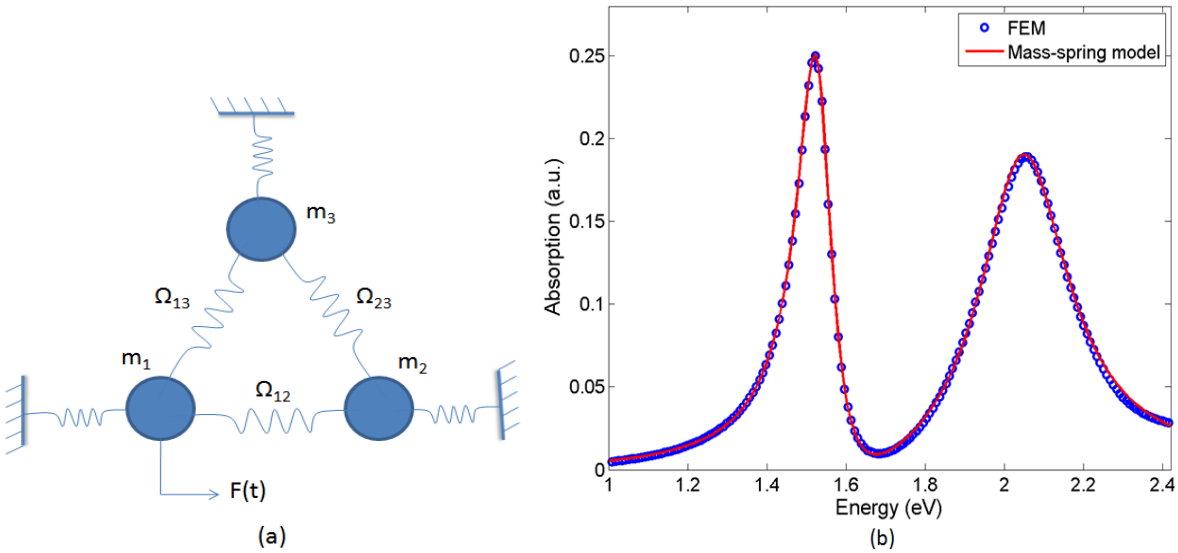

Figure 7. 1. (a) Three mass-spring coupled oscillator model. Oscillator $|1\rangle$ is driven by the time harmonic force $F(t)$. (b) Comparison between extinction cross section of MNC computed with FEM (blue circles) and the absorbed power by oscillator $|1\rangle$ (red solid line) using coupled oscillator analogy.

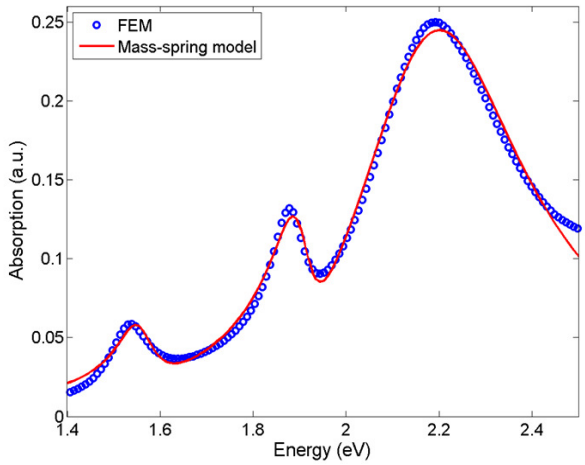

Figure 7. 2. Comparison between extinction spectrum of MNC computed with FEM (blue circles) and the absorbed power by oscillator $|1\rangle$ (red solid line) using three mass-spring coupled oscillator analogy at $\theta = 90^\circ$.

Next we rotate the MNC nanostructure 90° around *y*-axis due to which the incident field becomes aligned with the nanoparticle axis. For this axially polarized light, we obtained three extinction peaks in the spectrum as shown in figure 7.2. The broad peak represents

superradiant bright dipole mode, while the other two narrow peaks represents subradiant dark dipole modes. In this nanostructure, we obtained dual dipole-dipole Fano resonances. We used equation (7.2) to reproduced the optical response of this nanostructure, which agrees well with the extinction spectra calculated using FEM as shown by the red line in figure 7.2. The parameters obtained are ω_1 = 2.161 eV, ω_2 = 1.923 eV, ω_3 = 1.578 eV, γ_1 = 0.496, γ_2 = 0.067, γ_3 = 0.084, Ω_{12}^2 = 0.579, Ω_{13}^2 = 0.622 and Ω_{23}^2 = 0.003. So here, the three coupled oscillator analogy yields twin dipole-dipole Fano resonances.

The effect of symmetry breaking has been introduced in two types of conical nanostructures for a 0° rotation. The first one is a single conical nanoshell (CNS), where the inner core has been displaced 12 nm in the *y*-direction to make a non-concentric CNS (NC-CNS) and the second one is MNC nanostructure, where the inner core has been offset 18 nm in a similar style to make a non-concentric MNC (NC-MNC). By considering the NC-CNS nanostructure first, a dark quadrupolar and octupolar mode emerges in the spectrum at the higher-energy level, which couples to the superradiant dipole mode due to near field and induces Fano resonances as shown in figure 7.3(a). The oscillator $|2\rangle$ in figure 7.1(a) represents a quadrupole mode while the oscillator $|3\rangle$ represents an octupole mode. Both the oscillators $|2\rangle$ and $|3\rangle$ are connected to oscillator $|1\rangle$. So the two subradiant modes related to Fano resonances can only be excited by coupling with the oscillator $|1\rangle$. There is also a week coupling between oscillators $|2\rangle$ and $|3\rangle$, so a slight red-shift of the subradiant octupole mode will occur because of the additional interactions between the subradiant oscillators $|2\rangle$ and $|3\rangle$. By using equation (7.2), the optical response of NC-CNS is successfully reproduced as shown by the red lines in figure 7.3(a). Both the Fano resonances and higher order dark hybridized modes are well replicated. The parameters obtained are ω_1 = 1.556 eV, ω_2 = 1.794 eV, ω_3 = 1.589 eV, γ_1 = 0.173, γ_2 = 0.107, γ_3 = 0.006, Ω_{12}^2 = 0.470, Ω_{13}^2 = 0.70 and Ω_{23}^2 = 0.532.

Now by taking the second symmetry reduced nanostructure i.e., NC-MNC, we obtained four peaks and higher order Fano resonances in the extinction spectrum, which is calculated using FEM as shown in figure 7.3 (c) (blue circles). In this case, the three mass-spring analogy is not sufficient to produce the response of NC-MNC with four extinction peaks. For this reason, the three oscillator model has been extended to four oscillator model as shown in figure 7.3(b). The equations of motion of the oscillators $|1\rangle$, $|2\rangle$, $|3\rangle$, and $|4\rangle$ are,

$$\begin{aligned}
&\ddot{x}_1(t)+\gamma_1\dot{x}_1(t)+\omega_1^2x_1(t)-\Omega_{12}^2x_2(t)-\Omega_{13}^2x_3(t)-\Omega_{14}^2x_4(t)=Fe^{-i\omega t}\\
&\ddot{x}_2(t)+\gamma_2\dot{x}_2(t)+\omega_2^2x_2(t)-\Omega_{12}^2x_1(t)-\Omega_{23}^2x_3(t)-\Omega_{24}^2x_4(t)=0\\
&\ddot{x}_3(t)+\gamma_3\dot{x}_3(t)+\omega_3^2x_3(t)-\Omega_{13}^2x_1(t)-\Omega_{23}^2x_2(t)-\Omega_{34}^2x_4(t)=0\\
&\ddot{x}_4(t)+\gamma_4\dot{x}_4(t)+\omega_4^2x_4(t)-\Omega_{14}^2x_1(t)-\Omega_{24}^2x_2(t)-\Omega_{34}^2x_3(t)=0
\end{aligned} \qquad (7.3)$$

We ignored the weak coupling strengths (Ω_{23}^2, Ω_{24}^2 and Ω_{34}^2) between the oscillators $|2\rangle$, $|3\rangle$ and $|4\rangle$ to make the equation simpler. By using these assumptions, we solve equations (7.3) and reproduced the extinction spectra of NC-MNC due to the power absorbed by oscillator $|1\rangle$ from the external force as shown by the red line in figure 7.3(c). The parameters

achieved are ω_1 = 1.882 eV, ω_2 = 1.786 eV, ω_3 = 1.959 eV, ω_4 = 1.388 eV, γ_1 = 0.504, γ_2 = 0.0104, γ_3 = 0.233, γ_4 = 0.034, Ω_{12}^2 = 0.70, Ω_{13}^2 = 0.536 and Ω_{14}^2 = 0.674. The results agree well with each other, which indicate that the higher order Fano resonances obtained in plasmonic nanostructures can be described well by the mass-spring coupled oscillator analogy. So the mass-spring analogy has a great capability to fit to nanoscale systems but it demands many masses to correctly fit for higher order modes of the nanoscale systems.

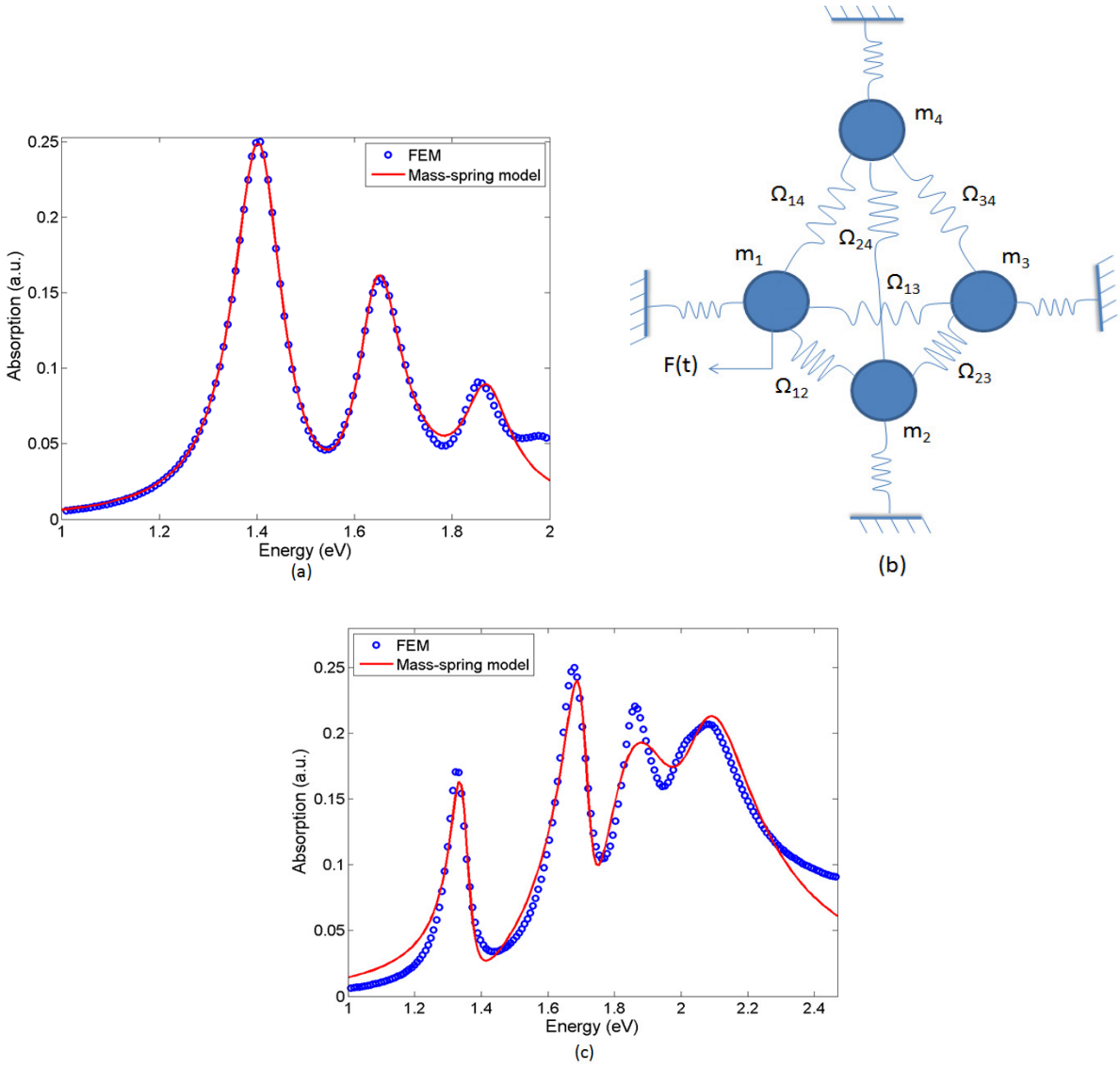

Figure 7. 3. (a) Comparison between extinction spectra of NC-CNS with 12 nm core offset, computed with FEM (blue circles) and the absorbed power by oscillator $|1\rangle$ (red solid line) using three mass-spring coupled oscillator analogy. (b) Four mass-spring coupled oscillator model. Oscillator $|1\rangle$ is driven by the time harmonic force *F(t)*. (c) Comparison between extinction spectrum of NC-MNC with 18 nm core offset computed with FEM (blue circles) and the absorbed power by oscillator $|1\rangle$ (red solid line) using four mass-spring coupled oscillator analogy.

7.3. Analytic expressions of Lorentzian and Fano asymmetric line shapes

We know from our previous knowledge that Fano resonances have been studied both experimentally and numerically in a wide range of plasmonic nanostructures and the optical response of the nanoparticles are mostly fitted and examined using coupled oscillators and other phenomenological models [13, 27, 36, 54]. Also, the quantum mechanical model suggested by Fano does not describe the role of intrinsic losses inherent to plasmonic systems, which is particularly significant because the mechanisms of energy transfer and energy losses in Fano resonant plasmonic systems are essential to understand. So, the interaction of the bright and dark modes in lossy materials is explained by Gallinet and Martin by developing a theory based on Maxwell's equations using the approach of Feshbach formalism [68, 133]. They have proposed general analytical expressions for the Lorentzian and Fano asymmetric line shapes with different parameters, where the existence of the two modes and their interactions can be clearly realized [41].

The symmetric Lorentzian line shape, which represents the resonance of a bright mode as a function of frequency ω is given by

$$\sigma_L(\omega) = \frac{a^2}{\left(\omega^2 - \omega_L^2 / 2W_L\omega_L\right)^2 + 1} \tag{7.4}$$

where 'a' is the maximum amplitude of the resonance, 'ω_L' is the resonance frequency, and 'W_L' is spectral width. The asymmetric Fano line shape, which arises from the interference of bright and dark modes is given by

$$\sigma_{F(i)}(\omega) = \frac{\left(\omega^2 - \omega_{F(i)}^2 \Big/ 2W_{F(i)}\omega_{F(i)} + q_{(i)}\right)^2 + b_{(i)}}{\left(\omega^2 - \omega_{F(i)}^2 \Big/ 2W_{F(i)}\omega_{F(i)}\right)^2 + 1} \tag{7.5}$$

where i = 1, 2, 3..., 'ω_F' is the resonance central spectral position, 'W_F' is the spectral width, 'q' is the asymmetry parameter, and 'b' is the modulation damping parameter emerging with intrinsic losses. The overall line shape of the plasmonic nanostructure is given by the product of symmetric and asymmetric resonant spectra.

$$\sigma_T(\omega) = \sigma_L(\omega)\sigma_{F(i)}(\omega) \tag{7.6}$$

Several plasmonic nanostructures have been demonstrated and their optical responses are fitted with the analytical expressions. For all the nanostructures, the illuminating electromagnetic field is linearly polarized, the electric field is directed along x and the wave propagates in z-direction.

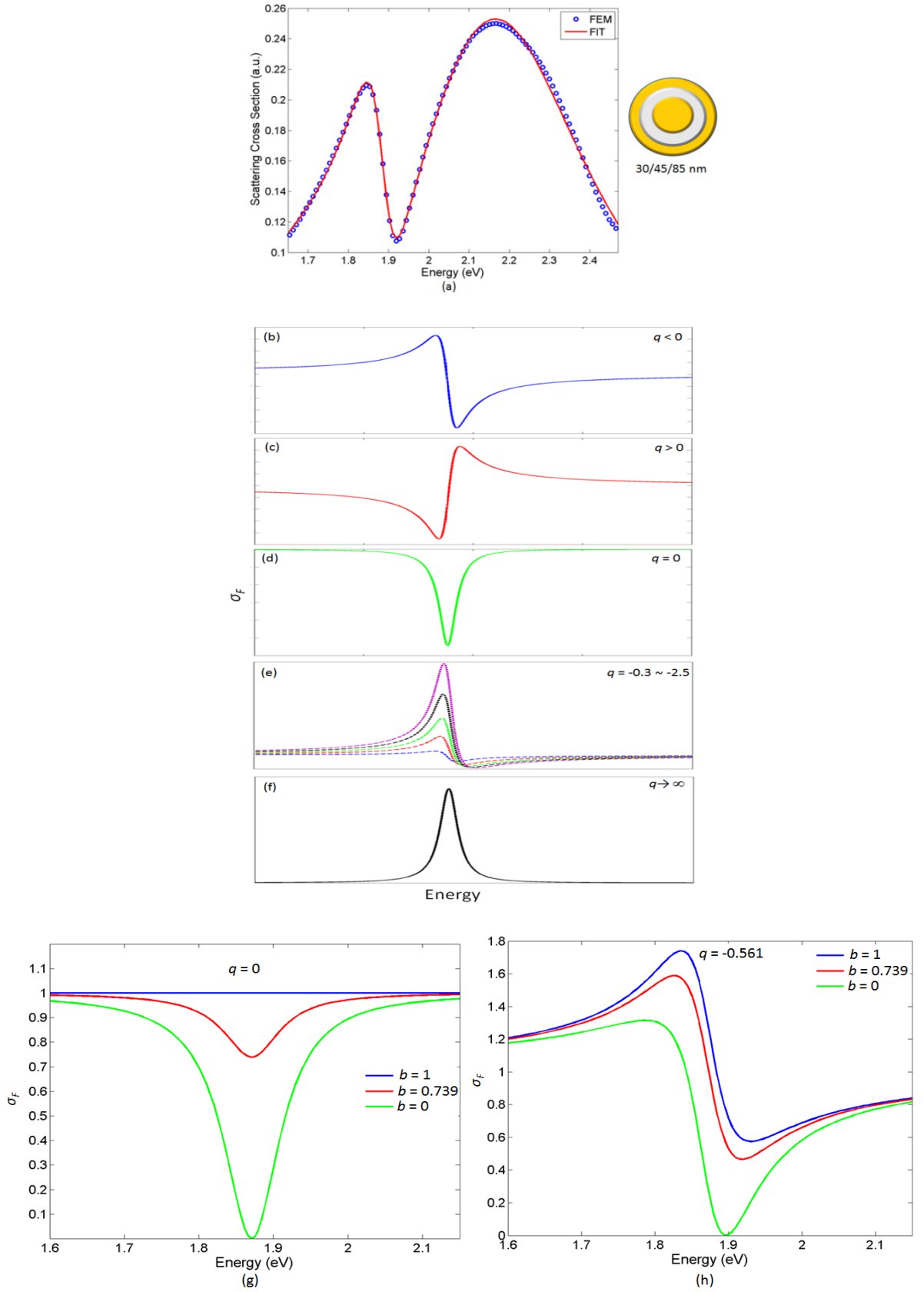

Figure 7. 4. Scattering spectra of MNS. Blue circles: numerical simulation (FEM) and red solid line: fit with equation (7.6). Panel (b)-(f) Different asymmetric line shapes obtained by varying the value of q using equation (7.5). In panel (e), asymmetric line shapes are attained using different values of q. Panel (g)-(h) shows the effect of the damping parameter b on the line shape.

We first consider a concentric three dimensional gold-silica-gold multilayered nanoshell (MNS) and fit its scattering spectra with equation (7.6). The MNS nanostructure consists of a broad bright mode and narrow dark mode and the coupling and interference of the two modes results in a Fano resonance as shown in figure 7.4. We fit the scattering spectra of MNS with equation (7.6) and obtained a very good agreement. Here the Lorentzian shape represents the bright dipolar mode while the Fano shape represents the interference between the bright and dark dipolar modes. The fit parameters obtained are a = 0.547, ω_L = 2.174 eV, W_L = 0.259 eV, ω_F = 1.871 eV, W_F = 0.046 eV, q = -0.561 and b = 0.739. All these parameters are used to reconstruct the bright and dark modes of MNS. The line shape of the asymmetry parameter q is shown in figure 7.4(b) using equation (7.5). The sign of q is monitored by the frequency difference between the bright and dark modes [22, 39, 41]. By changing the parameters of the MNS, the sign of q flips from -0.561 to 0.561, Panel (c). The frequencies of both the bright and dark modes will also be reversed in this case. Both the asymmetry parameter q and the modulation damping parameter b are the shape parameters and depend on how the resonance is examined. When q = 0, a symmetric dip emerges in the spectrum, which is known as Breit-Winger dip as shown in panel (d) [10, 13]. Panel (e) shows different values of q, representing asymmetric line shapes, which are also known as Feshbach resonances [10, 13]. For larger absolute values of the asymmetry parameter, the line shape appears more as symmetric, although the Fano nature would be still there, which can be recognized by the local minimum on one side of the peak. Panel (f) shows the case where $q \to \infty$, here the line shape obtained is Lorentzian because the Fano character is entirely disappeared, such resonance is also called Breit-Wigner resonance [10, 13]. These resonances are common in atomic and nuclear scattering and are achieved well in plasmonic nanostructures. Figures 7.4(g) and (h) shows the parameter b at two values of q. It has been observed that b produces a spectral broadening and damping of the asymmetry parameter. For very large value of b, the resonance appears as symmetric and adopts the shape of the response given in panel (f). So both the parameters b and q jointly describe the shape of resonance [68].

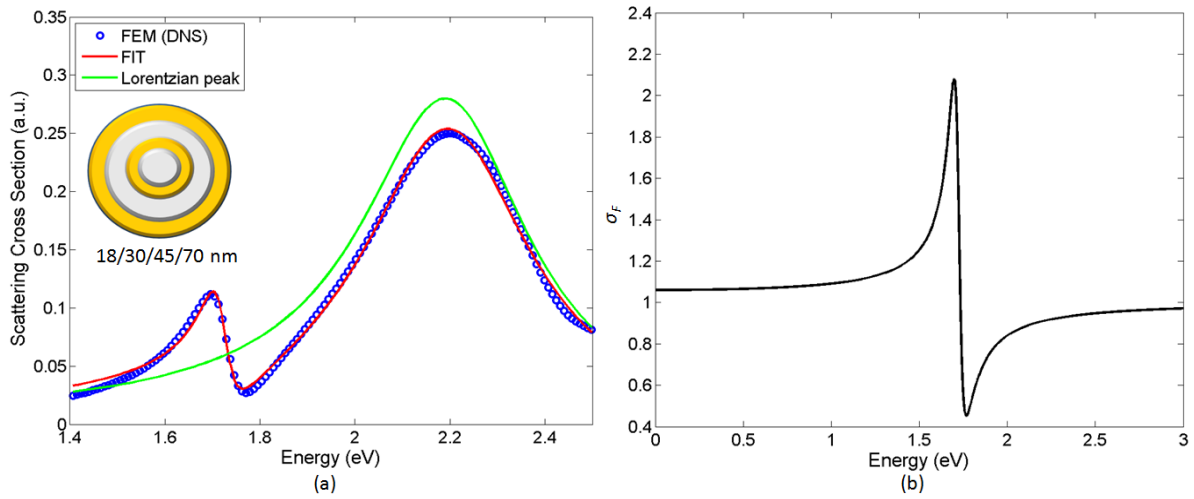

Figure 7. 5. (a) Scattering spectra of DNS nanostructure. Blue circles: numerical simulation (FEM) and red solid line: fit with equation (7.6). Green line represents the Lorentzian peak obtained from equation (7.4). (b) Asymmetric line shape acquired directly from equation (7.5).

The next nanostructure we considered is a double concentric silica-gold-silica-gold nanoshells (DNS) having dimensions 18/30/45/70 nm. This structure also exhibit a broad superradiant mode (bright) and a narrow subradiant mode (dark). The near field coupling of the two modes results in a Fano resonance as shown in figure 7.5(a). The scattering spectra of

DNS shows a good agrement by fitting with equation (7.6) as shown in figure 7.5(a). The fitting parameters obtained are a = 0.529, ω_L = 2.190 eV, W_L = 0.215 eV, ω_F = 1.721 eV, W_F = 0.033 eV, q = -0.770 and b = 0.940. The green line shows the line shape of the bright mode extracted using equation (7.4), which is obtained exactly at the same spectral position. Figure 7.5(b) shows the asymmetric line shape obtained using equation (7.5).

Figure 7.6 demonstrates the scattering spectra of a gold-silica-gold multilayered nanodice (MND) having dimensions 40/60/95 nm. This nanostructure exhibits the similar broad bright and narrow dark modes and a dipole-dipole Fano resonance. The scattering spectra of MND fitted with equation (7.6) shows a good agreement as shown in figure 7.6(a). The fit parameters acquired are a = 0.557, ω_L = 2.190 eV, W_L = 2.181 eV, ω_F = 1.772 eV, W_F = 0.038 eV, q = -1.173 and b = 0.996. The green line shows the line shape of the bright mode obtained using equation (7.4). Figure 7.6(b) shows the asymmetric line shape extracted using equation (7.5).

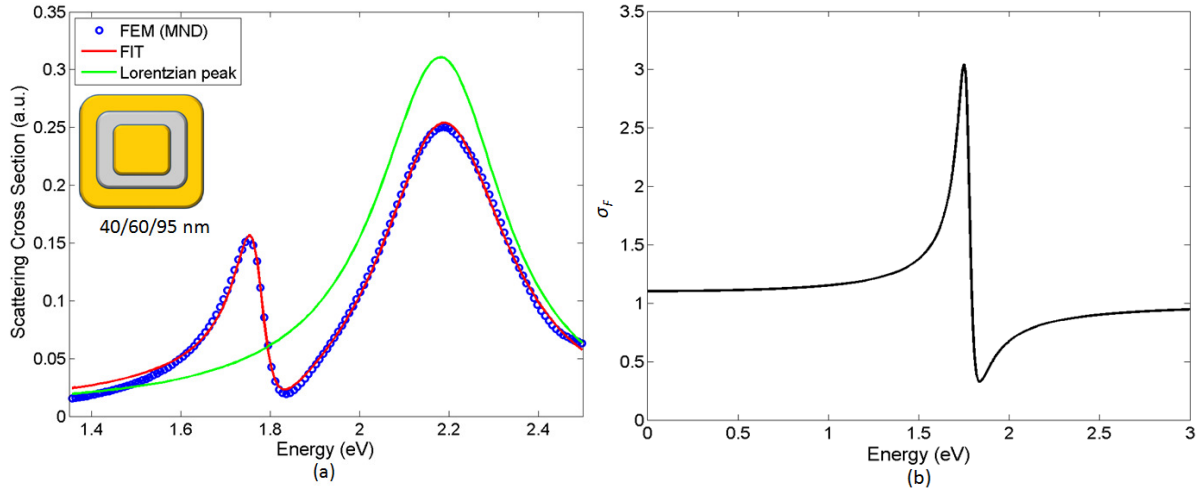

Figure 7. 6. (a) Scattering spectra of MND nanostructure. Blue circles: numerical simulation (FEM) and red solid line: fit with equation (7.6). Green line represents the Lorentzian peak obtained from equation (7.4). (b) Asymmetric line shape acquired directly from equation (7.5).

Figure 7.7(a) shows the geometry of a gold-silica-gold multilayered nanoellipsoid (MNE). Here E_1 denotes the inner ellipse having dimensions a_1-semiaxis = 40 nm, b_1-semiaxis = 30 nm, c_1-semiaxis = 30 nm, E_2 denotes the middle ellipse having dimensions a_2-semiaxis = 60 nm, b_2-semiaxis = 40 nm, c_2-semiaxis = 40 nm and E_3 denotes the outer ellipse having dimensions a_3-semiaxis = 75 nm, b_3-semiaxis = 55 nm, c_3-semiaxis = 55 nm, respectively. The scattering spectra of MNE show a good agreement by fitting with equation (7.6) as shown in figure 7.7(b). The fit parameters obtained are a = 0.537, ω_L = 2.145 eV, W_L = 0.174 eV, ω_F = 1.522 eV, W_F = 0.030 eV, q = -1.626 and b = 0.830. The green line shows the line shape of the bright mode obtained using equation (7.4). Figure 7.7(c) shows the asymmetric line shape obtained using equation (7.5).

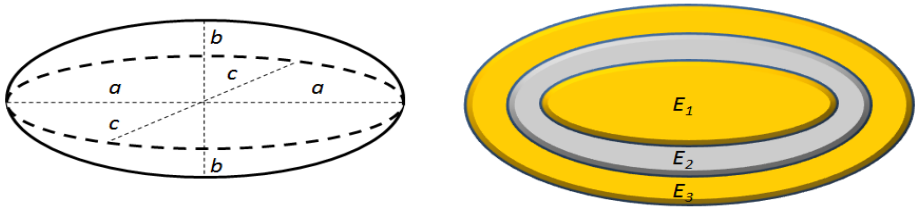

(a)

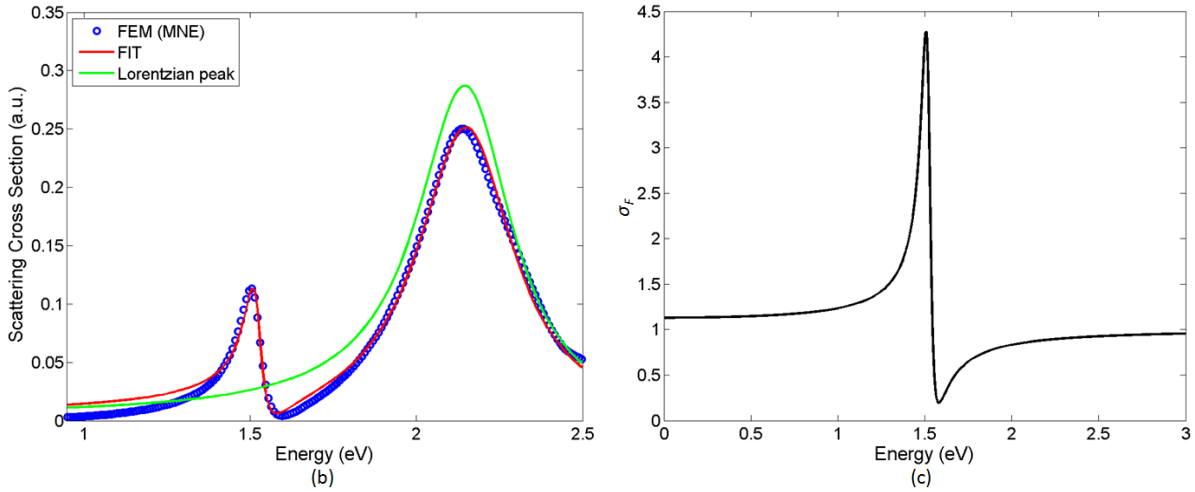

Figure 7. 7. (a) Sketches of single three dimensional nanoellipsoid and top view of a concentric MNE. (b) Scattering spectra of MNE nanostructure. Blue circles: numerical simulation (FEM) and red solid line: fit with equation (7.6). Green line represents the Lorentzian peak obtained from equation (7.4). (c) Asymmetric line shape acquired directly from equation (7.5).

Figure 7.8 shows the scattering spectra of a concentric gold-silica-gold multilayered nanocylinder (MNCD) having dimensions 20,60/30,75/45,95 nm. Both the bright and dark modes of MNCD fitted well with equation (7.6) as shown in figure 7.8(a). The fit parameters obtained are a = 0.553, ω_L = 2.253 eV, W_L = 0.178 eV, ω_F = 1.581 eV, W_F = 0.032 eV, q = -2.393 and b = 2.304. The green line shows the line shape of the bright mode obtained using equation (7.4). Figure 7.8(b) shows the asymmetric line shape obtained using equation (7.5).

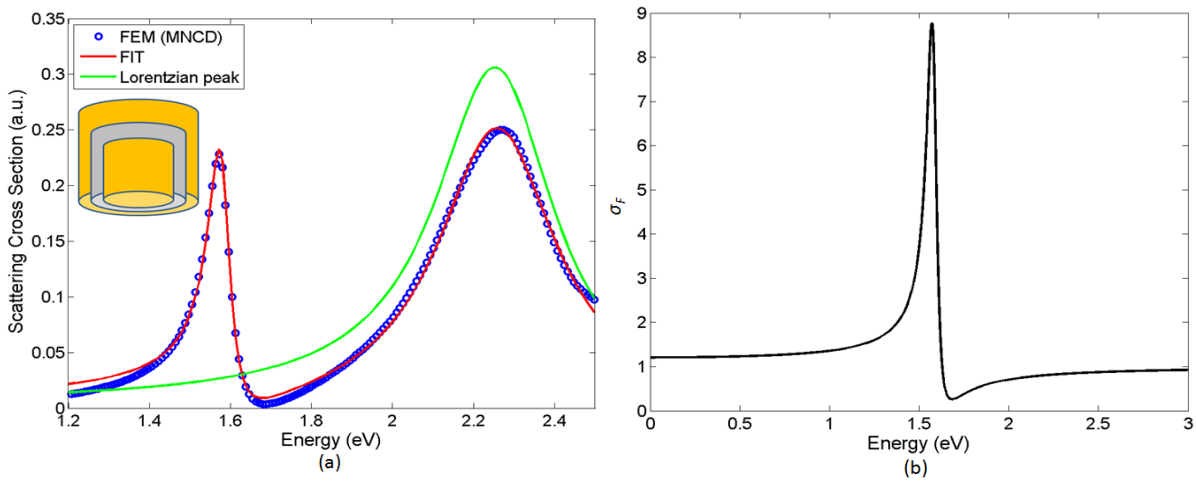

Figure 7. 8. (a) Scattering spectra of MNCD nanostructure. Blue circles: numerical simulation (FEM) and red solid line: fit with equation (7.6). Green line represents the Lorentzian peak obtained from equation (7.4). (b) Asymmetric line shape acquired directly from equation (7.5).

Figure 7.9 shows the scattering spectra of a concentric MNC having dimensions 40,50/55,65/85,95 nm. The scattering spectra shows a good agrement by fitted with equation (7.6) as shown in figure 7.9(a). The fit parameters obtained are a = 0.557, ω_L = 2.031 eV, W_L = 0.153eV, ω_F = 1.509 eV, W_F = 0.036 eV, q = -1.718 and b = 2.970. The green line shows the line shape of the bright mode obtained using equation (7.4). Figure 7.9(b) shows the asymmetric line shape obtained using equation (7.5). In figure 7.9(c), we considered the same geometry but with different dimensions i.e., 30,40/60,70/85,95 nm. The scattering spectra is fitted with equation (7.6). The fit parameters obtained are a = 0.706, ω_L = 1.686 eV, W_L =

0.086 eV, ω_F = 2.068 eV, W_F = 0.084 eV, q = 1.260 and b = 1.045. Here both the inner core and middle silica layer have been changed due to which the dark mode blue-shifts and the resonant frequency of asymmetric line shape is shifted from 1.509 to 2.068 eV. The phase of the bright mode is also switched and the sign of q flips from -1.718 to 1.260. Figure 7.9(d) represents the q, where the sign has been changed by varying the dimensions of MNC. Thus, we can flip the asymmetry parameter by changing the dimensions of the nanoparticle.

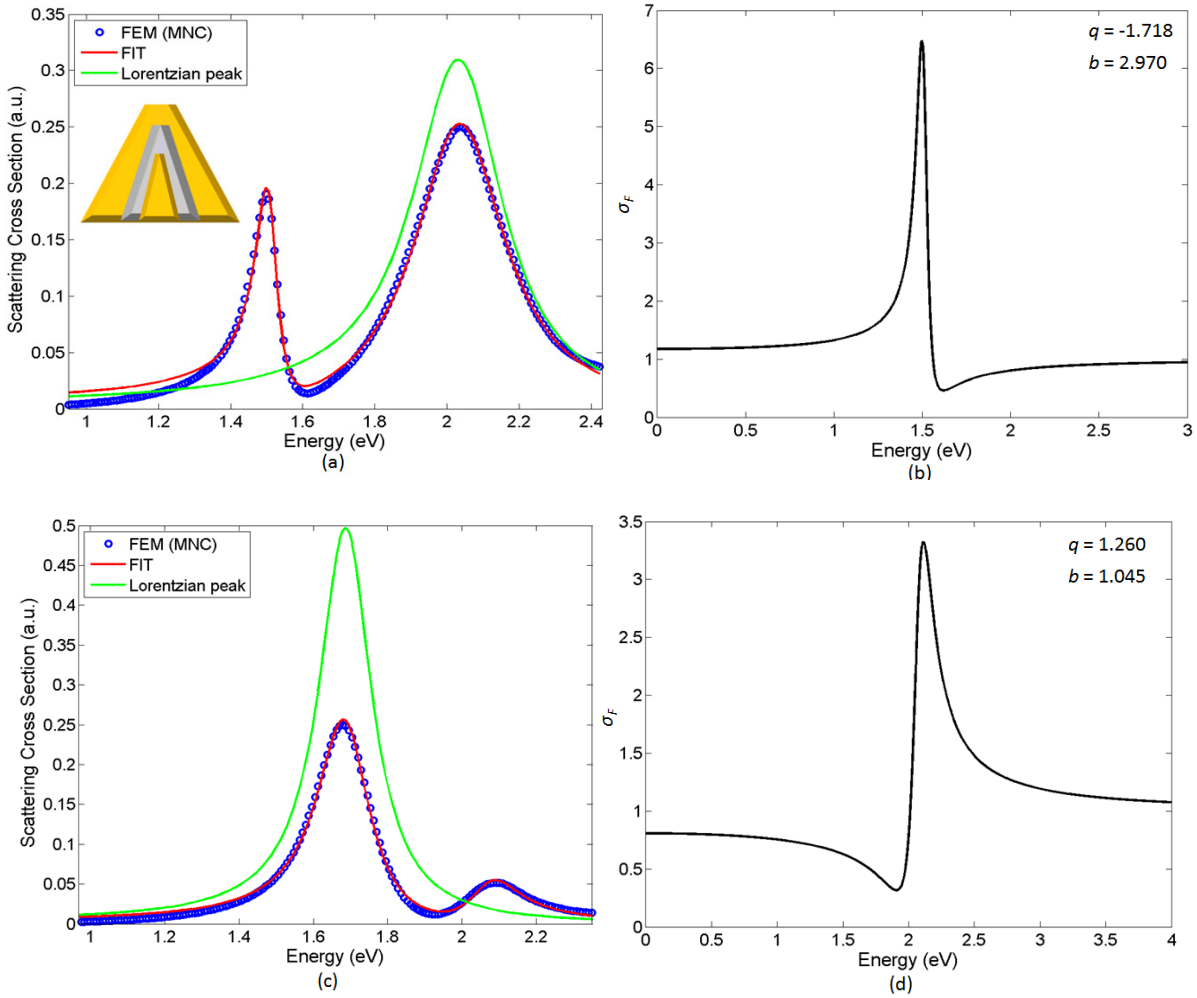

Figure 7. 9. Some typical fits of the scattering spectra of MNC using equation (7.6). (a) Shows a case, where the energy position of the dipolar bonding mode is lower than the position of the broad dipolar antibonding mode while in (c) the opposite is true. The calculated (FEM) and fitted curves are shown in blue circles and red line, respectively and the contribution of the Lorentzian peak was graphed using a green line. The obtained asymmetric Fano line shapes are represented in (b) and (d) using equation (7.5).

The progress in asymmetry parameter q, damping b, spectral positions and line widths of both the dark and bright modes with the variation of inner metallic cone's radius and height in MNC nanostructure are shown in figure 7.10. The absolute value of the q increases by increasing R_1 and then flip its sign from positive to negative by further increasing R_1, Figure 7.10(a). Here the spectral position of the dark mode surpasses the value of the bright mode. The modulation damping parameter shows almost a constant value between R_1 = 20 to 30 nm and then increases rapidly. At R_1 = 45 nm, the value of b droped sharply as shown in figure 7.10(b). Both the b and q are the shape parameters. By changing one of the parameter will change the total shape of the asymmetric resonance [22, 39, 41]. Figure 7.10(c) shows the spectral positions of both the bright and dark modes for various values of R_1. When R_1

increases from 20 to 30 nm, the spectral positions of both the bright and dark modes are almost the same. By further increases R_1, the asymmetric resonance strongly blue-shift. The bright mode's phase is also reversed. The energy shift in the asymmetric resonance is observed to be very large compared to its symmetric counterpart by varying R_1. Figure 7.10(d) shows the widths of both bright and dark modes. The width of the dark mode increases and then decreases sharply by increasing R_1. While the bright mode's width gets broadened with the increase in R_1.

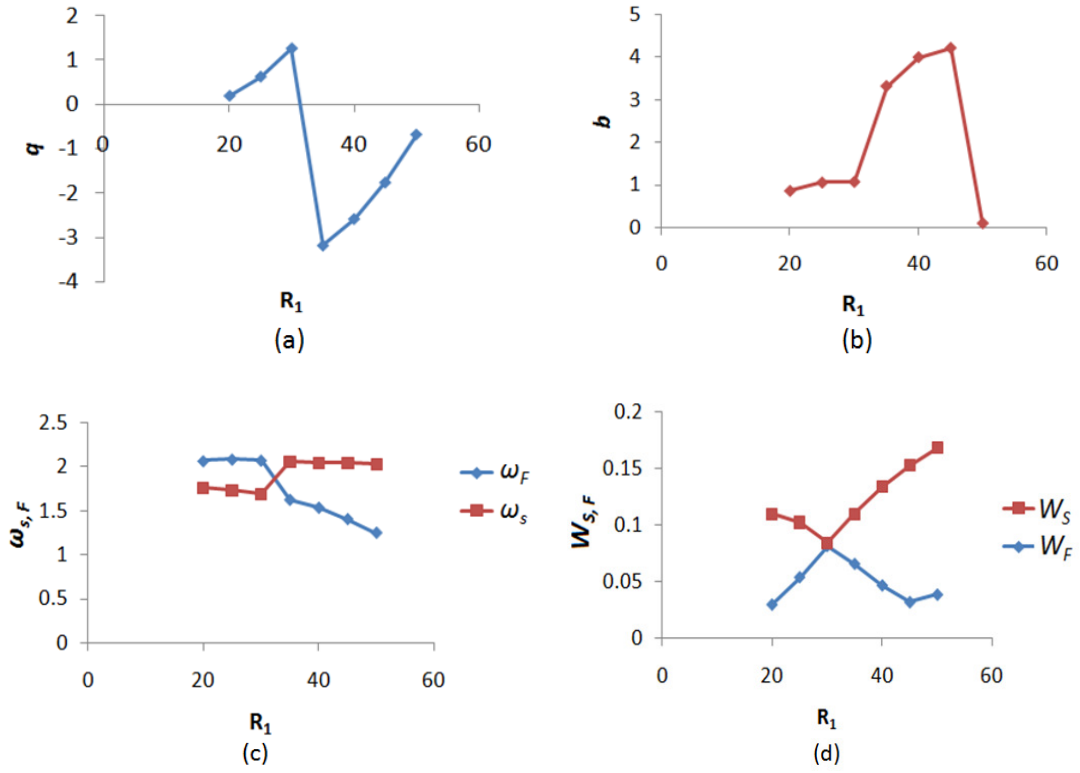

Figure 7. 10. (a) Asymmetry parameter (b) Damping (c) Spectral position and (d) Width of the symmetric and asymmetric resonances, obtained from the fits, as a function of R_1 for all the analyzed cases.

Figure 7.11 shows the scattering spectra of a concentric MNC by rotating the structure 90° around *y*-axis having dimensions 40,50/60,70/85,95 nm. Here the incident light is polarized along the nanoparticle axis and we obtained three scattering peaks and twin dipole-dipole Fano resonances in the spectrum. To verify our analysis, we used equation (7.6) to fit the scattering spectra of MNC and a very good agreement has been obtained. Since we have three peaks in the spectrum, so another asymmetric term has been added to equation (7.6) because here the bright dipolar mode is modulated by two Fano-like resonances. The fit parameters achieved are $a = 0.522$, $\omega_L = 2.150$ eV, $W_L = 0.173$ eV, $\omega_{F(1)} = 1.513$ eV, $W_{F(1)} = 0.045$ eV, $q_{(1)} = 0.264$, $b_{(1)} = 2.011$, $\omega_{F(2)} = 1.881$ eV, $W_{F(2)} = 0.041$ eV, $q_{(2)} = -0.406$ and $b_{(2)} = 0.979$. Unlike all the previous examples, the sign of the first asymmetry parameter observed here is positive although the asymmetric resonance is located on the lower energy shoulder of the symmetric resonance. However, the second asymmetry parameter has the similar negative sign like in the previous examples. Figure 7.11(b) shows the line shapes of both the asymmetric resonances with different signs of *q*. To our knowledge, this kind of simultaneous sign reversal occuring in a concentric nanostructure has never been reported before. This type of nanostructure, where dual dipole-dipole Fano resonances are observed, shows advantage over asymmetric nanostructures, as they are simple to synthesize and can be utilized in a broad range of technological applications.

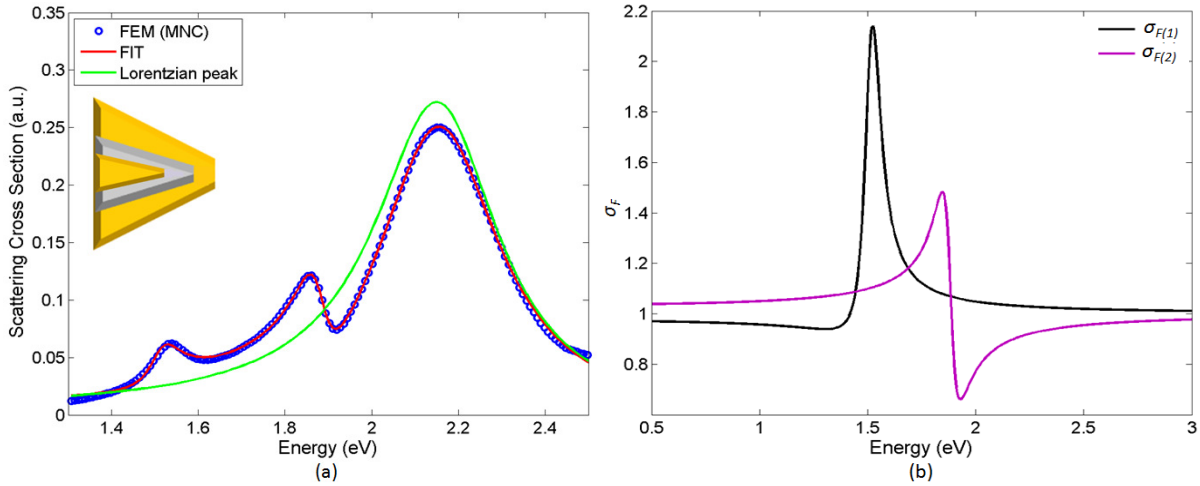

Figure 7. 11. (a) Scattering spectra of MNC nanostructure at θ = 90°. Blue circles: numerical simulation (FEM) and red solid line: fit with equation (7.6). Green line represents the Lorentzian peak obtained from equation (7.4). (b) Asymmetric line shapes acquired directly from equation (7.5).

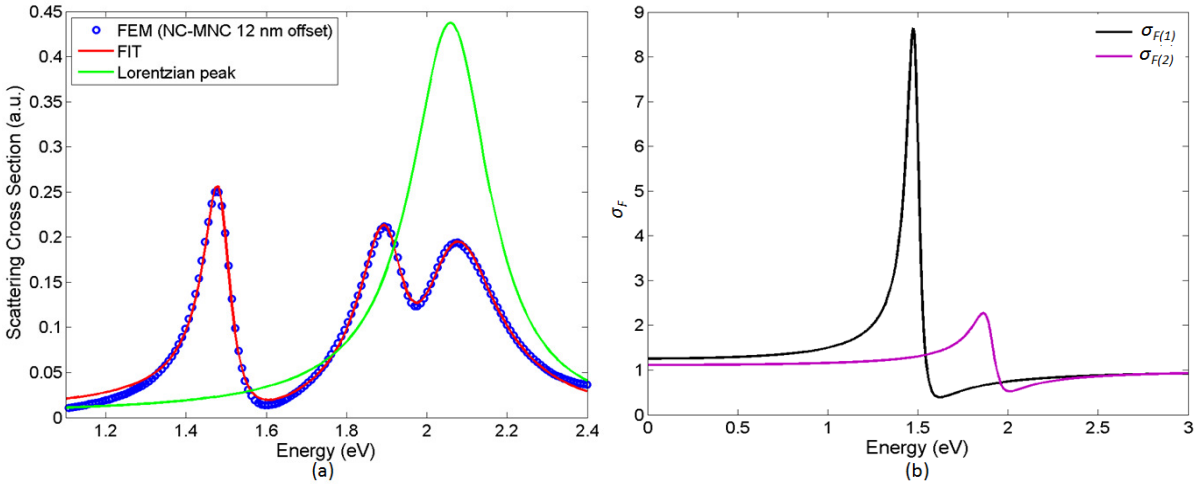

Figure 7. 12. (a) Scattering spectra of NC-MNC nanostructure with 12 nm core offset. Blue circles: numerical simulation (FEM) and red solid line: fit with equation (7.6). Green line represents the Lorentzian peak obtained from equation (7.4). (b) Asymmetric line shapes acquired directly from equation (7.5).

We also validated the analytical expressions of Lorentzian and Fano line shapes to a symmetry broken nanostructures. The nanostructure we chose is MNC having dimensions 40,50/60,70/85,95 nm. In order to break the symmetry of the structure, we offset the inner core 12 nm in the *y*-direction to make a NC-MNC. The scattering spectrum of NC-MNC is demonstrated in figure 7.12(a) where we obtained dipole and quadrupole Fano resonances at the lower-energy side. We used equation (7.6) by adding another asymmetric term and fitted with the scattering spectra of NC-MNC. Here the Lorentzian shape represents the bright dipolar mode while the first Fano shape represents the interference between the bright and dark dipolar modes and the second Fano shape represents the interference between bright dipolar mode and dark quadrupolar mode. A very good agreement has been obtained. The fit parameters achieved are a = 0.661, ω_L = 2.059eV, W_L = 0.118 eV, $\omega_{F(1)}$ = 1.486 eV, $W_{F(1)}$ = 0.041 eV, $q_{(1)}$ = -2.161, $b_{(1)}$ = 3.368, $\omega_{F(2)}$ = 1.904 eV, $W_{F(2)}$ = 0.067 eV, $q_{(2)}$ = -0.779 and $b_{(2)}$ = 1.185. Since both the asymmetric resonances are located at the left energy shoulder of the symmetric resonance, so the signs of q obtained are negative. The green line represents the

Lorentzian line shape extracted from equation (7.4). Figure 7.12(b) shows the asymmetric line shapes by using both the values of q.

We next move the inner cone further more (18 nm) in MNC nanostructure due to which an octupole Fano resonance is also come into view at the lower-energy side in the scattering spectrum as shown in figure 7.13(a). Two asymmetric terms have been added to equation (7.6) and fitted with the scattering spectrum of NC-MNC. Here the bright dipolar mode is modulated by the three Fano-like resonances. The fit parameters obtained are a = 0.586, ω_L = 2.064 eV, W_L = 0.141 eV, $\omega_{F(1)}$ = 1.330 eV, $W_{F(1)}$ = 0.025 eV, $q_{(1)}$ = -0.900, $b_{(1)}$ = 2.037, $\omega_{F(2)}$ = 1.675 eV, $W_{F(2)}$ = 0.052 eV, $q_{(2)}$ = -1.316 and $b_{(2)}$ = 1.562, $\omega_{F(3)}$ = 1.845 eV, $W_{F(3)}$ = 0.052 eV, $q_{(3)}$ = -0.706 and $b_{(3)}$ = 4.280. All the values of q are observed to be negative as expected because all the asymmetric resonances are located at the lower-energy shoulder of the symmetric resonance. The green line represents the Lorentzian line shape extracted from equation (7.4). Figure 7.13(b) shows the asymmetric line shapes which are obtained by using the numerical values of the parameters.

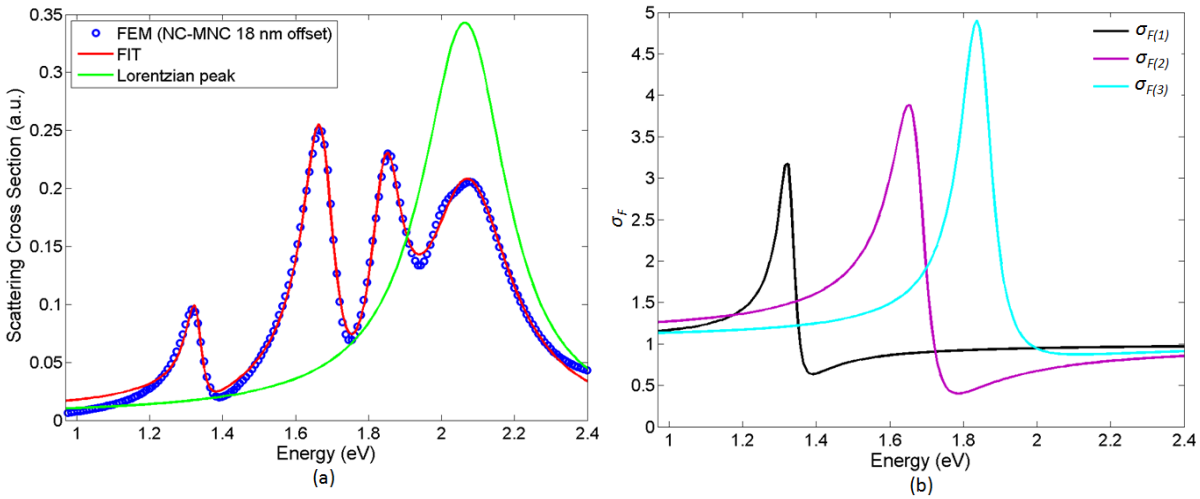

Figure 7. 13. (a) Scattering spectra of NC-MNC nanostructure with 18 nm core offset. Blue circles: numerical simulation (FEM) and red solid line: fit with equation (7.6). Green line represents the Lorentzian peak obtained from equation (7.4). (b) Asymmetric line shapes acquired directly from equation (7.5).

The analytical expressions of Lorentzian and Fano asymmetric line shapes based on Maxwell's equations enables the control of the line shape of plasmonic nanostructures and such nanostructures can be designed with specific spectral responses for applications like sensing, PIT and switching [41].

7.4. Conclusion remarks

In this chapter, the observation of higher order Fano resonances in plasmonic nanostructures are explained by a mass-spring coupled oscillator analogy and analytical expressions of Lorentzian and Fano asymmetric line shapes based on Maxwell's equations. The oscillator model presents a straight forward mechanical analogy to the coupling perceived in plasmonic nanostructure. However, it demands many masses to correctly fit for higher order modes of the nanoscale systems. The analytical expressions based on Maxwell's equations clearly describe the existence of Fano resonances in plasmonic nanostructures. The spectral position of the asymmetric resonance is obtained by the subradiant dark mode's frequency and perturbed by its coupling to the superradiant bright mode. The coupling of modes also provides the width of the asymmetric resonance. The analytical expressions

enables the control of the line shape of plasmonic nanostructures and such nanostructures can be designed for specific applications like sensing, PIT and switching.

Chapter 8

Summary

The work presented in this thesis provides a deeper understanding of the interactions between plasmon modes of neighboring metallic nanoparticles. We started our study from a multilayered spherical nanostructures and examined the fundamental properties of Fano resonances. Different kinds of new symmetry breaking schemes have been introduced to generate higher order Fano resonances. Two types of nanostructures have been investigated; a multilayered nanoshell and double nanoshells. Both the structures were established to offer distinct Fano resonances. The double nanoshell showed a better tunability of the resonant modes due to which it may be a good option for biomedical applications. However, the multilayered nanostructure provide multiple Fano resonances with comparitively large modulation depth, which can be used for plasmon line shaping and multi-wavelength SERS.

The effect of Fano resonances have also been investigated in the multi-component structure based on nanocones, which is proved to provide multiple Fano resonances with large modulation depths. Such nanostructure is also observed to be highly dependent upon the polarization of incident light due to which a set of unique Fano resonances have been achieved. The modulation depths of one or more of the multiple Fano resonances examined in spherical nanostructures are observed to be weak, which is a disadvantage for plasmon line shaping. However, the multilayered nanocone structure is found to exhibit prominent tunable Fano resonances with large modulation depths due to which it is highly suitable for plasmon line shaping by modifying the plasmon lines at variuos spectral locations simultaneously.

The idea of multilayered coated nanostructures have been extended to cubic, elliptical and cylindrical nanostructures with multi-components. These nanostructures exhibit the similar bright and dark modes and Fano resonances due to which, we end up with a conclusion that this trend is very general in bimetallic coated nanostructures. Among these nanostructures, the multilayered nanocylinder was verified to be greatly dependent upon the incident field polarization like the multilayered nanocone. A comparison of multilayered conical and cylindrical resonators has also been examined for the symmetric case, which proved that the conical resonator has the potential to provide multiple Fano resonances with large modulation depth even in the concentric case.

Plasmonic Fano like resonances have also been analyzed in a single conical nanoshell structure, which contains only a single metal piece. Such nanostructure also offers dimensional angularly selectivity of the plasmonic properties like the nanocups and gold nanoshell with holes but it has an advantage to exhibit Fano resonance in the spectrum, which can be used for additional applications like PIT and switching. The asymmetric single conical Fano resonator is found to be highly capable in the generation of higher order Fano resonances, which may be suitable for plasmon line shaping and SERS. The spectral sensitivity of asymmetric conical Fano resonator to the surrounding medium is also studied and high values of figure of merit and contrast ratio are observed, which shows the performance of Fano resonator as a biological sensor.

We also report the effect of Fano resonances in the polarization dependent dimer nanostructure based on gold nanocones. Several configuration of the conical nanodimer have been demonstrated, which suggest that the plasmon coupling in the dimer is not only

dependent on the interparticle distance and size of the nanoparticles but also on the spatial arrangement of the two components. The tunable strong Fano-like resonance in the dimer resonator can be useful for PIT and the local near fields in the “hot spots” are essential for the near field applications.

Eventually, the optical responses of different Fano resonators were successfully replicated through the mass-spring coupled oscillator analogy and the analytical model of Fano and Lorentzian line shapes developed by Gallinet and Martin. These analysis make the existence and understanding of Fano resonances easier in complex plasmonic nanostructures. The results obtained in this thesis open up the advantageous possibility of using the Fano resonance band for plasmon line shaping, PIT, switching and SERS applications.

References

1. Luk'yanchuk, B., et al., *The Fano resonance in plasmonic nanostructures and metamaterials.* Nature materials, 2010. **9**(9): p. 707-715.
2. Fano, U., *On the absorption spectrum of noble gases at the arc spectrum limit.* arXiv preprint cond-mat/0502210, 2005.
3. Fano, U., *Effects of configuration interaction on intensities and phase shifts.* Physical Review, 1961. **124**(6): p. 1866-1878.
4. Vittorini-Orgeas, A. and A. Bianconi, *From Majorana theory of atomic autoionization to Feshbach resonances in high temperature superconductors.* Journal of superconductivity and novel magnetism, 2009. **22**(3): p. 215-221.
5. Hessel, A. and A. Oliner, *A new theory of Wood's anomalies on optical gratings.* Appl. Opt, 1965. **4**(10): p. 1275-1297.
6. Landa, P.S., *Nonlinear oscillations and waves in dynamical systems*. Vol. 360. 1996: Springer.
7. Ueda, A. and M. Eto, *Resonant tunneling and Fano resonance in quantum dots with electron-phonon interaction.* Physical Review B, 2006. **73**(23): p. 235353.
8. Kobayashi, K., et al., *Fano resonance in a quantum wire with a side-coupled quantum dot.* Physical Review B, 2004. **70**(3): p. 035319.
9. Tang, T.T., et al., *A tunable phonon–exciton Fano system in bilayer graphene.* Nature nanotechnology, 2009. **5**(1): p. 32-36.
10. Miroshnichenko, A.E., S. Flach, and Y.S. Kivshar, *Fano resonances in nanoscale structures.* Reviews of Modern Physics, 2010. **82**(3): p. 2257.
11. Kelly, K.L., et al., *The optical properties of metal nanoparticles: the influence of size, shape, and dielectric environment.* The Journal of Physical Chemistry B, 2003. **107**(3): p. 668-677.
12. Lal, S., S. Link, and N.J. Halas, *Nano-optics from sensing to waveguiding.* Nature photonics, 2007. **1**(11): p. 641-648.
13. Giannini, V., et al., *Fano resonances in nanoscale plasmonic systems: a parameter-free modeling approach.* Nano letters, 2011. **11**(7): p. 2835-2840.
14. Chen, J., et al., *Plasmonic EIT-like switching in bright-dark-bright plasmon resonators.* Optics express, 2011. **19**(7): p. 5970-5978.
15. Lu, Y., et al., *Plasmonic electromagnetically-induced transparency in symmetric structures.* Optics express, 2010. **18**(13): p. 13396-13401.
16. Fang, Z., et al., *Removing a Wedge from a Metallic Nanodisk Reveals a Fano Resonance.* Nano letters, 2011. **11**(10): p. 2694-2701.
17. Chen, H., et al., *Observation of the Fano Resonance in Gold Nanorods Supported on High-Dielectric-Constant Substrates.* Acs Nano, 2011. **5**(8): p. 6754-6763.
18. Yang, Z.J., et al., *Fano resonances in active plasmonic resonators consisting of a nanorod dimer and a nano-emitter.* Applied Physics Letters, 2011. **99**(8): p. 081107-081107-3.
19. Yang, Z.J., et al., *Fano resonances in dipole-quadrupole plasmon coupling nanorod dimers.* Optics letters, 2011. **36**(9): p. 1542-1544.
20. Lopez-Tejeira, F., R. Paniagua-Dominguez, and J.A. Sanchez-Gil, *High Performance Nanosensors Based on Plasmonic Fano-Like Interference: Probing Refractive Index with Individual Nanorice and Nanobelts.* Acs Nano, 2012. **6**(10): p. 8989–8996.
21. Wei, H., et al., *Multipolar plasmon resonances in individual Ag nanorice.* Acs Nano, 2010. **4**(5): p. 2649-2654.

22. Peña-Rodríguez, O., et al., *Tunable Fano resonance in symmetric multilayered gold nanoshells.* Nanoscale, 2013. **5**(1): p. 209-216.
23. Bardhan, R., et al., *Nanosphere-in-a-Nanoshell: A Simple Nanomatryushka†.* The Journal of Physical Chemistry C, 2009. **114**(16): p. 7378-7383.
24. Ho, J.F., B. Luk'yanchuk, and J.B. Zhang, *Tunable Fano resonances in silver–silica–silver multilayer nanoshells.* Applied Physics A: Materials Science & Processing, 2012. **107**(1): p. 133-137.
25. Knight, M.W. and N.J. Halas, *Nanoshells to nanoeggs to nanocups: optical properties of reduced symmetry core–shell nanoparticles beyond the quasistatic limit.* New Journal of Physics, 2008. **10**: p. 105006.
26. Lassiter, J.B., et al., *Close encounters between two nanoshells.* Nano letters, 2008. **8**(4): p. 1212-1218.
27. Mukherjee, S., et al., *Fanoshells: nanoparticles with built-in Fano resonances.* Nano letters, 2010. **10**(7): p. 2694-2701.
28. Qian, J., et al., *Optical extinction properties of perforated gold-silica-gold multilayer nanoshells.* The Journal of Physical Chemistry C, 2012. **116**(18): p. 10349-10355.
29. Wu, D.J., S.M. Jiang, and X.J. Liu, *Tunable Fano resonances in three-layered bimetallic Au and Ag nanoshell.* The Journal of Physical Chemistry C, 2011. **115**(48): p. 23797-23801.
30. Cetin, A.E. and H. Altug, *Fano resonant ring/disk plasmonic nanocavities on conducting substrates for advanced biosensing.* Acs Nano, 2012. **6**(11): p. 9989-9995.
31. Fu, Y.H., et al., *Generating and Manipulating Higher Order Fano Resonances in Dual-Disk Ring Plasmonic Nanostructures.* Acs Nano, 2012. **6**(6): p. 5130-5137.
32. Habteyes, T.G., et al., *Theta-shaped plasmonic nanostructures: Bringing "dark" multipole plasmon resonances into action via conductive coupling.* Nano letters, 2011. **11**(4): p. 1819-1825.
33. Hao, F., et al., *Tunability of subradiant dipolar and fano-type plasmon resonances in metallic ring/disk cavities: implications for nanoscale optical sensing.* Acs Nano, 2009. **3**(3): p. 643-652.
34. Niu, L., et al., *Fano resonance in dual-disk ring plasmonic nanostructures.* Optics express, 2011. **19**(23): p. 22974-22981.
35. Sonnefraud, Y., et al., *Experimental realization of subradiant, superradiant, and Fano resonances in ring/disk plasmonic nanocavities.* Acs Nano, 2010. **4**(3): p. 1664-1670.
36. Verellen, N., et al., *Plasmon line shaping using nanocrosses for high sensitivity localized surface plasmon resonance sensing.* Nano letters, 2011. **11**(2): p. 391-397.
37. Verellen, N., et al., *Dark and bright localized surface plasmons in nanocrosses.* Optics express, 2011. **19**(12): p. 11034-11051.
38. Jian, Y. and V.D. Pol, *Nanocrosses with Highly Tunable Double Resonances for Near-Infrared Surface-Enhanced Raman Scattering.* International Journal of Optics, 2012. **2012**.
39. Gallinet, B. and O.J.F. Martin, *Relation between near–field and far–field properties of plasmonic Fano resonances.* Opt. Express, 2011. **19**(22): p. 22167-22175.
40. Zhang, J., et al., *Electromagnetically induced transparency in metamaterials at near-infrared frequency.* Optics express, 2010. **18**(16): p. 17187-17192.
41. Gallinet, B. and O.J.F. Martin, *Influence of electromagnetic interactions on the line shape of plasmonic Fano resonances.* Acs Nano, 2011. **5**(11): p. 8999-9008.
42. Verellen, N., et al., *Fano resonances in individual coherent plasmonic nanocavities.* Nano letters, 2009. **9**(4): p. 1663-1667.

43. Shao, L., et al., *Distinct Plasmonic Manifestation on Gold Nanorods Induced by the Spatial Perturbation of Small Gold Nanospheres.* Nano letters, 2012. **12**(3): p. 1424-1430.
44. Brown, L.V., et al., *Heterodimers: plasmonic properties of mismatched nanoparticle pairs.* Acs Nano, 2010. **4**(2): p. 819-832.
45. Banaee, M.G. and K.B. Crozier, *Mixed dimer double-resonance substrates for surface-enhanced Raman spectroscopy.* Acs Nano, 2010. **5**(1): p. 307-314.
46. Wu, D.J., et al., *Fano-like resonance in symmetry-broken gold nanotube dimer.* Optics express, 2012. **20**(24): p. 26559-26567.
47. Wu, D.J., S.M. Jiang, and X.J. Liu, *Fano-Like Resonances in Asymmetric Homodimer of Gold Elliptical Nanowires.* The Journal of Physical Chemistry C, 2012. **116**(25): p. 13745-13748.
48. Liu, H., et al., *Fano resonance in two-intersecting nanorings: Multiple layers of plasmon hybridizations.* Applied Physics Letters, 2012. **100**(15): p. 153114-153114-4.
49. Sheikholeslami, S., A. García-Etxarri, and J.A. Dionne, *Controlling the interplay of electric and magnetic modes via Fano-like plasmon resonances.* Nano letters, 2011. **11**(9): p. 2694-2701.
50. Klimov, V. and G.Y. Guo, *Bright and dark plasmon modes in three nanocylinder cluster.* J. Phys. Chem. C, 2010. **114**: p. 22398-22405.
51. Fan, J.A., et al., *Fano-like interference in self-assembled plasmonic quadrumer clusters.* Nano letters, 2010. **10**(11): p. 4680–4685.
52. Rahmani, M., et al., *Influence of plasmon destructive interferences on optical properties of gold planar quadrumers.* Nanotechnology, 2011. **22**(24): p. 245204.
53. Rahmani, M., et al., *Generation of pronounced Fano resonances and tuning of subwavelength spatial light distribution in plasmonic pentamers.* Opt. Express19 (6), 2011. **19**(6): p. 4949-4956.
54. Liu, S.D., et al., *Multiple Fano Resonances in Plasmonic Heptamer Clusters Composed of Split Nanorings.* Acs Nano, 2012. **6**(7): p. 6260-6271.
55. Wang, M., et al., *Subradiant Plasmon Modes in Multilayer Metal-dielectric Nanoshells.* The Journal of Physical Chemistry C, 2011. **115**(43): p. 20920-20925.
56. Chang, W.S., et al., *A Plasmonic Fano Switch.* Nano letters, 2012. **12**(9): p. 4977–4982.
57. Mirin, N.A., et al., *Perforated semishells: far-field directional control and optical frequency magnetic response.* Acs Nano, 2010. **4**(5): p. 2701-2712.
58. Talebi, N., et al., *Breaking the Mode Degeneracy of Surface-Plasmon Resonances in a Triangular System.* arXiv preprint arXiv:1202.5876, 2012.
59. McMahon, J.M., et al., *Correlating the structure, optical spectra, and electrodynamics of single silver nanocubes.* The Journal of Physical Chemistry C, 2009. **113**(7): p. 2731-2735.
60. Brongersma, M.L. and P.G. Kik, *Surface plasmon nanophotonics*. Vol. 131. 2007: Springer Dordrecht, The Netherlands.
61. Prodan, E., et al., *A hybridization model for the plasmon response of complex nanostructures.* Science, 2003. **302**(5644): p. 419-422.
62. Reed, J.M., et al., *Shape of Fano resonance line spectra calculated for silver nanorods.* Optics letters, 2011. **36**(22): p. 4386-4388.
63. Zhang, S., et al., *Substrate-induced Fano resonances of a plasmonic nanocube: a route to increased-sensitivity localized surface plasmon resonance sensors revealed.* Nano letters, 2011. **11**(4): p. 1657-1663.
64. Liu, N., et al., *Planar metamaterial analogue of electromagnetically induced transparency for plasmonic sensing.* Nano letters, 2009. **10**(4): p. 1103-1107.

65. Liu, N., et al., *Plasmonic analogue of electromagnetically induced transparency at the Drude damping limit.* Nature materials, 2009. **8**(9): p. 758-762.
66. Zhang, S., et al., *Plasmon-induced transparency in metamaterials.* Physical review letters, 2008. **101**(4): p. 47401.
67. Pryce, I.M., et al., *Highly strained compliant optical metamaterials with large frequency tunability.* Nano Lett, 2010. **10**(10): p. 4222-4227.
68. Gallinet, B. and O.J.F. Martin, *Ab initio theory of Fano resonances in plasmonic nanostructures and metamaterials.* Physical Review B, 2011. **83**(23): p. 235427.
69. Xu, H., et al., *Effects of symmetry breaking on plasmon resonance in a noncoaxial nanotube and nanotube dimer.* JOSA A, 2011. **28**(8): p. 1662-1667.
70. Pena-Rodriguez, O., et al., *Enhanced Fano resonance in asymmetrical Au: Ag heterodimers.* The Journal of Physical Chemistry C, 2011. **115**(14): p. 6410-6414.
71. Zhang, Y., et al., *Fano resonances in disk–ring plasmonic nanostructure: strong interaction between bright dipolar and dark multipolar mode.* Optics letters, 2012. **37**(23): p. 4919-4921.
72. Cui, X. and D. Erni, *The influence of particle shapes on the optical response of nearly touching plasmonic nanoparticle dimers.* Journal of Computational and Theoretical Nanoscience, 2010. **7**(8): p. 1610-1615.
73. Yun, B., et al., *Theoretical studies on the near field properties of non-concentric core–shell nanoparticle dimers.* Optics Communications, 2010. **283**(14): p. 2947-2952.
74. Tsai, C.Y., et al., *Plasmonic Coupling in Gold Nanoring Dimers: Observation of Coupled Bonding Mode.* Nano letters, 2012. **12**(3): p. 1648-1654.
75. Liusman, C., et al., *Surface-Enhanced Raman Scattering of Ag–Au Nanodisk Heterodimers.* The Journal of Physical Chemistry C, 2012. **116**(18): p. 10390-10395.
76. Slaughter, L.S., et al., *Effects of symmetry breaking and conductive contact on the plasmon coupling in gold nanorod dimers.* Acs Nano, 2010. **4**(8): p. 4657-4666.
77. Grillet, N., et al., *Plasmon coupling in silver nanocube dimers: resonance splitting induced by edge rounding.* Acs Nano, 2011. **5**(12): p. 9450-9462.
78. Mirin, N.A., K. Bao, and P. Nordlander, *Fano Resonances in Plasmonic Nanoparticle Aggregates†.* The Journal of Physical Chemistry A, 2009. **113**(16): p. 4028-4034.
79. Bao, K., N.A. Mirin, and P. Nordlander, *Fano resonances in planar silver nanosphere clusters.* Applied Physics A: Materials Science & Processing, 2010. **100**(2): p. 333-339.
80. Rahmani, M., et al., *Influence of symmetry breaking in pentamers on Fano resonance and near-field energy localization.* Optical Materials Express, 2011. **1**(8): p. 1409-1415.
81. Miroshnichenko, A.E. and Y.S. Kivshar, *Fano resonances in all-dielectric oligomers.* Nano letters, 2012. **12**(12): p. 6459-6463.
82. Sancho-Parramon, J. and S. Bosch, *Dark Modes and Fano Resonances in Plasmonic Clusters Excited by Cylindrical Vector Beams.* Acs Nano, 2012. **6**(9): p. 8415–8423.
83. Lassiter, J.B., et al., *Designing and deconstructing the Fano lineshape in plasmonic nanoclusters.* Nano letters, 2012. **12**(2): p. 1058-1062.
84. Cui, Y., et al., *Dynamic Tuning and Symmetry Lowering of Fano Resonance in Plasmonic Nanostructure.* Acs Nano, 2012. **6**(3): p. 2385-2393.
85. Woo, K.C., et al., *Universal scaling and Fano resonance in the plasmon coupling between gold nanorods.* Acs Nano, 2011. **5**(7): p. 5976-5986.
86. Dregely, D., M. Hentschel, and H. Giessen, *Excitation and tuning of higher-order Fano resonances in plasmonic oligomer clusters.* Acs Nano, 2011. **5**(10): p. 8202-8211.

87. Jiao, J. and Z. Wang, *Fano-chain: the Fano resonances in a nanoparticles chain.* 2012. **59**(16): p. 1434-1438.
88. Large, N., et al., *Plasmonic properties of gold ring-disk nano-resonators: fine shape details matter.* Optics express, 2011. **19**(6): p. 5587-5595.
89. Cetin, A.E. and H. Altug, *Fano-Resonant Ring/Disk Plasmonic Nanocavities on Conducting Substrates for Advanced Biosensing.* Acs Nano, 2012. **6**(11): p. 9989–9995.
90. Zhang, Y., et al., *Dipole, quadrupole and octupole plasmon resonance modes in non-concentric nanocrescent/nanodisk structure: local field enhancement in the visible and near infrared regions.* Optics express, 2012. **20**(3): p. 2924-2931.
91. Hao, F., et al., *Symmetry breaking in plasmonic nanocavities: subradiant LSPR sensing and a tunable Fano resonance.* Nano letters, 2008. **8**(11): p. 3983-3988.
92. Peña-Rodríguez, O. and U. Pal, *Geometrical Tunability of Linear Optical Response of Silica− Gold Double Concentric Nanoshells.* The Journal of Physical Chemistry C, 2010. **114**(10): p. 4414-4417.
93. Zhu, J., Y. Ren, and S. Zhao, *Refractive index sensitivity of gold double concentric nanoshells: Tuning the intensity discrepancy of two-band plasmonic absorption.* Sensors and Actuators B: Chemical, 2011. **161**(1): p. 1129–1134.
94. Khosravi, H., N. Daneshfar, and A. Bahari, *Theoretical study of the light scattering from two alternating concentric double silica-gold nanoshell.* Physics of Plasmas, 2010. **17**(5): p. 053302.
95. Weng, G., J. Li, and J. Zhao, *Biosensing potential of three-layered gold–dielectric–gold nanoshells: Sensitivity of inter distance of resonance light scattering peaks to the local dielectric environment.* Physica E: Low-dimensional Systems and Nanostructures, 2012. **44**(10): p. 2072–2077.
96. Peña-Rodríguez, O. and U. Pal, *Enhanced plasmonic behavior of bimetallic (Ag-Au) multilayered spheres.* Nanoscale research letters, 2011. **6**(1): p. 1-5.
97. Liu, C., C. Mi, and B. Li, *The Plasmon Resonances of Multilayered Gold Nanoshells and Their Potential Bio-applications.* Nanotechnology, IEEE Transactions on, 2011. **10**(99): p. 797-805.
98. Hu, Y., S.J. Noelck, and R.A. Drezek, *Symmetry Breaking in Gold− Silica− Gold Multilayer Nanoshells.* Acs Nano, 2010. **4**(3): p. 1521-1528.
99. Hu, Y., R.C. Fleming, and R.A. Drezek, *Optical properties of gold-silica-gold multilayer nanoshells.* Optics express, 2008. **16**(24): p. 19579-19591.
100. Wu, D., et al., *Modulation of anisotropic middle layer on the plasmon couplings in sandwiched gold nanoshells.* Gold Bulletin, 2012. **45**(4): p. 197-201.
101. Zhu, J., J.J. Li, and J.W. Zhao, *Frequency-Dependent Polarization Properties of Local Electric Field in Gold–Dielectric Multi-Nanoshells.* Plasmonics, 2012: p. 1-8.
102. Zhu, J., et al., *The effect of inserted gold nanosphere on the local field enhancement of gold nanoshell.* Materials Chemistry and Physics, 2012. **133**(2–3): p. 1060–1065.
103. Khlebtsov, B.N. and N.G. Khlebtsov, *Biosensing potential of silica/gold nanoshells: Sensitivity of plasmon resonance to the local dielectric environment.* Journal of Quantitative Spectroscopy and Radiative Transfer, 2007. **106**(1): p. 154-169.
104. Chen, Y., et al., *The Study of Surface Plasmon in Au/Ag Core/Shell Compound Nanoparticles.* Plasmonics, 2012: p. 1-5.
105. Xia, X., et al., *Engineering sub-100 nm multi-layer nanoshells.* Nanotechnology, 2006. **17**(21): p. 5435.
106. Ariga, K., et al., *Layer-by-layer self-assembled shells for drug delivery.* Advanced drug delivery reviews, 2011. **63**(9): p. 762-771.

107. Wu, D.J., S.M. Jiang, and X.J. Liu, *A tunable Fano resonance in silver nanoshell with a spherically anisotropic core.* The Journal of Chemical Physics, 2012. **136**(3): p. 034502.
108. Chen, H., et al., *Fano Resonance in (Gold Core)−(Dielectric Shell) Nanostructures without Symmetry Breaking.* Small, 2012. **8**(10): p. 1503–1509.
109. Maier, S.A., *Plasmonics: fundamentals and applications*. 2007: Springer.
110. Khoury, C.G., S.J. Norton, and T. Vo-Dinh, *Plasmonics of 3-D nanoshell dimers using multipole expansion and finite element method.* Acs Nano, 2009. **3**(9): p. 2776-2788.
111. Ewe, W.B., H.S. Chu, and E.P. Li, *Volume integral equation analysis of surface plasmon resonance of nanoparticles.* Optics express, 2007. **15**(26): p. 18200-18208.
112. Johnson, P.B. and R. Christy, *Optical constants of the noble metals.* Physical Review B, 1972. **6**(12): p. 4370-4379.
113. Bao, K., H. Sobhani, and P. Nordlander, *Plasmon hybridization for real metals.* Chinese Science Bulletin, 2010. **55**(24): p. 2629-2634.
114. Jian, Z., L. Jian-jun, and Z. Jun-wu, *Tuning the Dipolar Plasmon Hybridization of Multishell Metal-Dielectric Nanostructure: Gold Nanosphere in a Gold Nanoshell.* Plasmonics, 2011. **6**(3): p. 527-534.
115. Wu, Y. and P. Nordlander, *Plasmon hybridization in nanoshells with a nonconcentric core.* The Journal of Chemical Physics, 2006. **125**(12): p. 124708.
116. Chu, Y., M.G. Banaee, and K.B. Crozier, *Double-resonance plasmon substrates for surface-enhanced Raman scattering with enhancement at excitation and stokes frequencies.* Acs Nano, 2010. **4**(5): p. 2804-2810.
117. Rahmani, M., B. Luk'yanchuk, and M. Hong, *Fano resonance in novel plasmonic nanostructures.* Laser & Photonics Reviews, 2012.
118. Lassiter, J.B., et al., *Fano resonances in plasmonic nanoclusters: geometrical and chemical tunability.* Nano letters, 2010. **10**(8): p. 3184-3189.
119. Chen, Y.T., R.L. Chern, and H.Y. Lin, *Multiple Fano resonances in metallic arrays of asymmetric dual stripes.* Applied optics, 2010. **49**(15): p. 2819-2826.
120. Hu, Y.S., et al., *Enhanced Raman Scattering from Nanoparticle-Decorated Nanocone Substrates: A Practical Approach to Harness In-Plane Excitation.* Acs Nano, 2010. **4**(10): p. 5721-5730.
121. Liu, N., et al., *Three-dimensional plasmon rulers.* Science, 2011. **332**(6036): p. 1407-1410.
122. Wang, H., et al., *Symmetry breaking in individual plasmonic nanoparticles.* Proceedings of the National Academy of Sciences, 2006. **103**(29): p. 10856-10860.
123. Qian, J., et al., *Two-dimensional angularly selective optical properties of gold nanoshell with holes.* Optics express, 2012. **20**(13): p. 14614-14620.
124. King, N.S., et al., *Angle-and spectral-dependent light scattering from plasmonic nanocups.* Acs Nano, 2011. **5**(9): p. 7254-7262.
125. Ashayer, R., S.H. Mannan, and S. Sajjadi, *Synthesis and characterization of gold nanoshells using poly (diallyldimethyl ammonium chloride).* Colloids and Surfaces A: Physicochemical and Engineering Aspects, 2008. **329**(3): p. 134-141.
126. Sherry, L.J., et al., *Localized surface plasmon resonance spectroscopy of single silver nanocubes.* Nano letters, 2005. **5**(10): p. 2034-2038.
127. Oubre, C. and P. Nordlander, *Finite-difference time-domain studies of the optical properties of nanoshell dimers.* The Journal of Physical Chemistry B, 2005. **109**(20): p. 10042-10051.
128. Xi, Z., et al., *Improved sensitivity in a T-shaped nanodimer plasmonic sensor.* Journal of Optics, 2013. **15**(2): p. 025004.

129. Khan, A.D. and G. Miano, *Higher Order Tunable Fano Resonances in Multilayer Nanocones.* Plasmonics, 2013. DOI 10.1007/s11468-013-9505-2.
130. Nordlander, P., et al., *Plasmon hybridization in nanoparticle dimers.* Nano letters, 2004. **4**(5): p. 899-903.
131. He, J., et al., *A giant localized field enhancement and high sensitivity in an asymmetric ring by exhibiting Fano resonance.* Journal of Optics, 2013. **15**(2): p. 025007.
132. Joe, Y.S., A.M. Satanin, and C.S. Kim, *Classical analogy of Fano resonances.* Physica Scripta, 2006. **74**(2): p. 259-266.
133. Bhatia, A. and A. Temkin, *Line-shape parameters for^{1} P Feshbach resonances in He and Li^{+}.* Physical Review A, 1984. **29**(4): p. 1895.